Investigation of the micro- and macroscopic wear properties of cemented tungsten carbide for the wear lining material selection of chutes

by

Vivian Motlalepule Motsumi

A dissertation submitted to the Faculty of Engineering and the Built Environment, University of the Witwatersrand, Johannesburg, in fulfilment of the requirements for the degree of Master of Science in Engineering.

Johannesburg, 2021

DECLARATION

Declaration I, Vivian Motlalepule Motsumi, declare that the dissertation is my own work except where otherwise acknowledged. It is being submitted for the Degree of Master of Science in Engineering in the University of the Witwatersrand, Johannesburg. It has not been submitted previously at this or any other university for any degree or examination.

_____V.M Motsumi_____

(Candidate Signature)

____14th_____ **day of** _____December_____2021_____

ABSTRACT

A series of mechanical wear and electrochemical tests were carried out on three grades of WC-Co cemented carbides to investigate the tribological and corrosive properties of the hardmetals as viable protective liners for chutes and skips. The performance of the WC-Co hardmetal was compared to three different grades of high chromium white cast irons and Hadfield steel. The cobalt binder content and WC particles size were varied: the binder content ranged from 6-12 wt% and the grain size of the WC particles ranged from 0.4-2.3 µm. The cast irons varied in their chromium content: 20.2, 22.2 and 24.5 wt%Cr. The macroscopic abrasive wear mechanisms of the materials were investigated by conducting both dry and wet rubber wheel abrasion tests. The microscopic abrasive wear mechanisms were evaluated by using the pin-on-disc tribometer. Solid particle erosion wear tests and electrochemical wear tests were included in this work to aid in ranking the performance of the investigated materials.

The WC-Co alloys performed substantially good in both wear and corrosion, followed by the HCWCI alloys. The Hadfield steel showed poorest response against all the tests. WC-12Co, which consisted of the finest grain size and highest Co content, exhibited exceptional responses to the rubber wheel abrasion test and the pin-on-disc tribometer. WC-12Co also displayed good resistance against corrosive attack in 1M H_2SO_4. However, because of its brittle nature, WC-12Co succumbed to brittle wear mechanisms during solid particle erosion and it was the HCWCI alloys that had better responses to solid particle erosion wear. The HCWCI alloys also displayed exceptional resistance against the slurry abrasion test. The main damaging wear mechanisms that the WC-Co alloys experienced were found to be binder extrusion and WC particle fallout and the main damaging corrosion mechanism was found to be the dissolution of the cobalt binder phase. The main damaging wear mechanisms experienced by the HCWCI alloys were microploughing and carbide displacement whereas the Hadfield steel mainly experienced severe microcutting. The WC-Co alloys displayed a general trend of good resistance against wear and corrosion; however, their high density means they are heavy for the area they are required to cover. Therefore, it was concluded that the best material for the application of liners would the HCWCI-22.2Cr alloy.

DEDICATIONS

In memory of my father

Thangeni John 'Daddy Cool' Motsumi

When everything seemed impossible, you would ALWAYS render words or encouragement to me. Thank you for all the sacrifices. Thank you for all the lessons. Thank you for being strong for all of us until the very last day.

To mommy dearest, Mmatlala Mirriam Motsumi, thank you for the constant confidence you have in me. You are one of a kind. Your strength is contagious and so is your positive outlook on things. Your prayers moved mountains and for that I will forever be grateful.

And finally, I would like to dedicate this work to the one Who ordained this project and the one who orchestrated this journey with goodness, love and mercy, God. Thank You Lord.

ACKNOWLEDGEMENTS

Professor H.J Potgieter, for granting me the opportunity to do my postgraduate studies. I am truly grateful for the financial support and upkeep towards my research journey. Thank you for your exceptional supervision, patience and sacrifices. Thank you for availing yourself against all odds.

Dr. D. J. Whitefield, for his guidance and support, sacrifices and exceptional supervision. Thank you for always being available to attend to my inquisitive mind concerning our discussions about WC-Co cemented carbides, high chromium white cast irons and powder metallurgy. Your advice and insight will always be treasured.

The staff of School of Chemical and Metallurgical Engineering, Wits University, to Mrs. P. Dinham, Mrs. L. Herman and Mrs. R. Burns for their tireless assistance. To Ntate Shadrack for his eagerness to always assist in the metallography laboratory. Thank you, Mr R. Gurney, from the workshop for attending to my samples. To Mr. Donald Mahole, thank you for your patience and guidance during corrosion and wear training. To Dr. M. Bodunrin, thank you for your insight pertaining which approach to take for completing this dissertation.

Mintek, thank you Melanie Smit for providing the Hadfield steel sample.

Mitak, for providing the high chromium white cast iron samples.

To my siblings and niece, (Mpakeng Motsumi, Mimi Motsumi, Sello Motsumi, and Keorapetse Motsumi), thank you for always being understanding and supportive throughout this journey. You are all appreciated.

Friends and colleagues, Nwabisa Nkanyana, thank you for being my pillar through it all. Colleagues (to the CheMet 7th floor postgrad office 'crew', a thousand thanks for all the encouragement and constructive discussions. All of you made my stay worthwhile). Finally, to a stranger that became a very important person in my life, P. Motlhaga, thank you for being my calm in this storm.

Contents

LIST OF FIGURES

LIST OF TABLES

LIST OF ABBREVIATIONS

316 stainless steel (316 SS)
Backscattered electron (BSE)
Cermet (ceramic-metal composite)
Corrosion potential values (E_{Corr})
Corrosion rate (CR)
Current density (i_{corr})
Dry sand rubber wheel abrasion (DSRWA)
Energy dispersive x-ray spectrometry (EDS)
Face centred cubic (fcc)
Hexagonally packed (hcp) (hcp)
high chromium white cast irons (HCWCI)
Mechanically mixed layers (MML)
Normalised erosion rate (E_R)
Open circuit potential (OCP)
Pin-on-disc (PoD)
Scanning electron microscope (SEM)
Secondary electron (SE)
Silver/silver-chloride (SSE)
Single edge notched beam (SENB)
Single edge precracked beam (SEPB)
Single edge v-notched beam (SEVNB)
Slurry rubber wheel abrasion (SRWA)
Specific wear rate (Ks)
tungsten carbide cobalt (WC-Co)
Vickers hardness at an indention force of 30 kg (HV30)
Vickers indentation fracture toughness (VIF)
White cast irons (WCI)

Chapter 1

1. INTRODUCTION

1.1 Background and Motivation

Transfer components such as chutes and skips play an essential role during the transportation of ore from one part of the mine or mineral processing plant to another. The operating conditions and parameters like the force of impact of the load, the velocity and the frequency of impact of the particles at the point of contact during the loading and transporting of the ore are likely to cause mechanical failure. This mechanical failure is due to the progressive loss of the material of construction of the equipment (Cortie et al., 1996). This progressive loss of the solid-body material can also be accelerated by the presence of a corrosive material. The synergistic effect between wear and corrosion is known as tribocorrosion (Lopez-Ortega et al., 2018).

Ore-transporting equipment in transfer stations are typically subjected to wear by solid-state erosion, abrasion, adhesion and sliding (Roberts et al., 1996). Abrasion in particular has been found to account for up to 50 percent of the wear experienced in the industry with erosion wear coming a close second after it (Ahmed et al., 2017). It is thus not surprising that abrasion and erosion account for a substantial amount of the maintenance costs in the mining industry, especially given the abrasive nature (hardness, geometry, and size) of the ore and overburden handled on a daily basis. This type of wear causes micro furrows and grooves which in turn hinders the movement of the particles sliding down a chute, hopper or a skip (Bowditch, 2017). Wear cannot be eliminated completely, but its damages can be limited by critically identifying the wear mechanisms at play. Failure to identify the wear mechanisms that the components are mainly prone to could result in both direct costs (replacement of consumables) and indirect costs (inventory costs and production losses) due to the premature failure of the components (Neale, Tribology handbook, 1996). Therefore, to avoid lengthy plant downtimes and production losses, the knowledge of material selection and surface engineering should be applied in an innovative manner in order to reduce damages.

Improving the service life of components by minimizing wear in the mining industry has a direct effect on the overall performance of the plant and consequently the profitability. It is therefore critical to select materials and application-specific methods of reducing wear (Solomon, 2013). Conveyance components need to possess good combinations of mechanical and electrochemical properties because they are primarily subjected to two or more wear mechanisms. In other instances, these components are exposed to a corrosive environment which might further cause a synergistic degradation effect. Hard metals and hard composite materials are widely used in these kinds of applications where components experience extreme wear and corrosive conditions. Materials such as tungsten carbide cobalt are commonly used because of their high hardness, impact strength, corrosion resistance and reasonable fracture toughness properties (Glaeser, Materials for tribology, 1992).

The ranking and selection of wear and corrosive resistant materials as well as the application thereof depend significantly on the operating conditions that the component will be exposed to (Rathod et al., 2013). To simulate the operating conditions that transfer equipment experience in service, it is essential to consider the following parameters which include, but are not limited, to particle hardness, particle velocity, particle impact angle, particle geometry, chemical compositions/make-up, and the friability of the particle (Balasubramanian et al., 2008). This information can be used by engineers to make a viable decision regarding material selection and techniques of surface engineering to be used.

In this research, three wear resistant materials: tungsten carbide cobalt, Hadfield steel and white cast iron, will be subjected to a series of mechanical and wear tests in order to quantify and select the most suitable wear resistant plates to limit wear in chutes and skips at points of contacts. Electrochemical corrosion tests will also be conducted on the three materials.

1.2 Problem Statement and Research Questions

Lengthy and frequent plant downtimes due to mechanical failure of components as a consequence of industrial wear are increasingly a fact of life in the mining industry. Chutes and skips are critical for the continuous transportation of ore and overburden from one part of a plant to another. In order to prevent production stoppages and possibly a substantial loss

of capital due to repair downtime, there has been a need to design wear resistant liners for chutes and skips that would minimise wear related failures. The following research questions will be addressed:

- What are the main differentiating wear mechanisms between tungsten carbide cobalt, Hadfield steel and white cast iron?
- What is the relationship between the microstructural properties and mechanical properties and wear resistance of tungsten carbide cobalt, Hadfield steel and white cast iron?
- How do the electrochemical properties of these materials affect their wear rate?

1.3 Research Aim and Objectives

This research is aimed at evaluating the wear response of tungsten carbide cobalt, Hadfield steel and white cast iron and determining which is best suited to be used as a wear resisting liner material at points of high impact in chutes and skips. This will be achieved by:

- Conducting laboratory wear tests to establish which type of wear has a greater effect on tungsten carbide cobalt, Hadfield steel and white cast iron.
- Determining the wear mechanisms of tungsten carbide cobalt, Hadfield steel and white cast iron under different wear conditions.
- Perform both destructive and non-destructive tests in order to determine mechanical and physical properties of the materials.
- Perform electrochemical corrosion tests.
- Compare the results from the tests carried out in order to correlate the optimum wear, mechanical and electrochemical properties of the three metals.

1.4 Hypotheses

Tungsten carbide cobalt is harder than both Hadfield steel and most conventional white cast iron grades, and because an inversely proportional relationship exists between wear rate and the hardness of a material, the wear rate of tungsten carbide cobalt is expected to be minimal compared with that of Hadfield steel and white cast iron (Schubert et al., 1997; Panchal, 2016; Ahmed et al., 2017). However, tungsten carbide cobalt is expected to be prone to sudden

mechanical fracture due to rapid crack propagation because of its brittle nature when high impact forces are experienced. All three materials are, however, expected to outperform existing conventional wear lining plates for chutes and skips.

1.5 General Layout

This dissertation has been divided into five chapters and its general layout is as follows:

1. Chapter 1 (current) introduced the topic investigated and the motivation thereof.
2. Chapter 2 is the literature review, and it provides the background on transfer chutes and skips. It also gives literature on the investigated materials viz. WC-Co alloys, high chrome white cast iron alloys and Hadfield steel.
3. Chapter 3 details the methodology and experimental procedures used to investigate the physical, mechanical, tribological and electrochemical behaviour of the investigated metals.
4. Chapter 4 presents the results obtained.
5. Chapter 5 is a summary of the conclusions of this study.

Chapter 2

2. LITERATURE REVIEW

This chapter summarises the background on transfer chutes and skips. It further focuses on the minimisation of mechanical failures of chutes and skips as a result of mass loss at points of contact by using wear- and corrosion-resistant liners. Tungsten carbide cobalt, high chromium white cast iron and Hadfield manganese steel are considered as viable material choices to use as protective liners on chutes and literature on them is also summarised in this chapter.

2.1 Bulk Material Handling Equipment: Transfer Chutes and Skips

Product conveyance stations and transfer points are essential mechanical systems in the mineral processing industry. Chutes are transfer points where conveyor belts discharge into for gravitational transport of ore. The chute either further discharges the ore onto another conveyor belt or into a skip for further transportation of the ore from one place to another. The primary purpose of the chute is receiving ore from one point and discharging it to the required location. Chutes (Figure 2.1) also play an important role in preventing extensive abrasive wear and corrosion on conveyor belts by effectively handling the required quantity of the ore. This consequently allows the burden to be centrally and evenly deposited on the conveyor belt (Rozentals, 1992).

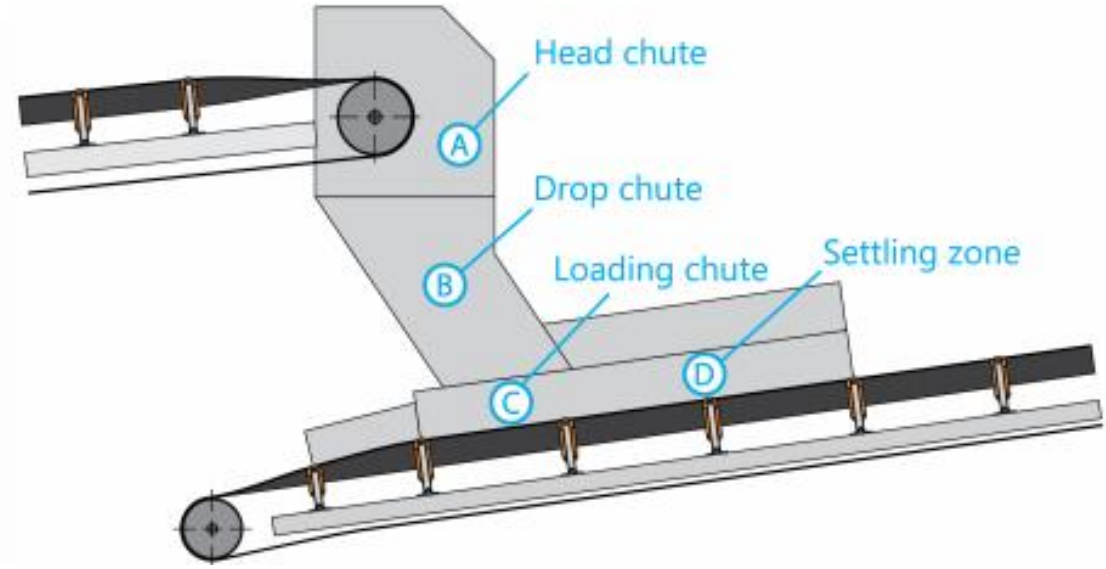

Figure 2.1: Schematic of a transfer chute *(Vreeburg, 2018)***.**

The design of a chute is generally centred on its specific application. Even though different industries have their own design rules, there still exists “rules of thumb” for designing a conventional transfer chute. Amongst the important design objectives of a chute is its ability to avoid premature mechanical failure of the chute itself as well as other peripheral components such as the skip, belt and hopper (Van Aarde, 2009). A poorly engineered chute that is prone to premature mechanical failure has a direct effect on the functionality of the conveyance equipment that precedes or/and follows it, and therefore the overall functionality of the plant (Page, 1991). This often results in the plant facing a substantial loss of revenue due to production inactivity during the repairing and replacement of components. One of the predominant causes of mechanical failure in chutes and skips is abrasive wear (Xia et al., 2019). This occurs when the surface of the transfer component suffers material loss due to the mechanical stress experienced when the particles handled make contact with the surface (Neale, 1996). The most severe wear is experienced at points where there is a sudden change in direction (Figure 2.2) (Roberts, Chute Performance and Design for Rapid Flow Conditions, 2003).

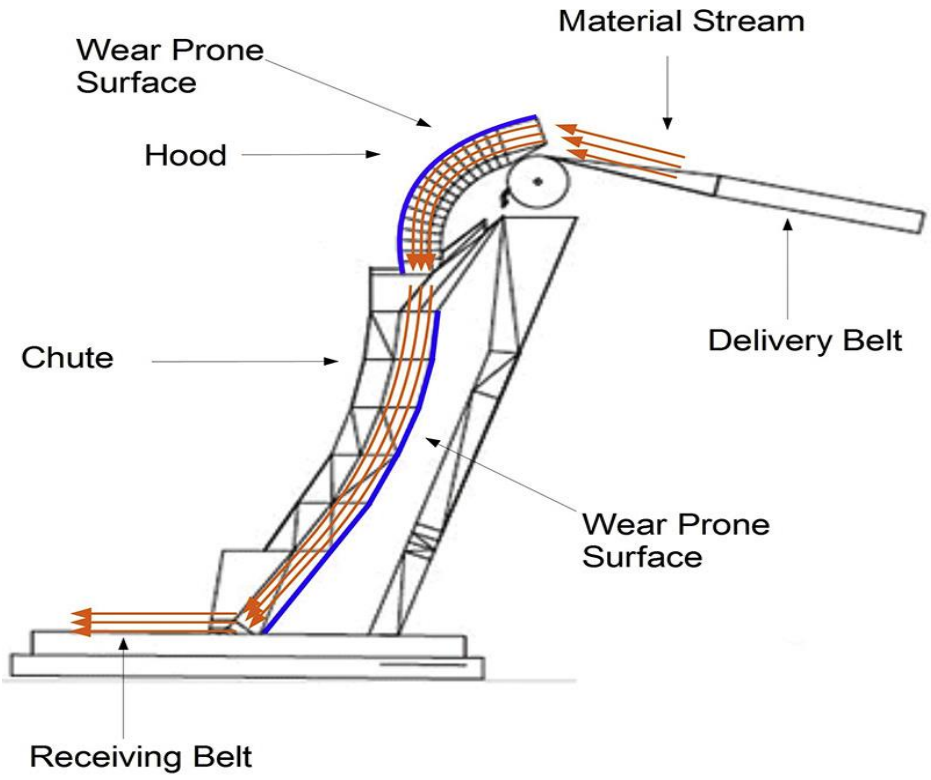

Figure 2.2: Zones that are prone to impact-abrasive wear in chutes *(Chen et al., 2017).*

There are multiple mechanisms of wear involved during the handling of ore in mines and understanding these mechanisms enables the engineer to design and develop components that are wear resistant and have a long service life (Rathod et al., 2013). One successful and commonly used method of protecting the surface of transfer components from deterioration as a result of abrasive wear is using wear lining plates. Although the lining of chutes and skips is a relatively simple concept, the study is made complex by a number of variables that need be considered such as the material's abrasivity, as well as conditions under which the equipment is being operated (Rozentals, 1992).

Lining plates or similar surface engineering methods are a means of protecting structures against damaging processes such as excessive wear and/or chemical attack. There are various types of protective liners and different application methods. Each approach is primarily guided by the elements that the structure will be exposed to. Economic considerations like

the cost of the materials, the application process and the maintenance of the plate of surface coat also governs the selection process.

2.2 Wear and Tribocorrosion Mechanisms

This work mainly focuses on the dominant wear mechanisms experienced by chutes and skips. It also focuses on the wear mechanisms that are mainly exhibited on tungsten carbide cobalt (WC-Co) during operation in the minerals handling industry. Therefore, understanding the basic wear mechanisms taking place on this material is essential. Corrosion and the effect of tribocorrosion on chutes and skips are also of interest and will be discussed.

2.2.1 Wear mechanisms

Wear is defined as the damage or deterioration on the surface of a solid body due to mechanical action, i.e., the progressive loss of material when the solid body has contact and relative motion against a counterbody (solid, liquid or gaseous), see Figure 2.3, (Zum Gahr, 1987).

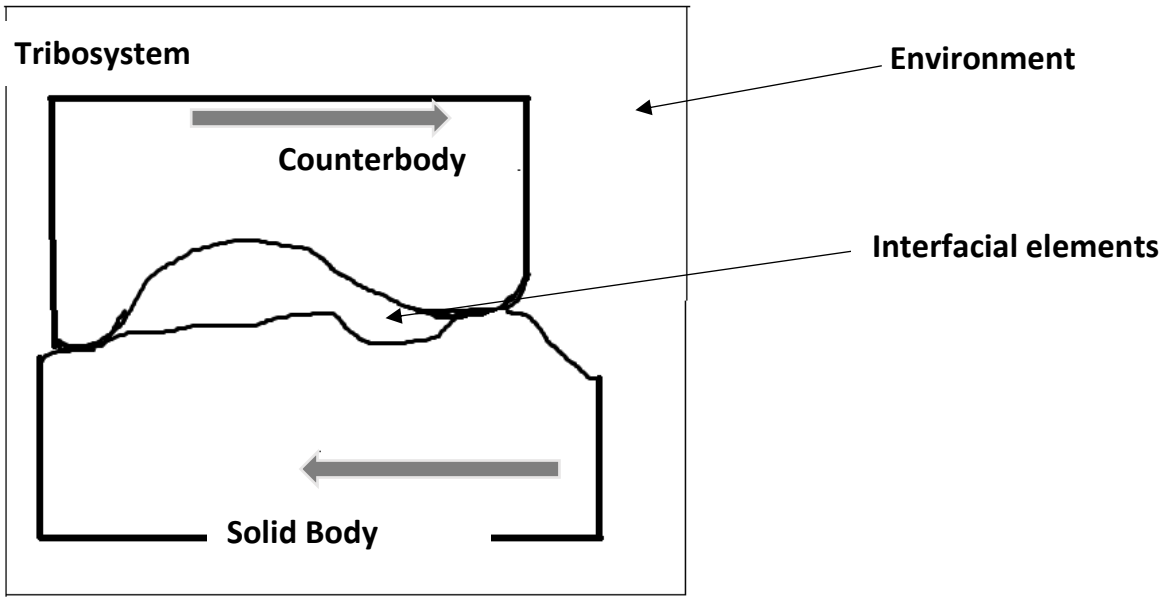

Figure 2.3: Schematic of the tribosystem. Adapted from *(Barao et. al, 2016).*

Wear is one of the characteristics of an engineering system called the tribosystem. The tribosystem consists of four elements:

- Solid body,
- Counterbody,
- Interfacial element and
- Environment.

Wear is divided into various categories depending on the nature and interaction of the elements of the tribosystem. The main categories of wear are solid particle erosion, slurry erosion, cavitation erosion, abrasive wear, sliding wear and adhesive wear. Wear by abrasion is the dominant wear mechanism experienced by chutes and skips (Xia et al., 2019). Other mechanisms of wear include solid particle erosion and wear by adhesion and pullout.

2.2.1.1 Abrasive wear

A wear mechanism is said to be abrasive when hard particles or protuberances (asperities) are forced against and slide along a surface causing the removal or displacement of material (Ndlovu, 2009). There are three conditions that are required for abrasive wear to occur, namely: an abrading particle that is harder than the surface being worn, a medium creating a contacting force between the particle and the surface being worn, as well as a sliding velocity (Glaeser, 1992). Abrasive wear can be divided into two categories: two-body wear and three-body abrasive wear. In two-body abrasive wear the damage is caused by the asperities of the particles on the counter-body whereas in a three-body abrasive wear, the abrading particles are free to rail and slide between two surfaces, (Figure 2.4) (Neale, 1996).

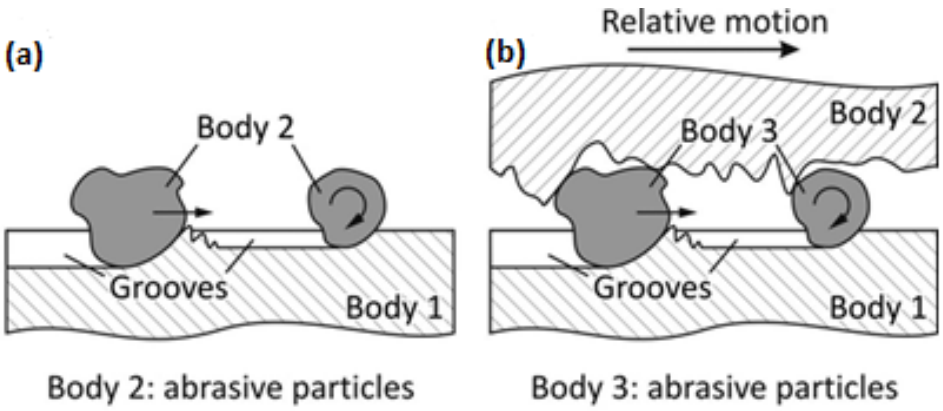

Figure 2.4: Abrasive wear process: two-body (a) and three body (b) *(Kandeva et al., 2016).*

The damage caused by two-body abrasive wear is about one magnitude greater than three-body wear (Abdelbary, 2014). This was found to be as a result of loose particles abrading the surface only 10% of the time and spending 90% of the time rolling (Chotěborský et al., 2009). The common abrasion wear process seen in chutes and skips is the two-body abrasion where the damage occurs as a result of sharp granular materials making contact with the structural components (Abdelbary, 2014). Figure 2.5 is a schematic of the material loss that occurs during two-abrasion wear in chutes and skips.

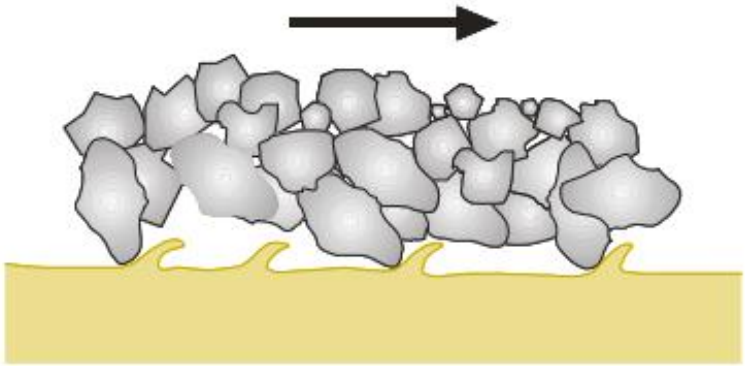

Figure 2.5: Schematic of the two-body abrasion wear that typically occurs in chutes and skips *(Abdelbary, 2014).*

There are three wear modes mostly occurring with steels experiencing abrasive wear that lead to material loss, namely: microploughing, microcutting, and microcracking. Microploughing can be identified by the surface material being pushed to both sides of a groove caused by the abrading particle and microcutting is identified by the formation of shavings, chips and fragments (Koji & Koshi, 2000). During microcracking large debris form as a result of crack formation caused by highly concentrated stresses that are imposed on hard materials by abrasive particles. Moreover, there are three types of material stresses in abrasive wear: gouging, high- and low-stress abrasion (Neale, 1996). Chutes and skips experience a two-body abrasive wear mechanism (with the exception of scraper conveyor chutes) and the two common modes of abrasive wear identified are microcutting and microcracking, the latter playing a more dominant role. The type of material stresses of abrasive wear seen in most chutes and skips in the mineral processing industry are gouging and low stress abrasion (Rozentals, 1992).

Ductile and brittle materials exhibit different modes of abrasive mechanisms. Ductile materials generally experience micro-cutting and micro-ploughing whereas micro-cracking is typically experienced by brittle materials. The main factor determining which abrasive mechanism plays a dominant role depends on the angle of attack of the abrasive particles (Bingley & Schnee, 2005). Wear resistant materials are selected based on their ability to resist large wear volumes from forming. These materials should be tough enough to prevent severe cracking and hard enough to resist ploughing and the removal of material due to cutting.

2.2.1.2 Adhesive and solid erosion wear

The other wear mechanisms are not as prominent as abrasive wear, but it is important to critically study their synergistic effect and their contribution towards material loss and ultimately the material's mechanical failure. Observations on transfer chutes and skips indicate that the products transported tend to erode on the grooves between the wear plates and ceramic tiles as well as on the grooves already created by the abrading particles on the wear plates and tiles (Van Aarde, 2009). In erosion, the extent of wear is primarily governed by the mass of the particles making contact with the surface, the striking velocity and the impact angle (Neale, 1996). Erosion is divided into two main categories: ductile erosion and

brittle erosion. The material removal on ductile materials usually occurs by plastic deformation and the material removal on brittle materials occurs by fracturing (Vaughan, 1991). Figure 2.6 depicts the eroding mechanisms occurring on ductile (a) and brittle (b) materials.

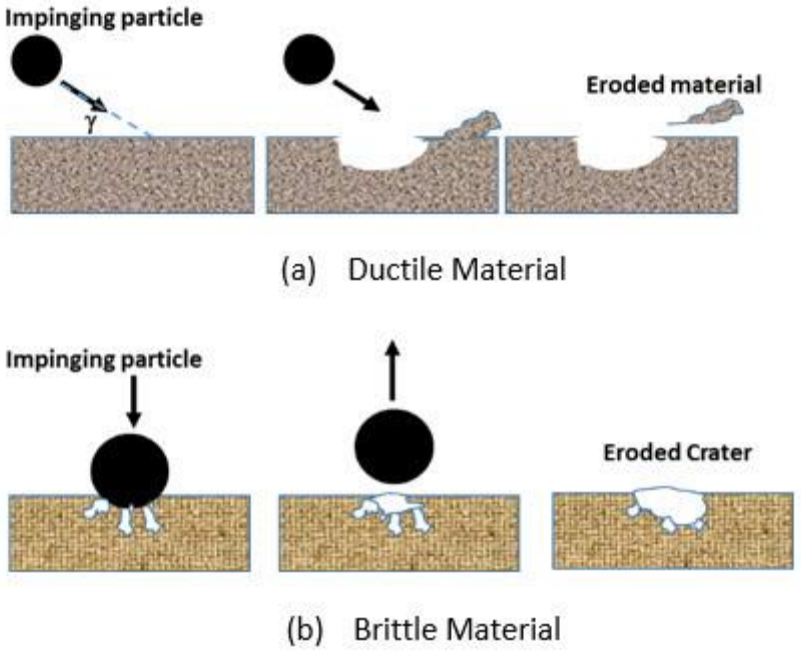

Figure 2.6: Erosion mechanism on a ductile and brittle material *(Elyyan, 2017).*

Erosion is defined as a process whereby material is removed from a surface when particles carried in either a fluid or dry medium strike the surface. The mode of erosion occurring on chutes and skips is called low speed erosion and it occurs when the transported particles impact the surface at an angle and bounces off, leading to material removal (Rozentals, 1992).

Adhesive wear (Figure 2.7) occurs when interfacial adhesive bonds form and break (Zum Gahr, 1987). The sliding of one material over the other causes localised pressure which then results in plastic deformation.

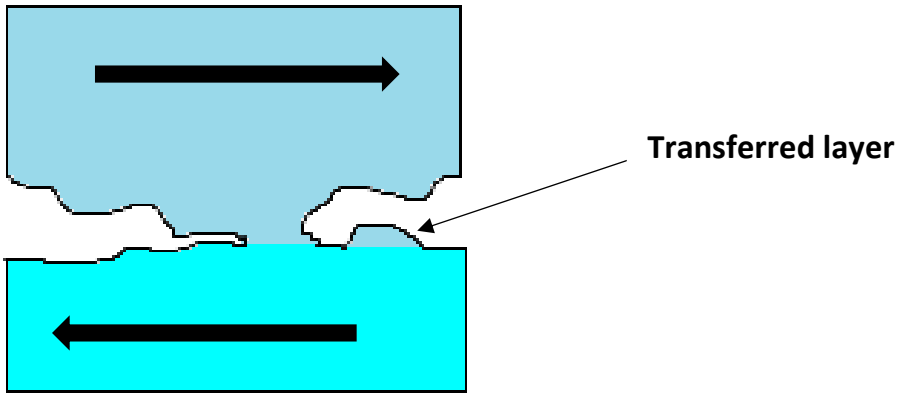

Figure 2.7: Schematic of adhesive wear. Adapted from *(Ndlovu, 2009)***.**

The strong bond formed by the asperities of the two materials adhere to each other leading to the transfer of material from the weaker material to the stronger one. While striking and sliding along the surface, the particles being transported can be embedded (adhered) into the surface causing a layer over the point of impact and subsequently acting as a wear resistant layer after some time (Neale, 1996).

2.2.2 Tribocorrosion

The main objective of conveyance stations in the mineral processing industry is to remain in service for the stipulated lifespan while operating optimally. Chutes and skips are not only subjected to degradation by mechanical wear processes, but their operating integrity is also affected by chemically aggressive atmospheres. Corrosion on chutes and skips mainly occurs where damp bulk materials are handled or where potentially reactive products are conveyed in a moist atmosphere. The electrochemical reactions occur when highly reactive products such as chemicals or contaminated material react with the metal of construction (Holmes, 1991). This ultimately leads to the deterioration of metal thus compromising the overall performance of chutes and skips. Therefore, the thermodynamics and kinetics of corrosion on materials and the dual tribo-corrosive effect should be adequately understood when selecting a protective lining material (Lopez-Ortega et al., 2018).

2.2.2.1 Tribocorrosion mechanisms

Tribocorrosion involves complex mechanical-chemical interactions between two bodies in relative motion (López-Ortega et al., 2018). It covers the science of surface transformation resulting from the interaction between the elements of tribology (wear, friction, and lubrication) and chemical environment (corrosion) (Fischer & Mischler, 2006; Mathew et al., 2009). Figure 2.8 shows the basic concept of tribocorrosion in a form of a flow diagram.

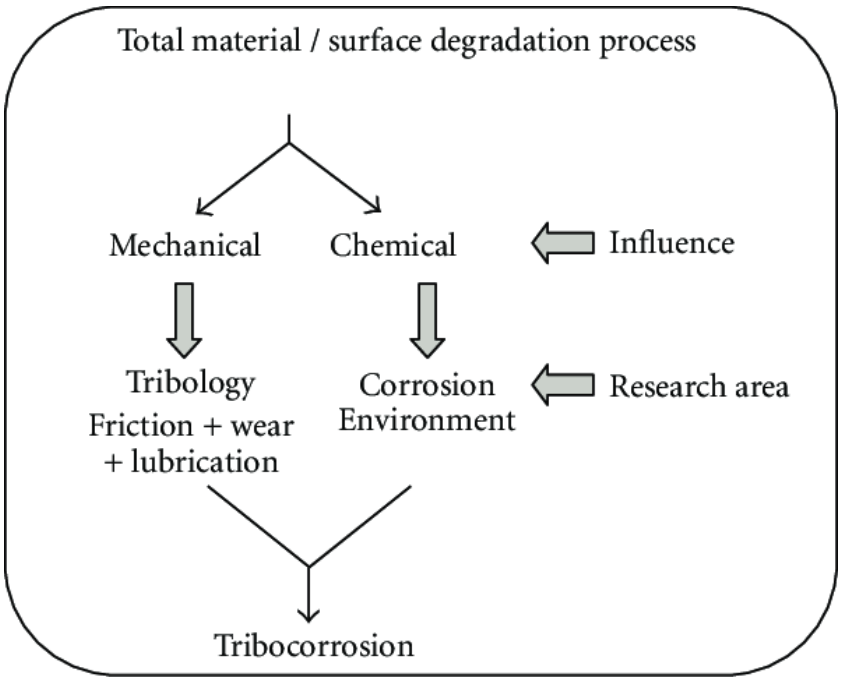

Figure 2.8: Basic concept of tribocorrosion *(Mathew et al., 2009).*

In tribocorrosion the surfaces of the materials experience both wear and corrosion. If the tribocorrosion process is not controlled then the materials involved undergo relative displacement, loss of performance and even system failure. Understanding the mechanisms of tribocorrosion is very important for the research, development and material selection for materials in service that are exposed to both mechanical and electrochemical attack (Mathew et al., 2009). The main characteristics of tribocorrosion include the following (Landolt, 2004; Celis et al., 2009):

- The transformation of the material is permanent,

- Occurs in conditions where mechanical contact like abrasion, sliding and erosion are present and
- Consists of numerous synergistic effects of chemical, mechanical, and/or electrochemical nature.

The parameters affecting tribocorrosion have a significant impact on the severity of the damage on the surface of the bodies. The main parameters involved are the type and range of the normal load, the contact size, the contact frequency, and the chemical environment. The composition, surface roughness, residual stresses and the crystallographic texture of the material are also important parameters that affect tribocorrosion (Celis, 2009).

Tribocorrosion consists of both the mechanisms of wear and corrosion. The main mechanisms of corrosion seen on the surfaces of the loaded and unloaded materials in the mining industry involve localised corrosion, abrasion-corrosion, and galvanic coupling (Celis, 2009; Czichoz et al., 2011). Amongst the common mechanisms of wear, tribochemistry is the most complex, but because of the nature of its occurrence, it is rarely associated as a damaging mechanism on chutes and skips (Marinescu et al., 2013).

2.2.2.2 Localised corrosion

Localised corrosion consists of intense forms of corrosion where the attack on localised sites is more destructive and rapid than it is on the rest of the surface (Frankel & Sridhar, 2008). Localised corrosion is defined as the selective breakdown of metal on the surface of a body. It occurs when the protective passive layer on the surface of a metal is removed in a corrosive environment. What makes localised corrosion one of the most damaging types of corrosion is because it simultaneously takes place with other destructive mechanical processes such as abrasion, erosion and mechanically induced stresses (Jones, 1996).

The fundamental understanding and prediction of localised corrosion (Figure 2.9) is a rather complex concept despite the vast research and advanced developments that has been made. The complexities arise from several reasons including the short timescale in which the entire process takes place (Frankel & Sridhar, 2008). The thickness of the passive film is almost the same size as the initiation sites. The similarity in sizes coupled with the small dimensions in which all events occur causes the pit growth to be sudden and fast (Holmes, 1991). This

further causes pit formation and growth to be very dynamic with frequently changing chemistries (Frankel & Sridhar, 2008).

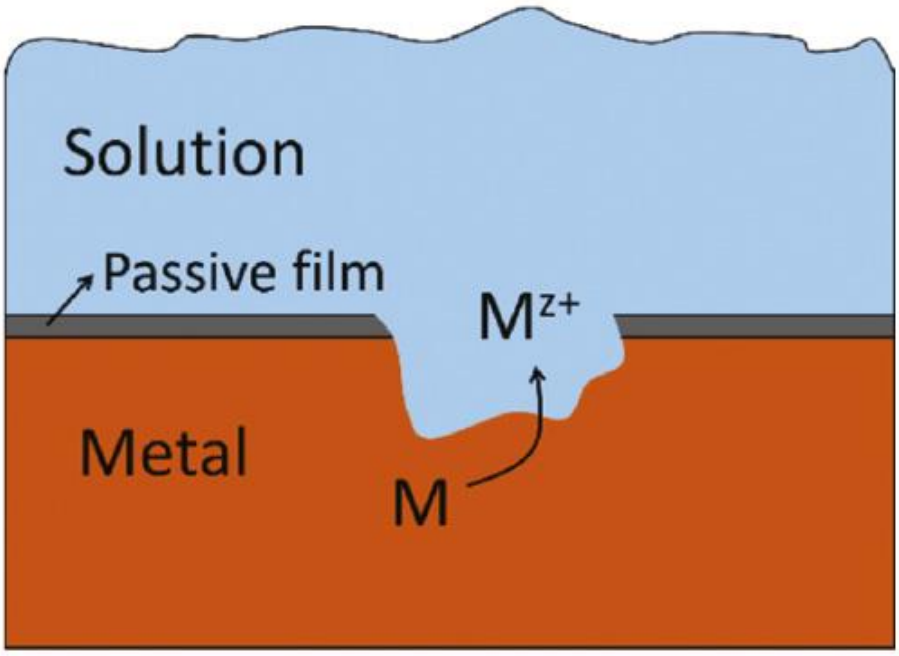

Figure 2.9: Schematic of the basic mechanism of localised corrosion *(Jafarzadeh et al., 2019).*

What makes the prediction and detection of localised corrosion even more complicated are the microenvironments in which the corrosive sites occur. These corrosive microenvironments are different from the bulk environment both in chemistry and stochastic nature (Cuffari, 2020).

There are many different forms of localised corrosion. Pitting corrosion and crevice corrosion are the two common localised forms of corrosion that are often observed on chutes and skips (Mishra & Pak, 2006). If the deterioration of the corrosion protective layer occurs under a confined space or deposit (such as a weld deposit or bold heads where the circulation of oxygen is restricted) then the attack is called “crevice corrosion”. If the initiation of the attack is on a free surface and grows into a “hole” or “cavity” the attack is termed “pitting corrosion”. Pitting and crevice corrosion both occur in stagnant microenvironments (Frankel & Sridhar, 2008; Cuffari, 2020).

Crevice corrosion (see Figure 2.10) occurs when the crevice (crack) accumulates water at its tip where the environment is slightly deoxygenated. The tip becomes anodic while the rest of the components remains cathodic creating a differential aeration cell (Revie & Uhlig, 2008).

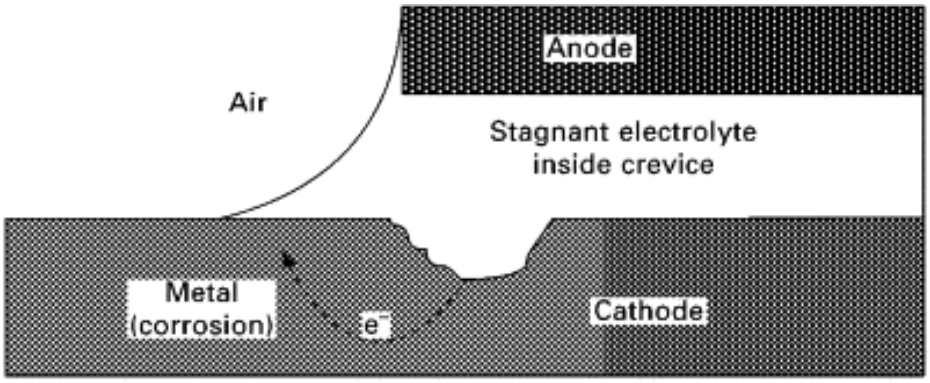

Figure 2.10: Schematic of the basic mechanism of crevice corrosion *(He et al., 2008).*

Pitting corrosion can occur either in chemically aggressive environments or in homogeneously normal environments. The former takes place when a defect-free surface is exposed to chemically damaging species like chloride which specifically target passive films (oxides). In homogeneous environments the pit initiation is caused by inclusions on the materials such as MnS on steels. However, in most instances, pit initiations can occur because of synergistic effects between both the aggressive environment and a defect on a material (WebCorr, n.d).

2.2.2.3 Galvanic corrosion

Galvanic corrosion (also known as bimetallic or dissimilar metal corrosion) occurs when the damage caused by corrosion results from the coupling of two dissimilar materials in an electrolyte. It is an electrochemical process induced by the presence of an electrolytic medium such as seawater. The two dissimilar metals are either immersed in a conductive liquid or regularly connected by moisture, creating a corrosive environment whereby one material corrodes in preference to another material (Frayne, 2010). The material that corrodes in preference to the other (at an accelerated rate in comparison to the other) will

behave as the anode while the protected metal behaves as a cathode (Frankenthal & Sinclair, 2001). A measurable potential difference between the two electrodes is the driving force behind the galvanic corrosion reaction. The larger the potential difference between the two metals, the faster the galvanic corrosion reaction occurs (Pirolini, 2015). Figure 2.11 is the schematic showing the galvanic corrosion process.

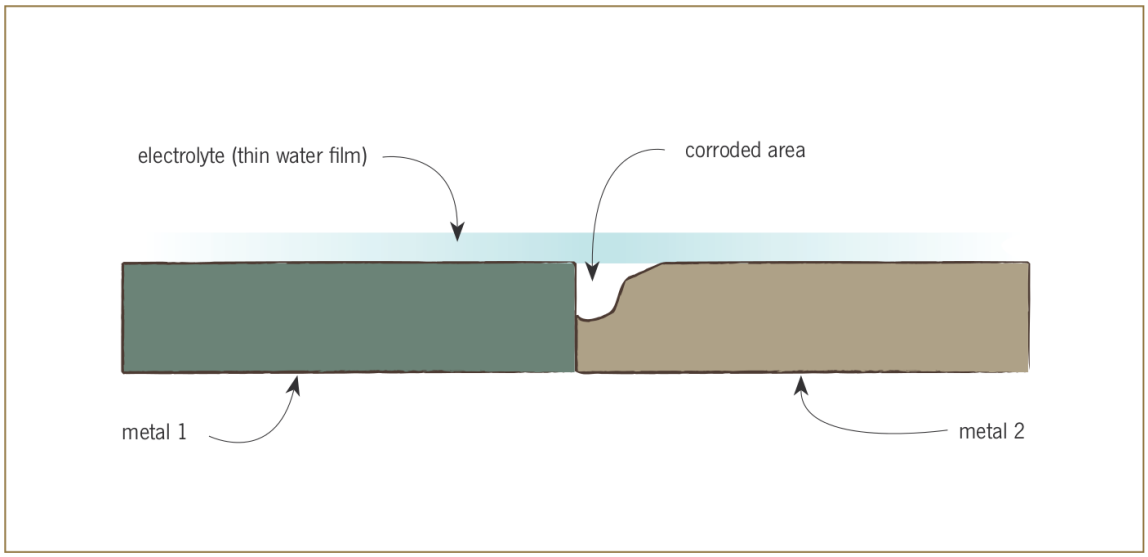

Figure 2.11: Schematic showing the process during the galvanic corrosion process *(Li, 2009).*

Galvanic corrosion occurs when the following conditions are satisfied (Frayne, 2010):

1. The metals must be dissimilar with different potential difference,
2. The metals must be in direct electric coupling (contact), and
3. A conductive path must be created when the metals are immersed or exposed in an electrolyte.

Galvanic corrosion only occurs when all three elements are present. In chutes and skips, this mode of corrosion happens mostly on and around bolts or welded regions were dissimilar materials are in direct contact with each other.

2.2.2.4 Abrasion-corrosion

The abrasive resistance of most equipment in the mining and transportation industry is not solely dependent on the properties of the materials of construction, but also on the loading

and the environmental conditions (Ball & Ward, 1985). Wear and corrosion processes consist of many complex mechanical and chemical mechanisms and the combined effect of the two processes can lead to significant material degradation (Schumacher, 1985). Research on abrasion-corrosion specifically plays a crucial role in the understanding of most tribological and chemical systems especially during the designing and selecting of corrosive-wear resistant materials mainly used in the mining and mineral processing industry (Allen, 1981). The damage caused by mechanical wear and corrosion on materials used in the mining and minerals processing industry has been traditionally accepted as inevitable. However, with the repairing and maintenance costs rising because of the combined effects of the two processes, there has been a need to improve the durability and efficiency of existing and new equipment (Allen, 1981).

Abrasion and corrosion processes have always been studied as two separate phenomena and their combined effect summed up for quantification. This was because of the complexities associated with the corrosion-wear processes and the multiple experimental variables that the material is subjected to such as pH, oxygen partial pressure, hardness of the two surfaces in relative motion, load and the passive film on the metal surface (Pitt et al., 1988). It was Zelders (1949) who carried out the first systematic research and investigation that linked the interaction between abrasion wear and corrosion and showed that the conjoint effect of the two processes creates greater damage than the summation of the individual processes. A method of measuring abrasive-corrosive wear resistance in the laboratory was developed by Ball and Böhm (1987). They simulated service conditions similar to those of transfer conveyors operating in gold mines on metals relative to mild steel. The tests were performed over a wide range of materials and the conclusions they made about the interaction between abrasion and corrosion on metal surfaces agreed with those made by Zelders (1949).

Research that followed provided more evidence that the synergistic interaction between abrasive and corrosive processes showed accelerated material loss and degradation on the surface of the metal (Pitt et al., 1988). From thereon, it has been evident that mechanical wear and corrosion affect each other interchangeably. The rate and thickness of the passive film, the friction, and surface properties of the metal affects the wear characteristics of the metal, whereas mechanical wear can, in turn, affect the rate of corrosive degradation of the

metal by interrupting the nature and formation of the passive film on the surface (Pitt et al., 1988).

2.2.2.5 Corrosion of WC-Co

The corrosion behaviour of the two-phased WC-Co alloys is predominately affected by the content of Co. In his work, Human (1994) showed that the process of corrosion on WC-Co hardmetals favours the selective dissolution of cobalt. He also found that the corrosion attack on the binder phase is strongly affected by the dissolution of tungsten in the cobalt during manufacturing (liquid phase sintering). The WC particles of the hardmetals can also corrode, but this only occurs at significantly high potentials (Sebeya, 2013). The process of corrosion of WC-Co hardmetals are shown in Equations 2.1 and 2.2 (Human, 1994).

$$Co \rightarrow Co^{2+} + 2e^{-} \quad \text{(Equation 2.1)}$$

$$WC + 5H_2O \rightarrow WO_3 + CO_2 + 10H^{+} + 10e^{-} \quad \text{(Equation 2.2)}$$

In their studies, Human and Exnar (1996) investigated the other properties of WC-Co hardmetals that could possibly influence their corrosion rate/resistance and it was found that grain size had no effect on the electrochemical attack of the hardmetals in 1M of H_2SO_4. The general trend observed was that the corrosion rate of WC-Co alloys increased with the increase in Co content.

2.3 Material Selection for Wear-Corrosion Resistant Liners

Material selection for a specific component is generally made based on the induced strain and stresses (acting forces) that the component is subjected to. Due to the intrinsic nature of wear, quantifying a specific material is a challenge (Zum Gahr, 1987). For instance, a specific type of material is able to show varying modes of wear and mechanisms when a force is imposed on it. This material of construction can exhibit excellent resistance to abrasion but show poor erosion resistance (Glaeser, 1992). It is thus worth noting that when selecting materials to be used for their ability to resist wear in chutes, the relative ranking of materials

is fundamentally dependent on the operating conditions as well as the mechanical properties which, when combined, must withstand the mechanical strains and stresses during operation.

The metallurgical properties of a material such as its hardness, strength and ductility are of utmost importance and should be taken into careful consideration during the ranking and selection of a wear resistant material for chutes and skips (Holmes, 1991). During the loading of material on chutes and skips the directly impacted zones can be expected to wear out more frequently than on the sides of the structures. These directly impacted areas should therefore be specifically addressed in order to prevent chutes from major damage (Gates, 2003). This can be achieved by protecting these regions of contact with special wear liners made from suitable materials (Holmes, 1991).

2.3.1 Hadfield manganese steel

Metallic and synthetic materials such as steels and rubber are broadly used as wear linings to prevent chutes and skips from major damage. Linings made from martensitic steels are frequently being replaced by alternative solutions because of their brittle and hard to fabricate nature (Sipos et al., 2013). Manganese steels and chromium molybdenum steels are also widely used for the lining of chutes and skips because of their excellent mechanical properties and resistance to wear. However, to prevent the cracking of these steels the thickness of manganese and chrome molybdenum has to be at least 25mm, making this a heavy and costly solution (Holmes, 1991).

It is well known that steels are common in the mining industry. This is because steels are easily available and can be manufactured easily. Steels are also extensively used in this industry because their mechanical and microstructural properties can be controlled by exploiting their phase transformations (Chintha, 2019). One steel that has been noted for its remarkable properties in the mining industry, is Hadfield steel. Hadfield steels are high manganese steel alloys that usually contain 10-14% manganese and 1.0-1.4% carbon in a 10:1 ratio (Srivastava & Das, 2008).

High manganese steels are traditionally used as wear-resistant alloys in harsh applications where high fracture toughness and moderate resistance to corrosion are required (Tikotkar,

2012; Xiaodong et al., 2009). The fine grain structure of high manganese steel enhances its mechanical properties and one way of achieving this type of a grain structure is by using low superheats during the pouring of the steel when casting. Alloying elements such as Ti can also be used as grain refiners in Hadfield steels (Havel, 2017). Other alloying elements such as Cr, Mo, and V are added for additional special applications such as increasing the solution-annealed hardness, tensile strength and the flow resilience of Hadfield steels (Sabzi & Farzam, 2019; (Havel, 2017). The as-cast condition of Hadfield steel has $(Fe,Mn)_3C$ carbides (Sant & Smith, 1985). In order to obtain an austenitic structure, the material is solution-annealed for a few hours at 1050°C and then quenched in water. What remains after a successful heat-treatment procedure is a uniform single-phase austenitic structured material at room temperature (Figure 2.12)(Brooks, 1996).

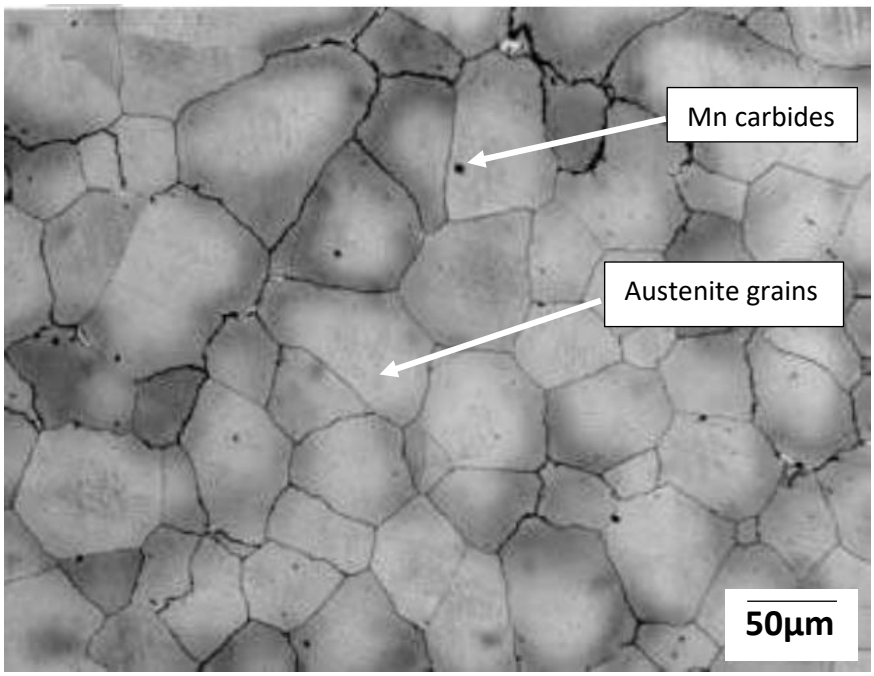

Figure 2.12: Microstructure of Hadfield steel after undergoing heat treatment *(Panchal, 2016)*.

The excellent toughness of Hadfield steel is due to its single austenitic phase structure after being heat-treated. The steel normally reaches a hardness of 220HB (222HV) after it has been annealed and water quenched. However, the hardness can reach approximately 500HB (531HV). This high level of hardness is as a result of the ability of this steel to work-harden. This occurs when a strong layer on the surface of the steel forms during deformation by

impact (Zhang et al., 2005). The strain hardening occurs as a result of large disturbances created in the lattice and crystals of the structure. The interior, however, still retains its toughness as the hardness increases (Zhang et al., 2005). The remarkable ability of the Hadfield steel to work-harden makes it amongst the best material choices for protection against different mechanisms of wear and corrosion. This material is frequently used in demanding applications where the main wear mechanisms are high load impact wear and high abrasive wear such as what is experienced in crushing and excavation equipment (Subramanyam et al., 1990).

There has been a considerable number of studies focusing on the mechanisms and rates of wear experienced by Hadfield steels during operation and it has been found that high impact and high abrasive (gouging) wear are the two dominant wear mechanisms experienced by these steels (Vdovin et al., 2018; Chintha, 2019). In order for this material to exhibit exceptional hardness and thus an effective wear resistant liner in chutes and skips, these two wear mechanisms have to be extremely high during operation (Subramanyam et al., 1990). Hadfield steels show poor wear resistance in cases where the working conditions are not severe enough for the surface to be sufficiently work-hardened (Efstathiou & Sehitoglu, 2009). The mistake that is mostly made when selecting Hadfield steel as a lining plate for chutes and skips against wear is overlooking the common failure mechanics that occur during operation on both the equipment that requires lining and the lining material itself. Microscopic observations show that Hadfield steels exhibit non-uniform deformation and work hardening on the surface (Olawale et al., 2013). This, coupled with localised strain and the fact that chutes and skips mainly exhibit low stress abrasion and low impact wear that may not be high enough to cause surface hardening, the Hadfield steel may prove to be a poor choice as a liner (Okechukwu et al. , 2011; Havel, 2017; Holmes, 1991).

Particle reinforced materials such as hardmetals and ceramics are gaining popularity in the mining industry because of their ability to offer dramatic wear improvement of about 10 times the life of martensitic steels (Gates, 2003).

2.3.2 Tungsten carbide cobalt

In metal matrix composites (hardmetals) the wear properties are the most important mechanical properties. This is because the metallurgical properties of hardmetals such as tungsten carbide-cobalt are favourable in applications where most materials would otherwise wear quickly (Ndlovu, 2009). Tungsten carbide-cobalt, otherwise known as cemented tungsten carbide, offers excellent wear properties due to the combination of hard carbide particles in a binder (Exner, 1979). Cemented tungsten carbides are hard monocarbide grains cemented in a soft binder matrix of tough cobalt metal by liquid phase sintering (Göken & Kempf, 2001). The high solubility of tungsten carbide in cobalt is a result of the intermolecular interaction when the two are brought together at high temperature. This excellent carbide wetting and adhesion result from the liquid cobalt capillary action during sintering to give a structure of low porosity. The resultant structure after sintering has little porosity, high strength, toughness and hardness that are ideal for wear lining plates of chutes and skips (Meredith & Milner, 1976). Figure 2.13 is an SEM micrograph of WC particles (lighter phase) cemented in a cobalt matrix (darker phase).

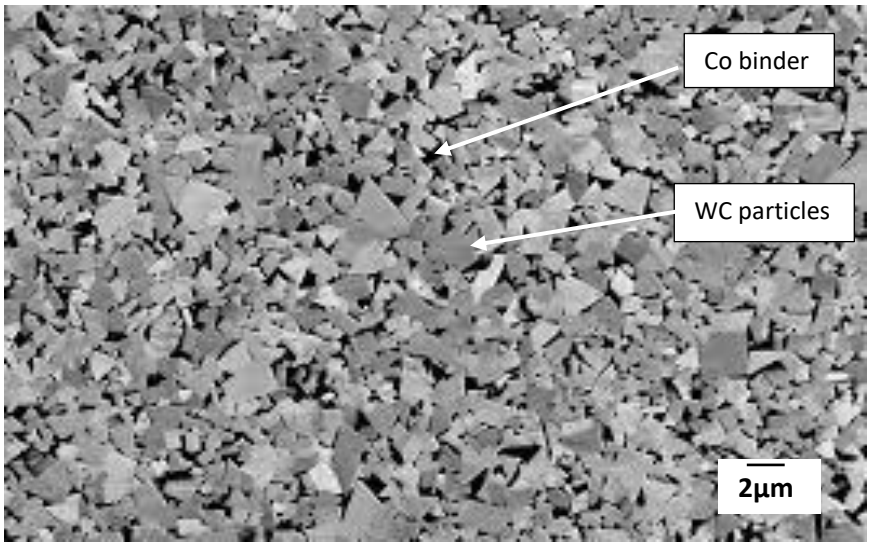

Figure 2.13: Tungsten carbide particles in a cobalt matrix *(Yousfi, 2016)*.

Cobalt is the commonly used binder for WC. This is because cobalt has excellent wetting and adhesion properties. Cobalt is also an excellent binder because of its capillary action during sintering allowing for the achievement of high densities (Da Silva et al., 2001). Cobalt exists

as two allotropes depending on the temperature it is exposed to. At temperatures below 417°C cobalt is stable as a hexagonally packed (hcp) structure whereas the face centred cubic (fcc) structure becomes stable up to its melting point of 1495°C (De la Peña O'Shea et al., 2009; Qiao, 2020; Ogwu & Davies, 1992).

The allotropic transformation of cobalt is also affected by the amount of WC dissolved between two carbide particles (the binder mean free path). Ultrafine structured hardmetals have a higher fcc/hcp ratio than conventional ones. This is due to a high concentration of tungsten in the binder phase (Jia & Fischer, 1998).

WC and W_2C are the two carbides that form when tungsten particles combine with carbon (Figure 2.14). The major carbide phase is the monocarbide WC which has a maximum microhardness of between 10Gpa to 24Gpa at room temperature (French & Thomas, 1965). WC has a simple hexagonal crystal form with two atoms per unit cell (Exner, 1979).

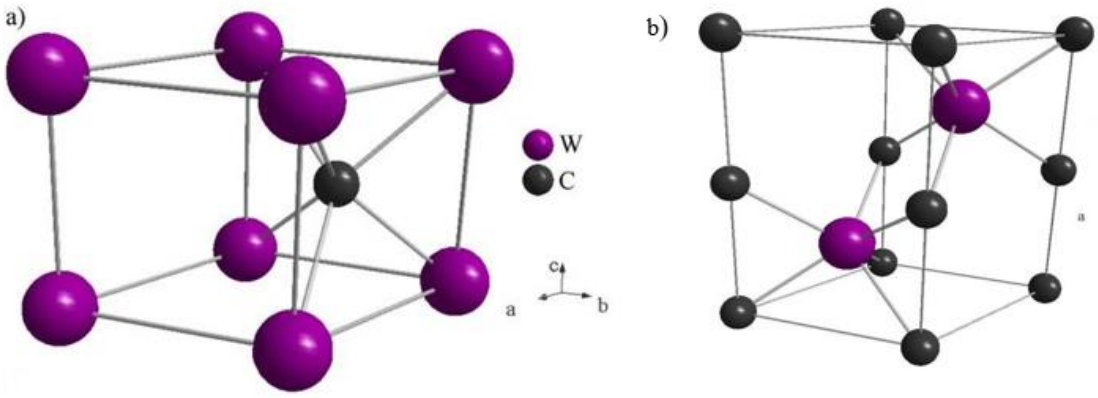

Figure 2.14: Structural representations of tungsten carbide: a) WC and b) W_2C *(Vallance et al., 2012).*

The microstructure of tungsten carbide accounts for the material's high hardness whereas the cobalt acts as the softer binder. Maximum impact and transverse rupture strength depend on the microstructural properties of tungsten carbide, such as grain size as well as weight content of the binder. Cemented tungsten carbide linings are not a popular solution against wear in the mining industry because of their weight and initial high costs. However, different methods of surface engineering for the application of this hardmetal that would reduce its

weight factor, are currently being designed. This would result in a solution that gives maximum protection against wear for chutes and skips at potentially lower cost. This could increase service life and prevent costly and repetitive down time (Holmes, 1991).

Another cermet (ceramic-metal composite) that has gained popularity in the mining industry as a protective liner against wear and corrosion is chromium carbide.

2.3.3 High chromium white cast iron

White cast iron is an alloy that is popularly used for structural components in the mine and mineral industry because of its exceptional resistance to abrasion and impact wear. The composition of the white cast iron, as well as its morphology, renders it brittle and difficult to machine but because of its high hardness, wear resistant properties and low costs, it is highly sought after as a wear resistant material in the mining and mineral processing industry (Imurai et al., 2015).

The white cast iron gets its name from the silver-like white cracks throughout the metal (CorrosionPedia, 2016). Its white surface is as a result of the carbide impurities that allow light through its cracks when fractured. White cast irons have a light appearance as a result of the absence of graphite. It is unique in a sense that it is the only member in the cast iron family where all the carbon content (mainly greater than 2%) exists only as carbide. The absence of graphite occurs during the solidification process where the carbon in solution precipitates into a metastable phase cementite (Fe_3C) (CorrosionPedia, 2016; Domeij, 2019). Low silicon content and the rapid cooling rates also allows for the formation of Fe_3C instead of graphite A typical microstructure of white cast irons consists of dendrites of pearlite (transformed austenite) in an interdendritic network of Fe_3C. The large white areas are the interdendritic networks of Fe_3C whereas the dark areas are pearlite (Figure 2.15) (Lavakumar, 2017).

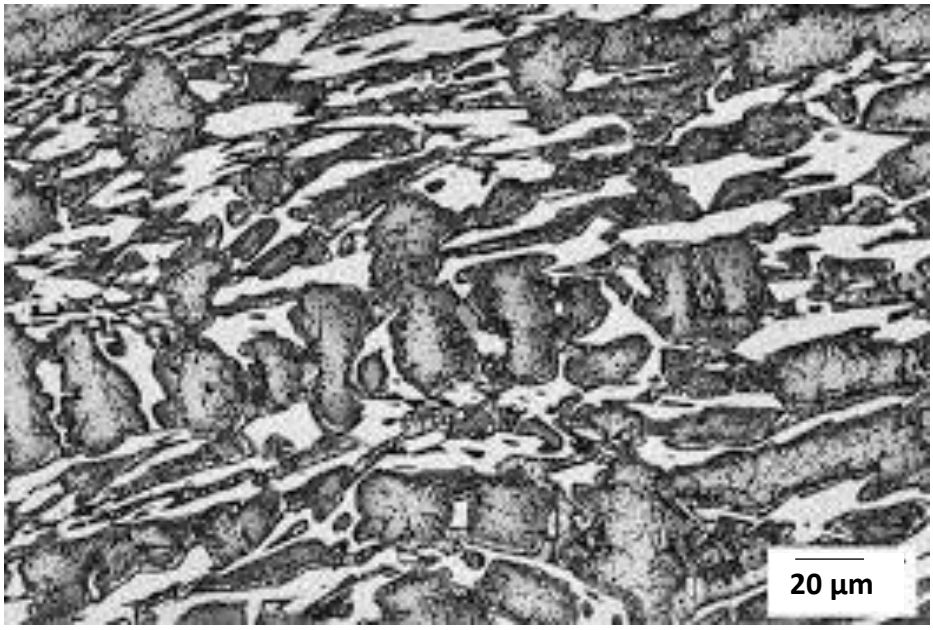

Figure 2.15: Optical micrograph showing microstructure of white cast iron *(Filipovic et al., 2012).*

Typical unalloyed white cast irons have Brinell hardness in the range of 375-600 and their high content of carbide impurities in their systems make it reasonable for white cast irons to be categorised under the cermet family.

White cast iron can be classified into three main categories (Ngqase & Pan, 2019):

1. Normal white cast iron,
2. Low-alloy white cast iron, and
3. High-alloy white cast iron.

Normal white cast irons consist only of C, Mn, P, Si, and S as alloying elements. Silicon in white cast irons causes the decomposition of cementite which results in graphite being released into the system. Because of its graphitising effect, silicon must exist in low contents (Rubin et al., 2018). Sulphur and phosphorous are cementite-stabilising agents in white cast irons. However, these elements are known to cause brittleness and must either be contained in small quantities or be controlled by adding manganese. Manganese controls the effects caused by P and S, and it also increases the strength of white cast irons. Vanadium is added to increase the bulk hardness in white cast irons by forming hard vanadium carbides (Liu et

al., 2005). The addition of vanadium acts as a eutectic carbides refiner and also increases the volume fraction of the M_7C_3 primary carbides (Filipovic et al., 2012).

Low-alloy white cast irons consist of a total mass fraction of alloying elements that is more than 5% whereas high-alloy white cast irons have a total mass fraction of alloying elements that is more than 5% (Ngqase & Pan, 2019). The three categories of white cast irons are found to have similar structures (Dogan et al., 1997). White cast irons are used as lining plates for hoppers, feeders and chutes where resistance against abrasion, impact, rolling and sliding is required. White cast irons with high chromium content (also known as abrasion resistant cast irons) are currently gaining recognition in applications where high abrasion and corrosion resistance is imperative (Ngqase & Pan, 2019).

White cast iron that consists of high chromium content, called high chromium white cast irons (HCWCI), fall under the high-alloy white cast irons category. The composition content of chromium is normally between 10-30 wt. %Cr and 2-3.5 wt. %C. This chromium content along with other alloying elements create a superior combination of toughness and abrasion and corrosion resistance (Karantzalis, 2009). High chromium white cast iron owes its exceptional wear and corrosion resistance properties to their Cr-rich carbide content. The toughness of the matrix also contributes to its good wear properties (Laird George, 2000; Doğan et al., 1997). Hypereutectic HCWCI have high volume fractions of hard carbides in their system which are ideal for better abrasion resistance (Liu et al., 2005). However, in their hypereutectic form, HCWCI alloys contain larger and coarser primary carbides that render them too hard and brittle for commercial use. Therefore, improvement to the microstructure by refining the eutectic carbides is essential. HCWCI can be used as hard-facing and as a coating on a materials surface (Lotta & Hannula, 2015).

High chromium white cast irons are not only exceptional against severe abrasive and erosive environments, but they have also proven to perform excellent against different corrosive environments. Their resistance to chemically attacking environments, such as reducing acids, has been found to be strongly influenced by the presence of high levels of alloying elements (Tanga et al., 2011). Tian et al. (2009) and El-Aziz et al. (2015) reported that alloys that contained high ratios of Cr/C in their microstructures were the most suitable in resisting damage by corrosion. This entails that the carbon content has to be relatively low so that

excess concentrations of chromium can be found in the matrix to further improve the corrosion resistance of the matrix (Tanga et al., 2011). Furthermore, El-Aziz et al. (2015) discovered in their work that a high volume fraction of large bulky primary carbides in the form M_7C_3 were advantageous against harsh corrosive environments over secondary carbides and primary eutectic carbides.

The deposition of HCWCI onto surfaces is a cost-effective technique that prevents accelerated mechanical failure of large structures such as chutes and skips. This is because overlaying methods like cladding and hardfacing techniques such as thermal spraying can easily cover large areas while providing exceptional tribo-corrosive resistance at a density that is half of that of tungsten carbide (Espallargas et al., 2013).

2.4 Mechanical Properties

2.4.1 Hardness and fracture toughness

The hardness and toughness of a material are the two most important mechanical parameters in engineering and material sciences. The hardness of a material as well as its toughness can reveal other important properties such as the material's strength, its wear resistance and ductility. This allows the engineer to determine the applications that the material is best suited for (Mulser et al., 2014).

The hardness of a material is an indication of its permanent (plastic) deformation. It is a measure of the material's ability to resist indentation, penetration and scratching. Therefore, the hardness of a material is an important property to know from a material selection standpoint for an application where wear is involved.

The hardness of a material is a relatively easy property to measure. There are different hardness testing methods that have developed over the centuries. The four most commonly and widely accepted methods for measuring hardness are (Obianyo, 2019):

1. Knoop hardness testing
2. Brinell hardness testing
3. Rockwell hardness testing
4. Vickers indentation hardness.

The most popular method for testing for hardness on hardmaterials like cermets is the Vickers indentation test. Figure 2.16 is a pictorial representation of the indentation testing method. The Vickers hardness test is an optical testing method that makes use of the size of the indentations in order to measure the hardness value. The indentations (the diagonals) are left by a diamond indenter of a specified load. The indenter (commonly 30kgf) is a square-based pyramid having included angles of 136°. The smaller the indent on the surface of the test piece the harder the material is (Broitman, 2016).

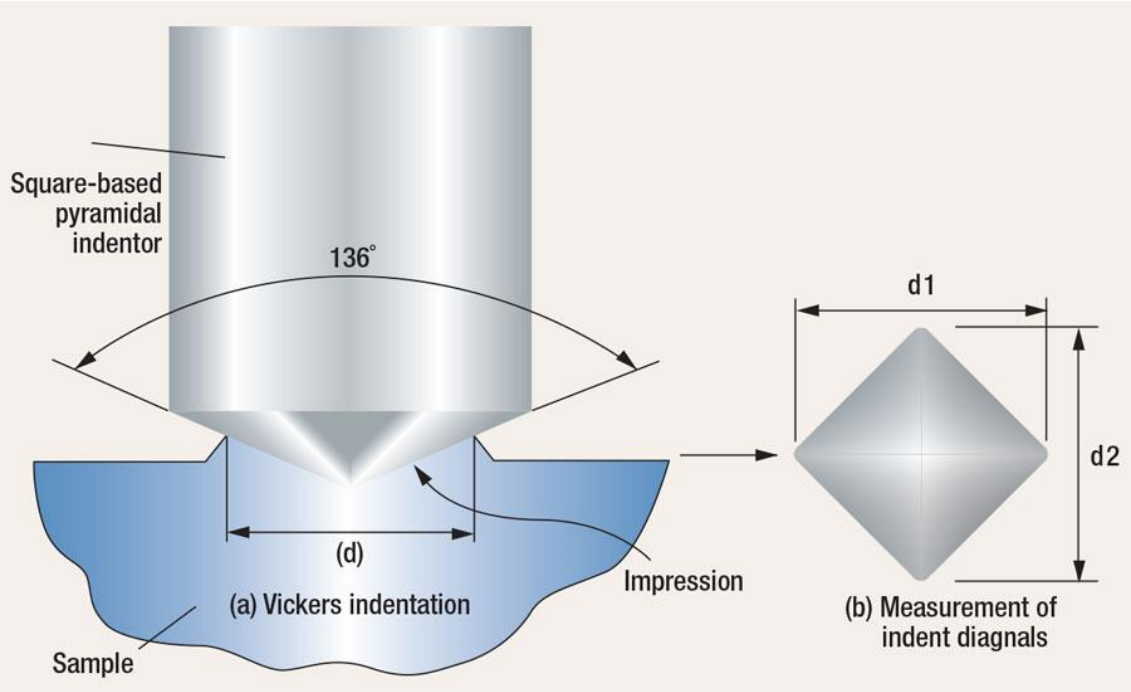

Figure 2.16: Schematic of a Vickers hardness indentation testing method *(Byrd, 2016).*

The Vickers indentation test can also be used to measure the fracture toughness of materials that are too hard and brittle for conventional hardness testing methods like the single edge notched beam (SENB), single edge precracked beam (SEPB), and single edge v-notched beam (SEVNB). The fracture toughness of hardmetals such as WC-Co is measured using the Vickers indentation fracture toughness (VIF) method. The VIF method makes use of the length of the four cracks emanating from the vertices of the indent. The Palmqvist crack model is then applied to determine the toughness value of the materials.

When applying the Palmqvist crack model in order to measure the toughness of a hard and brittle material the following parameters are used: the length of the cracks (T), the diagonal

of the indentation (d), the applied force load (P) and the empirical constant (a) (Roebuck et al., 2008).

The advantage of performing the Palmqvist crack toughness over common testing methods is that it is a very quick and easy test to perform. Another advantage of the VIF is that it requires a small testing area, therefore, a small testing piece (Roebuck et al., 2008). Figure 2.17 and Figure 2.18 show the application of the Palmqvist model graphically.

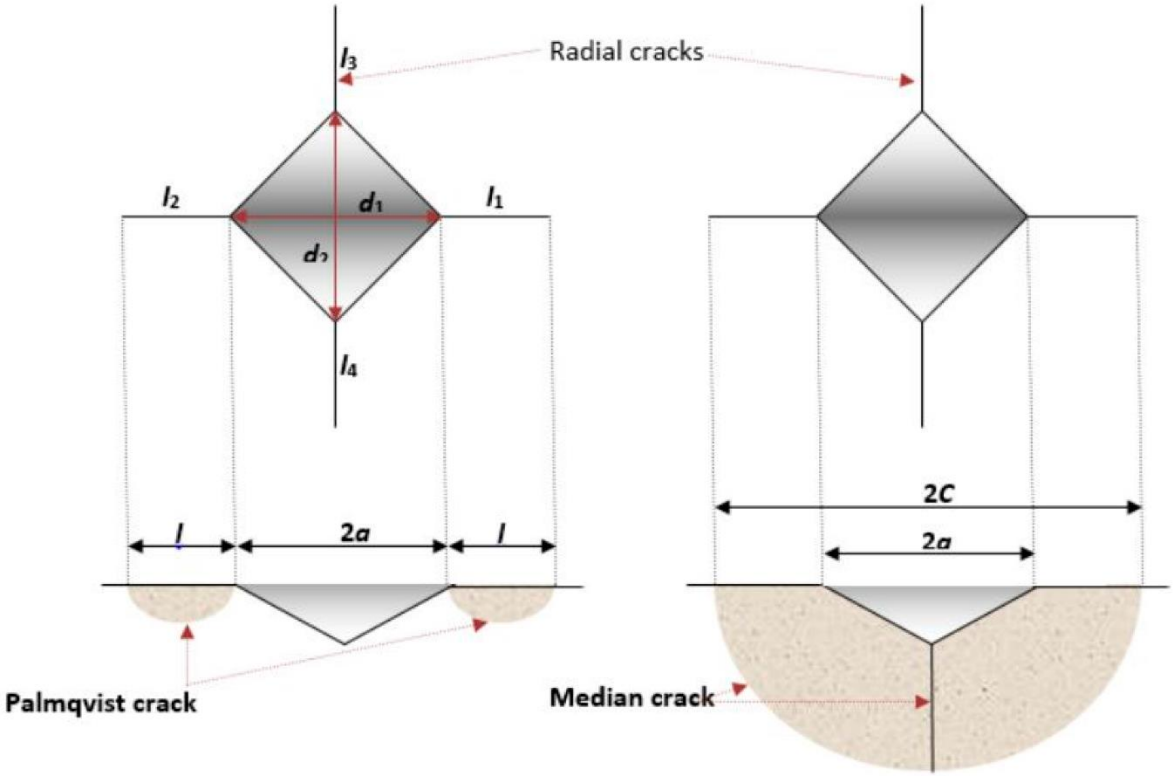

Figure 2.17: Schematic of the Vickers indentation and Palmqvist cracks *(Fabijabić et al., 2017).*

The lengths of the cracks are predominately affected by the residual stresses. The stresses are most likely to be more prominent in fine-grained microstructures (Fabijabić et al., 2017).

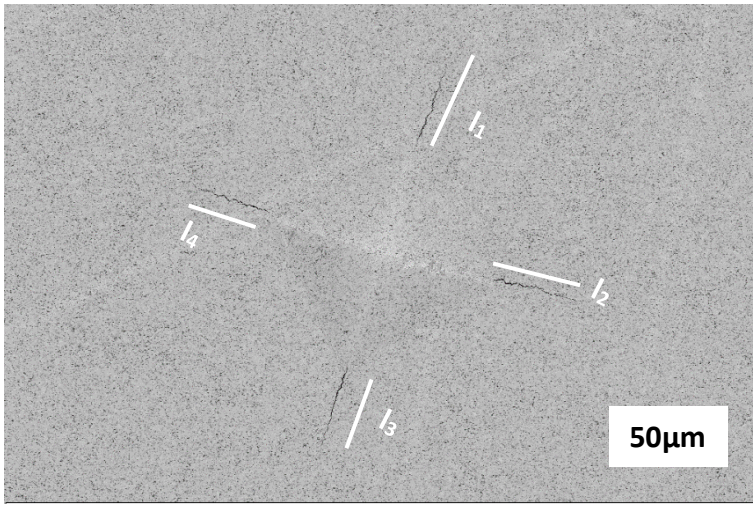

Figure 2.18: SEM micrograph of WC-Co showing cracks emanating from the corners of the indentation.

2.5Mechanical and Microstructural Effects on Wear

The mechanical and microstructural properties of materials play an integral role in the selection of a suitable liner against different wear mechanisms. Properties such as the surface hardness of a material, grain size distribution, and its chemical makeup to name a few, are important in determining the resistance of the material against industrial/ mining applications and longevity during its application.

WC-Co cemented carbides

The grain size of the WC particles and the amount of the Co binder predominately dictates the mechanical properties and wear responses of the cemented tungsten carbide alloys. The grain size and the binder content influence the wear rates of the alloys and therefore, their suitability as liners in chutes and skips.

Ndlovu (2009) reported that the hardness of the WC-Co alloys investigated increased with a decrease in the grain size of the WC particles and a decrease in its binder content. This combination between grain size and binder content results in lower wear rates. This phenomenon was observed by Engqvist et al., (2000) that small particles suspended in a Co binder increased hardness of the alloys without compromising their surface toughness

(Ndlovu, 2009). Figure 2.19 shows the micrograph of worn surfaces of WC-20Co alloys after sliding pin-on-disc sliding wear. The micrographs show that the smaller WC grains exhibited less damage when compared to the larger grains.

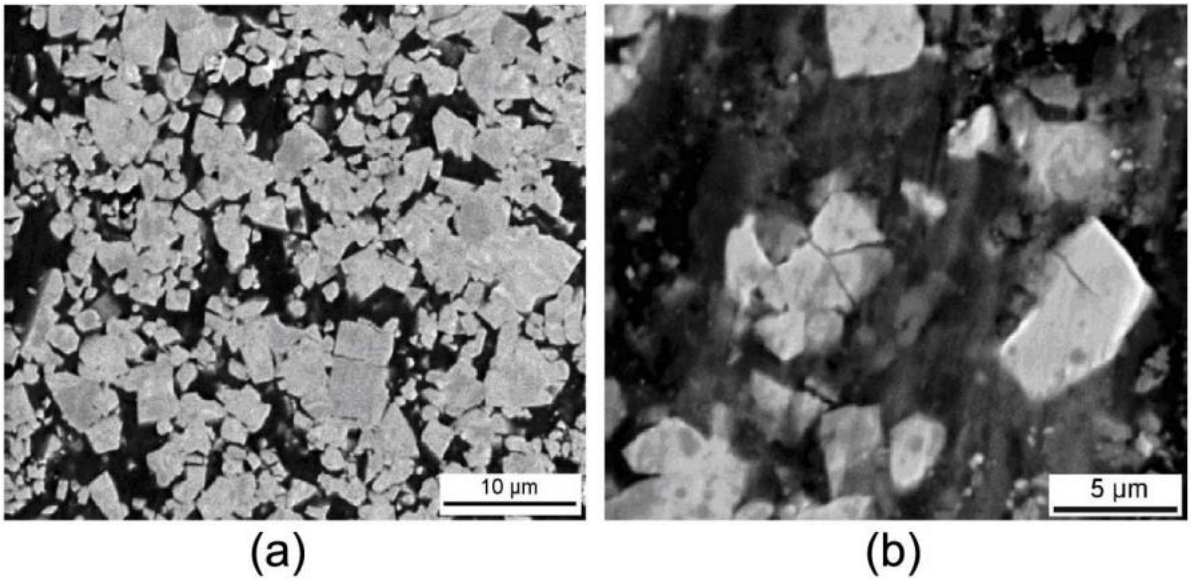

Figure 2.19: Surface of the worn surfaces of WC-20Co showing: (a) WC grain size of 1.3 µm and (b) WC-20Co grain size of 1.5 µm against pin-on-disc sliding wear (*Pirso et al., 2004)*.

High chromium white cast irons

High chromium cast irons are known to have high hardness values and wear resistant properties due to their mechanical and microstructural characteristics (Xu and Li, 2006). HCWCI alloys owe their exceptional abrasion resistance properties to the formation of primary carbides (M_7C_3). These carbides are mainly rich-in-chromium particles that are distributed in an austenitic matrix (Paz-Trivino et al., 2020). The chromium-rich primary carbides are formed by segregation during solidification and the higher the volume fraction of these carbides, the more wear resistant the alloys become (Atamert & Bhadeshia, 1990). Figure 2.20 shows an optical micrograph of the microstructure of Cr-rich primary carbides dispersed in a fully austenitic matrix.

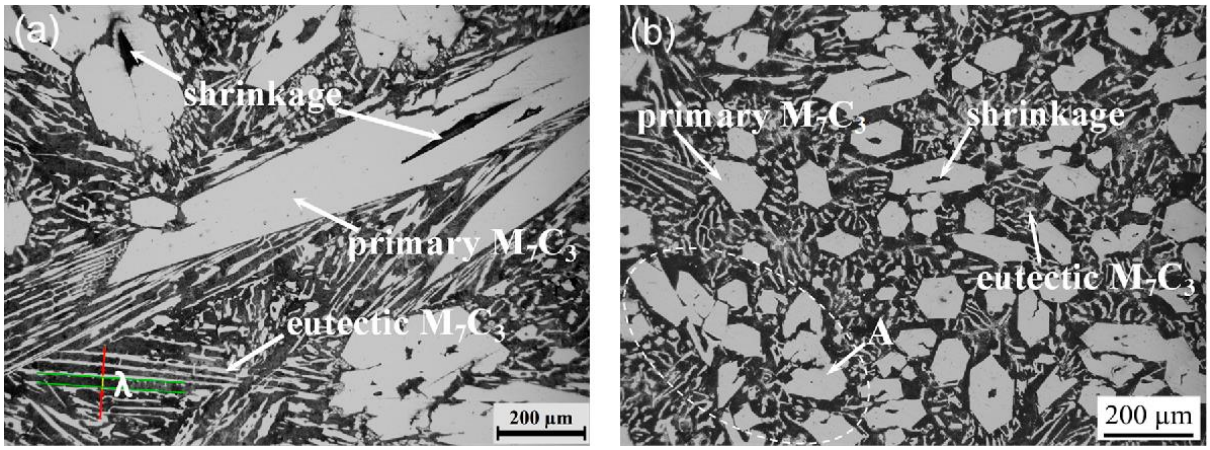

Figure 2.20: Micrograph of high chromium white cast iron microstructure *(Lv et al., 2018).*

Atamert and Bhadeshia (1990) reported that the austenitic matrix of iron-based alloys contributes to the wear resistance also play a vital role in offering good resistance to wear due to its work-hardening abilities. However, Jacuinde and Rainfath (2001) found in their work that there was no appreciable difference in the resistance against wear between the martensitic matrix and the austenitic one. Which, according to their work, indicates that the chemical composition, morphology, and size of the carbides had a greater effect on the wear rate than the matrix.

Hadfield steel

As mentioned before, high manganese steel owes its remarkable toughness, strength and resistance to abrasion wear to the steel's work-hardening ability when subjected to services where the impact force is extreme and frequent enough to cause plastic deformation (Mahlami & Pan, 2014). In their work Prieto et al. (2015) showed that the hardness of Hadfield steel increases during wet slurry abrasion, resulting in a decrease in its wear rate. Figure 2.21 shows the slip lines dislocations occurring on the austenitic grains.

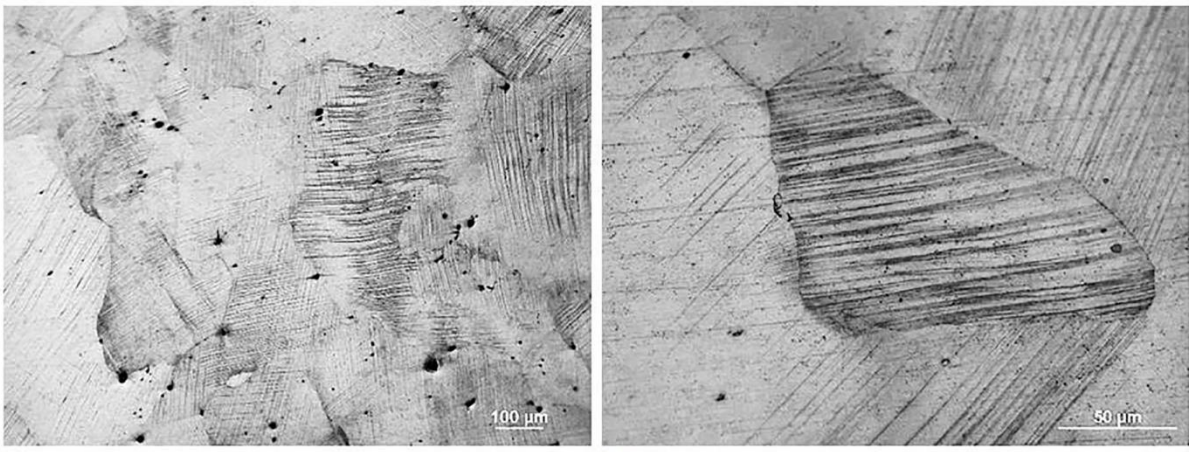

Figure 2.21: Optical micrograph of the Hadfield steel showing the mechanical slip planes induced during deformation *(Venturelli et al., 2018).*

The increase in hardness is induced by the generated dislocations within the crystal structure of the material where blocks of crystal slide and impede over each other along crystallographic planes known as slip planes (Mahlami & Pan, 2014). The more the pile up of dislocations against the slip plane barriers in the crystal lattice, the higher the strain-hardening (work-hardening) produced. Srivastava and Das (2019) added that the resistance of the Hadfield steel is attributed to its precipitated carbides (mostly $(Fe, Cr)_3C$) along the austenitic grain boundaries, leading to a decrease in mass loss during wear. However, Dastur and Leslie (1981) concluded that the hardness and wear resistance is likely due to the material's general dislocation structure than the specificity of its microstructure.

2.6 Wear Testing

2.6.1 Abrasion testing

Abrasion tests are conducted in order to determine the abrasion wear resistance of different materials (Adamiak, 2012). They are used to simulate the low and high stress abrasion encountered in most more conveyance equipment in the mining and mineral processing industry (Rendón & Olsson, 2009). Wear damage by abrasion is qualitatively measured by the materials change of mass and dimensions (Adamiak, 2012). Abrasion wear tests can be conducted using either a wet or dry abrasive medium.

2.6.1.1 Dry sand rubber wheel abrasion

The dry sand rubber wheel is a three-body abrasion test (Figure 2.22). The system is conducted according to the ASTM G65 practices (ASTM G65-16e1, 2016). It consists of loose abrading particles that are continuously fed at a constant rate of 300-400 grams per minute (Nahvi, 2009). The specimen is mainly a rectangular block that is pressed against a rubber wheel at an applied force of 130N.

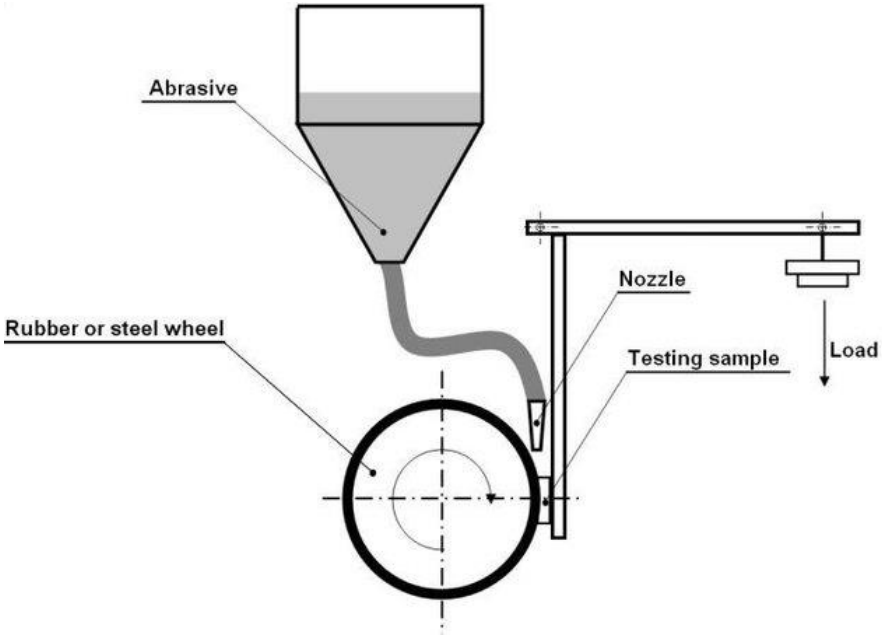

Figure 2.22: Schematic diagram of the ASTM G65 dry sand rubber wheel abrasion test rig *(Pejaković et al., 2015).*

2.6.1.2 Slurry rubber wheel abrasion

The slurry rubber wheel abrasion test (ASTM G105) makes use of a circulating slurry abrading medium that is passed between a rotating wheel and the sample (ASTM G105-20, 2020). The normal load is commonly set at 8N at a constant speed 110 revolutions per minute. The mixture is continuously agitated in the slurry bath. Wear damage is caused by the abrading particles against the sample (Jaimes, 2013). Figure 2.23 is a schematic of the slurry rubber wheel abrasion tribometer.

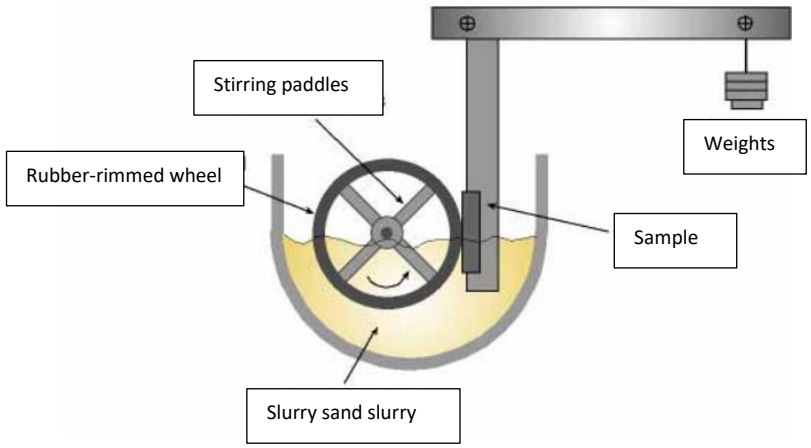

Figure 2.23: Schematic diagram of the ASTM G105 slurry rubber wheel abrasion test rig *(Gee, et al., 2002).*

2.6.2 Dry solid particle erosion testing

The process of solid particle erosion causes material removal of the structural component as a result of the impingement of blasting particles against the surface of the material. The process affects the integrity of the appearance and service life of the structure (Friedrich, 2015). The standard methods for carrying out dry solid particle erosion tests are used to measure the progressive loss of material as a result of a succession of impacts between the abrading medium and a solid surface (ASTM G76-18, 2018). The eroding medium can either be a liquid or solid. The main significant use of this technique is to screen and rank materials according to their resistance to erosion, their performance and reliability due to solid particle impingement. The test variables and parameters are characterised according to the abrading particle's impact speed, the particle's feed rate, the impact angle as well as the composition and size of the material and component (Alqallaf et al., 2020). Figure 2.24 is a schematic of the solid particle erosion wear tribometer.

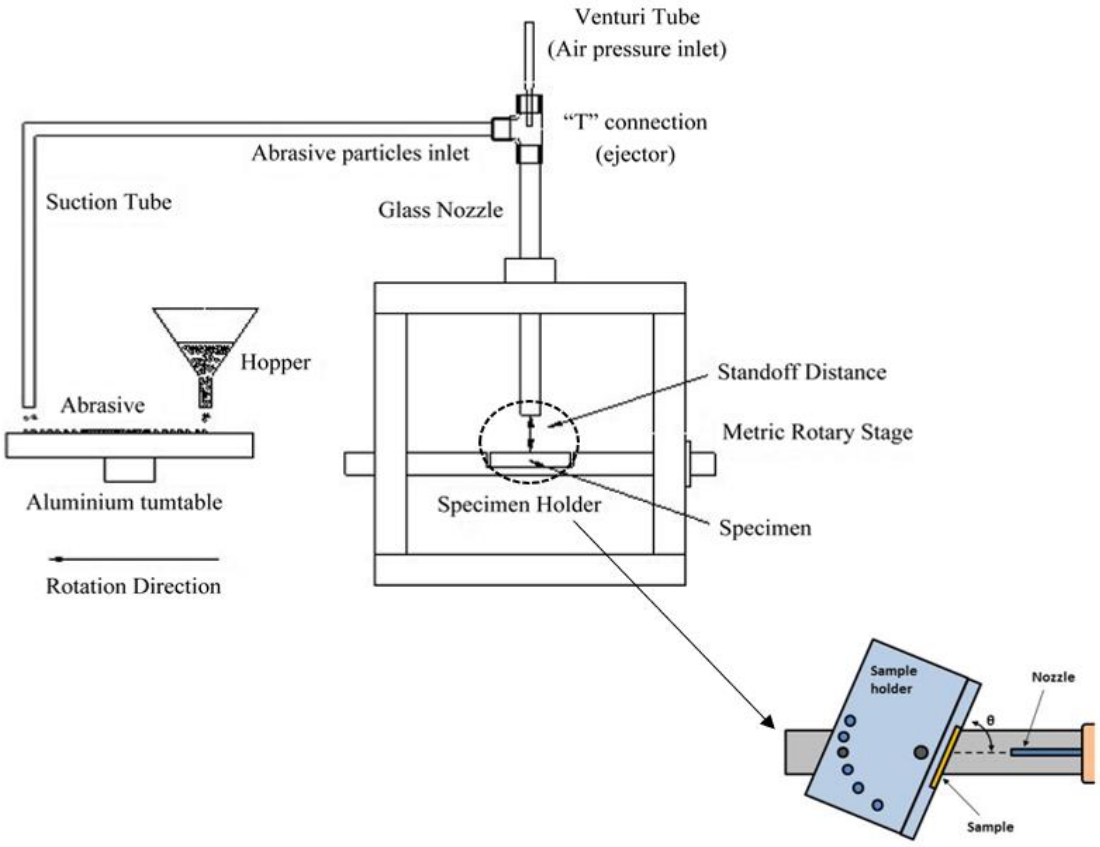

Figure 2.24: Schematic of the solid particle dry erosion test rig *(Laguna-Camacho et al., 2013).*

The slope of the mass loss vs time elapsed plot is used to determine the erosion rate according to the ASTM G76. The erosion rate ($mg.min^{-1}$) divided by the flow of the abrasive particles ($g.min^{-1}$) gives the average erosion value of the material. The average erosion value is reported as ($mm^3.g^{-1}$) (ASTM G76-18, 2018).

2.6.3 Pin-on-Disc sliding wear testing

The sliding wear and friction coefficient can be investigated using different methods and arrangements. The different arrangements can be divided into two categories: asymmetric and symmetric. Symmetric rigs are generally ring-on-ring configurations where the contact is either face-to-face or along the line whereas in asymmetric arrangements, which are the most common, the pin is loaded and pressed against either the flat side of the disc or along the rim (Hutchings, 1992). For this research, a pin-or-disc rotating tribometer (Figure 2.25) was used

to evaluate the sliding wear and friction properties of the investigated samples. Figure 2.26 is a coefficient of friction profile plotted as a function of the sliding distance during testing of the work conducted by Salguero et al. (2018).

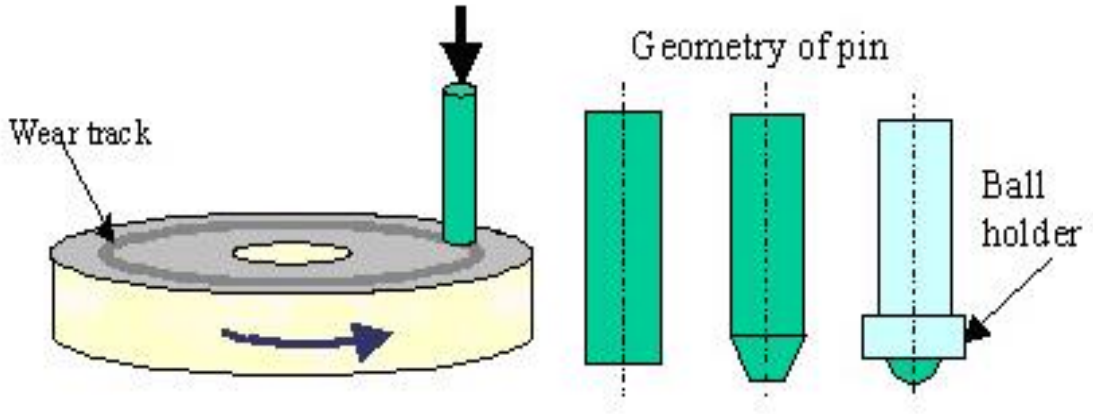

Figure 2.25: Schematic diagram of a pin-on-disc tribometer *(Li, n.d).*

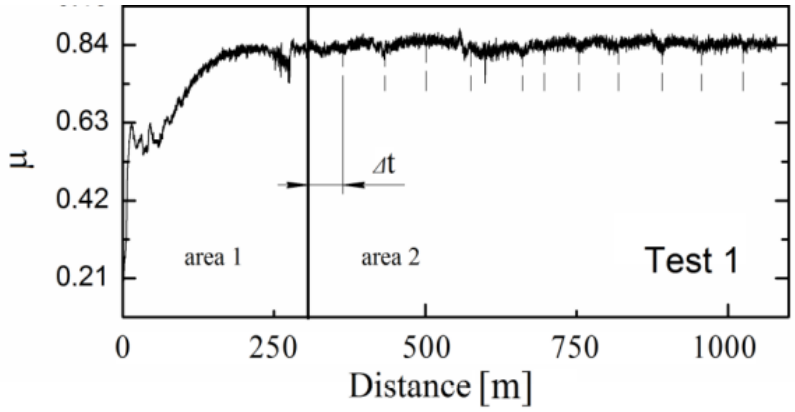

Figure 2.26: Coefficient of friction curve plotted as a function of the sliding distance during testing *(Salguero et al., 2018).*

The pin-on-disc (PoD) laboratory technique is used to determine the sliding wear mechanisms and friction behaviour of materials (Nair et al., 2009). This kind of a tribometer extends the abrasive wear analysis seen when particles slide against their counterparts such as when the transported ore abrade the surface of chutes and skips upon loading. The wear mechanisms seen during the pin-on-disc wear test are somewhat identical to those seen with the rubber wheel abrasion wear tests. The study by Salguero (2018) showed that abrasive mechanisms

prior to adhesion were seen during PoD testing. The abrasion and adhesion mechanisms can be determined via the scanning electron microscope and energy dispersive spectroscopy. Adhesion mechanisms exist when there is a presence of a different alloy composition(s) embedded on the surface of the disc.

2.7 Electrochemical Testing

Electrochemical testing methods are a simple and inexpensive way of obtaining reliable electrochemical properties pf materials (Dugas et al., 2019). For this project, the corrosion behaviour of the specimen was investigated using potentiodynamic anodic polarisation measurements. These polarisation measurements are a way of characterising metals by their current-potential properties (Konadu, 2009). Potentiodynamic polarisation measurements are carried out by a potentiostat which detects the relative susceptibility of materials to localised corrosion. This is done by detecting the different polarisation characteristic of different metallic materials such as the pitting potential, open circuit potential and passivation potential (Munir et al., 2016).

The potentiostat detects the initiation of localised corrosion by recording the potential (driving force) at which the system experiences a rapid increase of the anodic current (rate of reaction) (Eliaz, 2019). The polarisation characteristic is then plotted by measuring the current response as function of the applied potential (Konadu, 2009). The potentiostat is connected to a three-electrode polarisation cell consisting of a graphite counter electrode, a silver/silver-chloride (SSE) electrode and a working electrode. The reference electrode is submerged in a potassium chloride (3M KCl) solution.

Potentiodynamic anodic polarization curves (Figure 2.27 and 2.28) are then generated according to the parameters set on the potentiostat software. Figure 2.29 is a schematic of the polarisation scan showing the Tafel plots from which the E_{corr}, i_{corr}, βa and βc are determined.

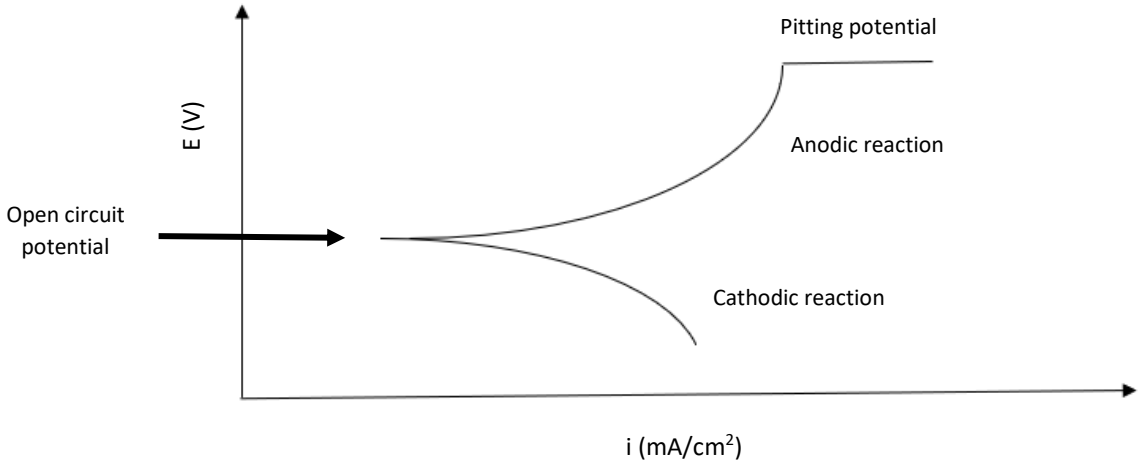

Figure 2.27: Linear potentiodynamic polarisation curve with labels depicting a material that shows an active and pitting phase *(López-Ortega et al., 2018)*.

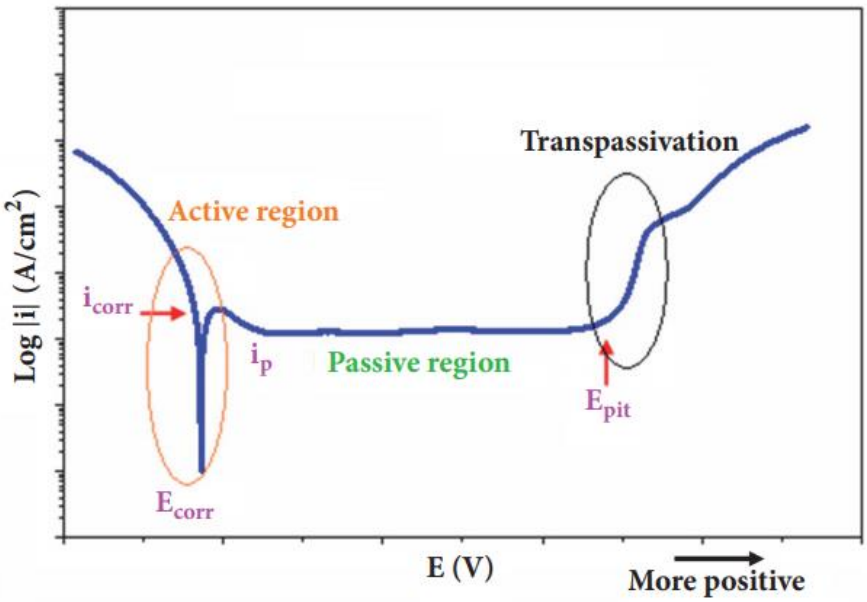

Figure 2.25: Schematic of a potentiodynamic polarisation curve depicting the active, passive and transpassive regions of a material *(López-Ortega et al., 2018).*

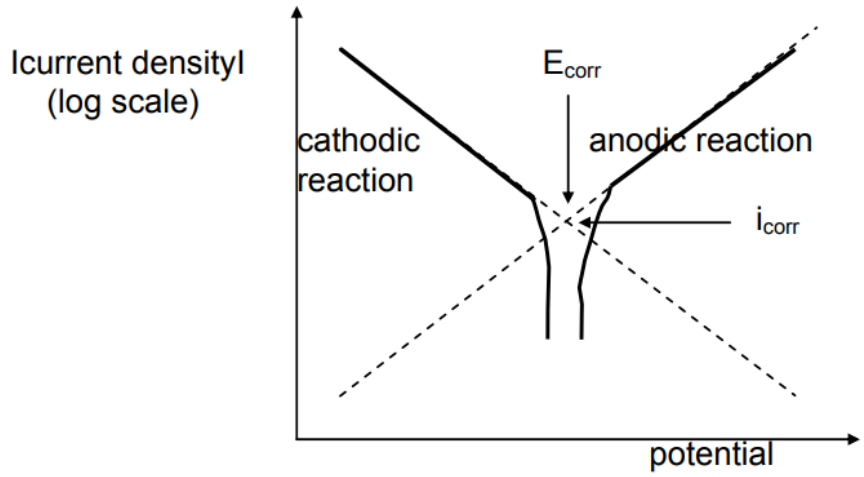

Figure 2.29: Schematic of the polarisation scans showing the Tafel plots from which the i_{corr}, β_a and β_c are determined *(Sacks, 2002).*

The Tafel slopes from the polarisation plots were used to determine the values of i_{corr} at points of intersection between the cathodic and anodic Tafel slopes. This is the point where $i_{ox} + i_{red} = 0$. The i_{corr} values are then used to calculate the corrosion rate of the materials using equation 2.3 which was derived from Faraday's Law (Jones, 1992).

$$CR\ (mmpy) = 3270\,\frac{i_{corr} \times EW}{\rho} \qquad \text{(Equation 2.3)}$$

Where

mmpy is millimetres per year

i_{corr} is the corrosion current density in A/cm^2

Where EW is the equivalent weight of the alloys in g

ρ is the density of the tested metal (g/cm^3).

Chapter 3

3. EXPERIMENTAL PROCEDURES

The metallographic preparation and the experimental methods used to characterise and analyse the mechanical and chemical quality properties of tungsten carbide cobalt, Hadfield steel and white cast iron samples are described in this chapter. The experimental procedures used in investigating the wear behaviour of the samples are also outlined in this chapter. It should be noted that the samples investigated in this work are as-received materials. The original state of the samples before any tribological, mechanical and chemical tests was determined using a light optical microscope, scanning electron microscopy and energy dispersive x-ray analysis. Chapter 3 is divided into four main sections as follows:

- 3.1 covers the metallographic preparations of the samples and methods of analysing the microstructure and phases of the materials,
- 3.2 describes the physical and mechanical testing methods,
- 3.3 describes the wear experimental techniques used for quantifying the material, and
- 3.4 describes the electrochemical techniques used for quantifying corrosion of materials

3.1 Metallographic Preparation and Microstructure & Phase Analysis

3.1.1 Metallographic preparation

This section describes the typical metallographic preparation of materials prior to the experimental tests conducted for this investigation. The specific standards for the metallographic preparation of the samples for the mechanical, tribological and electrochemical tests are mentioned under the test procedures.

The chemicals and consumables used for the preparation and mechanical testing are given in Table 3.1.

Table 3.1: Chemicals and consumables used in metallography and testing.

Chemicals/Consumables	Purpose
Potassium ferricyanide	Murakami's reagent
Potassium hydroxide	Murakami's reagent
Nitric acid	Nital
Methanol	Nital
Sulphuric acid	Corrosive medium for electrochemical tests
Ethanol	Washing surface of specimen
Alumina	Abrasive particle
Silica sand abrasive	Abrasive particle
Silicon carbide paper	Surface grinding/polishing
Diamaxx	Polishing
Bakelite resin	Hot mounting
Ball bearing (pins)	Sliding wear tribometer

3.1.1.1 Cutting of samples

The samples were cut using a Struers Secom cutting machine from the School of Chemical and Metallurgical Engineering. A cross-section of the sample was cut using a Struers 12cm diamond cut-off wheel. The wheel speed was set at 3500rpm and at a feed rate of 0.002mm/s. The cut length was set to 40mm and a finished cut was achieved in approximately 30minutes. Water was used as the coolant.

3.1.1.2 Sample mounting

The samples were mounted to support materials during the following steps: polishing, scanning electron microscopy, light optical microscopy and on the pin-on-disc wear

tribometer. A Struers polyfast resin was used on an Opal 410 mounting machine. The machine was set at 250 bar and 200°C. Water was used as a coolant.

3.1.1.3 Grinding and polishing of samples

Grinding and polishing was conducted on the exposed cut section of the samples in order to remove any damage caused during cutting. The samples were wet-ground and polished to produce a smooth surface for microstructural and mechanical testing. The Saphir 520 was used to grind and polish the surface of the samples and 220, 320, 500, 600 and 1200 grit silicon carbide paper wheels were used to grind and polish the samples to achieve different surface finishes for different testing procedures. Polishing cloths and Diamaxx (1 and 3µm) were also used to achieve a mirror finish surface.

3.1.2 Microstructure and phase analysis

The optical microscope and the scanning electron microscope (SEM) were used to examine the microstructure, surface morphology and chemical analysis of the investigated samples in their as received condition and after all the tests. The optical microscope used was an Olympus SC50. The SEM used was the Zeiss high vacuum scanning electron microscope with an energy dispersive x-ray spectrometry (EDS). The SEM-EDS operated at 20 keV and the micrographs were taken in both backscattered electron (BSE) and secondary electron (SE) mode.

3.2 Physical and Mechanical Testing

3.2.1 Physical testing

3.2.1.1 Density measurements of the materials

A Sartorius ED2245 densimeter was used to measure the density of the samples. The samples were first cleaned with 98% ethanol and then washed with distilled water. They were then air dried to remove any moisture.

The samples were first air-weighed to measure the dry mass and then weighed again in distilled water to measure the suspended weight. From there the density of the samples was calculated and displayed on the densimeter (Figure 3.1).

Figure 3.1: Macrograph of the densimeter used to measure the density of the investigated samples.

3.2.1.2 Magnetic saturation measurements

The magnetic saturation of a material is the highest magnetisation that can be induced in that material by a strong magnetic field (Brookes, 1975). In cemented carbides, the magnetic saturation of the binder is associated with the amount of antiferromagnetic components dissolved in it. For a WC-Co system, the magnetic saturation of Co is an indirect measurement of the content of C in the alloy. This is because maximum magnetisation induced in the ferromagnetic Co binder is affected by the solubility of W during sintering; the maximum magnetisation decreases linearly with the increasing solubility of W. Additionally, the degree of solubility of W in Co is dependent on the amount of C in its system-the less C in the system,

the higher the solubility. This relationship makes it possible to determine the amount of C in the system in a non-destructive way (Ngqase & Pan, 2020).

The ferromagnetic binder will show a low magnetic saturation when there are more antiferromagnetic components dissolved in it. The fraction between the measured magnetic saturation of Co (CoM) and the known wt% of Co is calculated in order to determine whether the alloy has a composition in the eta-phase (η-phase). A CoM/Co fraction lower than 0.7 indicates that the composition of the cemented carbide is in the η-phase. CoM/Co fraction higher than 0.7 indicate that the compositions of the alloys are in a region with large brittle and hard η-phase particles (Tran, 2018).

The actual binder magnetic saturation values were determined using the REEF-LEX magnetic analyser shown in Figure 3.2.

Figure 3.2: Macrograph of a magnetic saturation analyser.

3.2.2 Hardness

The hardness of the samples was determined using the Vickers hardness test. The tests were carried out on the surface of the polished samples. The indentations were made with a load of 30kg (HV_{30}) for 10 seconds. Five indentations were made on each sample at different locations and the average hardness number was calculated. Equations 3.1 and 3.2 were used to calculate the hardness number from the indentations (Roebuck, 2006). Figure 3.3 is an example of the diamond indentation on hardmetals.

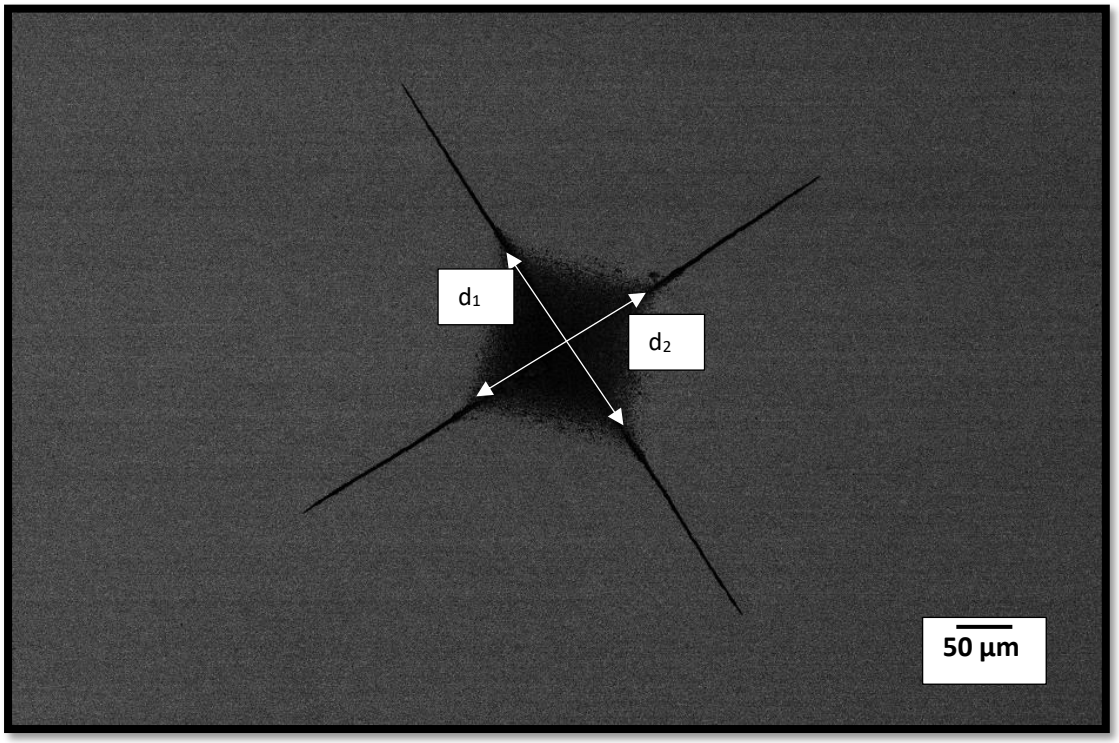

Figure 3.3: SEM-BSD micrograph of one of the investigated tungsten carbide cobalt sample showing the Vickers hardness indentation.

A LECO V-100-A2 diamond indenter was used to conduct the tests. Equation 3.2 was used to calculate force (F) in Newtons.

F (applied force) = M × g (Equation 3.1)

Where M is the indentation force of 30 kg and g is gravitational acceleration (9.82 $m.s^{-2}$).
The Vickers hardness at an indention force of 30 kg (HV_{30}) value is calculated as follows:

$$HV_{30} = \frac{F}{A} = \frac{F(0.1891)}{(d_1+d_2)^2} \quad \text{(Equation 3.2)}$$

Where

F is the applied force

A is the indentation area

d_1 and d_2 are the indentation diagonals

3.2.3 Palmqvist toughness

The toughness of the materials was obtained using the Vickers Indentation Fracture Toughness (VIFT), or also known as the Palmqvist toughness test method. This method is used on hardmetals (such as cermets) since these materials are typically too hard and brittle for conventional fracture testing methods (Roebuck & Bennett, 2005). The Palmqvist toughness was calculated by measuring the crack lengths created by the Vickers indentations at a force of 30 kgf (Figure 3.4). The crack lengths (l_1, l_2, l_3, and l_4) were measured from each vertex of the four corners of the diamond indentations and summed to calculate the Palmqvist toughness, W.

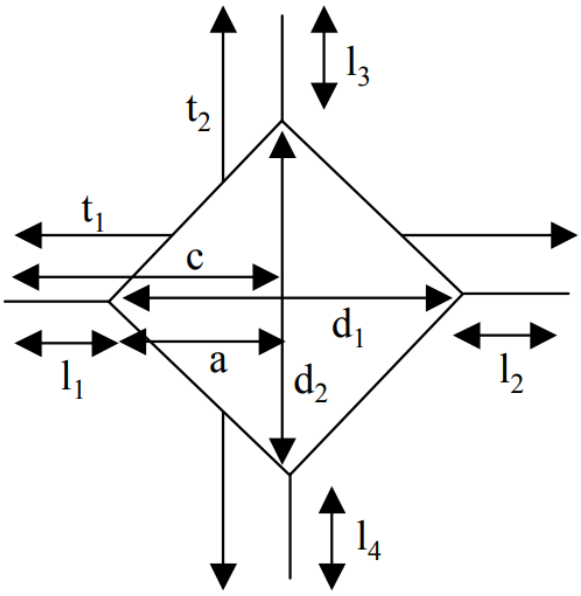

Figure 26.4: Schematic diagram of the cracks created during the diamond indentations *(Roebuck & Bennett, 2005).*

The Palmqvist toughness value is calculated as follows (Roebuck & Bennett, 2005):

$$W_K = A\sqrt{HV}\sqrt{W_G} \qquad \text{(Equation 3.3)}$$

Where A is a constant with the value 0.0028, HV is the hardness value of the material at a load of 30 kgf and it is expressed in $N.mm^{-2}$. W_K is expressed in $MPa.\sqrt{m}$. $W_G$is the ratio of the indentation load (L) to the total crack length (T).

$$W_G = \frac{L}{T} \quad \text{(Equation 3.4)}$$

T is the sum of the crack lengths emanating from the indentation corners.

$$\text{Total crack length, } T=l_1+l_2+l_3+l_4 \quad \text{(Equation 3.5)}$$

W_G is expressed in units of $N.mm^{-1}$ ($J.m^{-2}$), i.e. the strain energy release rate.

3.3 Wear Testing

3.3.1 Rubber wheel abrasion tests

The dry sand rubber wheel abrasion (DSRWA) and slurry rubber wheel abrasion (SRWA) tests were performed on tungsten carbide cobalt, Hadfield steel and white cast iron samples. The sample preparation and testing procedures are described in this section. The sample preparation and experimental procedure for the dry sand and slurry rubber wheel abrasion tests were conducted according to the ASTM G65 and ASTM G105 (ASTM G65-16e1, 2016; ASTM G105-20, 2020) standards, respectively. The mechanisms of wear and the wear effects on the surface of the samples after the tests were carried out were analysed using optical microscopy.

3.3.1.1 Sample preparation

The samples were sectioned into 70x25x5mm rectangular blocks for the DSRWA test and 18x18x5mm blocks for the SRWA test. The sectioned samples were ground using 200 and 600 grit silicon carbide papers. The samples were washed with ethanol before being polished to achieve a mirror finish. The samples were then weighed using the LABOTEC Precision scale with a precision of 0.0001g.

3.3.1.2 Abrasion wear testing procedure

The parameters used to conduct the dry and slurry abrasion wear tests are listed in Tables 3.2 and 3.3, respectively.

Dry sand rubber wheel abrasion test

The samples were placed in a sample holder and pressed against the rubber wheel with the help of the externally applied load. The silica sand was fed at a constant rate of 400 grams per minute. The macrograph of the dry sand rubber wheel abrasion equipment used for this test is shown in Figure 3.5.

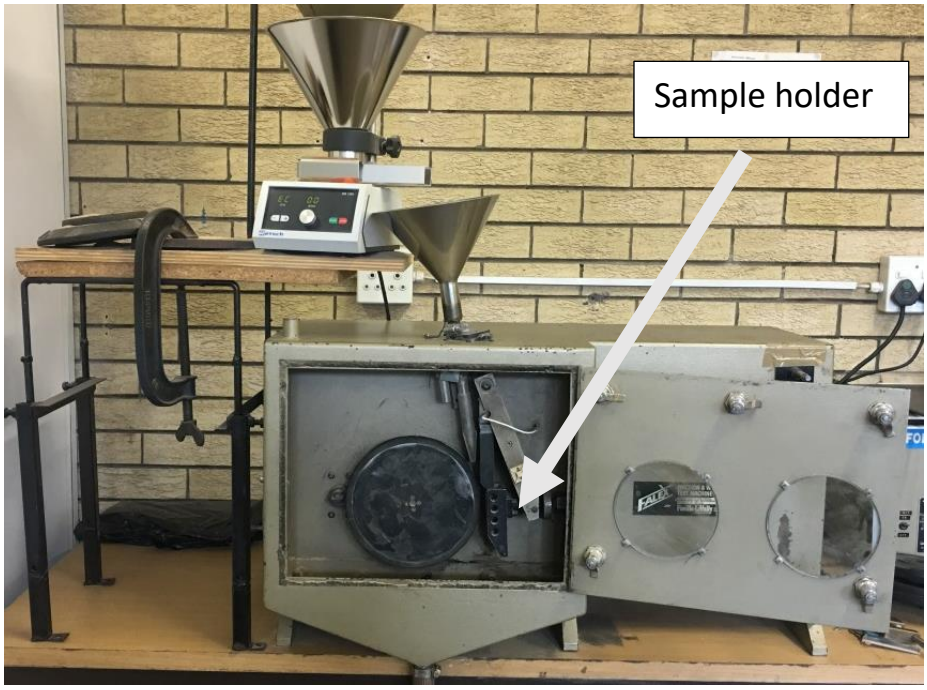

Figure 3.5: Macrograph of the dry sand rubber wheel abrasion test equipment.

Table 3.2: Dry sand rubber wheel abrasion test parameters.

Wheel	GG25 (cast iron alloy)
Rubber	Chlorobutyl
Hardness of rubber	A-60 Durometer
Diameter of wheel	228.6mm
Rotational wheel speed	200 rpm
Abrading medium	Silica sand
Hardness of abrading medium	1100 HV (200g load)
Flow rate of abrasive	400 g/min
Average particle size of abrading medium	300 µm
Load applied	130N

The test was allowed to run for 10 minutes and was repeated three more times for a cumulative duration of 40 minutes. After each 10minute interval the samples were washed with water to remove any debris and then rinsed with ethanol. The samples were also weighed after each 10minute interval to determine the weight loss. From the mass loss data, the volume loss and wear rate were calculated. The mass loss was converted to volume loss in order to avoid confusion with the wear results due to the variation of density (Equation 3.6) (ASTM G65-16e1, 2016). The specific wear rate (K_s) of the samples was determined using Equation 3.7 (Hutchings, 2017).

$$V = \frac{Mass\ (g)}{Density\ (g/cm^3)} \times 1000 \qquad \text{(Equation 3.6)}$$

$$K_s = \frac{Vi}{F \times S} \qquad \text{(Equation 3.7)}$$

Where F is the applied load (N), S is the sliding distance (m), and V_i is the wear volume of the samples (mm^3).

Slurry rubber wheel abrasion test

Similar to the ASTM G65, the samples are placed in a sample holder and pressed against the rubber wheel with the help of the applied load. The abrading medium was then introduced in between the rubber wheel and the sample (ASTM G105-20, 2020). The abrading medium used was silica sand mixed with water to create a 60:40 ratio slurry. The mechanisms of wear and the wear effects on the surface of the samples after the tests were carried out were analysed using an SEM and optical microscopy. The macrograph of the slurry sand rubber wheel abrasion equipment used for this test is shown in Figure 3.6.

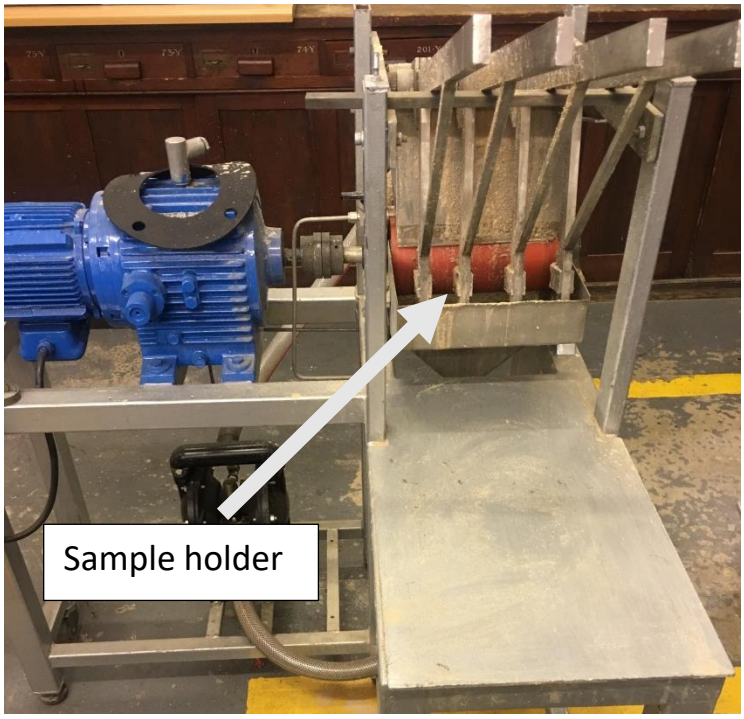

Figure 3.6: Slurry rubber wheel abrasion test equipment.

The samples were weighed before and after each testing period. For each sample, the test was conducted for 10minutes. The samples were washed with water to remove any debris, rinsed with ethanol, dried, and then weighed to determine the mass loss. The test was repeated three more times and weighed after each 10minute interval. The volume loss was calculated using Equation 3.6. The normalised wear rate of the samples was determined using Equation 3.8 (Gee et al., 2002).

$$K = \frac{V}{N \times t}$$ (Equation 3.8)

Where V is the wear volume in mm^3, N is the applied force in Newton and t is the sliding time in seconds.

Table 3.3: Slurry rubber wheel abrasion test parameters.

Wheel	GG25 (cast iron alloy)
Rubber	Thermoplastic Polyurethane Elastomer
Hardness of rubber	A-60 Durometer
Diameter of wheel	178mm
Rotational wheel speed	74 rpm
Abrading medium	Silica sand
Hardness of abrading medium	1100 (200g load)
Flow rate of abrasive	150 g/min
Average particle size of abrading medium	300 µm
Load applied	25N

3.3.2 Dry erosion test

This test technique is used to determine material loss by solid-particle impingement. The dry solid-particle erosion tests were conducted according to the ASTM G76-18 (2018) specifications. The angle of impingement was kept constant at 45° and the feed rate was set at 120 g/min. The impact speed was kept constant at 30m/s. The alumina oxide eroding particles had a hardness of 1875 Vickers unit and a particle sizes in the range of 125–150 µm. The mechanisms of wear and the wear effects on the surface of the samples after the tests were carried out were analysed using an SEM and optical microscopy. The dry solid-particle erosion wear test equipment is shown in Figure 3.7.

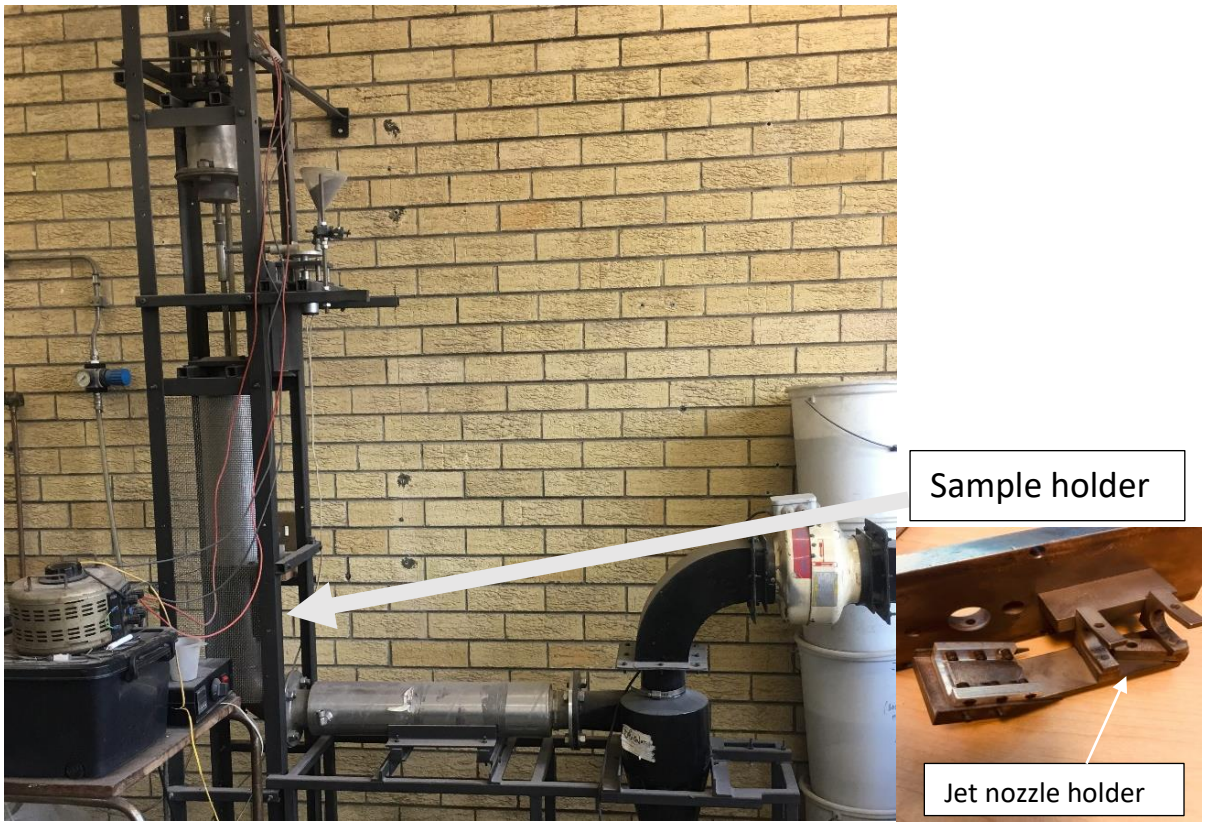

Figure 3.7: Dry solid-particle erosion wear test equipment.

3.3.2.1 Sample preparation

The samples were sectioned into 70×25×5mm pieces and ground to a 400-grit size using silicon carbide abrasive paper and cleaned with alcohol to remove any debris. The samples were washed with distilled water and dried before being mounted into the erosion test sample holder.

3.3.2.2 Erosion wear testing procedure

Each testing interval lasted for 30 minutes. The samples were washed with ethanol and distilled water before weighing to remove any of the worn particles or abrading alumina that might be embedded on the sample surface. The test was repeated for three more 30 minutes sessions for a total testing duration of 2 hours. The Vickers hardness measurements were taken after every 30 minute interval. The samples were quantified according to the ASTM G76-18 (2018) standards and the results recorded for the mass loss of the test sample. The amount of wear of the samples was estimated by measuring the mass of the samples before

and after each run. The steady erosion rate, E_r, was determined using Equation 3.9 (Mohanta & Acharya, 2015). The normalised erosion rate (E_R) was calculated using Equation 3.10.

$$E_r = \frac{\Delta W_C}{\Delta W_S} \quad \text{(Equation 3.9)}$$

Where ΔW_C is the mass loss of the eroded sample and ΔW_S is the total mass of the erodent used during the test.

$$E_R = \frac{\Delta W_C}{\Delta t} \quad \text{(Equation 3.10)}$$

Where Δt is the eroding time in minutes.

3.3.3 Pin-on-disc wear test

The pin-on-disc wear test was used to simulate the sliding tribological characteristics of the investigated discs i.e. tungsten carbide cobalt, Hadfield steel and white cast iron. This section describes the sample preparation and experimental procedure for conducting the pin-on-disc wear test according to the ASTM G99 specifications.

The friction behaviour, wear rates and effects, and the wear mechanisms involved during the pin-on-disc process were studied. The surfaces of the investigated samples were evaluated against the 316 stainless steel ball pins which had a hardness of 749 Vickers unit. The mechanisms of wear and the wear effects between the ball pins and the sample discs were analysed using an SEM, EDS, and optical microscopy. The friction behaviour between the pin and the disc was evaluated and illustrated using the CoF (coefficient of friction) versus sliding distance using the values generated by the pin-on-disc CSM InstrumX software. The volume losses of both the wear scar of the pin and the wear track of the disc were used as control parameters for studying the sliding wear effects of the samples, as specified in the ASTM G99-15 (2015) standards.

3.3.3.1 Sample preparation

The as received samples were first hot mounted using a Struers Cito-press 10 mounting machine. This was done so that the samples would fit into the sample-holding stage of the pin-on-disc equipment. The samples were wet-ground using 320 and 1200-grit silicon carbide papers. Thereafter a 3 µm cloth and a Diamaxx diamond slurry were used to polish the surface of the samples and give it a mirror finish.

3.3.3.2 Sliding wear testing procedure

The pin-on-disc tribometer tests were carried out using the CSM Instruments tribometer under dry, unlubricated conditions. The parameters were set using the installed CSM IntsrumX software. The same software was used to obtain the coefficient of friction (µ) versus sliding distance (m). The load, wear track radius, linear speed, turning speed and sliding distance were kept constant as listed in Table 3.4. Figure 3.8 below is a macrograph of the pin-on-disc tribometer used to conduct the sliding wear tests.

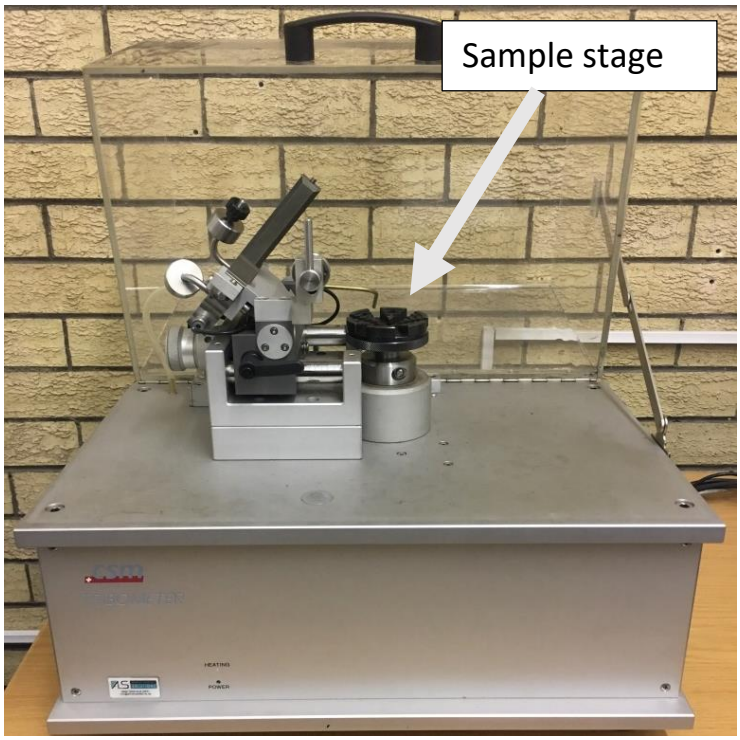

Figure 3.8: Macrograph of a pin-on-disc tribometer used to conduct the sliding wear tests.

Table 3.4 The parameters used for the slurry rubber abrasion tribometer tests.

Normal load (N)	Sliding radius (mm)	Linear speed ($m.s^{-1}$)	Turning speed (rpm)	Sliding distance (m)
5	3.0	0.1	318	500

The test samples were washed after the tests were completed. The microscopic effects of the sliding wear tests were analysed using the SEM and EDS. The SEM was used to analyse the wear mechanisms present during the testing process. The EDS was used to examine the composition on the wear tracks on the discs after the tests were carried out. This gave insight on which elements from the pins adhered to the discs during the testing process. The visual inspections were carried out using an optical microscope with a Nikon SMZ 745T stereoscope.

The wear results of the pin are reported as volume loss in cubic millimeters as specified in the ASTM G99-15 (2015). The pin volume losses were quantified using Equations 3.11 and (ASTM G99-15, 2015). Figures 3.9 (a) and (b) show the micrographs of the wear scar on the 316 stainless steel ball pins and the wear track on the WC-6Co disc.

$$V_{pin} = \frac{\pi \text{ (wear scar diameter, mm)}^4}{64 \text{ (sphere radius, mm)}} \qquad \text{(Equation 3.11)}$$

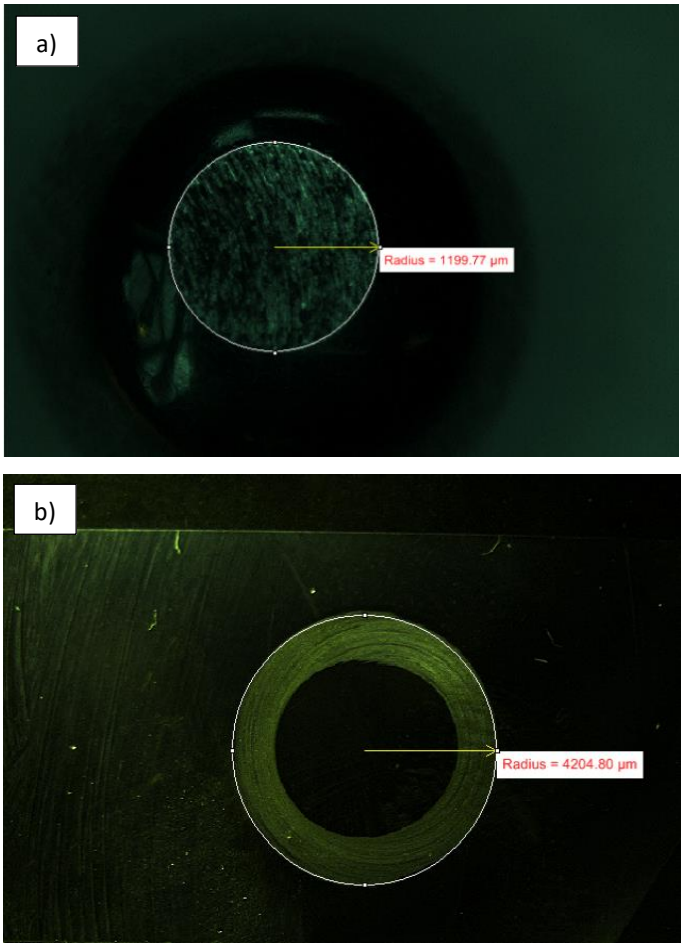

Figure 3.9: Stereoscope micrographs of (a) wear scar on the 316 stainless steel ball pin and (b) wear track on WC-6Co sliding wear.

The friction behaviour of the materials is quantified using the coefficient of friction (CoF) versus sliding distance plot generated by the CSM InstrumX pin-on-disc software. The specific wear rates (k_s) exhibited by the pins against the discs were calculated using Equation 3.12 in the units $mm^3.N^{-1}m^{-1}$.

$$K_s = \frac{(\text{volume loss, } mm^3)}{(\text{normal force, N})(\text{sliding distance, m})} \qquad \text{(Equation 3.12)}$$

3.4 Electrochemical Testing

3.4.1 Potentiodynamic polarization scan test

The potentiodynamic polarization scans and the linear potentiodynamic measurements were performed according to the ASTM G59-97 (2014). The electrochemical tests were performed on the tungsten carbide cobalt, Hadfield steel, and white cast iron samples. The sample preparation and experimental procedure are described in this section.

3.4.1.1 Sample preparation

The as received samples were prepared according to the ASTM G59-97 (2014) standards. The samples were sectioned into 10x10x5mm blocks using a Struers Secotom-10 precision cutting machine. The samples were cleaned with ethanol after cutting to remove any debris caused during cutting. The test surface of the samples was wet-ground using a 340-grit silicon carbide paper and then wet-polished using 600-grit silicon carbide paper until the surface was free from coarse scratches. The tested area for all samples was kept at 0.25cm^2. Figure 3.10 is a schematic of the testing samples' area.

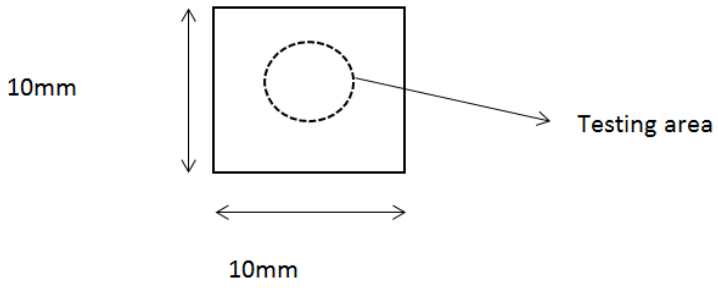

Figure 3.10: Schematic showing the testing area on the samples.

3.4.1.2 Potentiodynamic corrosion testing procedure

1M H_2SO_4 was used as the testing solution. A fresh batch was prepared for each test. A cylindrical three-electrode 900ml Pyrex glass cell was used for this experiment. The cell consists of a graphite counter electrode, a silver/silver chloride reference electrode immersed in a 3M KCl solution and the working electrode. The potentiodynamic polarization scans were

carried out at room temperature (25±1°C) in a water bath where the temperature could be closely regulated. The electrodes were connected to an Autolab potentiostat (Figure 3.11) and the parameters were defined from the Nova Software. The test procedure was set as follows:

1. Open circuit potential (OCP) for 1hour.
2. Linear potentiodynamic scans.

The scans were carried out from -0.2V versus the OCP to 1.5 V versus the reference electrode. The scan rate and step potential were set at 5mV/s and 1.6mV, respectively.

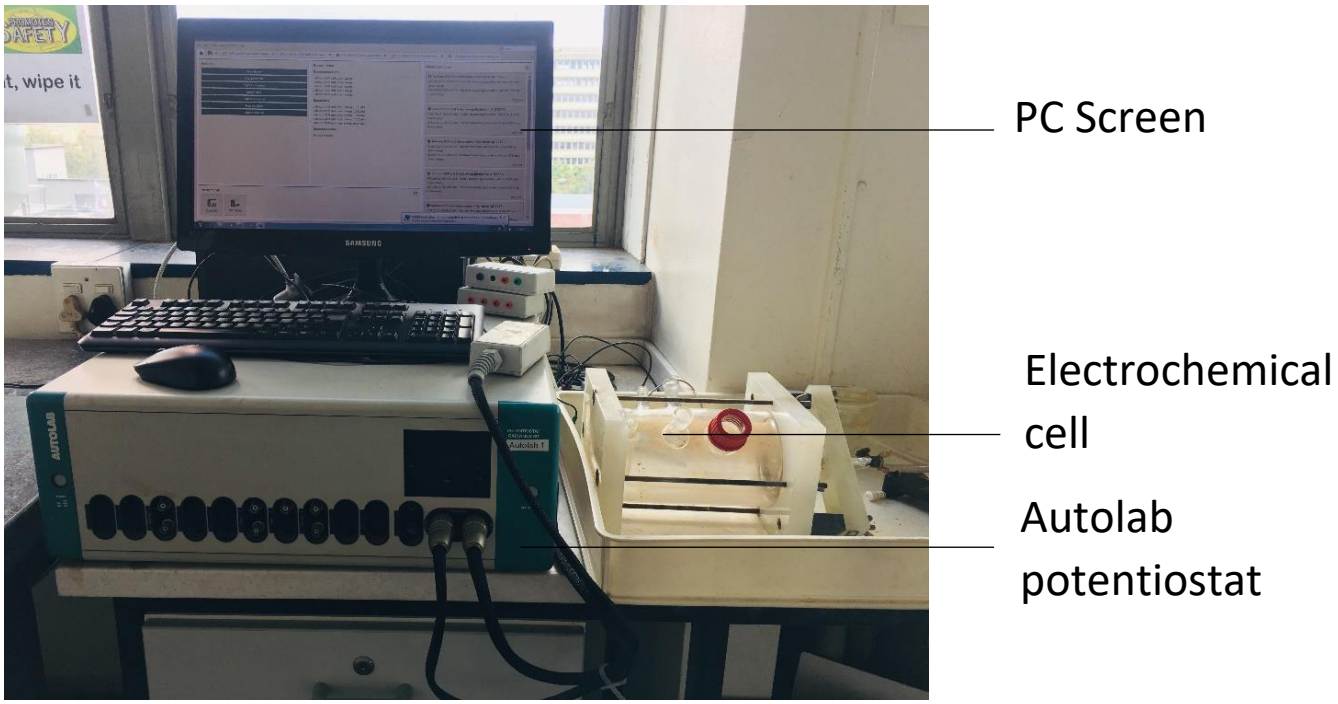

Figure 3.11: Macrograph of the electrochemical setup for conducting potentiodynamic scans.

The microstructural characteristics of the samples were observed using a Zeiss optical microscope and the morphological qualitative analyses of the samples were quantified using the SEM-EDS.

Chapter 4

4. RESULTS

4.1 Material Characterisation

4.1.1 As-received materials

4.1.1.1 Cemented carbides (WC-Co)

In this study, three grades of WC-Co, three grades of HCWCI and Hadfield steel samples were investigated. The physical, mechanical, and chemical properties of the samples were analysed in order to ascertain the selection of the material best suited as a lining material to prevent wear and chemical corrosion.

The binder content of the WC-Co samples ranged between 6-12 wt%. The grain sizes were analysed using the ImageJ software and the grain sizes ranged from 0.4-2.3 µm. The compositions of the WC-Co hardmetals are listed in Table 4.1.

The Vickers indentation hardness values, grain size values, Palmqvist toughness values and binder contents of the WC-Co alloys are listed in Table 4.2. Table 4.3 lists the density and magnetic saturation values of the WC-Co samples. Figure 4.1 is a graphical representation of the hardness values of the samples versus their Palmqvist toughness. The optical microscope and SEM micrographs of WC-6Co, WC-8Co, and WC-12Co are given in Figure 4.2 (a, b, and c) and 4.3 (a, b, and c), respectively.

Table 4.1: The nominal composition of the investigated WC-Co alloys.

Samples	Composition (wt%)			
	W	C	Co	Cr
WC-6Co	86.0	7.9	6.1	
WC-8Co	83.2	9.1	7.8	
WC-12Co	79.6	7.5	12.0	0.9

Table 4.2: The Vickers indentation hardness values, Palmqvist toughness values and binder contents of the WC-Co alloys.

Sample	Co content (wt%)	Grain size of WC (µm)	Hardness (HV_{30})	Total Measured Crack length (µm)	W_G (Jm^{-2})	W_K ($MPa.m^{1/2}$)
WC-6Co	6.0	2.2	1428.0	268.6	1095.4	11.0
WC-8Co	8.0	2.3	1294.0	193.3	1522	12.3
WC-12Co	12.0	0.4	1612.0	304.6	966.0	10.9

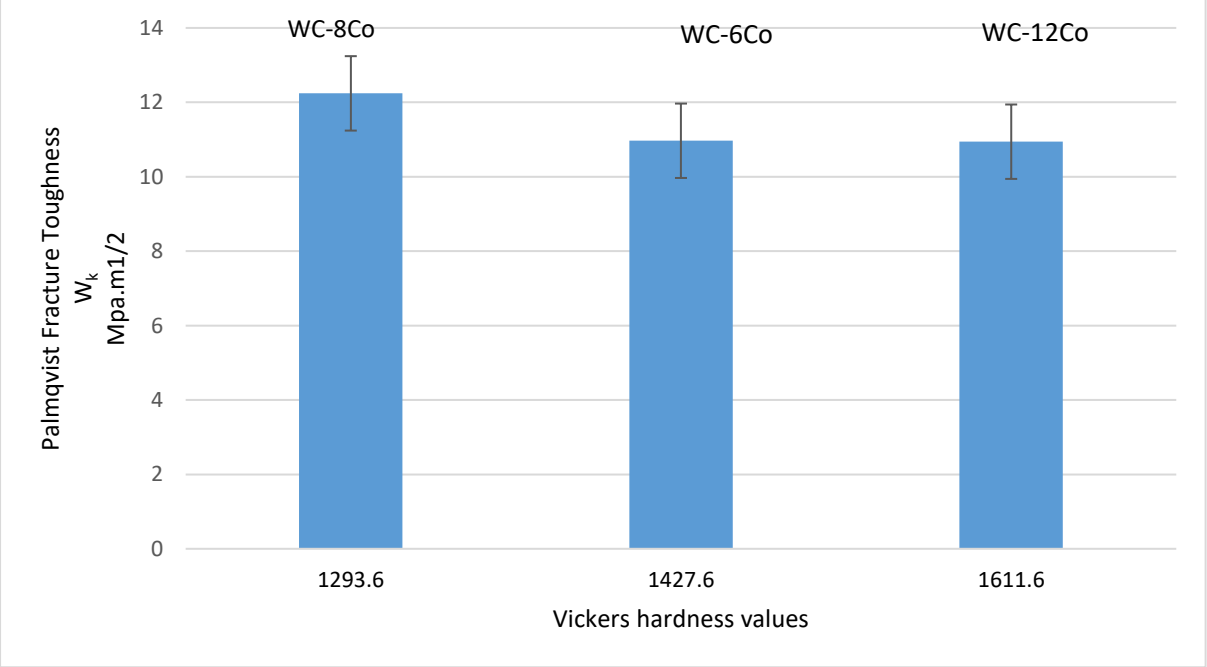

Figure 4.27: Vickers hardness values of the three WC-Co alloys plotted against Palmqvist toughness.

Table 4.3: Physical properties of the WC-Co samples.

Sample	Density ($g.cm^{-3}$)	Measured magnetic saturation ($\mu Tm^3.kg^{-1}$)	CoM/Co fraction
WC-6Co	14.94	5.0	0.82
WC-8Co	14.74	6.2	0.79
WC-12Co	14.13	8.5	0.71

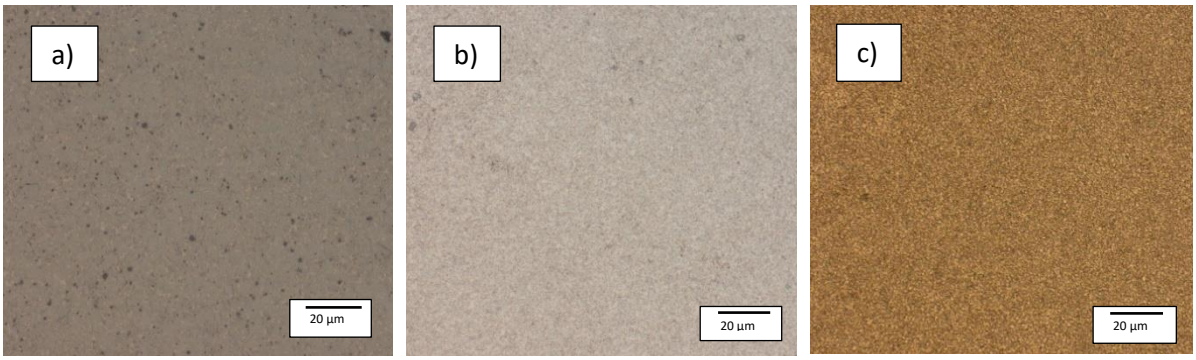

Figure 4.28: Optical microscope micrographs of (a) WC-8Co, (b) WC-12Co, and (c) WC-6Co.

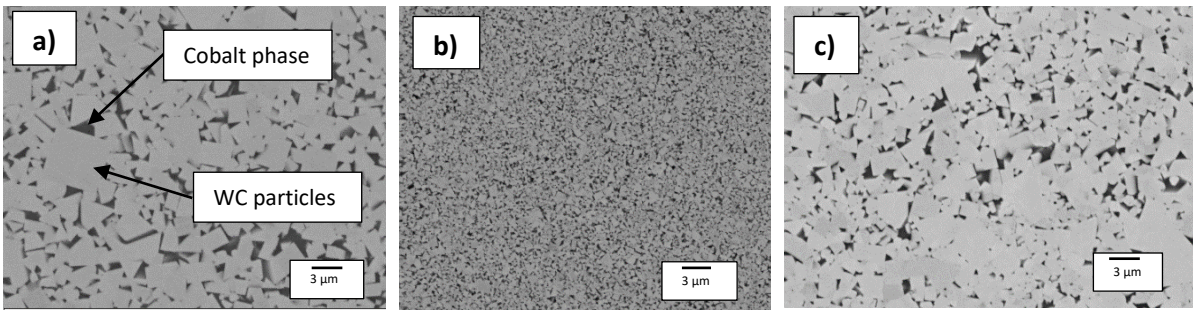

Figure 4.29: SEM-BSD micrographs of the investigated WC-Co alloys: (a) WC-8Co, (b) WC-12Co, and (c) WC-6Co.

Generally, the bulk hardness of WC-Co alloys decreases when the content of the Co matrix increases provided the WC grain size remains similar (Ndlovu, 2009; Ma et al., 2017). However, the investigated WC-12Co (which contains the highest Co content) exhibited the highest hardness value of 1612 HV_{30}. This increased hardness can be explained by the alloy's

refined grain structure caused by the chromium addition. The hardness values of cemented carbides have the tendency of increasing with decreasing grain sizes (Saito et al., 2006). Structures with fine grains have larger WC particle surface area to volume ratios, which in turn means that the structures have surfaces that consist of densely packed hard WC particles such as seen with binderless tungsten carbide alloys (Ndlovu, 2009; Ma et al., 2017). This makes it difficult for the material to plastically deform during hardness indentations. The WC-6Co and WC-8Co alloys had similar grain sizes in their structures hence the previously stated relationship between the Co content and hardness came to effect. This was shown when the alloy with the lowest Co content (WC-6Co) exhibited the highest Vickers hardness value.

The same explanation holds for the Palmqvist toughness values of the alloys. The total measured crack length of WC-12Co was expected to be smaller than the lengths of the other two WC-Co alloys because it contained the highest Co content. But because of its refined structure which consists of hard, brittle and highly densified WC particles, WC-12Co exhibited longer and more defined Palmqvist crack lengths hence a lower fracture toughness. The same trend in the Palmqvist fracture toughness values can be observed in the work conducted by Antonov et al. (2017). In their study, WC-Co samples of similar Co content (6, 8, and 15wt%) and grain sizes were investigated, and it was found that their finest WC-15Co sample exhibited the lowest Palmqvist fracture toughness when compared to the coarser structures of WC-6Co and WC-8Co samples.

From the tabulated physical properties of the three WC-Co samples (Table 4.7), it was observed that WC-12Co exhibited the lowest CoM/Co fraction value of 0.71. WC-6Co had the largest CoM/Co fraction value of 0.82 and WC-8Co at 0.79. The CoM/Co fraction values of the cemented carbides indicate that the compositions of the samples are in a region with large and hard η-phase particles (Luyckx, 1997; Tran, 2018). Because the values are not too high off above the stipulated CoM/Co fraction value of 0.7, they were rendered good quality for this study. WC-12Co further exhibited the lowest measured density compared to WC-6Co and WC-8Co because of their refined size. WC-12Co has the highest Co to WC ratio and therefore it is less dense than the other two WC-Co samples.

4.1.1.2 High chromium white cast irons (HCWCI)

Table 4.4 lists the compositions of the HCWCI alloys and Table 4.5 is the summary of their density values, chromium content and Vickers hardness values. It should be noted that even though Table 4.5 consists of the carbon values of the HCWCI samples, their accurate nominal values are unknown even though their EDS peaks are accurately recorded. This could be as a result of a contaminated SEM chamber as carbon is the common specimen contaminator. Therefore, carbon will be omitted when conducting further material analysis and calculations on HCWCI samples in order to maintain the accuracy of the results.

The optical microscope micrographs of HCWCI-1, HCWCI-2, and HCWCI-3 are given in Figures 4.4, 4.5 and 4.6, respectively. The SEM micrographs of HCWCI-1, HCWCI-2, and HCWCI-3 are given in Figure 4.7 (a, b, c), respectively. The Palmqvist fracture values are unavailable since the materials are not hard enough to produce cracks upon indenting when using the Vickers hardness indentation technique at a force of 30kgf, hence an equal and fair comparison was impossible.

HCWCI-3 had the highest Cr content of 24.5 wt%. It also contained a number of alloying elements including Si, Mn, and Ni. These alloying elements generally form carbides in preference to Cr (Marimuthu & Kannoorpatti, 2016). It was thus expected that HCWCI-3 will consist of complex carbides in its system. HCWCI-2 generally contained the highest content of carbon and had the second highest Cr content of 22.2 wt%. HCWCI-2 had no other alloying elements except for Si at 0.4 wt%. HCWCI-1 had the lowest Cr content of 20.2 wt%. HCWCI-1 also contained Si, Mn and V in its system. Thus, just like HCWCI-3, HCWCI-1 will form complex carbides with these alloying elements in preference to Cr. The Cr/C ratio of the alloys could not be determined because of the inability to obtain the accurate values of the carbon content. All three investigated HCWCI alloys consist predominately of Cr-rich primary carbides and eutectic primary carbides (in a form of M_7C_3) in a fully austenitic matrix.

Vickers macro-hardness indentation measurements (HV_{30}) showed HCWCI-1 as having the highest hardness value of 829 HV_{30}, followed by HCWCI-3 at 760 HV_{30}. HCWCI-2 exhibited the lowest hardness value of 687 HV_{30}. Even though HCWCI-1 had the lowest Cr content, it exhibited the highest hardness value. This is primarily as a result of the presence of vanadium in its system which is responsible for increasing hardness in white cast irons (Mampuru et al.,

2016). HCWCI-1 also contains a significantly high amount of carbon which is essential for the formation of other hard complex carbides.

HCWCI-3 was expected to exhibit the highest bulk hardness due to its high Cr content, but because of its high carbon content and silicon content (which behaves as a grain refining and graphitising agent), its bulk hardness was compromised. This occurs when the decomposition and releasing of graphite causes the cementite in the system to be unstable (Lai et al., 2016; Powell & Randle, 1997; Jacuinde & Rainforth, 2001).

HCWCI-2 and HCWCI-3 (Figures 4.5 and 4.6, respectively) exhibited larger primary carbides in their microstructures than HCWCI-1 (Figure 4.4). This is because of their increased Cr contents which promotes the formation of Cr-rich carbides. HCWCI-3 exhibited larger longitudinal primary carbides and larger hexagonally shaped transverse primary carbides as seen in Figure 4.6 (a). This is because Cr stabilizes carbides during the solidification of white cast irons hence promoting the formation and dispersion of hard Cr-rich and (Fe, Cr_x)C_Y carbides (Ngqase & Pan, 2020). All three alloys contained a high density of rod-shaped and isolated M_7C_3 carbides which are expected when the Cr content exceeds 15%. This type of a microstructure is essential for applications where abrasive wear resistance and impact toughness is required (Powell, 1980).

Upon close inspection of the SEM micrographs, cracks on and around the grain boundaries of carbides (dark phases) can be observed. Eutectic and primary carbides are critical positions where the initiation and propagation of such defects occur because of their hard and brittle nature (Fan et al., 2019). The crack initiation and growth may be as a result of the stress induced by the matrix during solidification (Tchuindjang et al., 2015). The defects might also be caused during sample preparation (sectioning, grinding, polishing, or etching).

Table 4.4: Nominal compositions of the investigated HCWCI alloys.

Sample	Composition							
	Cr	C	Si	Fe	Mn	S	Ni	V
HCWCI-1	20.2	18.4	0.2	60.0	0.7			0.5
HCWCI-2	22.2	12.2	0.4	65.2				
HCWCI-3	24.5	13.9	0.9	58.2	0.9	0.3	1.3	

Table 4.5: Density, Vickers hardness and chromium content values of the HCWCI alloys.

Sample	Chromium content (wt%)	Density ($g.cm^{-3}$)	Vickers hardness (HV_{30})
HCWCI-1	20.0	5.28	829
HCWCI-2	22.0	5.91	687
HCWCI-3	25.0	5.59	760

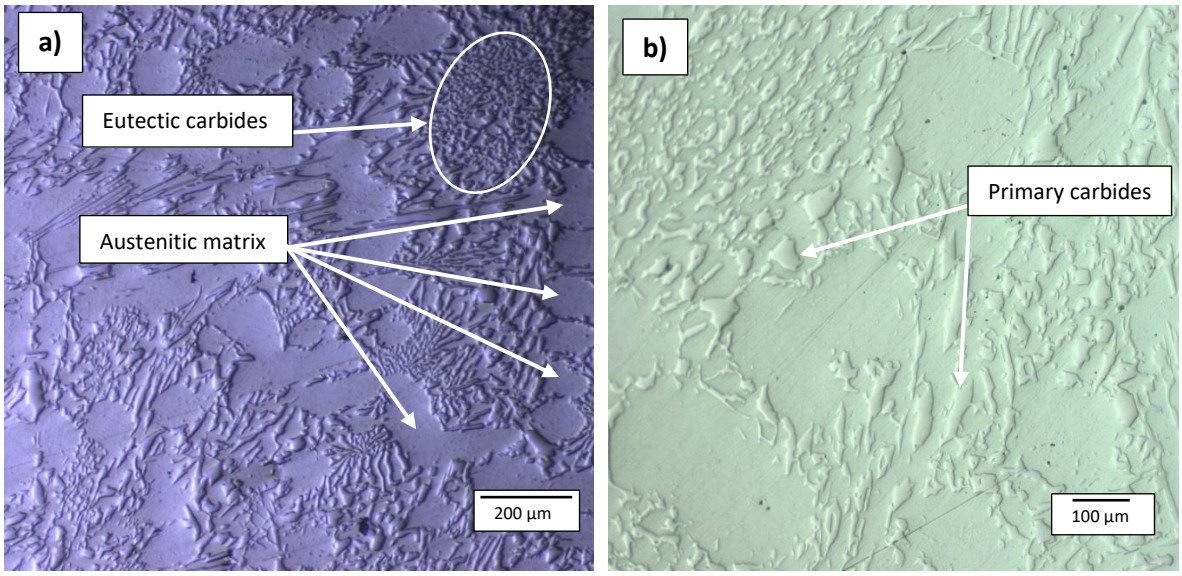

Figure 4.30: Optical microscope micrographs of the investigated high chromium white cast iron alloy: (a) HCWCI-1 at 50x and (b) HCWCI-1 at 200x.

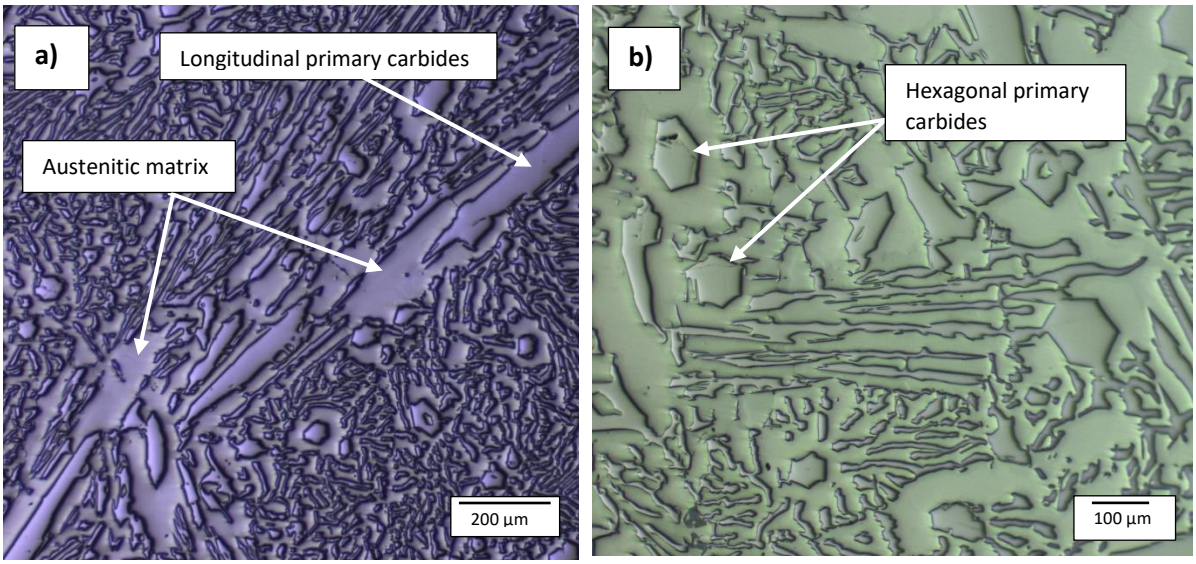

Figure 4.31: Optical microscope micrographs of the investigated high chromium white cast iron alloy: (a) HCWCI-2 at 50x and (b) HCWCI-2 at 200x.

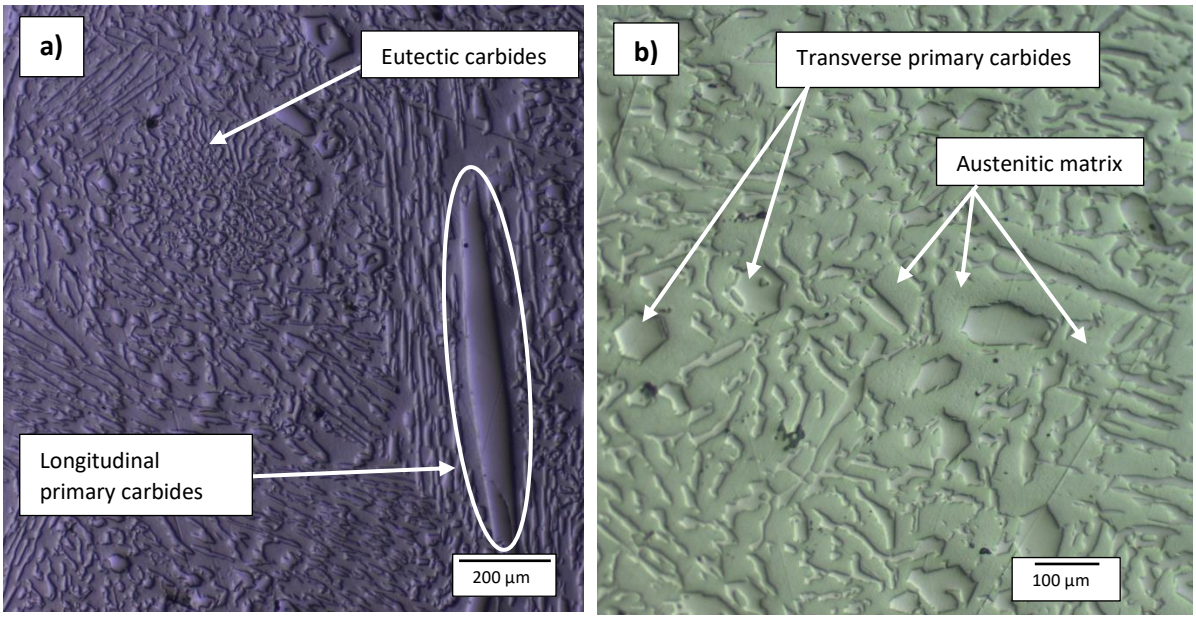

Figure 4.32: Optical microscope micrographs of the investigated high chromium white cast iron alloy: (a) HCWCI-3 at 50x and (b) HCWCI-3 at 200x.

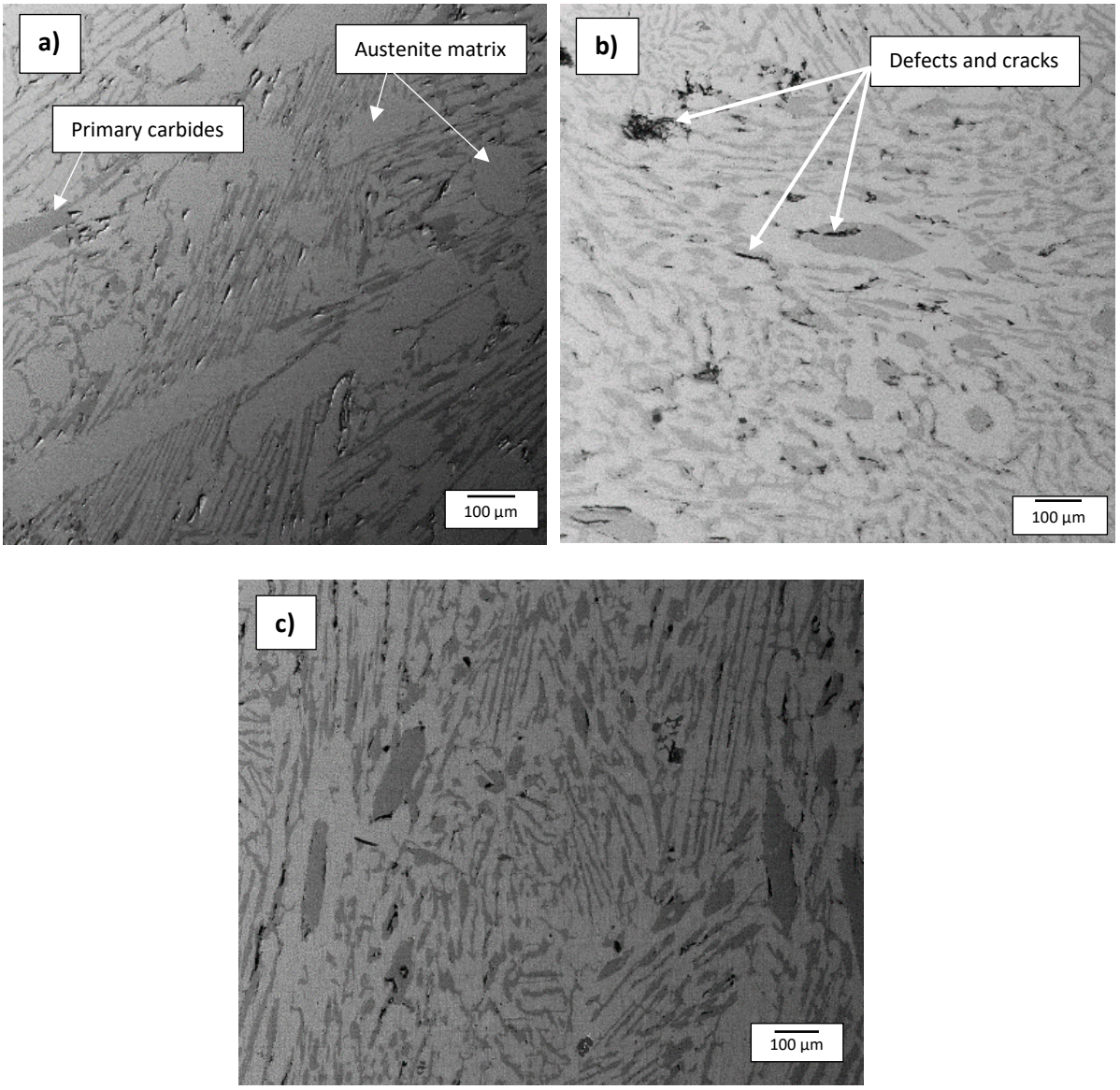

Figure 4.33: SEM micrographs of the investigated high chromium white cast iron alloys: (a) HCWCI-1 (BSD), (b) HCWCI-2 (SE), and (c) HCWCI-3 (BSD).

4.1.1.3 Hadfield steel

Table 4.6 lists the nominal composition of the as-received Hadfield steel. Table 4.7 summarises the carbon and manganese content as well as its density and Vickers hardness value. The optical and SEM micrographs of the investigated Hadfield steel are presented in Figures 4.8 and 4.9, respectively.

The Mn and C composition of the investigated Hadfield steel are 12.4% and 1.1%, respectively. This makes the steel's Mn/C composition ratio within the original standards of the austenitic

manganese steel. This ratio is essential for applications where the wear resistance, toughness and work-hardening properties are required (Havel, 2017). The Mn and Mo behave as austinite stabilizers whereas Si is classified as a 'steel killer'. However, any amount of Si that is above 0.5 wt% is detrimental to the work-hardening ability of Hadfield steel (Sabzi & Farzam, 2019). The Hadfield steel consists of a Cr content of 0.3 wt%. This alloying element is essential for the yield strength and corrosion resistance of the Hadfield steel.

The slip bands that are shown in Figure 4.8 (a) might be caused either during the sectioning, grinding, or polishing during sample preparation. The as-received Hadfield steel sample exhibited a hardness of 250 HV_{30}.

Table 4.6: Nominal compositions of Hadfield steel (wt%).

Sample	C	Si	Mn	P	S	Cr	Ni	Mo	Cu	Al	N	Fe
Hadfield steel	1.08	0.58	12.4	0.035	<0.001	0.34	0.04	0.46	0.03	0.03	0.02	Bal.

Table 4.7: Chemical and physical properties of the Hadfield steel.

Sample	Carbon content (wt%)	Manganese content (wt%)	Density ($g.cm^{-3}$)	Vickers hardness (HV_{30})
Hadfield steel	1.08	12.4	6.33	250

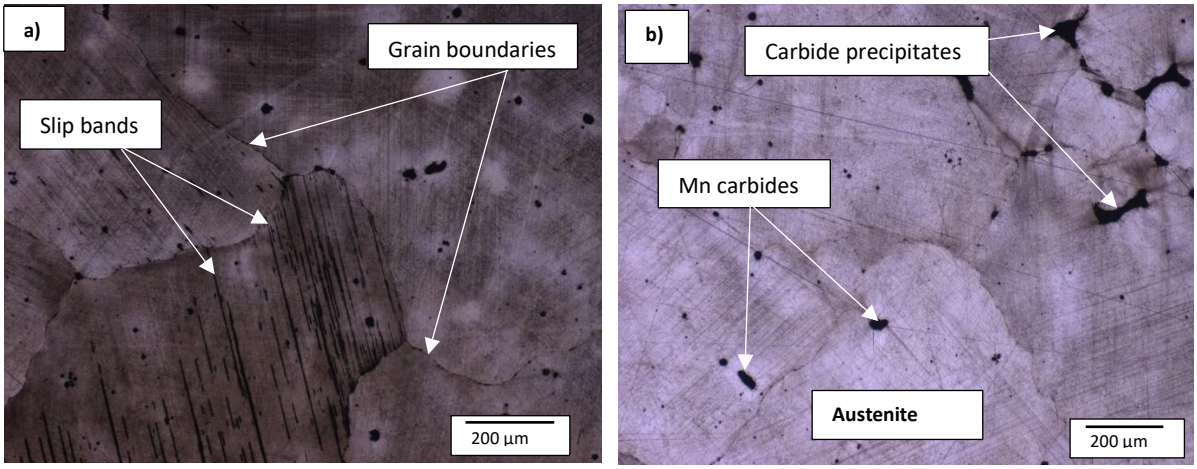

Figure 4.34: Optical microscope micrographs of the investigated Hadfield steel showing the grain boundaries, slip bands and carbide precipitates.

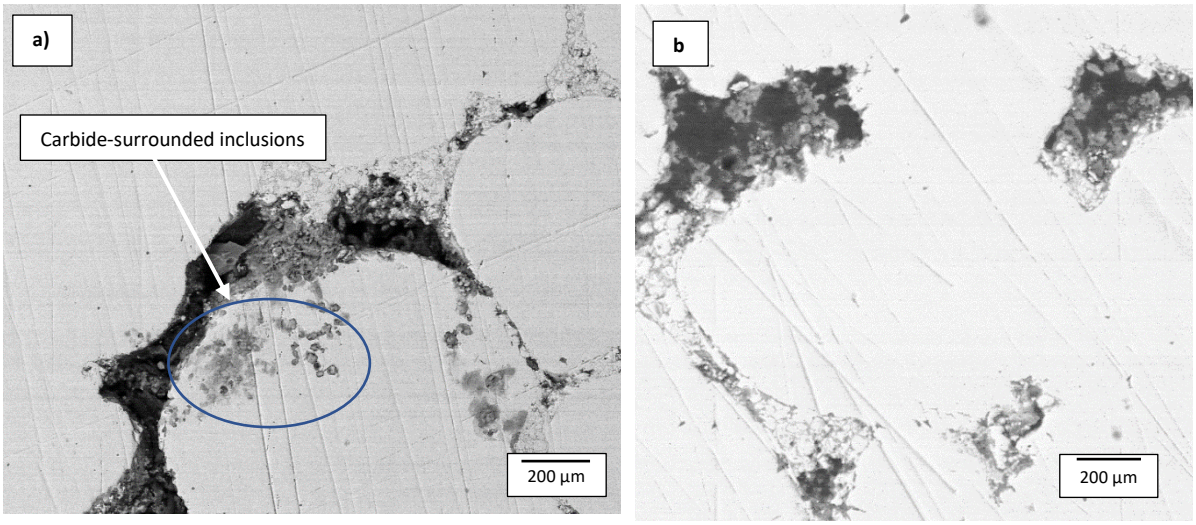

Figure 4.35: SEM-BSD micrographs of Hadfield steel showing the carbide-surrounded inclusions.

4.1.2 As-received materials: summary

WC-12Co had a smaller grain size structure because it contained traces of Cr which acts as a grain size refiner. WC-6Co and WC-8Co alloys had no other alloying elements hence their grains were similar in sizes and form. WC-12Co exhibited the highest Vickers macrohardness value

between the three WC-Co alloys investigated. WC-12Co also exhibited the lowest Palmqvist toughness values as a result of its refined grain structure.

Vanadium seemed to have had a stronger effect at increasing the bulk hardness of the HCWCI alloys than Cr. This was seen with HCWCI-1 having a higher Vickers hardness value than HCWCI-3, which had the highest Cr value. From inspecting the optical and SEM micrographs of the HCWCI alloys, the HCWCI-1 alloy had smaller primary carbides. This can be primarily accounted to by its low chromium content and traces of vanadium.

Hadfield steel exhibited the lowest Vickers hardness value of all the investigated materials and WC-12Co had the highest Vickers hardness value. The investigated HCWCI alloys and the Hadfield steel did not produce any cracks during the Vickers indentation measurements which, by default, implies they are tougher than the WC-Co alloys.

4.2 Slurry Rubber Wheel Abrasion Wear Results

The dry and slurry rubber wheel abrasion test results for the investigated materials are presented in this section. The damages caused by the dry and wet silica sand abrading against the surface of the samples were quantified using their respective volume losses. Their resistance to wear was determined by their respective specific wear rates.

4.2.1 Slurry abrasion wear rates

Figures 4.10-4.12 graphically presents the volumetric wear losses and Vickers hardness values of the WC-Co alloys plotted as a function of the abrading duration. The graphs for the HCWCI alloys are presented in Figures 4.13-4.15 and that of Hadfield steel is presented in Figure 4.16. Table 4.8 summarises the specific wear rates and Vickers hardness values of all the investigated samples after 40 minutes of abrasion.

From Figures 4.10-4.12, it was observed that WC-12Co experienced the least wear volume loss of 0.014 mm^3 in the first 10 minutes of abrasion, followed by WC-8Co which experienced a wear volume loss of 0.339 mm^3. WC-6Co experienced the highest wear volume loss of 0.937 mm^3. The same wear volume loss trend is observed throughout the entire abrading duration. WC-12Co experienced the least overall volume loss whereas the highest wear loss was experienced by the WC-6Co alloy. This trend was observed in the work by Ndlovu (2009) where the wear volume loss increased with an increase in the grain size.

All the WC-Co alloys experienced an increase in hardness during the course of the abrasion process. The highest increase in hardness is observed with WC-8Co, followed by WC-12Co. The least increase was observed with WC-6Co.

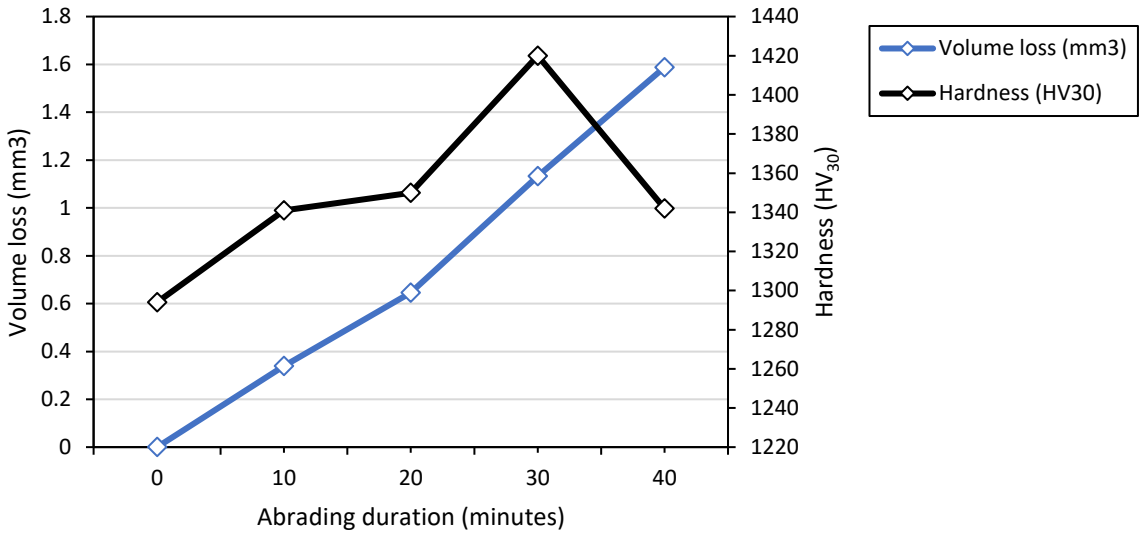

Figure 4.10: Volumetric wear losses and Vickers hardness values of the WC-8Co plotted as a function of the abrading duration.

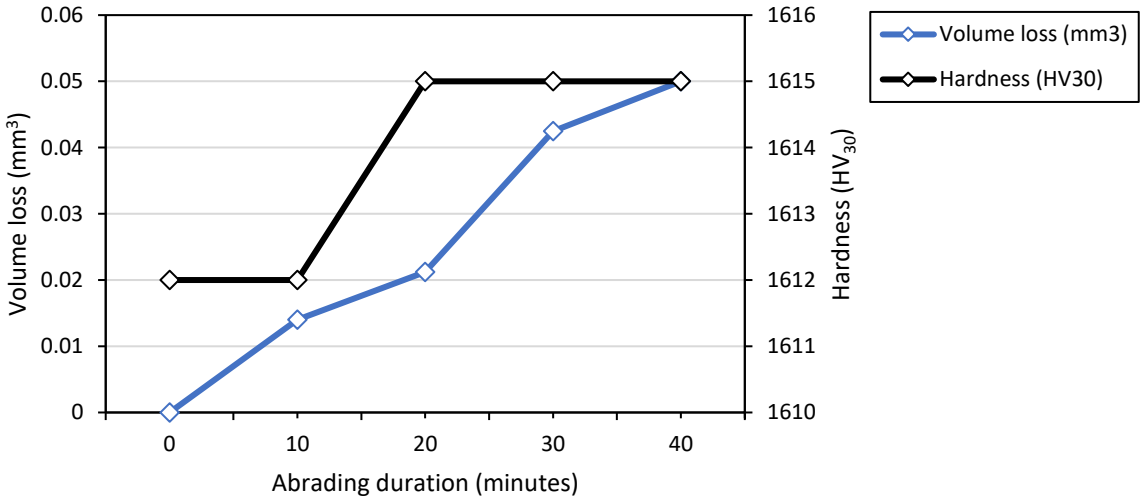

Figure 4.361: Volumetric wear losses and Vickers hardness values of the WC-12Co plotted as a function of the abrading duration.

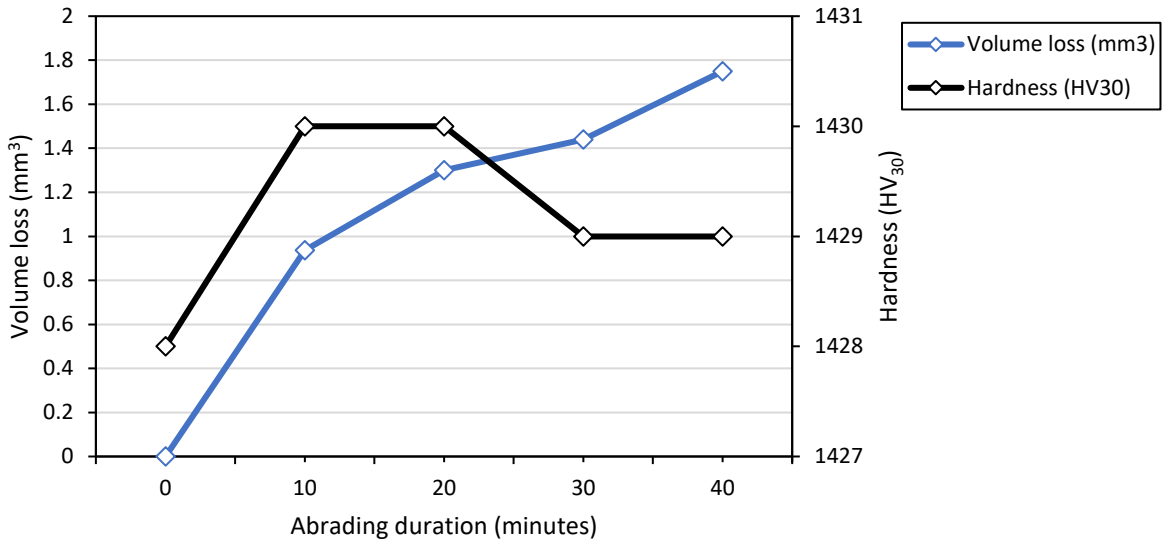

Figure 4.12: Volumetric wear losses and Vickers hardness values of the WC-6Co plotted as a function of the abrading duration.

The slurry abrasion results for HCWCI alloys (Figures 4.13-4.15) show HCWCI-2 as having experienced the least volume loss in the first 10 minutes of abrasion. The highest wear volume loss was experienced by HCWCI-1. The HCWCI-1 alloy experienced an overall cumulative volume loss of 31.48 mm^3. The HCWCI alloy that experienced the least volume loss was HCWCI-2 at 7.5 mm^3. HCWCI-3 experienced an overall cumulative wear volume loss of 11.35 mm^3.

HCWCI-2 and HCWCI-3 followed the same hardness trend. They both had slight hardness increases and then experienced a decrease during the last abrading intervals. HCWCI-1, however, only experienced an increase in hardness between 30-40 minutes and decreased steadily between 0-30 minutes.

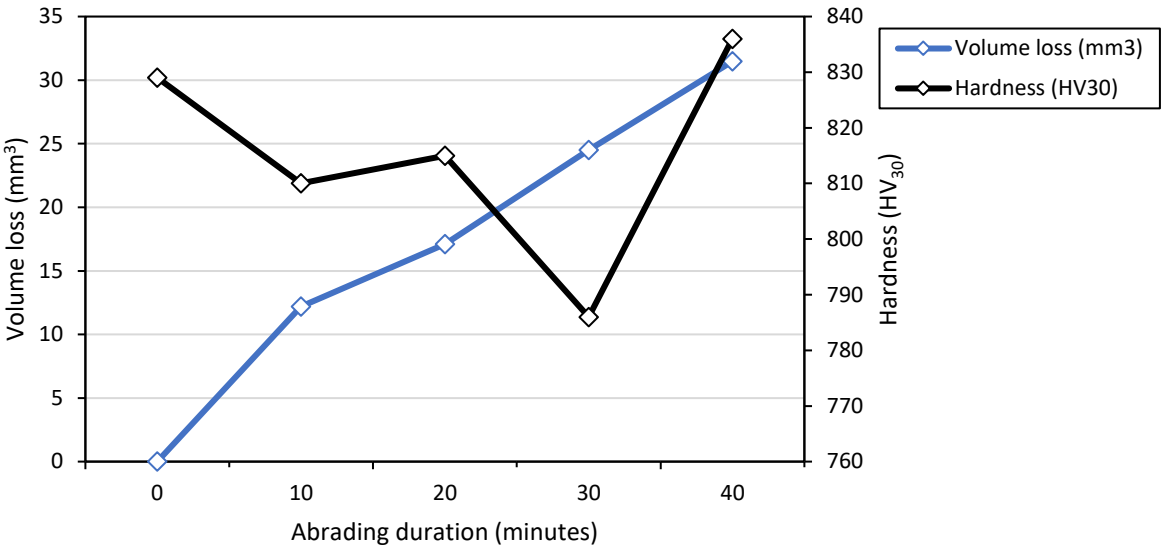

Figure 4.13: Volumetric wear losses and Vickers hardness values of the HCWCI-1 plotted as a function of the abrading duration.

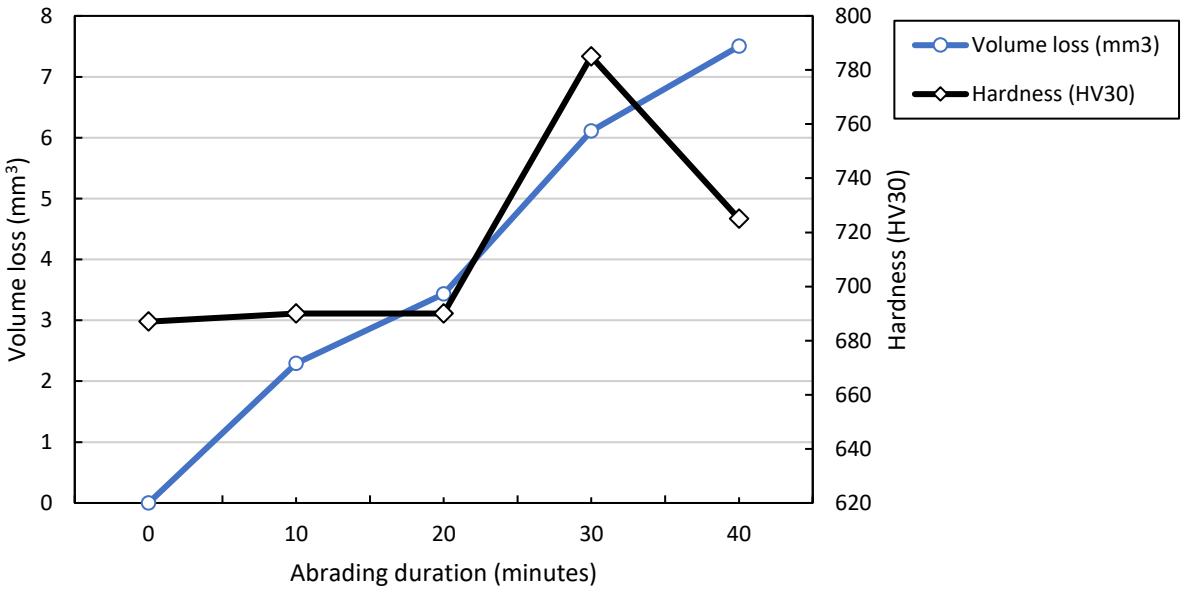

Figure 4.14 Volumetric wear losses and Vickers hardness values of the HCWCI-2 plotted as a function of the abrading duration.

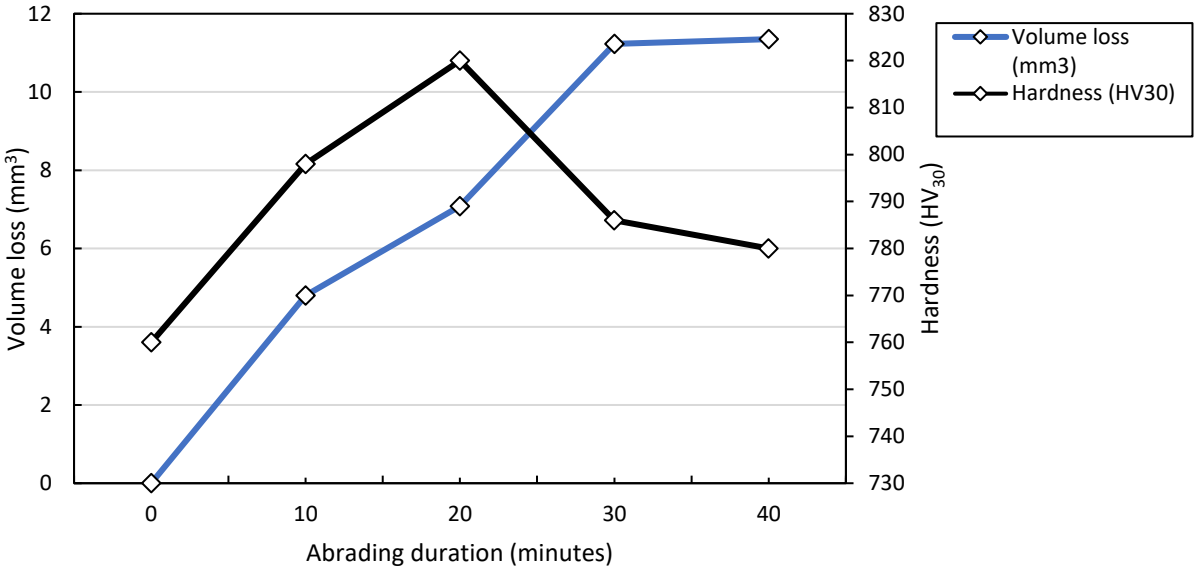

Figure 4.15 Volumetric wear losses and Vickers hardness values of the HCWCI-3 plotted as a function of the abrading duration.

Hadfield steel experienced the highest volumetric loss of the investigated samples. Hadfield steel experienced a wear volume loss of 99.04 mm^3 in the first 10 minutes. At 40 minutes steel experienced an overall wear volume loss of 158.72 mm^3. Hadfield steel had an overall Vickers hardness increase of 50 and then started decreasing after 20 minutes of abrasion.

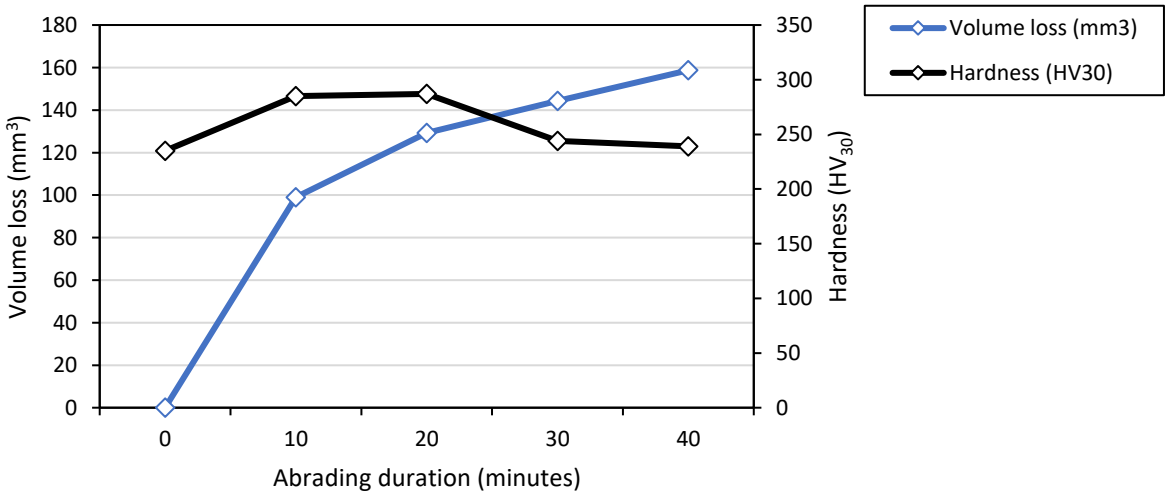

Figure 4.16: Volumetric wear losses and Vickers hardness values of the Hadfield steel plotted as a function of the abrading duration.

The specific wear rate values summarised in Table 4.8 show that the WC-Co alloys exhibited the highest resistance to slurry abrasion wear. WC-12Co experienced the highest resistance to slurry abrasion wear, followed by WC-8Co and then WC-6Co. This is in accordance with the work conducted by Ndlovu (2009) where the finer grained WC-Co with the highest cobalt content (15wt%) experienced lower abrasion rates than the courser WC-Co alloys.

Between the HCWCI alloys, HCWCI-2 experienced the highest resistance to slurry abrasion wear followed by HCWCI-3. HCWCI-1 experienced the least resistance to slurry abrasion. This was explained by Lu et al. (2001) and the explanation they gave was that the volume fraction of the matrix plays a major role in determining the wear resistance of white cast irons (WCI) under low stress abrasion conditions. The higher the volume fraction of the matrix relative to the eutectic carbides, the lower the resistance to wear. Hadfield exhibited the lowest resistance to the abrasion wear. The steel experienced a specific wear rate of two magnitudes higher than that of WC-12Co and one magnitude higher than HCWCI-2. Hadfield steel had the lowest Vickers hardness value after the abrading duration and WC-12Co exhibited the highest.

Table 4.8: Specific wear rates of the investigated samples and their Vickers hardness values after slurry abrasion.

Sample	Specific wear rate, k_s ($mm^3/N.m$) $\times 10^{-4}$	Vickers hardness (HV_{30})
WC-8Co	0.393	1342
WC-12Co	0.012	1615
WC-6Co	0.432	1429
HCWCI-1	7.780	836
HCWCI-2	1.850	725
HCWCI-3	2.810	780
Hadfield steel	39.200	239

4.2.2 Slurry abrasion wear rates: summary

The WC-Co alloys exhibited the highest resistance to slurry abrasion wear, followed by the HCWCI alloys and lastly, the Hadfield steel. The best performing alloy against the slurry abrasion test was WC-12Co. The specific rate of the WC-12Co alloy was smaller by a magnitude of three when compared to the specific rate of the Hadfield steel. WC-8Co was the best performing alloy after WC-12Co.

From the HCWCI alloys, HCWCI-2 showed the highest resistance to wear followed by HCWCI-3. HCWCI-1 exhibited the lowest resistance to the slurry abrasion wear test.

4.2.3 Slurry abrasion wear effects and mechanisms

The worn surfaces of the WC-Co alloys, HCWCI alloys, and the Hadfield steel were analysed by observing the top view sections. Optical microscopy micrographs were used to determine the mechanisms experienced by the three different materials during slurry abrasive wear process. Figure 4.17 (a, b, c) shows the optical micrographs of WC-8Co, WC-12Co, and WC-6Co, respectively. Figure 4.18 (a, b, c) presents the optical micrographs of HCWCI-1, HCWCI-2, and HCWCI-3, respectively. The optical microscope of Hadfield steel is presented in Figure 4.19. Table 4.9 is the summary of the wear mechanism during the abrasion wear of the WC-Co alloys, HCWCI alloys, and the Hadfield steel.

All the WC-Co alloys appeared to have regions of thin layers of smeared Co matrix (dark patches) at zones where the alloys experienced intensive wear. The smudged layers of Co appeared to be more prominent in WC-6Co as more ripples and Co displacement can be seen occurring. WC-12Co showed a small region where the extrusion of the binder occurred and the WC-8Co alloy showed even smaller regions where binder deformation occurred. The holes and depressions of the surfaces show that the WC grains were removed.

Particle pull-out happens at regions where the surface experienced large non-uniform loads. The WC particles could have been removed whole or could have first experienced microfragmentation before removal. WC-8Co exhibited several holes and depressions which shows a severe case of WC grain pull out. The holes and depressions also show binder pull

out. The fracturing of WC was observed to have occurred with WC-6Co and WC-8Co. Grooves (microploughing and microcutting) did not seem to have occurred with the WC-Co alloys and the reason for that was because the external load was small, and the abrading particles were not hard enough against the surfaces of the cemented carbides (Özkavak *et al.,* 2019). According to Ndlovu (2009) the microcracking of the WC-Co was expected throughout the worn surface, but the cracks could not be seen under the optical microscope.

The parallel grooves seen on the HCWCI alloys indicate that microploughing took place. The deeper and wider the grooves are, the more dominant the wear mechanism on the surface is. All three HCWCI alloys experienced microploughing. Larger and wider grooves were seen with the HCWCI-1 and HCWCI-3 alloys. The hardest two HCWCI alloys, HCWCI-1 and HCWCI-3 samples also experienced a thicker engraved impression where the rotating rubber wheel made most contact with the surfaces, causing a reduction in thickness. This reduction in the thickness of the samples was accelerated by the subsequent fracturing and cutting of the material that was protruded to both sides of the grooves during microploughing. The reduction in thickness of the samples can be also attributed to the microcutting wear mechanism that took place during the abrasion process. The dominating wear mechanism changed from microploughing to microcutting after a period. This is caused by the decrease in wear resistance from both the matrix and the hard carbides (Xu et al., 1993).

The matrix was worn off preferentially and displaced during the abrasion process while most of the primary eutectic carbides were exposed and/or pulled out from the matrix. The deformation of the matrix and the pulling out of the carbides are as a result of the lack of resistance from the hard matrix and carbides. This weakens the wear resisting integrity of the material causing it to be damaged. This further causes the decrease in the bulk hardness of the materials.

The HCWCI-2 alloy exhibited more exposure of the carbides after abrasion. The holes and depressions on the surfaces of the alloys also indicate that gouging took place. All three alloys showed regions where the carbides were either exposed or removed but it was the HCWCI-3 alloy that showed more deep grooves and gouging dimples.

Hadfield steel experienced two main wear mechanisms: microploughing and microcutting. During the analysis of the worn surface of the Hadfield steel, continuous grooves with and

without any material build-up was observed. This shows that both microploughing and microcutting occurred simultaneously (Tressia et al., 2017). During further abrasion, the work-hardened superficial layer is cut off by the abrading particles, causing a decrease in the steel's hardness as observed in Figure 7 (Prieto et al., 2015). During further observation of the worn surface, the microscope showed microcracks around the precipitated carbide inclusions. The cracks emanated from the induced stress caused by the external normal load and the entrapped abrading particles. The optical micrographs of the cracks could not be captured because they occurred deep within the depression zone where the rubber wheel made the most contact with the sample therefore making it difficult to obtain clear and high-resolution images.

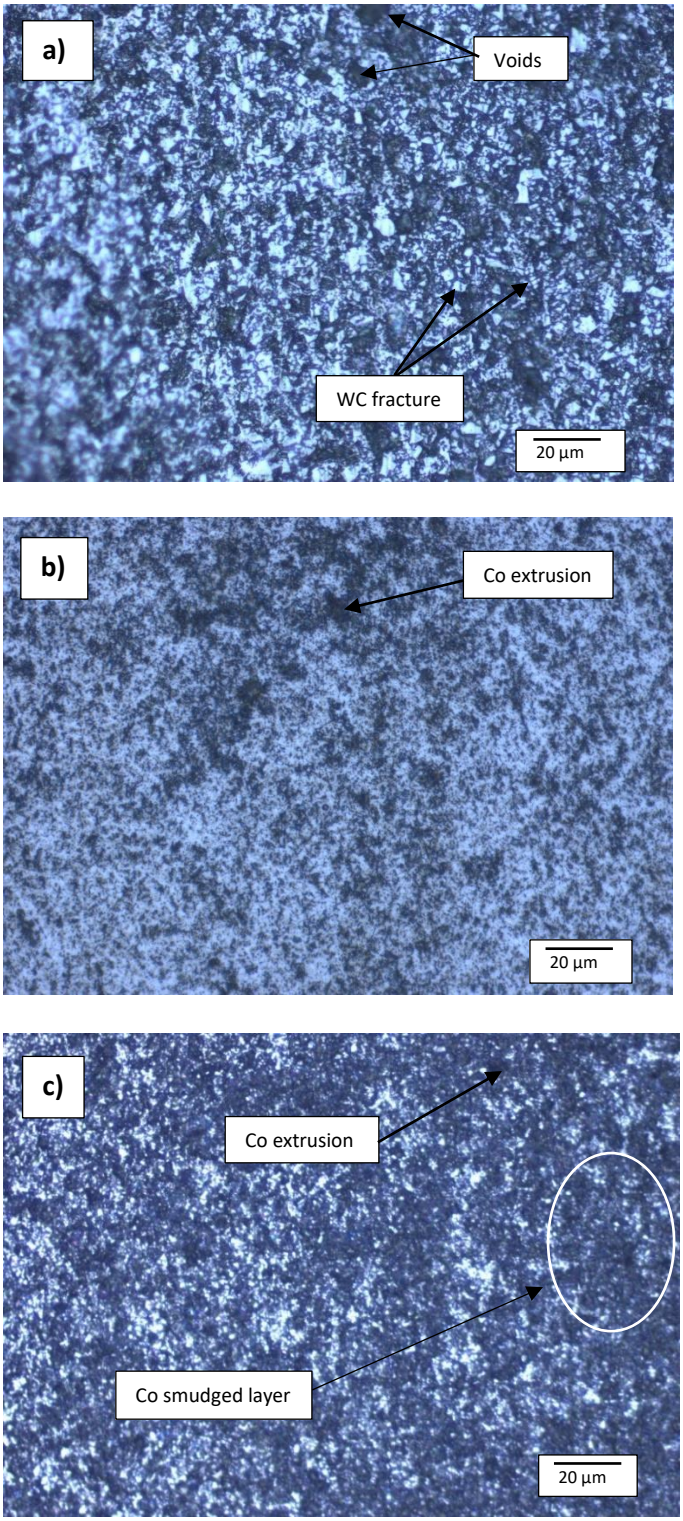

Figure 4.17: Optical micrographs showing the wear mechanisms during slurry abrasion wear of: (a) WC-8Co, (b) WC-12Co, and (c) WC-6Co alloys.

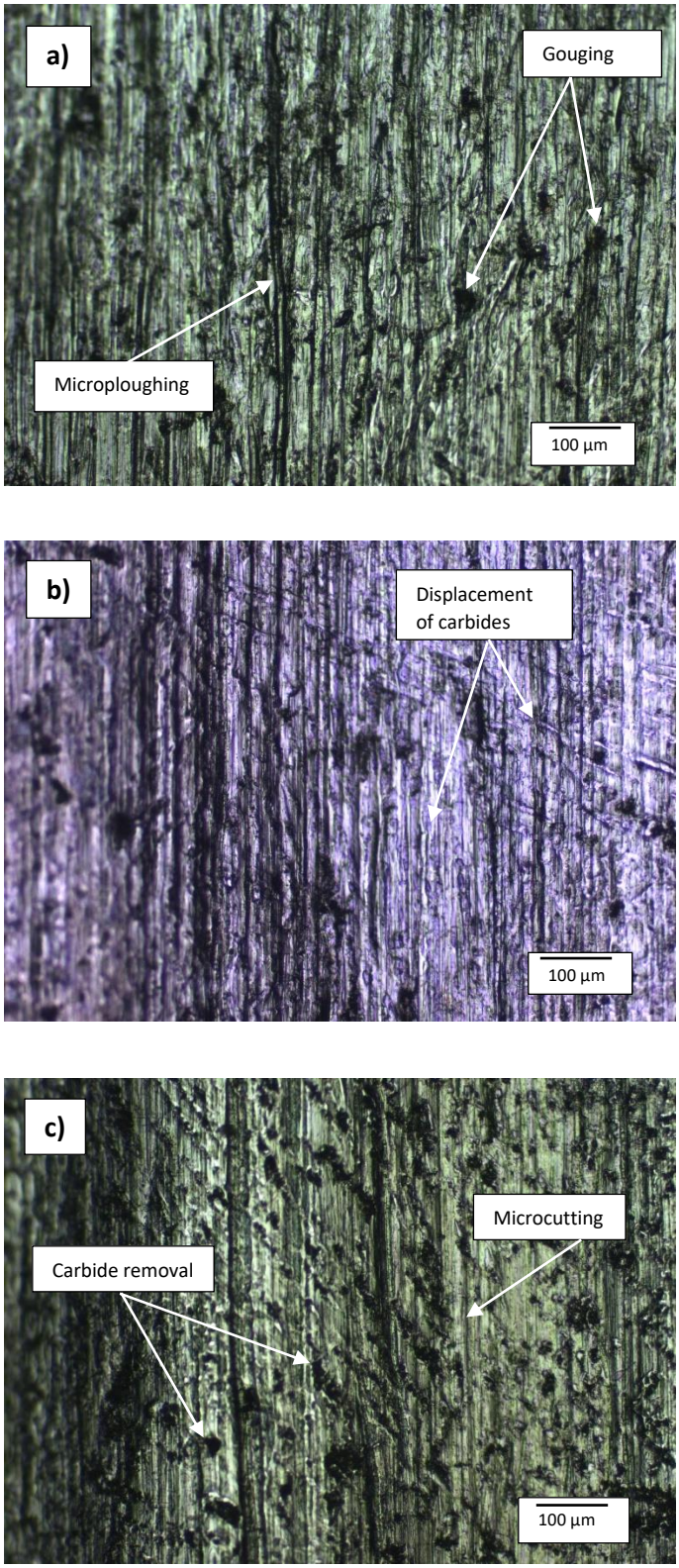

Figure 4.18 Optical micrographs of the HCWCI alloys showing the wear mechanisms during slurry abrasion wear.

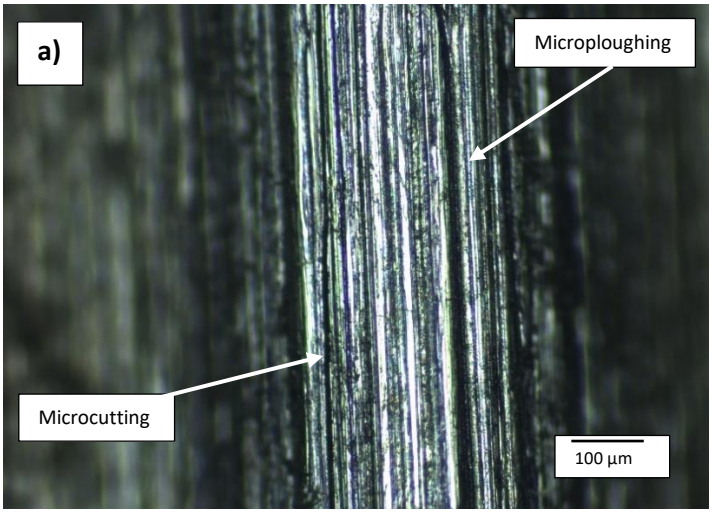

Figure 4.19: Optical micrographs of the Hadfield steel showing the wear mechanisms during slurry abrasion wear.

Table 4.9: Summary of the dominant wear mechanisms of the samples during slurry abrasion.

Wear mechanism	WC-Co alloys	HCWCI alloys	Hadfield steel
Microploughing	No	Yes, extensive on the HCWCI-1 and HCWCI-3	Yes
Microcutting	No	Yes	Yes
Grain pull out	Yes, seen mainly in the WC-8Co	Yes, mainly the removal of eutectic carbides	No
Binder extrusion	Yes, voids and Co displacement observed	Yes, displacement of the austenitic matrix	No
Microgouging	No	Yes, seen mainly with the HCWCI-1	No
Microcracking	Possible	No	Yes, seen around the precipitated carbide inclusions
Microfracturing	Yes, mainly on coarse WC particles	No	No

4.3 Dry Sand Abrasion Rubber Wheel Abrasion Wear Results

4.3.1 Dry sand abrasion wear rates

This section only includes the dry sand rubber wheel abrasion test results of the Hadfield steel. The other two alloys, viz. WC-Co and HCWCI alloys, were not included. This is due to the fact that the dimensions of the as-received WC-Co and HCWCI alloys were too small for the dry sand abrasion tribometer sample holder. The damages caused by the dry sand abrading against the surface of the Hadfield steel sample were quantified using its volume losses. The Hadfield steel's resistance to wear was determined by the steel's specific wear rate.

Figure 4.20 presents the volumetric wear loss and Vickers hardness values of the Hadfield steel plotted as a function of the abrasion duration. Table 4.10 is the specific wear rate and Vickers hardness value of the steel after 40 minutes of abrasion.

In the first 10 minutes of abrasion, the steel experienced a wear volume loss of 71 mm^3 and the Vickers hardness value increased from 250 to 275 HV_{30}. The overall wear volume loss experienced by the Hadfield steel during abrasion was 109.8 mm^3. The steel's Vickers hardness increased to a maximum of 289 HV_{30} during 20 minutes of abrasion. Thereafter, the hardness of the steel started decreasing, which resulted in a sudden steep increase in the wear volume loss. Prieto et al. (2015) explained in their work that the probable reason why high manganese steel decreases in hardness after a period of abrasion work on it was that the work-hardened superficial layer ends up being shaved off by the abrading particles, causing a decrease in the steel's hardness (Prieto et al., 2015). Hadfield steel exhibited a lower overall wear volume loss during dry sand abrasion wear than it did during slurry abrasion wear. This can be attributed to the steel's work-hardening properties under the larger forces exhibited by the dry sand rubber wheel tribometer.

The exhibited specific wear rate of the Hadfield steel during dry sand abrasion wear (Table 4.10) was 1.5×10^{-4} mm^3/N.m. This specific wear rate is a magnitude lower than the specific wear rate experienced during the slurry abrasion wear. This lowered wear rate can be attributed to the remarkable work-hardening of the steel during abrasion.

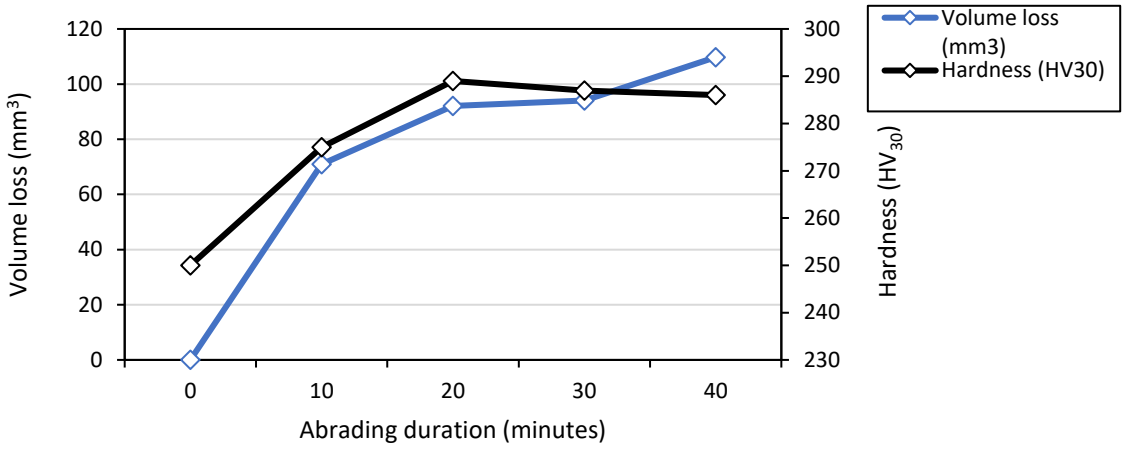

Figure 4.20: Volumetric wear losses and Vickers hardness values of the Hadfield steel after dry sand abrasion plotted as a function of the abrading duration.

Table 4.10: Specific wear rate and Vickers hardness value of the investigated Hadfield steel after dry sand abrasion.

Sample	Specific wear rate, k_s ($mm^3/N.m$) $\times 10^{-4}$	Vickers hardness (HV_{30})
Hadfield steel	1.47	286

4.3.2 Dry sand abrasion wear effects and mechanisms

The same main wear mechanisms experienced by the steel during slurry abrasion wear were exhibited by the steel during dry sand abrasion wear. Microploughing and microcutting were seen to have occurred on the worn surface of the Hadfield steel. Grooves with no build-up were seen to be less prominent on the surface of the sample that underwent dry abrasion wear and more prominent on the Hadfield sample that underwent slurry abrasion wear. This occurred due to the high friction experienced by the sample as a result of a larger external normal load acting against it, causing a much smoother surface finish. Figure 4.21 presents the optical micrographs of the Hadfield steel after undergoing dry sand abrasion wear.

The Hadfield sample also experience microcracking around the precipitated carbide inclusions. However, this mechanism could not be observed via the optical microscope as the abrasion groove was too deep to obtain clear and high-resolution images.

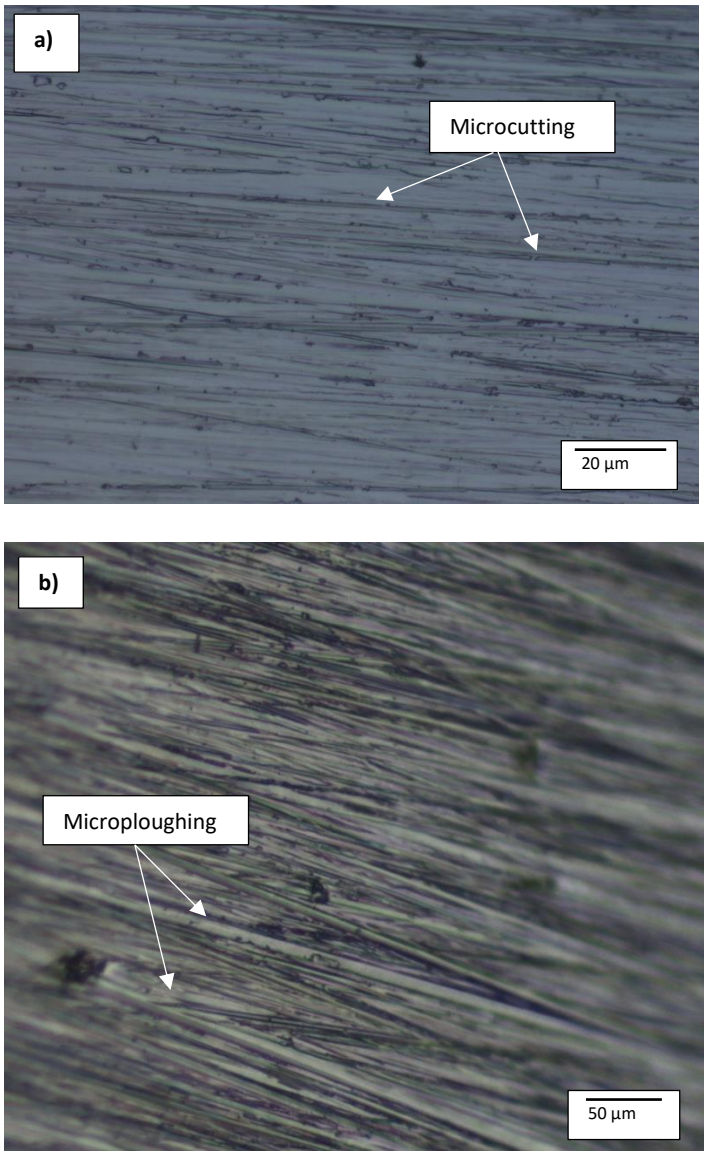

Figure 4.21: Optical micrographs of the Hadfield steel showing the wear mechanisms during dry sand abrasion wear.

4.4 Erosion Results

The effect of air jet solid-particle erosion was investigated on the surface of three grades of WC-Co samples. Three grades of HCWCI and Hadfield steel samples were also investigated.

The erosion behaviour and wear mechanisms of the samples was analysed using SEM micrographs. The tests were carried out using one set of controlled parameters. The impingement angle, jetting velocity and erodant feed rate were kept constant for all the tests. The erosion behaviour of the materials was assessed by paying attention to the morphology on impact sites, the erosion rates and the mechanisms of erosion.

4.4.1 Erosion behaviour

The effects of air jet erosion on the investigated samples are presented in Figures 4.22-4.28. The effects are quantified as mass loss of the eroded material as a function of the eroding time. The Vickers hardness values of the samples after every testing interval are also presented. The steady state erosion rates (E_r) at 120 minutes and the normalised erosion rates of the investigated samples at 30 minutes are listed in Table 4.11.

WC-Co cemented carbides

The cumulative mass loss versus eroding time graphs for WC-Co show varying mass losses and Vickers indentation hardness values, as presented in Figures 4.22-4.24. WC-12Co showed the highest cumulative mass loss of the three WC-Co samples and WC-6Co experienced the lowest mass loss.

The first 30 minutes of erosion showed different mass loss trends: WC-8Co experienced the lowest mass loss at 70.2mg followed by WC-6Co with a mass loss of 83.3mg and then WC-12Co at 104.6mg. The overall mass loss of WC-6Co, WC-8Co and WC-12Co were 206.7, 305.6 and 414mg, respectively.

All the WC-Co samples experienced an increase in hardness during the first 30 minutes eroding interval. The hardness of WC-12Co increased by 4.2%. The hardness of WC-6Co increased by 5.7% and WC-8Co increased by 19.1%. The pattern of the hardness of the samples follows no clear trend after 30 minutes of testing, other than the fact that it increases and decreases randomly with eroding time. This random increasing and decreasing of the hardness values could be caused by the jetting dynamics that occurred during the eroding process where the erodant may have been hitting the surface of the samples at different

locations during the 30minute intervals when the samples were removed and inserted again for analysis. Therefore, the erodant could have been hitting more harder (WC particles) or softer (Co matrix) phases at some point.

The highest increase in hardness during the span of the erosion tests was observed with WC-8Co at 90 minutes. The increase was by 385 HV_{30} from the original hardness value. WC-6Co had a hardness increase of 97 $HV_{30}$from its original value and WC-12Co had an increase of 67 HV_{30}. These values are in concurrent with the mass loss values experienced by the samples. The higher the increase in hardness during erosion, the lower the value of the eroded mass.

In the study by Feng et al. (2020), it was found that an increase in the Co matrix content of their investigated WC-Co samples lead to the decline in the erosion resistance of the cemented carbides. They also observed that a smaller WC particle size structure compromised the sample's resistance to erosion. Their findings are in accordance with the erosion results exhibited by the WC-Co alloys in this study.

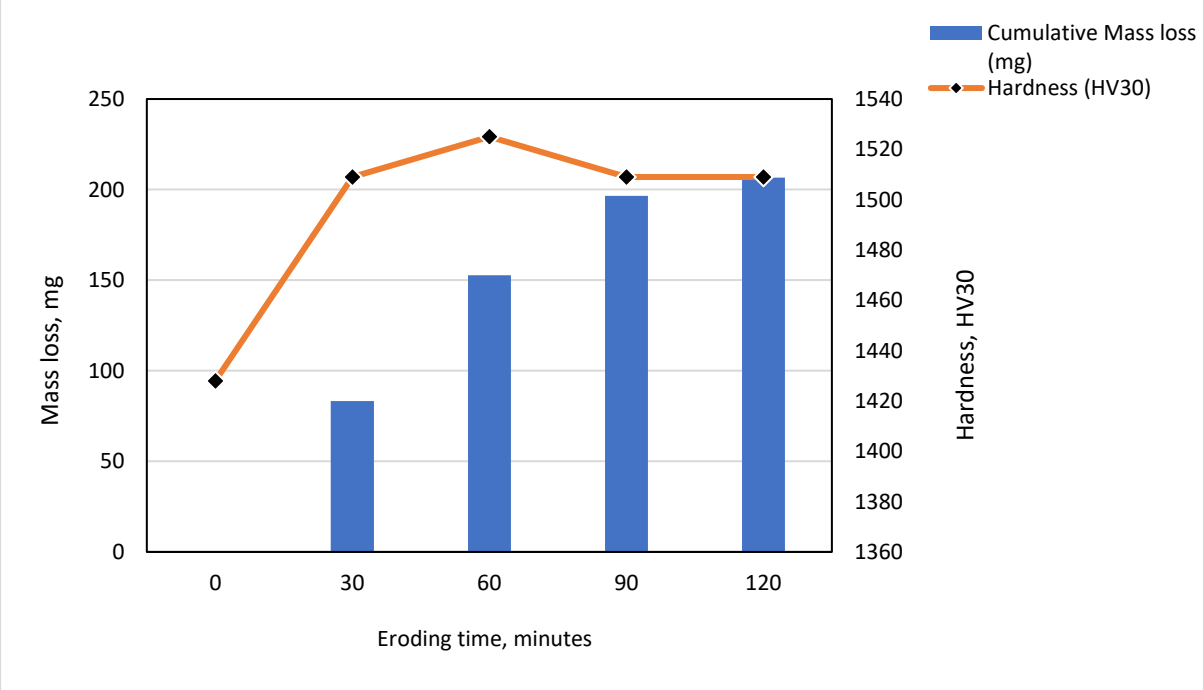

Figure 4.22: Erosion behaviour of WC-6Co graphically presented as cumulative mass loss (primary) and Vickers hardness (secondary) plotted as functions of eroding time.

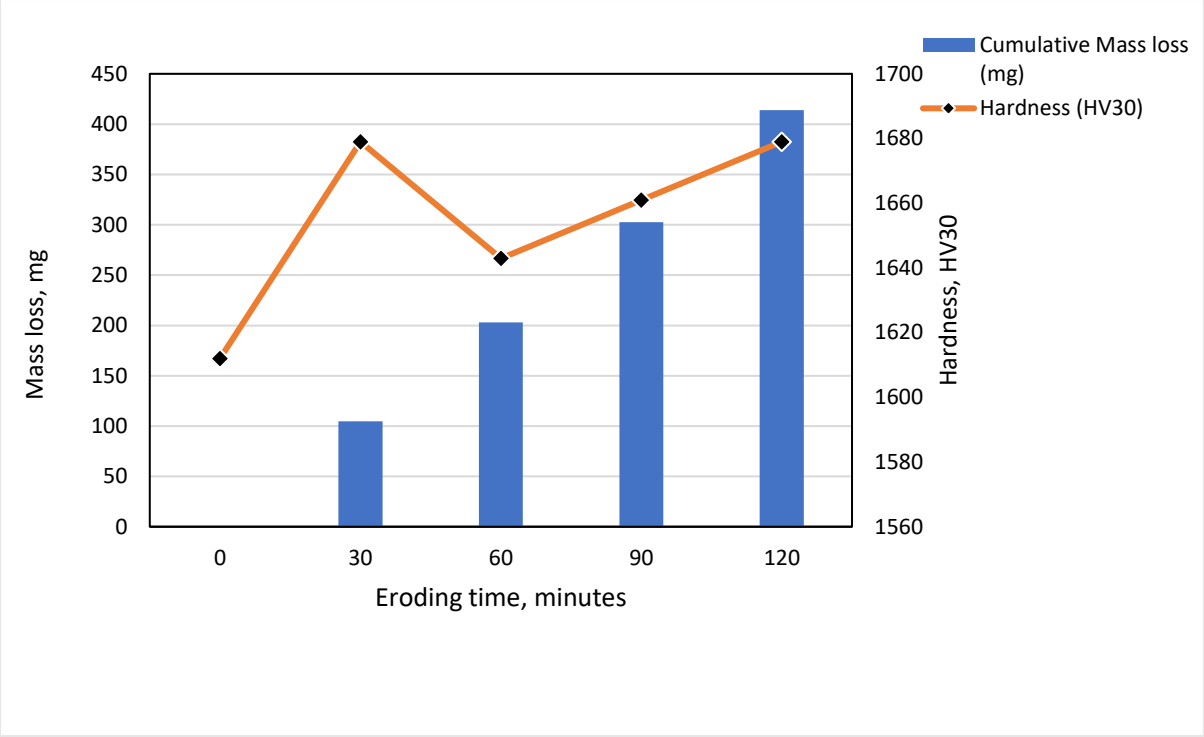

Figure 4.23 Erosion behaviour of WC-12Co graphically presented as cumulative mass loss (primary) and Vickers hardness (secondary) plotted as functions of eroding time.

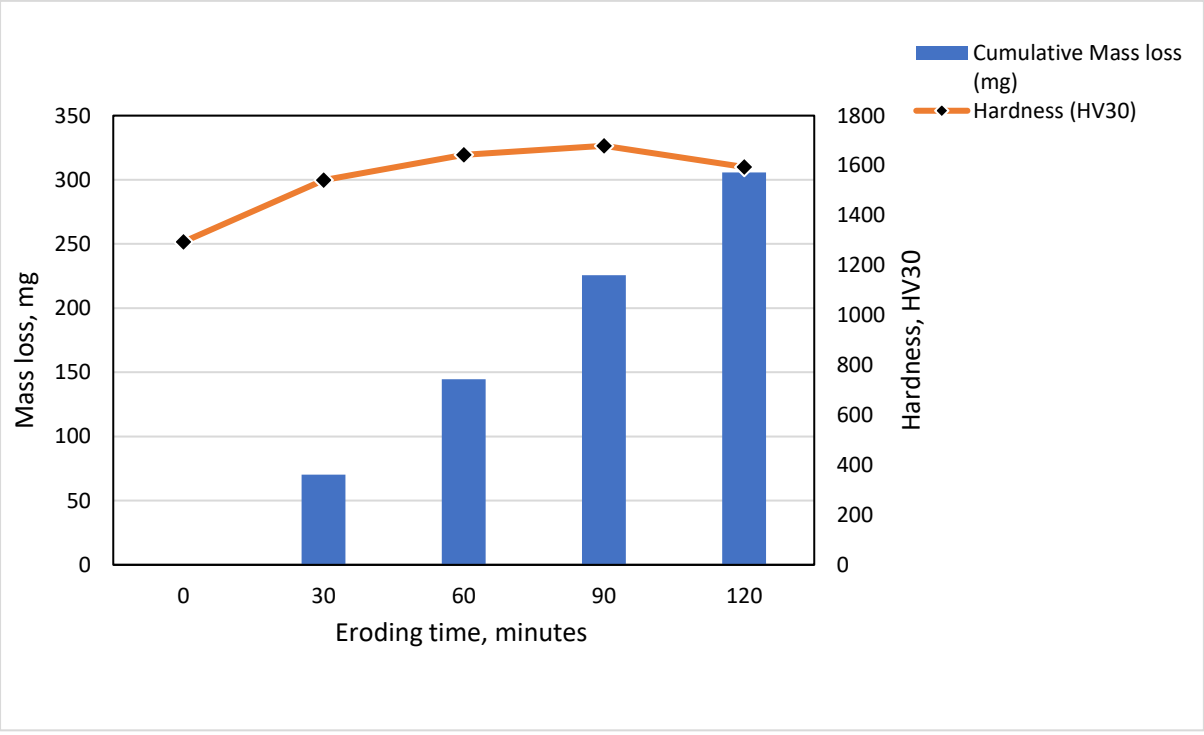

Figure 4.24: Erosion behaviour of WC-8Co graphically presented as cumulative mass loss (primary) and Vickers hardness (secondary) plotted as functions of eroding time.

HCWCI alloys

Figures 4.25-4.27 are graphical presentations of the HCWCI erosion test results. HCWCI-2 showed the highest cumulative mass loss of the three grades of HCWCI alloys. The cumulative mass loss of HCWCI-2 was 268.9mg followed by HCWCI-3 at 97.5mg. HCWCI-1 exhibited the lowest mass loss at 80.3mg. Both HCWCI-2 and HCWCI-3 contained larger volume fractions of carbides than the HCWCI-1 alloy which, according to the work conducted by Sapate and RamaRao (2004), proved to be detrimental to their resistance to erosion hence why HCWCI-2 and HCWCI-3 exhibited the highest loss. HCWCI-1 also contained vanadium in its system. Vanadium forms vanadium carbides which are harder than the primary M_7C_3 carbides. The addition of Vanadium may also have strengthened the austenitic matrix which in turn may have improved its fracture strength causing the resistance of material removal by erosion in HCWCI-1 (Liu et al., 2005).

The highest increase in hardness (HV_{30}) observed with the HCWCI alloys during the span of the erosion tests was seen with HCWCI-2. The increase was by 82 HV_{30} from the original hardness value. HCWCI-3 had a hardness increase of 69 HV_{30} from its original value, but HCWCI-1 did not exhibit a hardness increase. The same trends were observed in the work conducted by Yousif and Ataiwi (2017) and Yaer et al. (2007) where they reported that the white cast irons (WCI) samples exhibited an increase in hardness due to work hardening after erosion. They concluded that this was due to the surface hardness and strain hardening properties of the alloys during erosion (Bitter, 1962). HCWCI-2 exhibited the highest cumulative mass loss of the three HCWCI samples and had the highest hardness increase. HCWCI-1 had no hardness increase during erosion, but it exhibited the lowest mass loss.

The relationship between the initial hardness and the total mass loss experienced by the HCWCI alloys is not the same as seen with the WC-Co alloys. In fact, the relationship is the total opposite. In the case of the WC-Co alloys, the hardest sample (WC-12Co) exhibited the highest overall mass loss whereas for the HCWCI alloys, the hardest sample (HCWCI-1) exhibited the least overall mass loss. This observation can be attributed to the different

morphological and chemical makeup of the alloys. This difference in the morphology and chemical makeup between the alloys may lead to the alloys experiencing different mechanisms during solid particle erosion, hence, the different responses to erosion.

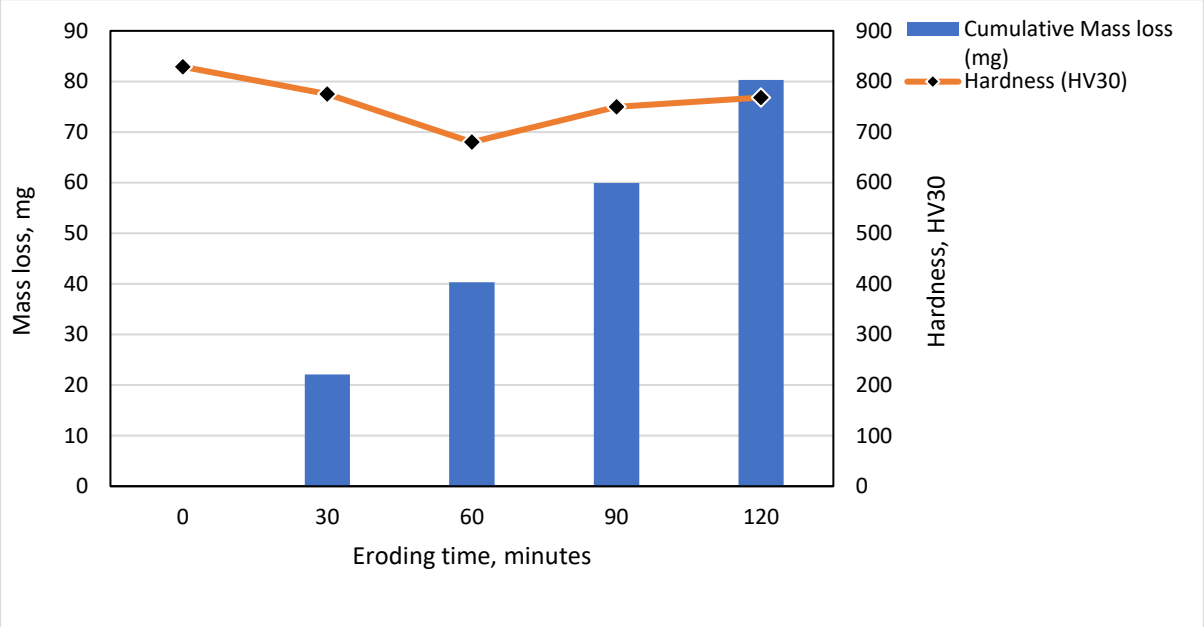

Figure 4.25: Erosion behaviour of HCWCI-1 graphically presented as cumulative mass loss (primary) and Vickers hardness (secondary) plotted as functions of eroding time.

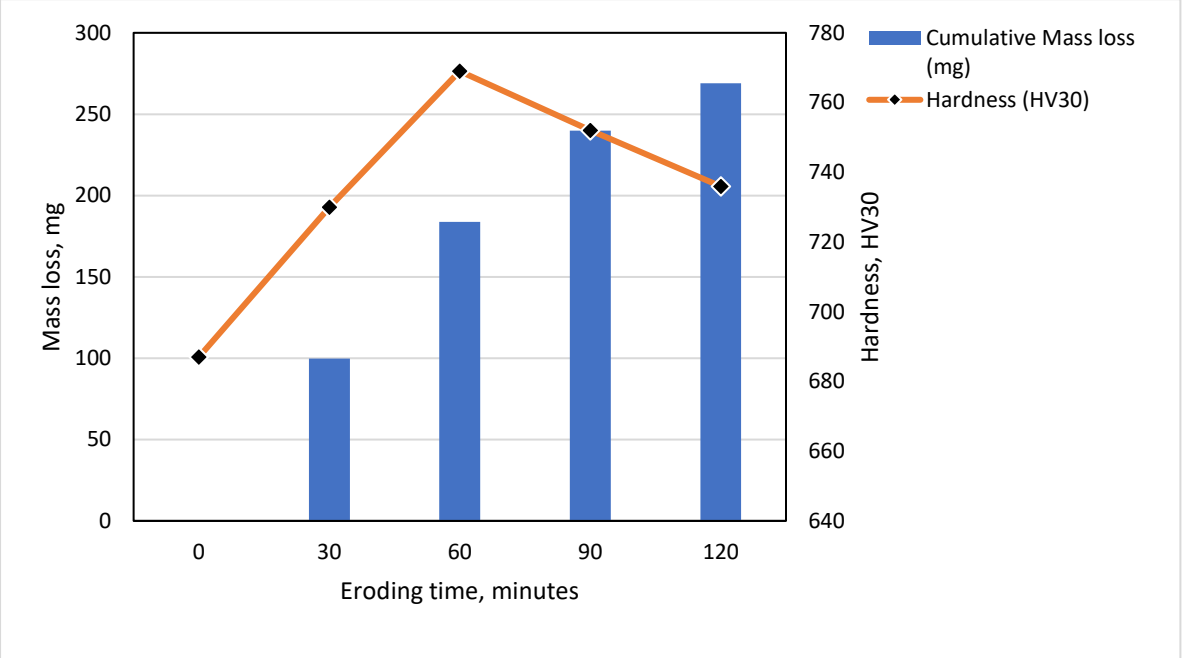

Figure 4.26: Erosion behaviour of HCWCI-2 graphically presented as cumulative mass loss (primary) and Vickers hardness (secondary) plotted as functions of eroding time.

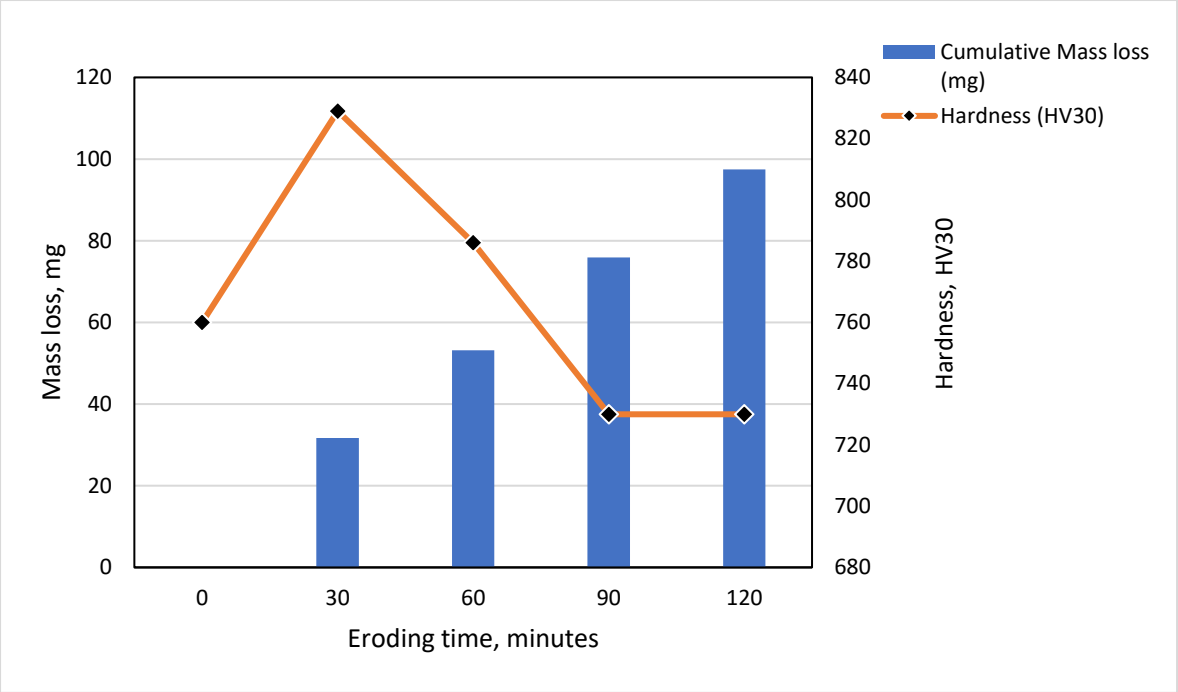

Figure 4.27: Erosion behaviour of HCWCI-3 graphically presented as cumulative mass loss (primary) and Vickers hardness (secondary) plotted as functions of eroding time.

Hadfield steel

The graphical presentation of the erosion wear behaviour of Hadfield steel in terms of its mass loss is presented in Figure 4.28. Hadfield steel experienced a cumulative mass loss of 1068.5 mg, which makes it the sample that experienced the highest mass loss. The Hadfield steel sample experienced a mass loss of 401.5 mg in the first 30 minutes of erosion. The mass loss accumulated to 673.4mg in the first hour of erosion and increased to 945mg after 1 hour and thirty minutes.

Hadfield steel also experienced an increase in the hardness value during the first two eroding intervals. This can be attributed to the material's work-hardening properties (Yildizli et al., 2005; Sabzi and Farzam, 2019; Xiayun et al., 2011). The hardness value decreased after 90 minutes eroding time. The steel experienced an increase of 25 HV_{30} i n the first 30minutes of erosion. Hadfield steel reached its highest Vickers value at 60 minutes. The hardness increased by 51 HV_{30} from its as-received state. The highest increase in hardness during the

span of the erosion tests is observed at 60 minutes with a hardness increase of 51 from the starting hardness value.

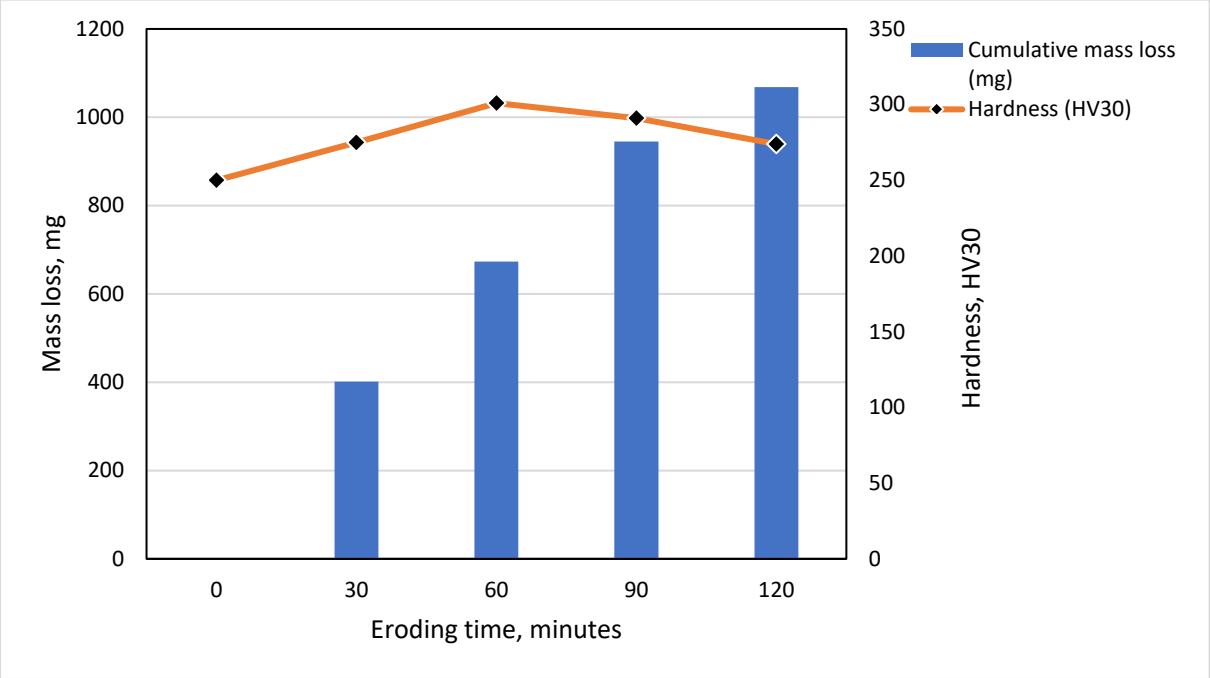

Figure 4.28: Erosion behaviour of Hadfield steel graphically presented as cumulative mass loss (primary) and Vickers hardness (secondary) plotted as functions of eroding time.

The steady state and normalised erosion rates of the investigated samples indicated that Hadfield steel exhibited the highest erosion rate values between WC-Co and HCWCI. This was expected since the Hadfield steel has no hard composite in its structure. This is also in line with the relationship ductile materials have with low impingement angles. Ductile materials readily deform upon solid particle impact at low impingement angles (around and lower than 45°) which was the angle used in this study (Kamran et al., 2011; Hutchings, 1983).

Between the WC-Co alloys, WC-6Co exhibited the lowest steady state erosion rate at 120 minutes and WC-12Co showed the highest steady state erosion rate. At 30 minutes, WC-8Co exhibited the lowest normalised erosion rate and WC-12Co showed the highest normalised erosion rate. One would expect that WC-12Co would experience the lowest erosion rates because it is the hardest of the three WC-Co alloys, however, Antonov et al., (2017) recorded that the overall morphology of cemented carbides controlled the erosion rate. From the work

hardening trends observed in Figures 4.22-4.24, WC-12Co might have experienced the highest erosion rates because it exhibited the lowest total hardness increase during erosion. The same trend was also observed by Antonov et al. (2017) where fine-grained materials were found to be easily damaged and exhibited the highest erosion wear rates.

Amongst the HCWCI alloys, HCWCI-2 exhibited the highest steady state and normalised erosion rates. HCWCI-1 had the lowest value of the erosion rates. This trend between work hardenability and erosion rate was not the same as observed with the WC-Co alloys. The higher the hardness increase during the erosion of HCWCI alloys, the higher the erosion rate values were.

Table 4.11: Steady state erosion rates (E_r) at 120 minutes and normalised erosion rates of the investigated samples at 30 minutes.

Samples	Steady state erosion rate, E_r, $\times 10^{-5}$ ($g.g^{-1}$)	Normalised erosion rate, E_R, $\times 10^{-3}$ ($g.min^{-1}$)
WC-6Co	1.44	2.78
WC-8Co	2.12	2.34
WC-12Co	2.88	3.49
HCWCI-1	0.56	0.74
HCWCI-2	1.87	3.33
HCWCI-3	0.68	1.06
HS	7.42	13.38

4.4.2 Erosion wear effects and mechanisms

The wear damages and mechanism experienced by the investigated materials after undergoing solid particle erosion wear are presented in this section. The SEM micrographs used to examine the erosion wear mechanisms the WC-Co cemented carbides are given in

Figure 4.29. The SEM micrographs of the HCWCI alloys and Hadfield steel are presented in Figures 4.30 and 4.31, respectively.

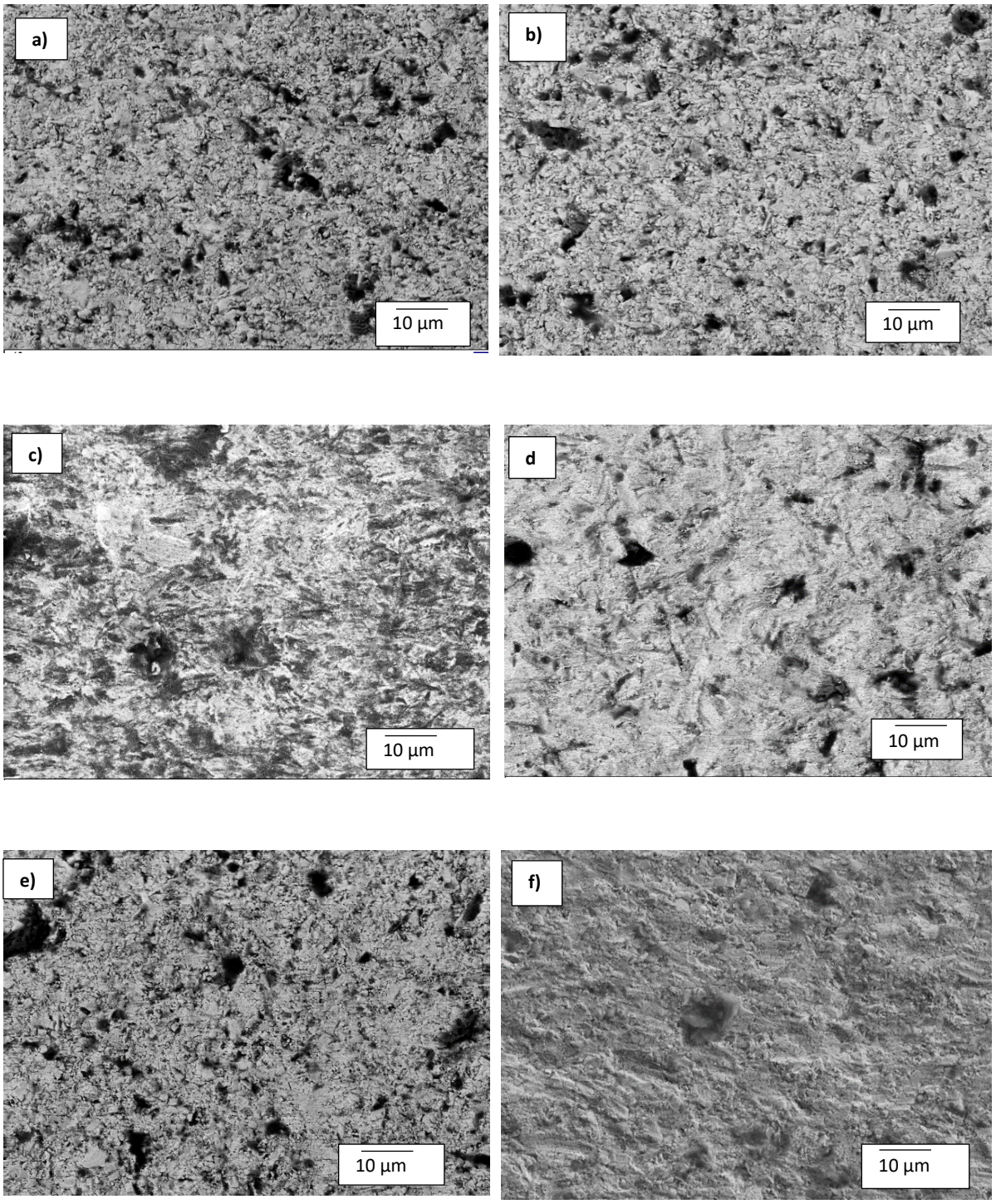

Figure 4.29: SEM-BSD micrographs showing the erosion wear mechanisms of: (a-b) WC-6Co, (c-d) WC-12Co, and (e-f) WC-8Co.

The investigated WC-Co cemented carbides experienced varying ductile-brittle mass loss wear mechanisms during the erosion process. The main erosion wear mechanism was the extrusion of the binder, formation of cracks around the grain boundaries and the refinement of WC particles by fragmentation, and WC pull-out.

Mechanically mixed layers consisting of a ceramic phase, binder phase and the embedded Al_2O_3 eroding particles were also observed occurring on the surfaces of the target materials. The mechanically mixed layers (MML) occurring on the worn surfaces were seen to be frequent with WC-6Co and are noticed by the smoky grey looking patches in Figure 4.29 (a, b). The MML regions can be seen occurring less frequently with the WC-8Co alloy and rarely with the WC-12Co alloy because of the manner in which the WC particles were closely packed to each other restricting sufficient exposure of the ductile binder. This type of a wear mechanism occurs in ductile phases and it is not completely deleterious because, for a short period of time, the embedded Al_2O_3 particles and the refined pieces of WC act as a protective layer for that particular region against further deterioration (Finnie, 1960; Tilly, 1973). The cobalt binder also experienced extrusion as the impacting particles penetrated the surface, resulting in the excessive removal of the displaced binder in a form of chips this form of mechanism. The craters formed then act as sites where the erodant can embed itself inside and behave as a protective shield against further impacting by the eroding particles.

The refined structure of WC-12Co, experienced removal of large fragments from its surface. The fragments contained very small WC particle still bounded by cobalt whereas the two coarser grained cemented carbide alloys mainly experienced individual WC particle pull-out. However, in both cases, the removal of material was caused by the localised stress response of the binder to erosion attack which resulted in the preferential removal of cobalt and ultimately, the removal of the unsupported WC particles. Pugsley and Allen (1999) suggested in their work that this transition in material removal of the binder to the WC particles is related to the scaling effect seen with most composite materials like high chromium cast irons. The removal of large fragments can be seen occurring more frequently with the WC-12Co and can be noticed on the SEM micrographs by the dark pits and depressions left behind on the surfaces.

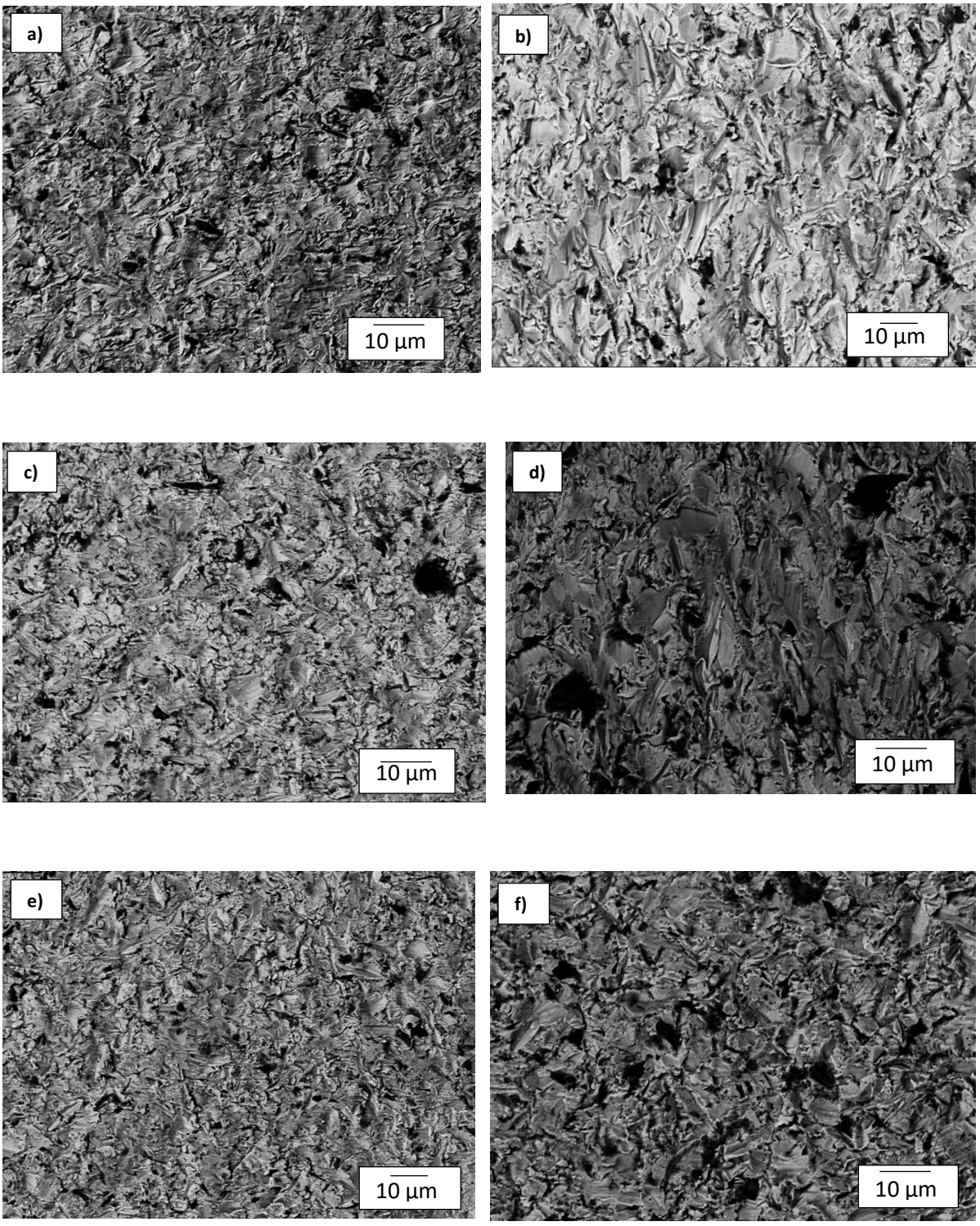

Figure 4.30: SEM-BSD micrographs showing the erosion wear mechanisms of: (a-b) HCWCI-1, (c-d) HCWCI-2, and (e-f) HCWCI-3.

The investigated HCWCI alloys, like any other metals that contain ceramic particles dispersed in a soft matrix, experienced a mixed ductile-to brittle (or vice versa) response during solid particle erosion wear. The predominant erosion mechanisms of material removal were observed to be edge fracture of the carbides (brittle) and extensive edge rounding occurring on the ductile matrix. Deep short grooves with material pushed on either side of the indentations (indentations with extruded" lips") were also observed occurring on the eroded alloys, indicating that the matrix experienced microploughing. However, ductile cutting of the matrix was more prominent than microploughing. Sepate and RamaRao (2005) reported similar matrix removal mechanisms.

The alloys also experienced lateral fracturing of the carbides, resulting in the removal of the second phase particles from the matrix by the process of fatigue (Finnie, 1972; Hutchings, 1981). The occurrence of this material removal mechanism can be noticed by the deep holes left behind after the carbides were removed. HCWCI-2 (Figure 4.30 (c) and (d)) showed larger and frequent deep poles relating to a higher volume fraction of the removal of the hard carbides. High volume fraction of large carbides proved to be detrimental to the alloy's resistance to erosion and this was reflected in its relatively high wear rates. Aptekar and Kosel (1985) reported the same trend in their work where the large bulky primary carbides provided adverse responses to wear by erosion. HCWCI-1 experienced the least occurring large carbides, hence it experienced the least erosion rate. Furthermore, the small and frequently dispersed eutectic primary carbides protected the matrix from excessive material removal.

In Figure 4.31 it is possible to observe the wear scars on the Hadfield steel that were left behind by the Al_2O_3 particles after erosive wear. Because the Hadfield steel was a lot softer than the other metals, larger grooves and indentations were seen occurring more frequently on the surface of the Hadfield steel than on the other investigated metals.

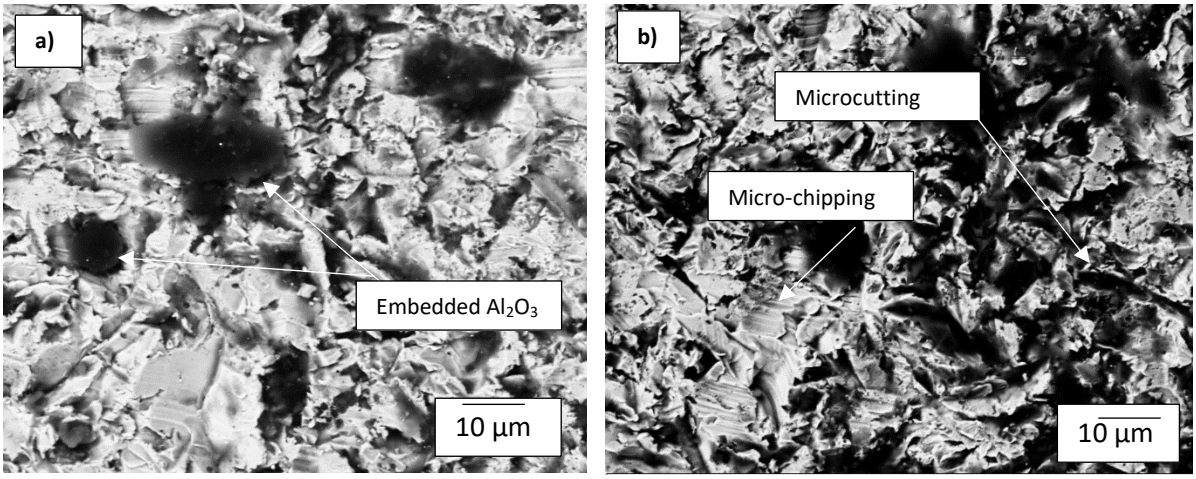

Figure 4.31: SEM-BSD micrographs showing the erosion wear mechanisms of: (a-b) Hadfield steel.

The predominant mass loss wear mechanisms were observed to be ductile cutting, ploughing action, and pitting. Fragments of wear debris and eroding particles were also found embedded on the surface of the worn surface. The craters formed by large particles impacting the surface of the steel had smaller fragments of fractured eroding particles and wear debris embedded inside. The same material mass loss mechanisms were also observed and recorded in the work by Laguna-Camacho et al. (2012). Cracks can be seen emanating from regions into which large Al_2O_3 were embedded into. Some of the deep grooves were flattened due to successive impacts during the erosion process. The sliding and abrading action (microcutting) contributed the most to the mass loss seen occurring with the Hadfield steel during erosion just as seen with the work conducted by Yildizli (2005). Striations were seen occurring on the worn surfaces, showing the severe plastic deformation that took place from the surface experiencing fatigue.

4.4.3 Erosion results: summary

The solid particle erosion behaviours of WC-Co alloys, the HCWCI alloys, and Hadfield steel were investigated. It was found that:

- WC-12Co exhibited the highest erosion rate (steady state and normalised) out of the three WC-Co alloys and WC-6Co performed better against erosion. The WC-Co alloys

experienced the poorest overall resistance against erosive wear when compared with the result exhibited by the HCWCI alloys.

- Between the HCWCI alloys, HCWCI-1 was the alloy that showed the least susceptibility to damage by erosion, whereas HCWCI-2 performed the poorest.
- Hadfield steel exhibited the highest overall mass loss and therefore showed the highest erosion rate.

The dominating wear mechanisms seen on the surfaces of WC-Co alloys were the extrusion of the binder, grain pull-out and fragmentation removal. Edge fracturing of the carbides (brittle) and extensive edge rounding occurring on the ductile matrix were the main mechanisms found to occur in HCWCI alloys. The dominant wear mechanisms exhibited by the Hadfield steel sample was microploughing and microcutting.

4.5 Pin-On-Disc Sliding Wear Results

The sliding wear of materials is affected by a variety of parameters, including the sliding velocity, lubrication on disc, the normal force on the pin, temperature, the roughness on the pin and disc, and the particle grain size of the disc (Stachowiak et al., 2004). However, only the volume loss of the pin will be used as a control parameter to quantify the sliding wear of the investigated materials. The wear rates of the pins against the discs are documented in this section.

4.5.1 Coefficient of friction behaviour

The CoF versus sliding distance plots for the WC-Co alloys are graphically presented in Figure 4.32 and those of the HCWCI alloys and Hadfield steel are presented in Figure 4.33 and 4.34, respectively. Figure 4.35 is a graphical presentation of the CoF versus sliding distance of all the investigated samples. Figure 4.36 presents the mean value and standard deviation of the CoF of all the samples. Table 4.12 shows the CoF of all the samples at 0.0189m, 50m, 300m, and 500m, showing the three stages of CoF detected during the sliding process. The periodicity (Δt in seconds) of the three stages is represented as follows:

- Stage 1: 500 seconds between the sliding distance of 0.0189m to 50m

- Stage 2: 2500 seconds between the sliding distance of 50m to 300m
- Stage 3: 2500 seconds between the sliding distance of 300m to 500m

Table 4.12: The CoF values of the investigated samples at the three different stages of the sliding process.

Samples	Run-in stage	Stage 1	Stage 2	Stage 3
WC-6Co	0.92	0.72	0.79	0.84
WC-8Co	0.75	0.70	0.69	0.70
WC-12Co	0.88	0.83	0.81	0.75
HCWCI-1	0.79	0.72	0.53	0.64
HCWCI-2	0.77	0.59	0.56	0.67
HCWCI-3	0.81	0.77	0.70	0.04

The CoF values were found to rapidly increase during the first few meters of the sliding process before reaching steady state at around 100m into the sliding. The friction values tend to subsequently decrease in the second stage and increase steadily again as they reach steady state again in the third stage (Chowdhury et al., 2014). These trends can be observed in Table 4.12 and Figure 4.35 for all the investigated materials, except for the HCWCI alloys where the CoF of HCWCI-3 decreases in the third stage. HCWCI-3 has the greatest overall decrease in the friction value in the third stage followed by HCWCI-1 then HCWCI-2. Kang and et al. (2001) established that an inversely proportional relationship exists between the Cr content and the CoF value of the high chromium cast iron. This relationship was seen occurring between HCWCI-1 and HCWCI-3. HCWCI-2 deviated from this relationship and a plausible reason why is because of the large and hard Cr-carbides that increased the friction between the surface of the alloy and the asperities of the pin.

The CoF results for the WC-Co samples in Figure 4.32 show that the WC-6Co has the highest CoF value of 0.92 in the run-in stage followed by WC-12Co with a value of 0.88 and then WC-8Co with a friction value of 0.75. This behaviour is in agreement with literature reports where the highest peaks of friction are expected in the run-in stage (Bhushan, 1999; Israelachvili,

1995; Blau, 2005; Masilela, 2008; Hernandez, 2014). The same trend can be observed with the HCWCI alloys, Figure 4.33, where the highest CoF peaks are observed in the run-in stage. HCWCI-3 has the highest CoF of the three HCWCI samples with a value of 0.81 followed by HCWCI-1 at 0.79 and then HCWCI-2 at 0.77.

However, for Hadfield steel, the CoF results show a different trend to that of the WC-Co and HCWCI samples. For Hadfield steel, Figure 4.34, the highest friction peak was observed in the last stage at a value of 0.950. This shows that the build-up of wear debris on the edges of wear track occurs at the last stage of sliding the process. This build-up of wear debris also accounts for the increased friction between the two surfaces as these debris must be pushed along the wear track.

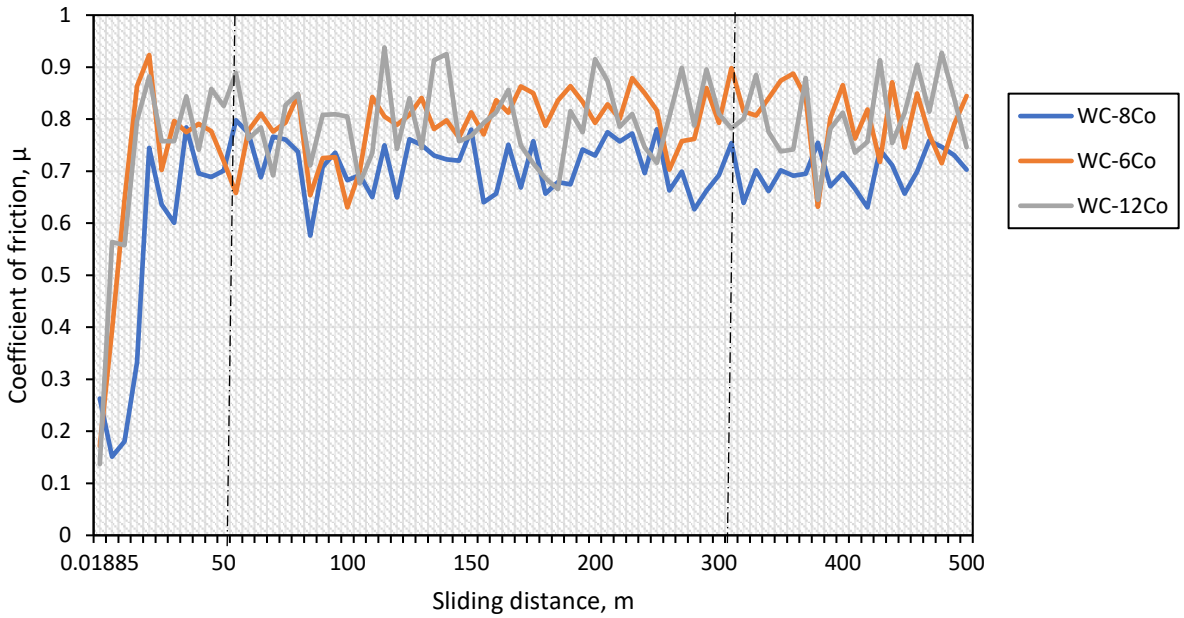

Figure 4.32: CoF versus sliding distance for the WC-Co alloys.

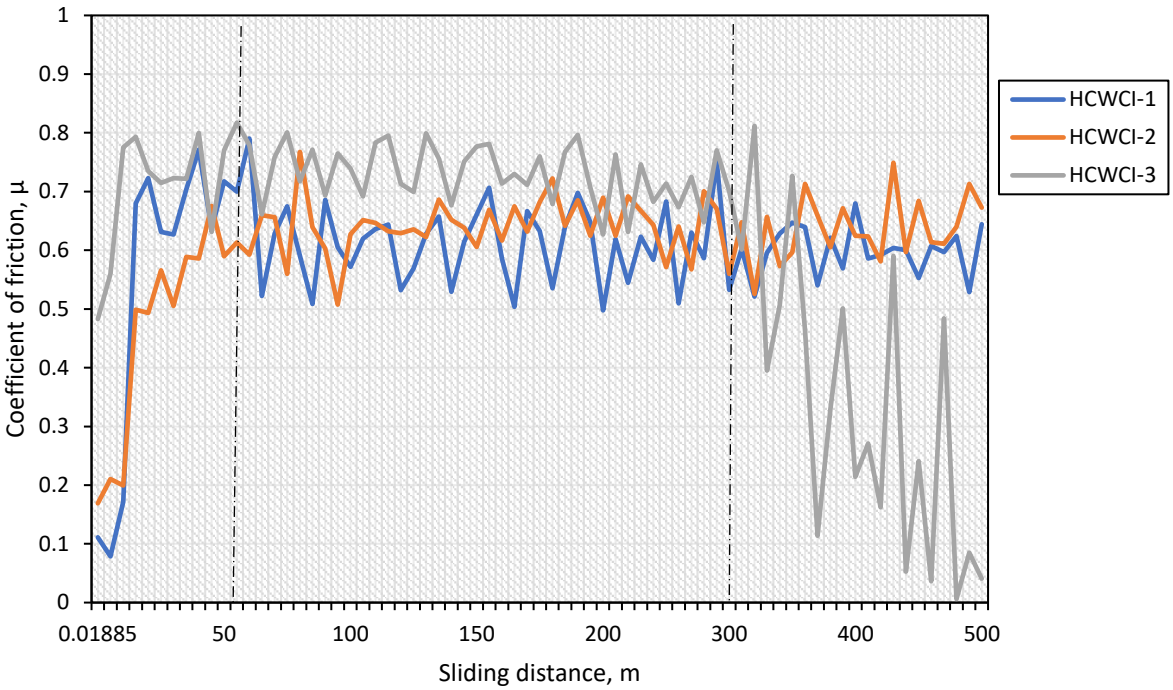

Figure 4.33: CoF versus sliding distance for the HCWCI alloys.

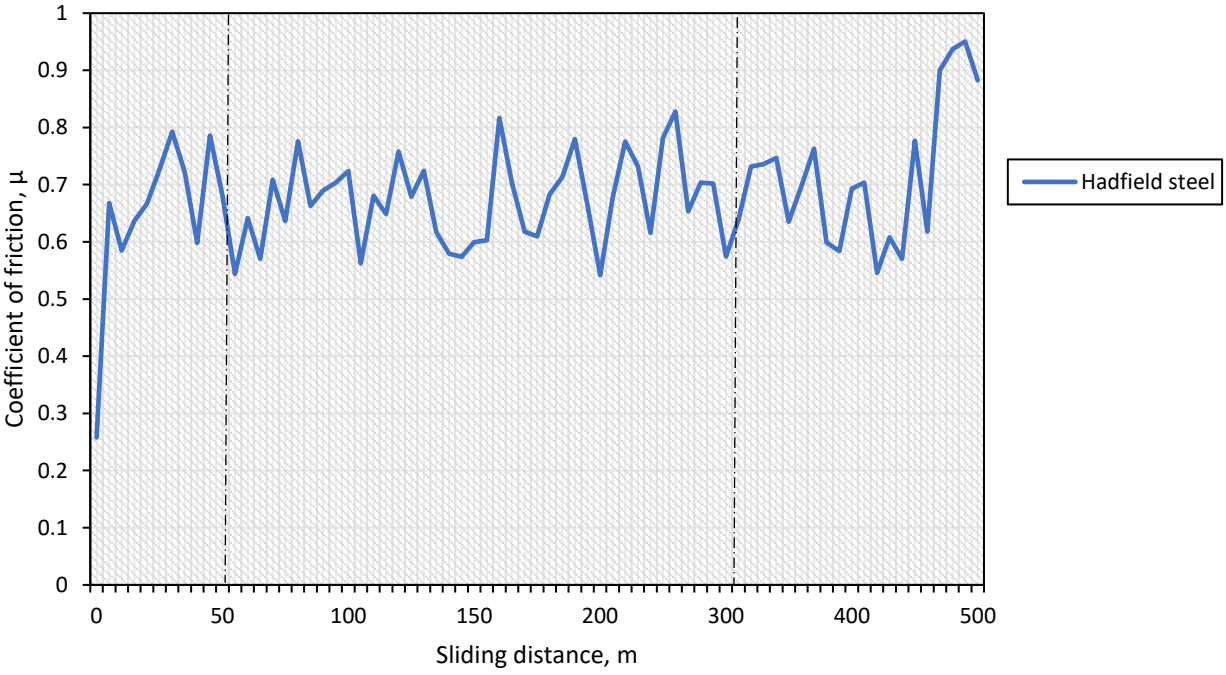

Figure 4.34: CoF versus sliding distance for the Hadfield steel.

The highest average CoF values were observed for the WC-Co samples, followed by the Hadfield steel. Figure 4.35 also shows that the HCWCI samples exhibited the lowest average CoF values with the lowest average obtained for HCWCI-3 at 0.585. The lowest CoF peak value is observed in Figure 4.36 with HCWCI-3 at 0.006 and the highest CoF value belonging to WC-12Co at 0.938.

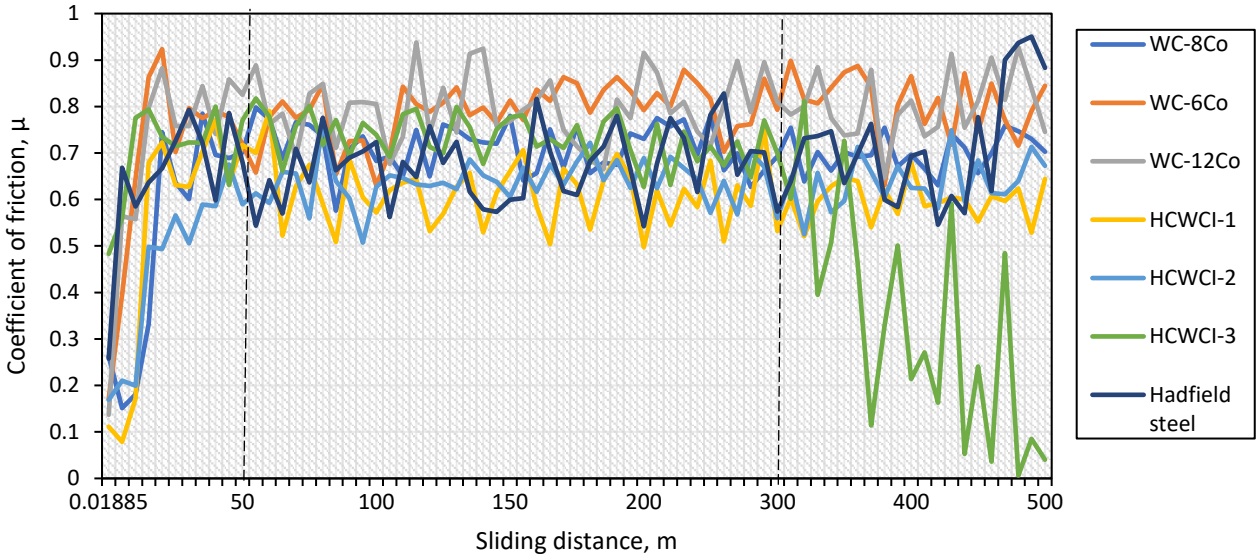

Figure 4.35: CoF versus sliding distance plots for the WC-Co alloys, the HCWCI alloys and Hadfield steel.

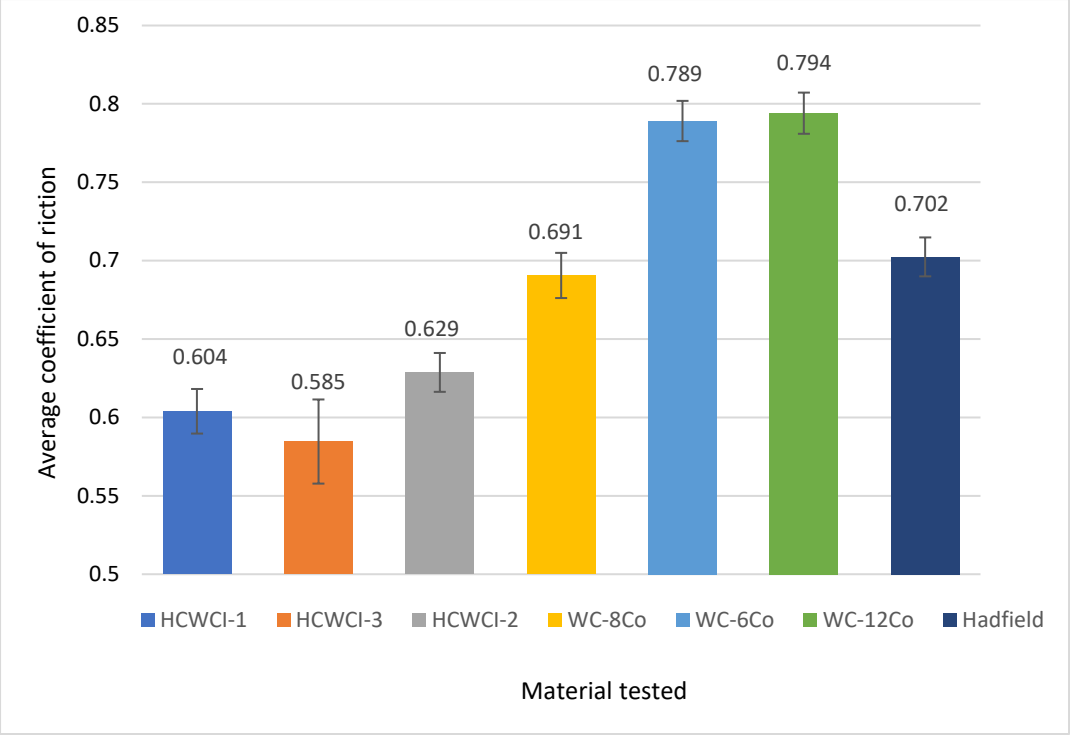

Figure 4.36: Mean value and standard deviation of the CoF of all the investigated materials.

4.5.2 Wear rates

In this section the results of the wear volume of the type 316 stainless steel (316 SS) pin are presented. The sliding speed was kept constant at 0.1 $m.s^{-1}$. The average volume loss of the pin are listed in Table 4.13 together with their respective specific wear rates after the sliding tribometer test. The as-received hardness values of the investigated samples are also shown in Table 4.13. The applied normal force was kept constant at 5N.

Table 4.13: Volume loss, specific wear rate and hardness values of the investigated materials.

Disc material	Pin volume loss (mm^3)	Specific wear rate ($mm^3/N.m$) ($\times 10^{-4}$)	Vickers Hardness HV_{30} (kgf/mm^2)
WC-6Co	0.27 ± 0.02	1.09	1428
WC-8Co	0.39 ± 0.02	1.55	1294
WC-12Co	0.24 ± 0.01	0.96	1612
HCWCI-1	0.47 ± 0.03	1.88	829
HCWCI-2	0.50 ± 0.02	2.00	687
HCWCI-3	0.39 ± 0.01	1.56	760
Hadfield	0.09 ± 0.01	0.36	250

In Table 4.13, a clear volume loss pattern can be observed with the pins. The pin for Hadfield steel exhibited the lowest volume loss, followed by the WC-Co pins. The pins used for the HCWCI samples had the highest volume loss with HCWCI-2 exhibiting the highest of the investigated samples at a pin volume loss of 0.50 mm^3. WC-8Co showed the highest pin volume loss amongst the WC-Co samples at 0.39 mm^3 with the lowest belonging to WC-12Co at 0.24 mm^3.

The stereoscope microgaphs for WC-8Co, WC-6Co, and WC-12Co are presented in Figures 4.37-4.39, respectively. The stereoscope micrographs for HCWCI-1, HCWCI-2, and HCWCI-3 are presented in Figure 4.40-4.42. Figure 4.43 presents the stereoscope mircrographs of the pin wear scar and the disc wear track of Hadfield steel.

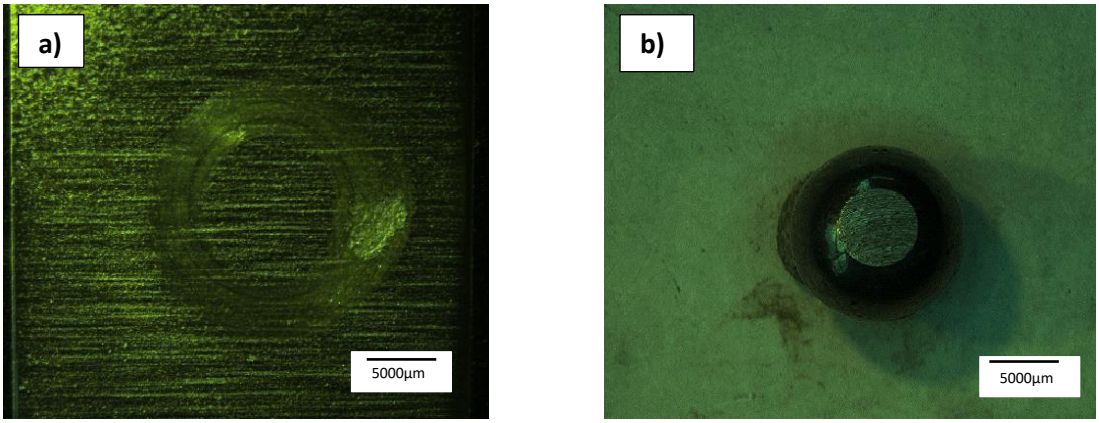

Figure 4.37: Stereoscope microcraphs of the (a) WC-8Co disc and (b) pin wear damage.

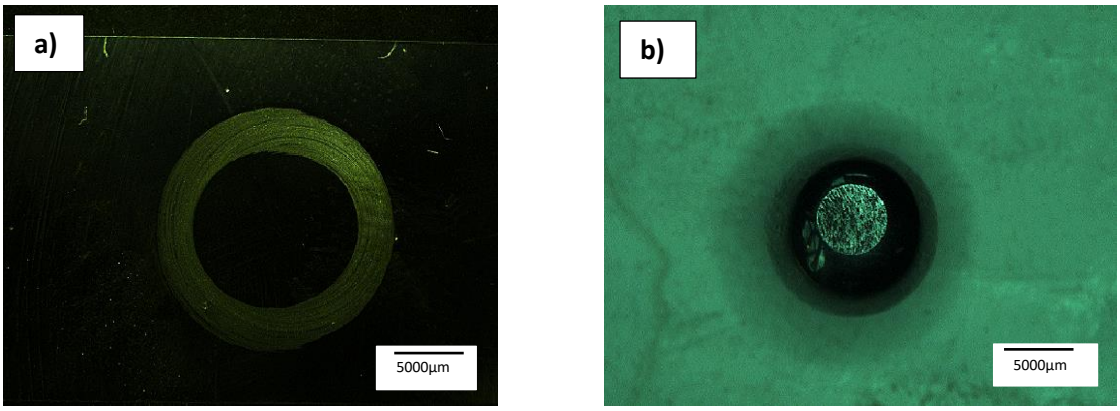

Figure 4.38: Stereoscope microcraphs of the (a) WC-6Co disc and (b) pin wear damage.

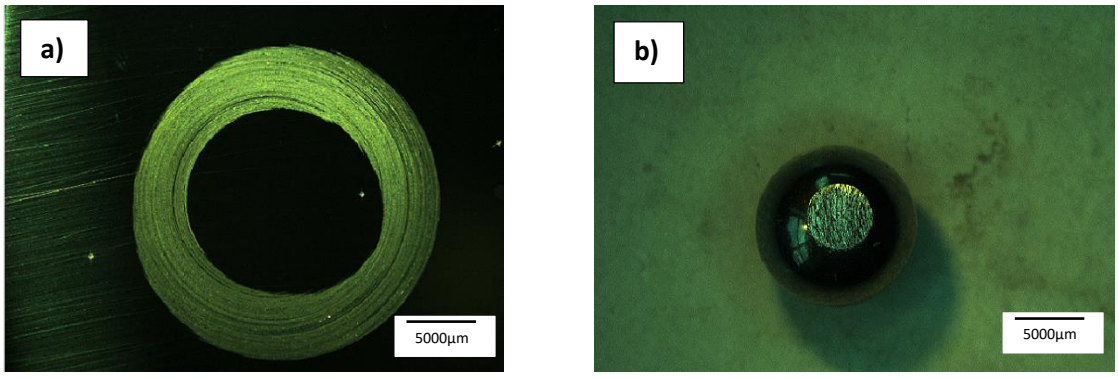

Figure 4.39: Stereoscope microcraphs of the (a) WC-12Co disc and (b) pin wear damage.

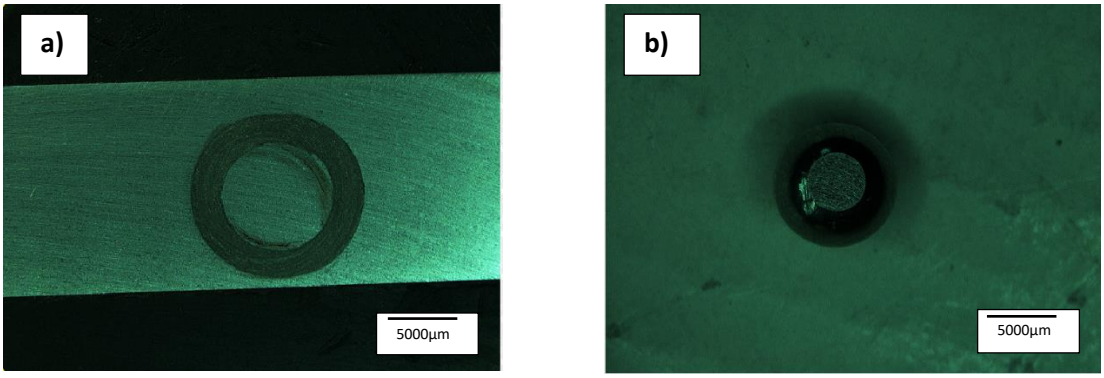

Figure 4.40: Stereoscope microcraphs of the (a) HCWCI-1 disc and (b) pin wear damage.

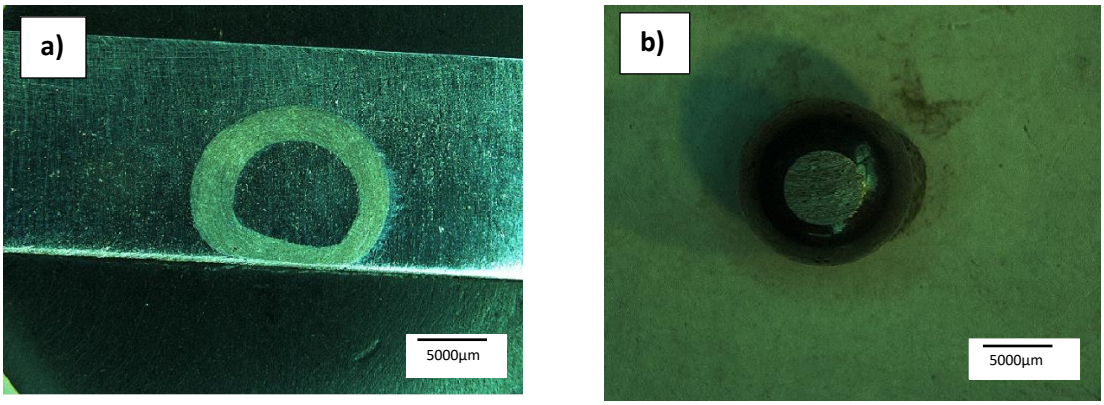

Figure 4.41: Stereoscope microcraphs of the (a) HCWCI-2 disc and (b) pin wear damage.

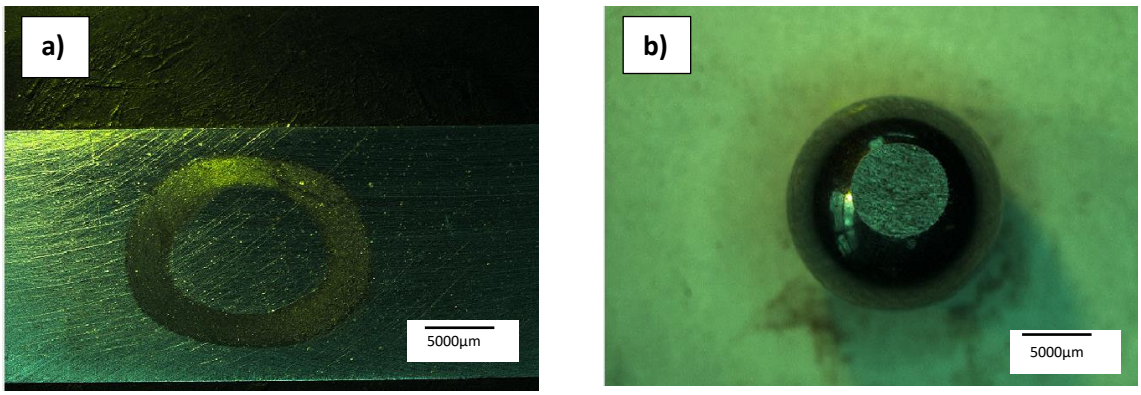

Figure 4.42: Stereoscope microcraphs of the (a) HCWCI-3 disc and (b) pin wear damage.

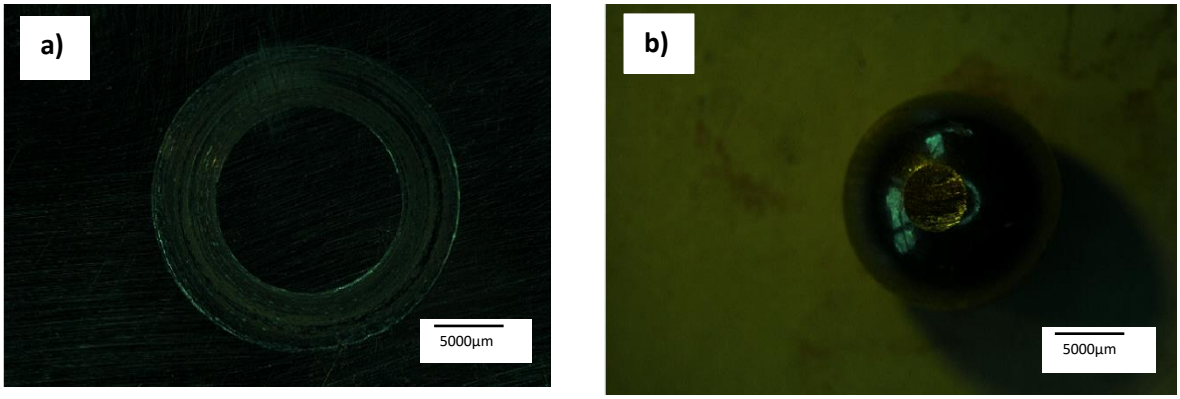

Figure 4.43: Stereoscope microcraphs of the (a) Hadfield steel disc and (b) pin wear damage.

The specific wear rates of the pins are graphically presented in Figure 4.44. The highest wear rate was observed with HCWCI-2 at 2.0×10^{-4}. HCWCI-1 had the next highest wear rate of 1.88×10^{-4} followed by HCWCI-3 at 1.56×10^{-4}. Hadfield steel pin had the lowest wear rate value of 0.36×10^{-4}, followed by WC-12Co and then WC-6Co at 0.96×10^{-4} and 1.09×10^{-4}, respectively.

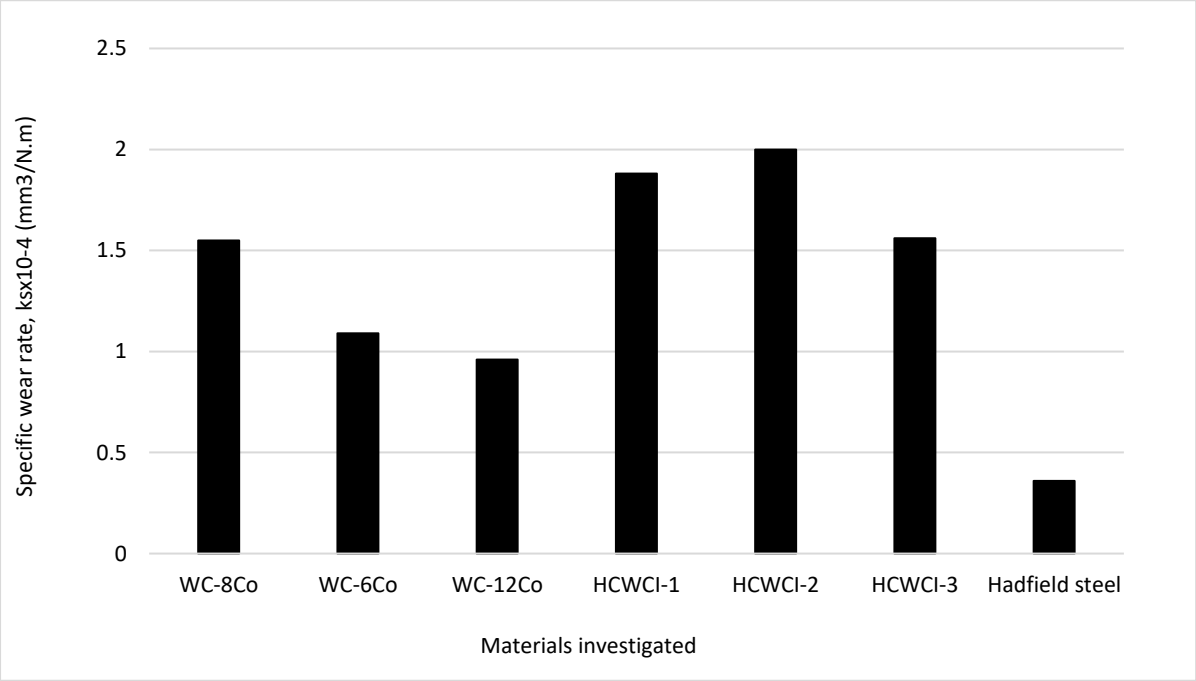

Figure 4.44: Specific wear rates of the pins against the investigated materials.

Figure 4.44 also presents the hardness values of the samples. There appears to be no general pattern between the hardness and specific wear rate of the samples. WC-12Co and WC-8Co, which had the highest and lowest Vickers hardness values of 1612 and 1294, respectively, exhibited the two highest wear rates whereas the second hardest material, WC-6Co, exhibited the lowest wear rate of the WC-Co alloys.

4.5.3 Wear effects and mechanisms

The sliding wear damages and mechanisms on the WC-Co samples and the other investigated samples are presented in this section. SEM-EDS micrographs are used to examine the wear effects and damage on the wear tracks. The SEM-EDS micrographs of WC-8Co, WC-12Co, and WC-6Co alloys are presented in Figures 4.45, 4.46, and 4.47, respectively. Figures 4.48, 4.49, and 4.50 are the SEM-EDS micrographs of the HCWCI alloys and Figure 4.51 presents the SEM-EDS micrographs of the Hadfield steel after undergoing sliding wear.

Upon close examination using the naked eye, the wear track impressions made by the 316 SS pins on the WC-Co discs had a smooth and shiny appearance. Low magnification SEM micrographs revealed small islands of dark patches distributed across the wear tracks of the alloys. EDS revealed that the dark patches were transferred layers of the 316 SS pin material that was adhered on the surface of the WC-Co discs during sliding wear. These dark adhered black patches of the 316 SS pin were more prominent on the WC-12Co and WC-8Co alloys. Holes and depressions were also observed on the surfaces of the WC-Co alloys. These holes indicate that the alloys experienced WC grain and cobalt pull out. This type of wear mechanism is also known as galling and it is common during sliding wear of cobalt-based alloys. Galling of metallic materials occurs when there is an atomic bond followed by the fracturing of the adhered material onto the other (Haynes, n.d).

The WC grain pull out mechanism was more prominent with the WC-6Co and WC-8Co alloys. The normal load exerted on the discs during sliding wear and the hardness of the pins were not severe enough to produce any other wear mechanisms on the WC-Co alloys. This observation was made based on the fact that the WC grains were visible through the translucent layer of the 316 SS pins proving that the pins did not do any damage on the surface of the WC-Co alloys.

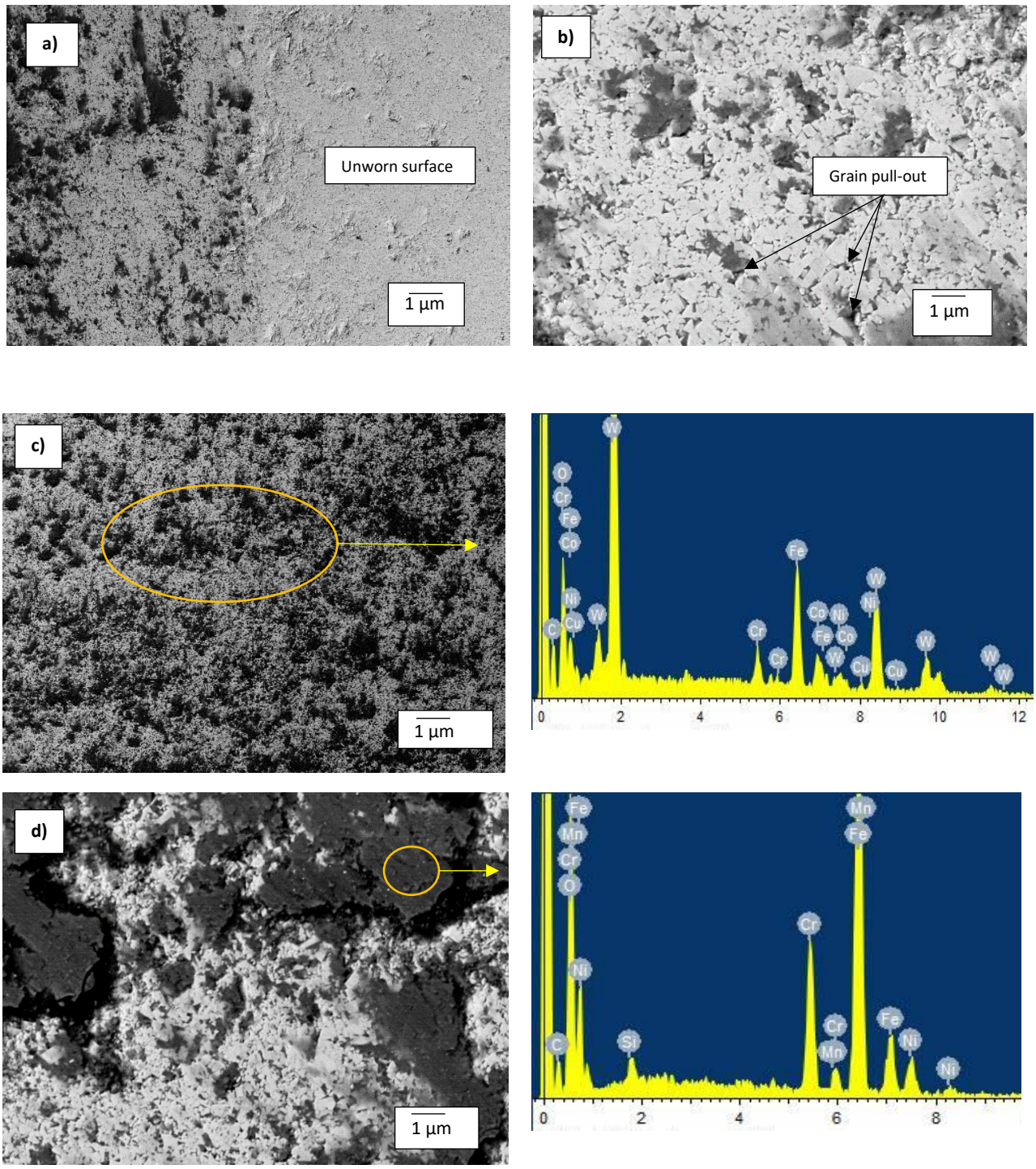

Figure 4.45: SEM-BSD micrographs of the wear mechanisms of WC-8Co after sliding wear test.

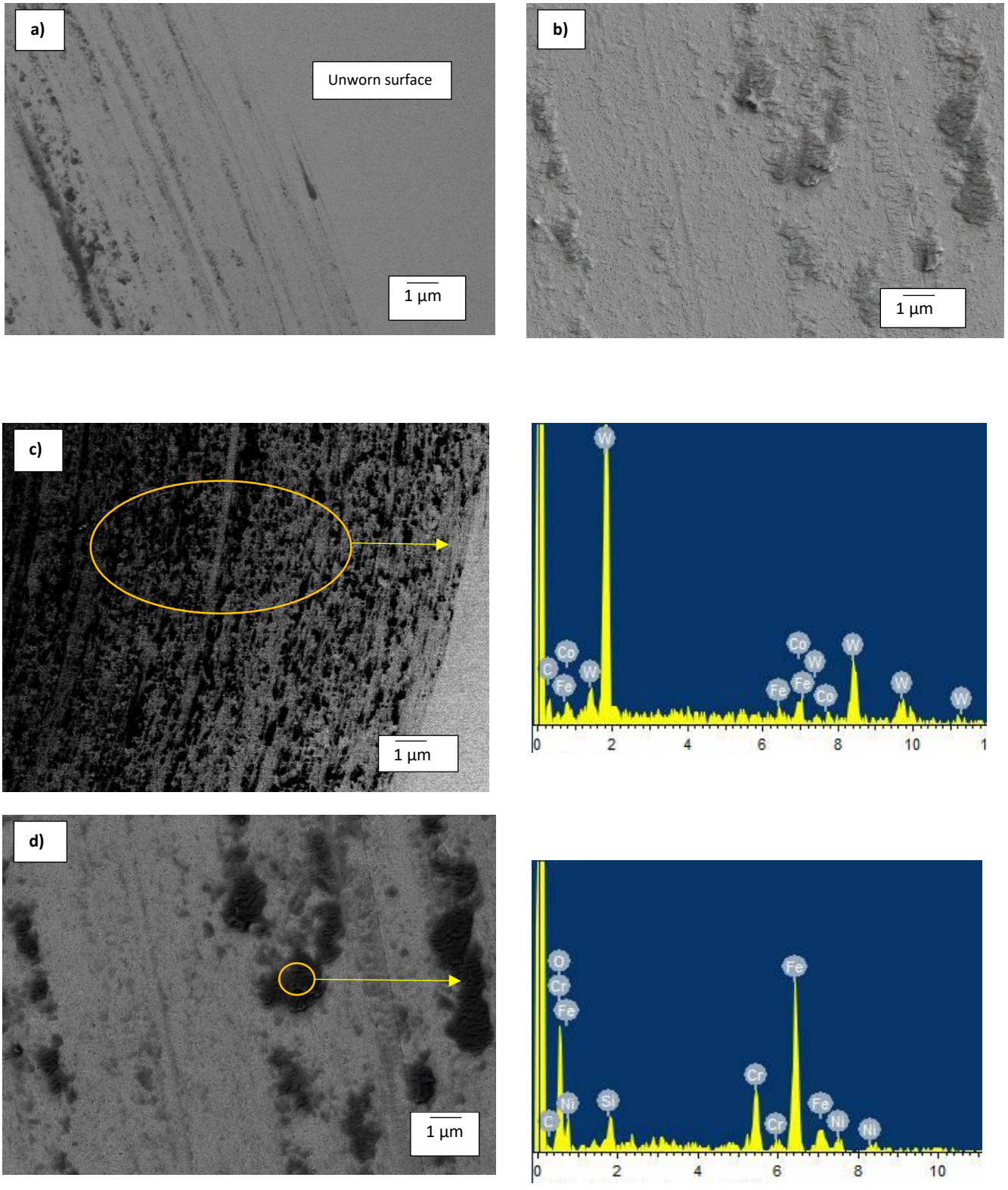

Figure 4.46: SEM (BSD and SE) micrographs of the wear mechanisms of WC-12Co after sliding wear test.

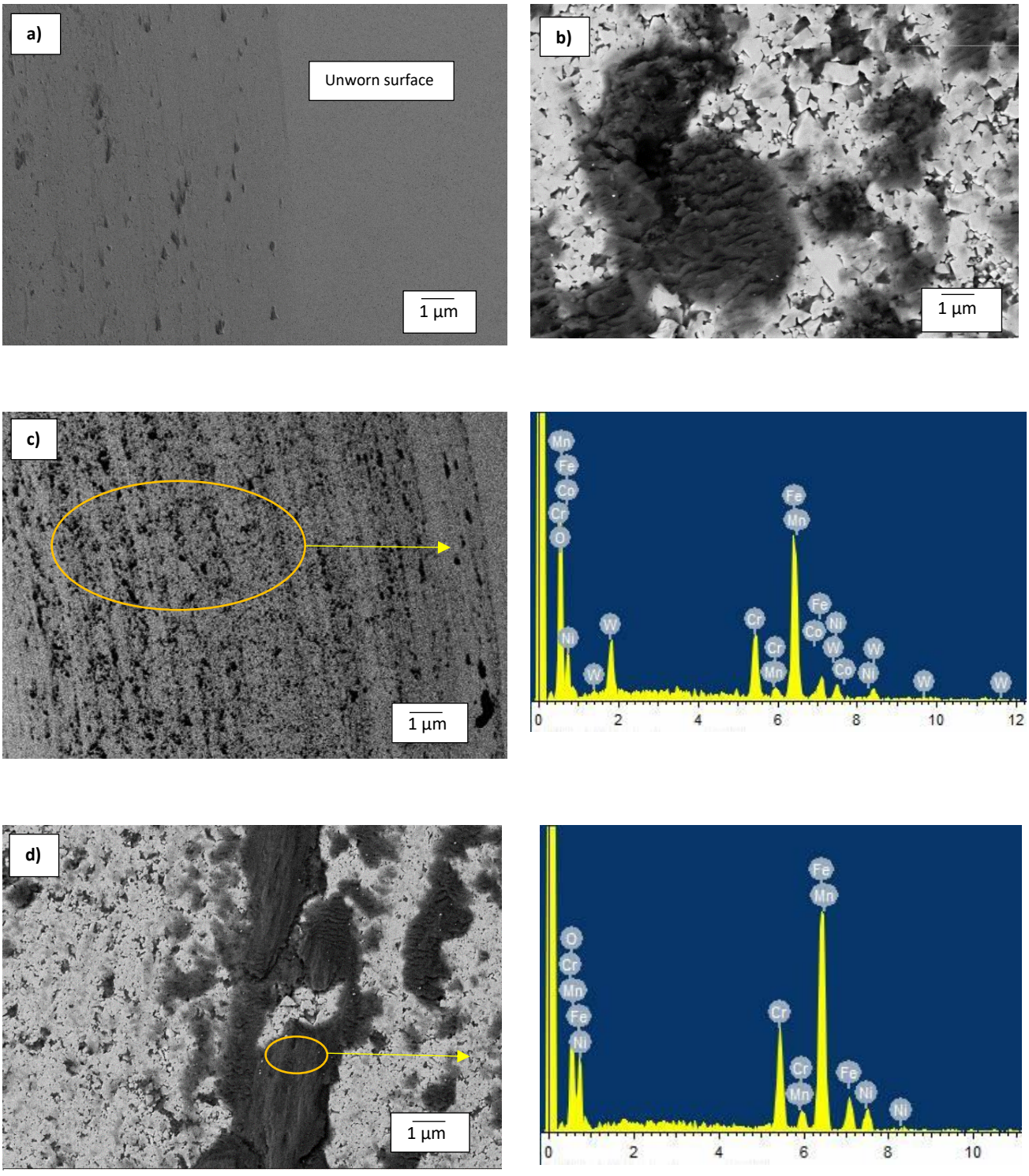

Figure 4.47: SEM-BSD micrographs of the wear mechanisms of WC-6Co after sliding wear test.

Figures 4.48-4.50 are the SEM-EDS micrographs of the HCWCI alloys showing the wear mechanisms of the worn surfaces during the pin-on-disc sliding wear tests. The main mechanism seen occurring on the worn surfaces of the HCWCI alloys was the extrusion of

both the carbides and the matrix. The extrusion of the carbides can be recognised by how pressed down they are as seen in Figure 4.48 (c). The occurrence of the extrusion of the matrix can be observed by the manner in which the worn regions created ripples and ridges on top of each other as seen occurring prominently in Figure 4.48 (b and c). The appearance of the scale-looking bulges was caused by the particles (carbides and matrix debris) that were pulled out (galling), displaced and reattached to a different region on the surface (Jiang et al., 2019).

Other dominant wear mechanisms that were seen to have occurred on the surface of the alloys before the layering by the matrix were microploughing and microcutting. These two wear mechanisms were recognised by the parallel continuous grooves around the wear tracks of the alloy. The impressions left by microploughing and microcutting are seen mostly on the HCWCI-1 alloy. Material removal of the primary carbides might also have occurred by the microfracturing of thin layers (delamination) during localised straining induced by the normal load (Atapek & Polat, 2013).

EDS conducted on the alloys show a considerate amount of Ni on the surfaces. This indicates that the transference of material from the pins to the matrix occurred, proving that the adhesion of the pins to the matrix was one of the wear mechanisms. EDS also showed a substantial amount of oxygen on the surface of the samples, proving that oxides from the pins (in the form of Fe_3O_4) were attached to the alloys during sliding wear which indicates that the materials were subjected to oxidative wear (Jiang et al., 2019).

Figure 4.49 and 4.50 (c) shows spalling of the primary carbides of the HCWCI-2 and HCWCI-3 alloys, respectively. No spalling can be seen occurring on the other alloy. Microcracking was seen to have occurred on the HCWCI-3 alloy and not so much on the other two.

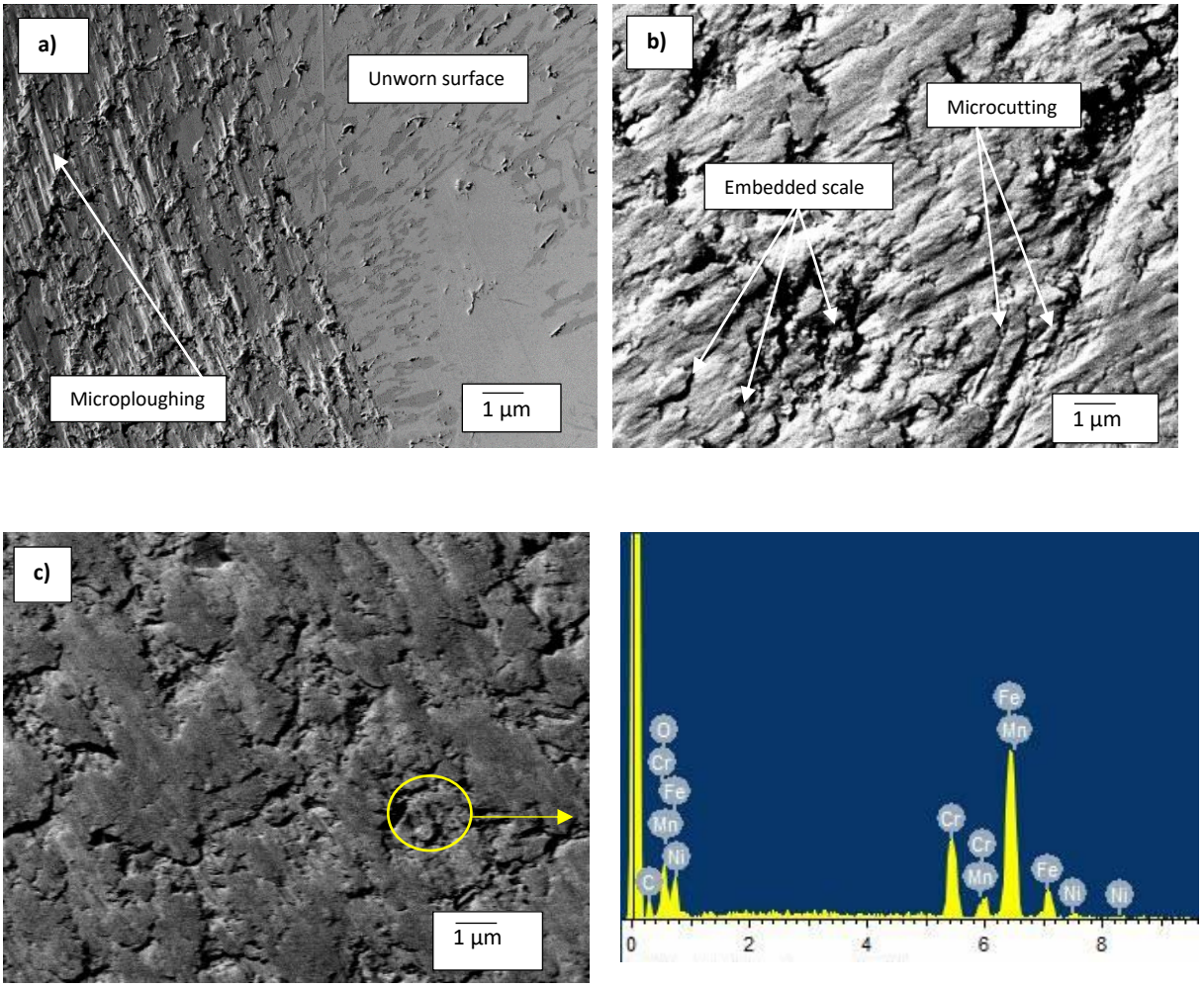

Figure 4.48: SEM (BSD and SE) micrographs of the wear mechanisms of HCWCI-1 after sliding wear test: (a) microploughing, (b) microcutting and scales of the displaced material debris, and (c) adhesion of pin on alloy.

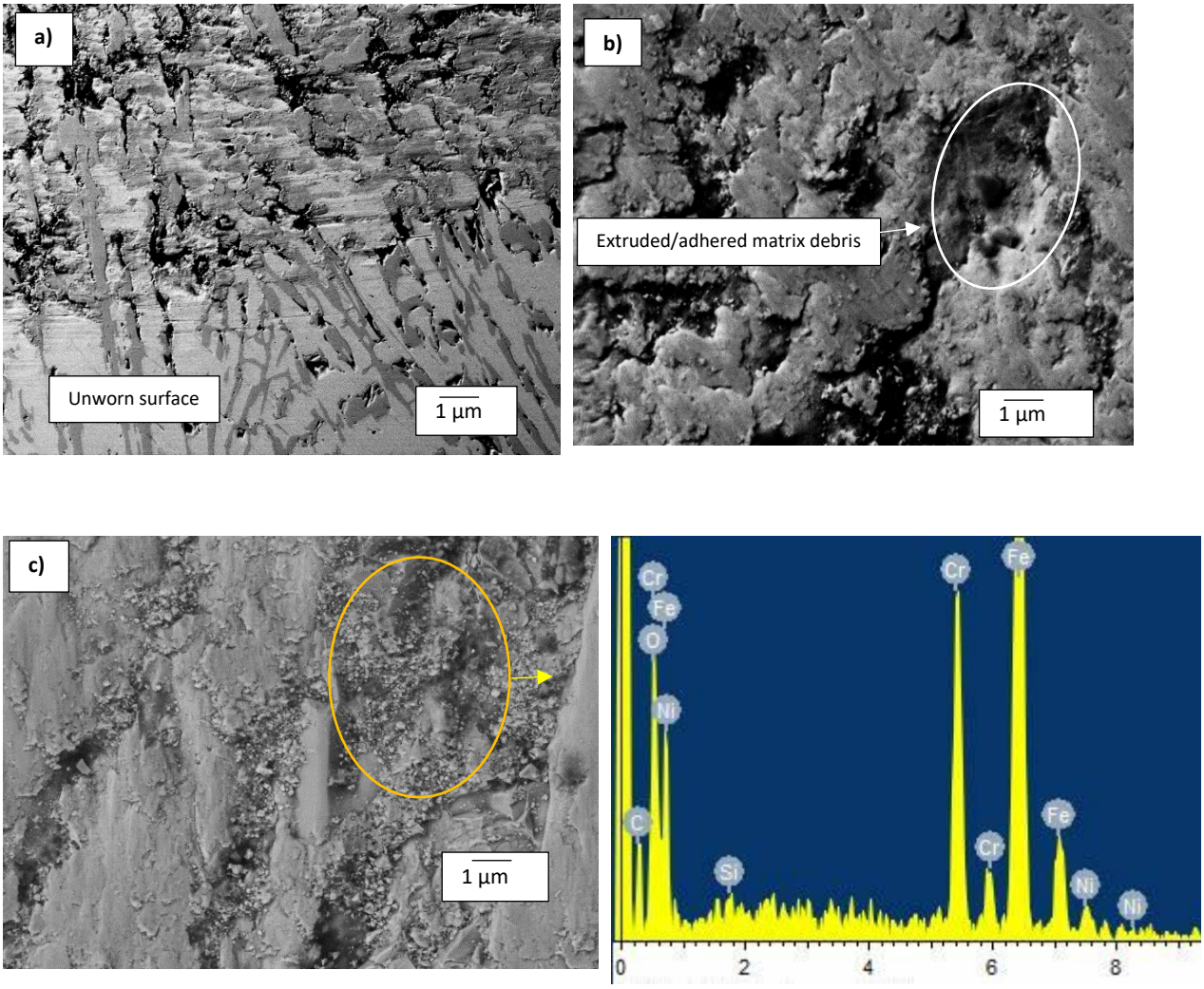

Figure 4.49: SEM-BSD micrographs of the wear mechanisms of HCWCI-2 after sliding wear test: (a) microploughing and microcutting, (b) extruded matrix, and (c) spalling and fracturing of the carbides seen on the bottom regions.

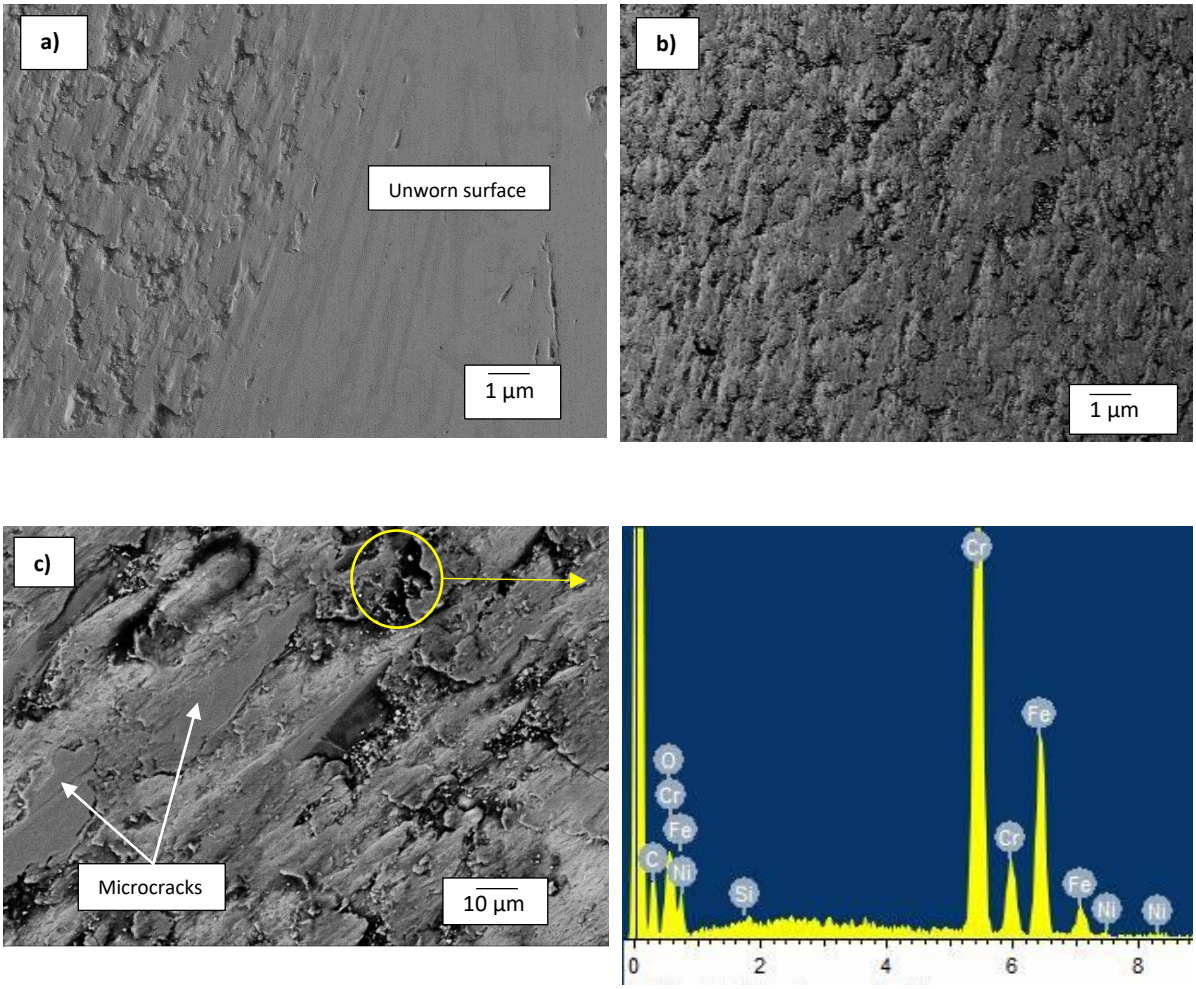

Figure 4.50: SEM (BSD and SE) micrographs of the wear mechanisms of HCWCI-3 after sliding wear test: (a) microploughing and microcutting, (b) displacement and covering of the matrix over the worn region, and (c) microcracking of carbides, spalling seen on the bottom regions and adhesion of pin onto the alloy.

The SEM-EDS micrographs of the Hadfield steel after undergoing sliding wear are presented in Figure 4.51. The main sliding wear mechanisms observed occurring on the Hadfield steel surfaces were microploughing, microcutting and spalling (delamination) as seen with the work conducted by Dalai et al. (2018). The same wear mechanisms (ploughing, cutting, and delamination of the austenitic matrix) were reported by Srivastava (2008). Another wear mechanism seen during the sliding wear test was the extrusion of the austenite matrix. The extruded matrix can be seen piling around the hard precipitated carbides in the opposite direction of the rotation of the discs (Figure 4.51 (c)). The scuffing/galling of the matrix and its adherence to the pins.

It was further found that the regions surrounding the black inclusions were oxide covered carbides which show that the steel experienced oxidation wear (Bhattacharyya, 1966). These inclusions were found by EDS to be oxide contaminated material (mostly in the form of an iron oxide) adhered to the matrix from the pins. Table 4.14 summarises the main wear mechanisms of the samples during pin-on-disc.

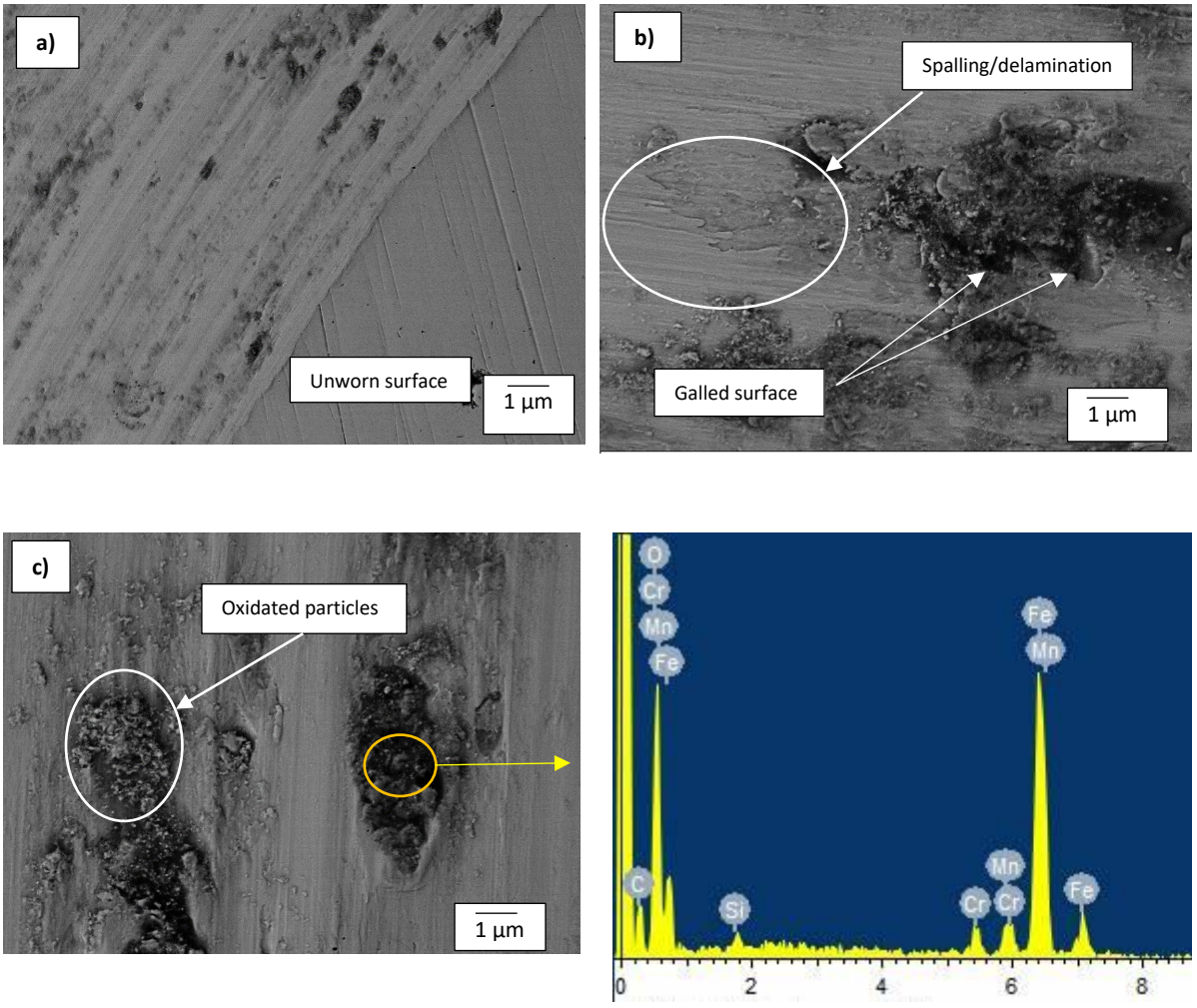

Figure 4.51: SEM-BSD micrographs of the wear mechanisms of Hadfield steel after sliding wear test: (a) microploughing and microcutting, (b) spalling and delamination of the matrix, and excessive galling of the Hadfield steel, and (c) oxidation wear.

Table 4.14: Summary of the dominant wear mechanisms of the investigated alloys during pin on disc sliding wear.

Wear mechanism	WC-Co alloys	HCWCI alloys	Hadfield steel
Microploughing	No	Yes, extensive on the HCWCI-1	Yes
Microcutting	No	Yes, extensive on the HCWCI-1	Yes
Grain pull out	Yes, seen mainly in the WC-6Co and WC-8Co alloys	Yes	No
Binder extrusion	Yes	Yes, displacement of the austenitic matrix. Carbide extrusion was experienced too.	Yes
Pin adhesion/galling of matrix	Yes, both pin adhesion and matrix galling	Yes, mainly seen on the austenite matrix	Yes
Microcracking	No	Yes, seen around the precipitated carbide inclusions	No
Microfracturing	No	Yes, especially of the carbides.	No
Spalling/delamination	No	Yes	Yes, although more spalling
Oxidative wear	No	Yes	Yes

4.6 Corrosion and Electrochemical Results

The potentiodynamic polarisation scans results are detailed in this section. The electrochemical behaviour of the WC-Co alloys, HCWCI alloys and Hadfield steel samples in 1 M H_2SO_4 is also included in this section. The optical microscope and SEM were used to analyse the morphology of the samples after the electrochemical tests and the micrographs thereof are presented in this section.

4.6.1 Open Circuit Potential (OCP)

The OCP (E_{OC}) values and the variations therein were measured for an hour in 1M H_2SO_4 as presented in Figure 4.52. The recorded OCP values started off unstable, displaying random fluctuations in the first few minutes of measuring. The Hadfield steel was observed to be the alloy showing less stability, followed HCWCI-3 and then HCWCI-1. WC-12Co displayed the highest starting potential (most noble) and continued to finally stabilise at the highest potential than the other investigated metals. The HCWCI-3 alloy was observed to have displayed the lowest starting potential (least noble) and continued to stabilise at the lowest potential when compared to the other metals. The WC-Co alloys behaved similar as a group and displayed similar trends during the course of measuring the OCP so was the potential behaviour of the iron-based alloys (HCWCI alloys and the Hadfield steel).

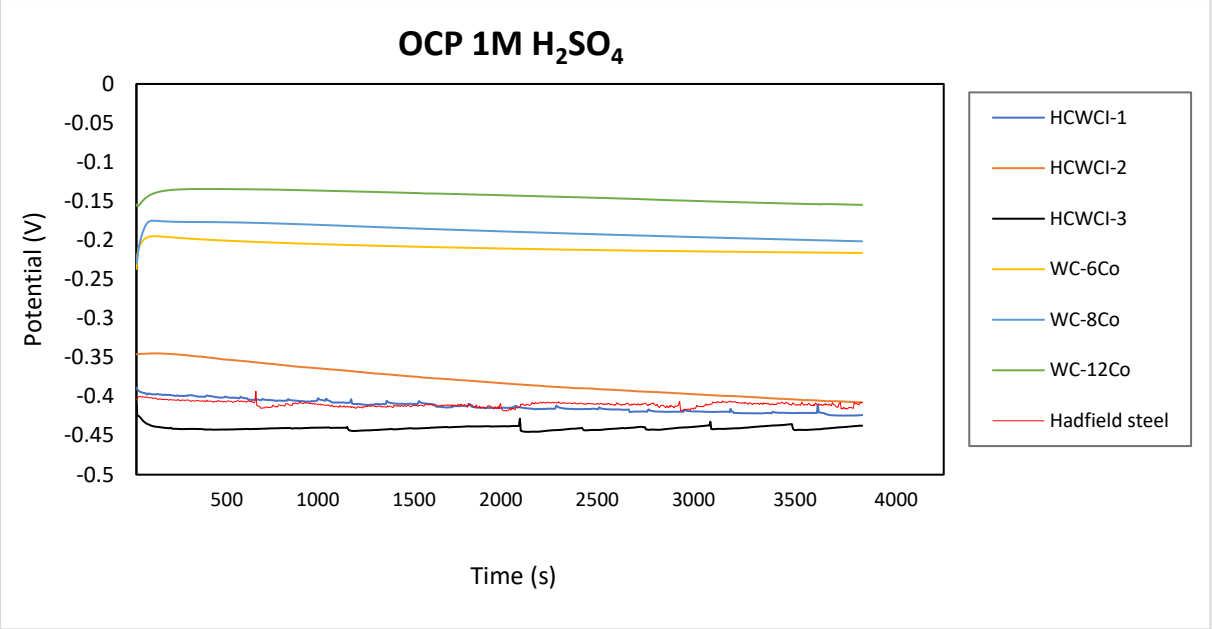

Figure 4.52: Open Circuit Potential behaviour of the investigated metals in 1M H_2SO_4.

4.6.2 Potentiodynamic polarisation responses and corrosion rates

The polarisation scan curves are presented in Figure 4.53. The curve profiling of the samples showed a typical active-psuedopassive transition behaviour (although showing small passive regions) with the exception of HCWCI-2 which did not show any passive behaviour which is in contrast with expected responses reported by other researchers. Again, the WC-Co curves behaved similarly as a group and in the same fashion, the iron-based metals profiled similar curves. Comparing the potentials of WC-6Co and WC-8Co, WC-6Co displayed a lower tendency to corrode. This was expected because WC-6Co contained a smaller amount cobalt in its system which, as outlined in Chapter 2, directly influences the corrosion of WC-Co cemented carbides.

The WC-12Co alloy exhibited the best resistance to corrosion based on its measured potential during the potentiodynamic scanning. Since WC-12Co contains the highest content of the binder phase, one would expect WC-12Co to exhibit the highest tendency to corrode when compared to the other two WC-Co alloys. However, the alloy has a very refined structure that consists of WC particles that are very closely packed to each other. This kind of a structure prevents the binder phase from being too exposed to the corroding medium, hence preventing excessive corrosion. Additionally, the alloy also has traces of Cr which has been

proven to beneficial to the WC-Co ability to resist corrosion under acidic conditions (Mori et al., 2001).

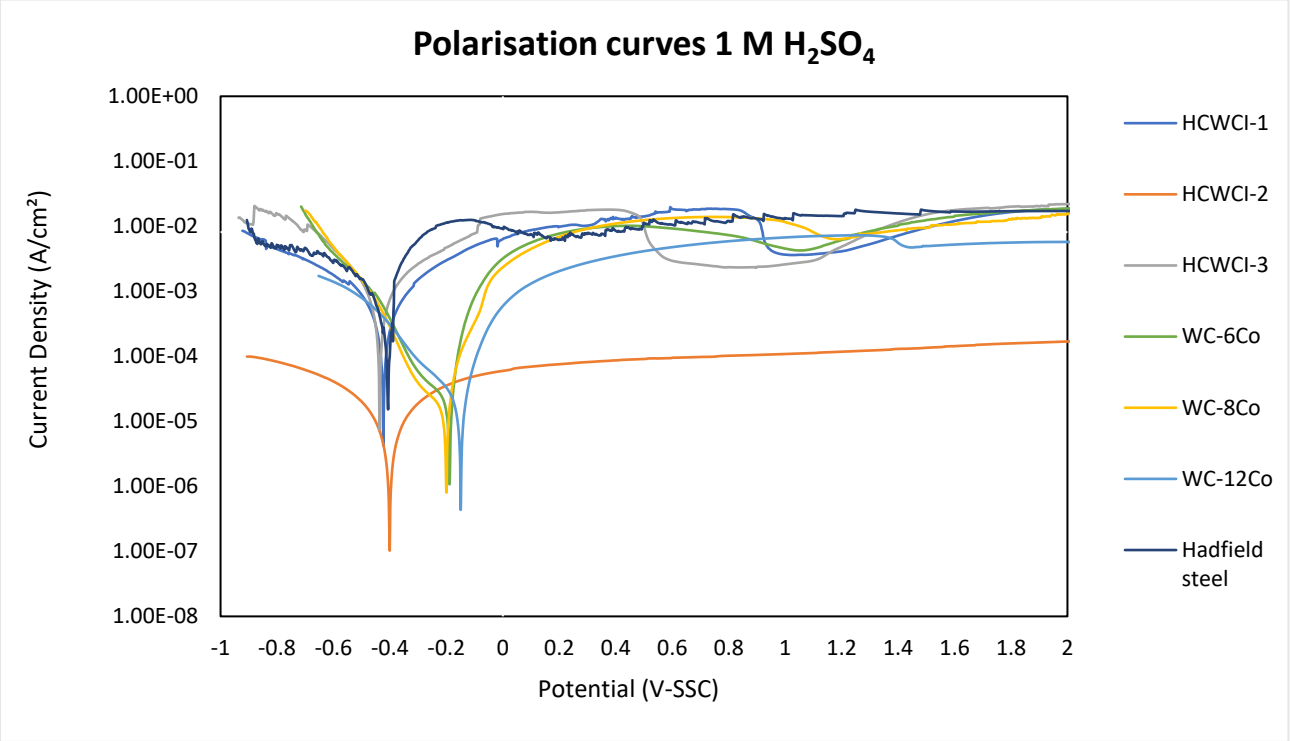

Figure 4.53: Potentiodynamic polarisation curves of the WC-Co alloys, HCWCI alloys and Hadfield in 1 M H_2SO_4.

Table 4.15 presents a summary of the electrochemical parameters of the WC-Co, HCWCI and Hadfield steel alloys obtained from the electrochemical polarisation scans using 1M H_2SO_4 as a corroding medium. The corrosion potential values (E_{Corr}) of the WC-Co alloys became less noble with an increase of cobalt with an exception being the E_{Corr} value exhibited by WC-12Co. WC-12Co also exhibited the lowest current density (i_{corr}) and the lowest corrosion rate since there is a positive correlation between corrosion current density and corrosion rate (a directly proportional relationship). The i_{corr} value of WC-6Co was larger than the i_{corr} exhibited by WC-8Co which is in contrast to the responses observed and reported in literature (Human & Exner, 1996; Machio et al., 2013). Generally, the i_{corr} value of WC-Co cemented carbides with lower cobalt is expected to be lower (comparing the two WC-Co alloys that have similar grain sizes and with no other alloying elements). However, corrosion rate (CR) of WC-6Co alloy was

greater than that of WC-8Co. WC-6Co showed a CR that was a magnitude larger than both WC-8Co and WC-12Co. β_a and β_c followed the same trend as content of the binder and increase with the increasing value of Co.

Although there was little difference between the E_{Corr} values of the HCWCI alloys, HCWCI-2 showed the most noble E_{Corr} value than the other HCWCI alloys. An increase in Cr was advantageous to HCWCI-2 and detrimental to HCWCI-3. This trend was observed with the alloys' i_{corr} and CR values. An increase of Cr from 20wt% (HCWCI-1) to 22wt% (HCWCI-2) had a tremendous effect on the i_{corr} and CR value as both values decreased by an order of magnitude of three and two, respectively. A further increase of Cr to 25wt% (HCWCI-3) had an adverse effect on the alloy's resistance to corrosion. HCWCI-3 experienced a corrosion rate increase by two orders of magnitude from HCWCI-2 but was still slightly more resistant to corrosion than HCWCI-1. This influence of Cr on the resistance of the high chromium cast iron against corrosion was also observed by other researchers (Marimuthu & Kannoorpatti, 2016). The β_a and β_c followed no general trend other than they followed the pattern that i_{corr} and CR followed upon the increasing of the Cr content.

Hadfield steel exhibited the poorest resistant to corrosion compared to the other investigated metals but exhibited an E_{Corr} value that was similar to that displayed by the cast iron alloys. The i_{corr} and CR values of the Hadfield steel were very similar to those of HCWCI-1.

Table 4.15: Electrochemical parameters of the investigated materials.

Sample	E_{corr} (V)	i_{corr} ($\mu A/cm^2$)	β_a (V/Dec) $\times 10^{-3}$	B_c (V/Dec) $\times 10^{-5}$	CR (mmpy)
WC-6Co	-0.189	399	25.3	28.8	0.09
WC-8Co	-0.199	359	20.8	25.3	0.10
WC-12Co	-0.149	185	7.3	6.1	0.04
HCWCI-1	-0.423	1033	20.5	13.8	0.35
HCWCI-2	-0.401	9.96	0.2	209	1.93×10^{-3}
HCWCI-3	-0.437	801	18.7	45.6	0.19
HS	-0.406	1084	57.0	16.8	0.45

4.6.3 Analysis of the surfaces of the samples after electrochemical test

The surfaces of the investigated materials were analysed after the electrochemical tests were carried out. SEM and optical microscopy micrographs were used to examine the corrosion products and damage that were incurred by the samples. The EDS analyses are not included in this section however, the corrosion products remaining on the surfaces contained sulphur and oxygen, serving as proof that the samples experienced H_2SO_4 corrosive attack.

WC-Co cemented carbides

The SEM and optical micrographs for the WC-Co alloys are presented in Figure 4.54 and Figure 4.55, respectively. The SEM micrographs of WC-6Co and WC-8Co were all observed under the same magnification of 2000x except for WC-12Co which was taken at 5000x. This was because the corrosion products left on the WC-12Co were very small compared to the other two WC-Co alloys.

The SEM micrographs of the three investigated WC-Co alloys displayed different topographical morphologies after electrochemical tests were conducted on them. However, WC-6Co and WC-8Co exhibited similar characteristics to each other that were very different from what was observed on the surface of the WC-12Co alloy. WC-6Co and WC-8Co both showed cracks on their surfaces into which the corrosive medium preferentially dissolved. Sebeya (2013) reported the same continuous cracked film on the surface of the WC-10Co sample he investigated under the same corrosive environment. With WC-6Co (Figure 4.54(a)) the cracks formed by the corrosion product can be seen forming a skeleton around individual WC particles whereas with WC-8Co, the cracks were formed around an agglomeration of WC particles. It is not clear as to why that was the case as both alloys exhibited a negligible difference in their CR values. WC-12Co contained translucent patches of the corrosion product. The corrosion product layers were discontinuous and had different size and did not seem to have severely penetrated and attacked the binder as observed with the other two WC-Co alloys. The optical micrographs of the WC-Co alloys show WC-8Co (Figure 4.55 (b)) as showing the most severe corrosion attack on its surface. Localised corrosion in the form of large pits can be seen occurring mostly with the WC-8Co alloy which was observed occurring in the work conducted by Bricín et al. (2019).

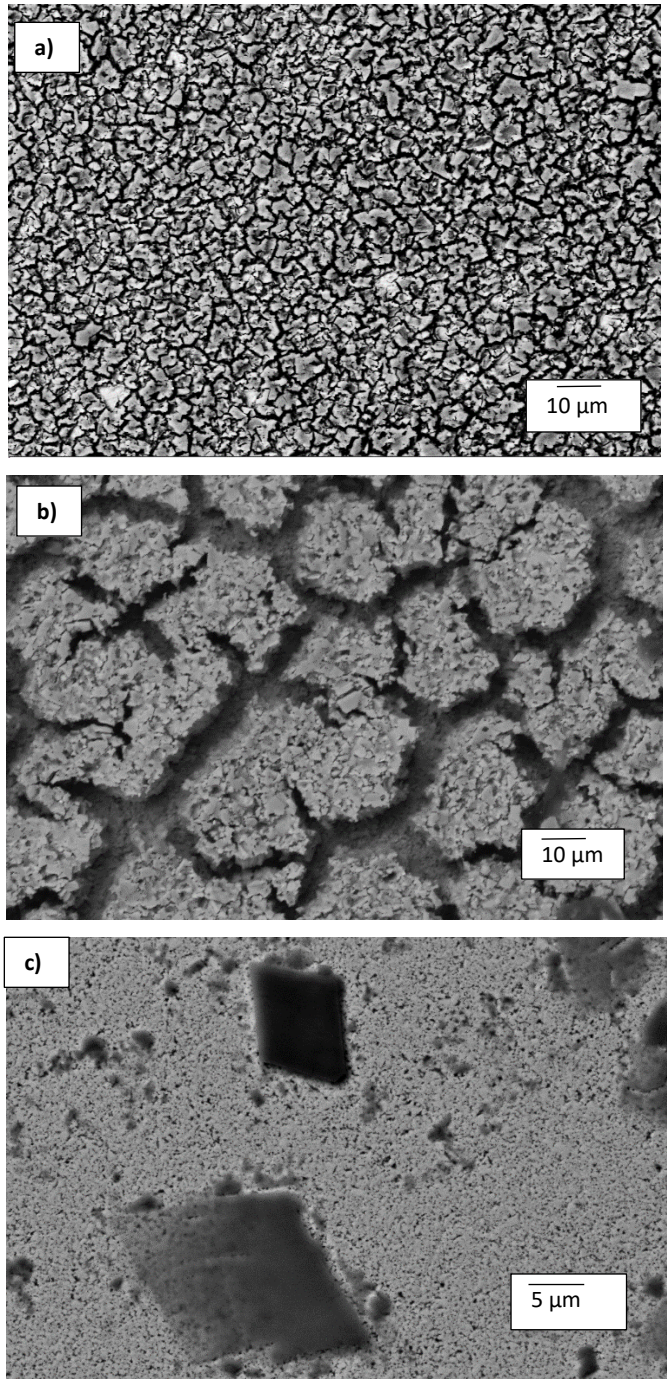

Figure 4.54: SEM-BSD micrographs of: (a) WC-6Co, (b) WC-8Co and (c) WC-12Co after undergoing electrochemical tests in 1M H_2SO_4.

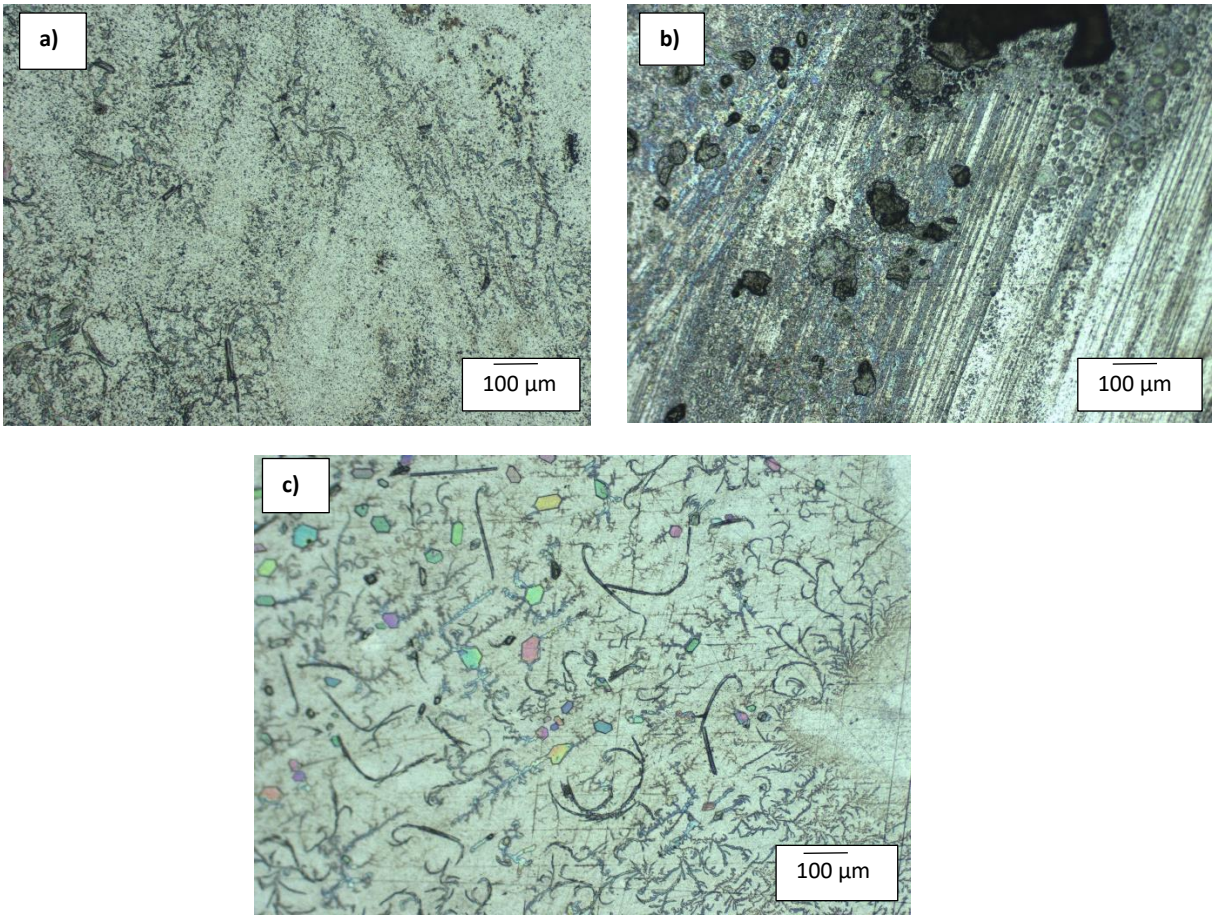

Figure 4.55: Optical micrographs of: (a) WC-6Co, (b) WC-8Co and (c) WC-12Co after undergoing electrochemical tests in 1M H_2SO_4.

HCWCI alloys

The SEM and optical micrographs for the HCWCI alloys are presented in Figure 4.56 and Figure 4.57, respectively. Figure 4.56 (a and b), (c and d), and (e and f) present the SEM micrographs of HCWCI-1, HCWCI-2, and HCWCI-3, respectively whereas, Figure 4.57 (a and b), (c and d), and (e and f) present the optical micrographs of HCWCI-1, HCWCI-2, and HCWCI-3, respectively.

From the presented SEM micrographs, it can be observed that HCWCI-1 experienced the harshest corrosion attack after polarisation tests in 1M H_2SO_4. The appearance of the corroded surface of the HCWCI-1 alloy is in alignment with its high current density and corrosion rate. HCWCI-1 underwent uniform corrosion damage on its surface, and this can be

characterised by the manner in which corrosive medium dissolved into the matrix, leaving out a slightly corroded skeleton structure of the primary eutectic carbides.

The corroded surface of the HCWCI-2 alloy (Figure 4.56(c and d)) portrays a strange corrosion morphology. Some regions of the surface (see Figure 4.56 (a)) which were completely exposed to the corrosive medium, appear like they did not undergo any corrosive attack. However, upon close inspection, mechanisms of chemical attack were slightly visible on the matrix proving that there was evidence of corrosion that took place. Additionally, the corroded grain boundaries around the Cr-rich primary carbides provide further proof that the surface did in fact undergo corrosion. Lack of obvious corrosion mechanisms like pitting or cracks of the matrix of HCWCI-2 is an indication that the alloy exhibited good resistance behaviour during electrochemical tests. This can be confirmed by the same observation recorded by Beimeng et al. (2013) and the alloy's low current density and corrosion rate.

Similar to HCWCI-1, HCWCI-3 was expected to exhibit severe corrosion attack on its matrix. This was expected because HCWCI-3 displayed a similar structure to that of HCWCI-1 which consists of a relatively high volume fraction of eutectic primary carbides than HCWCI-2. HCWCI-1 and HCWCI-3 suffered more from localised corrosion than HCWCI-2 as shown in Figure 4.57. This phenomenon was also observed by El-Aziz (2015) where the structure that contained a volume fraction of eutectic primary carbides exhibited the most severe localised corrosion in the form of pits and microcrevices.

The only characteristic that the HCWCI alloys had in common was the inert behaviour the primary carbides exhibited during anodic polarisation tests. The corrosive damages in all the alloys were observed occurring on their matrices.

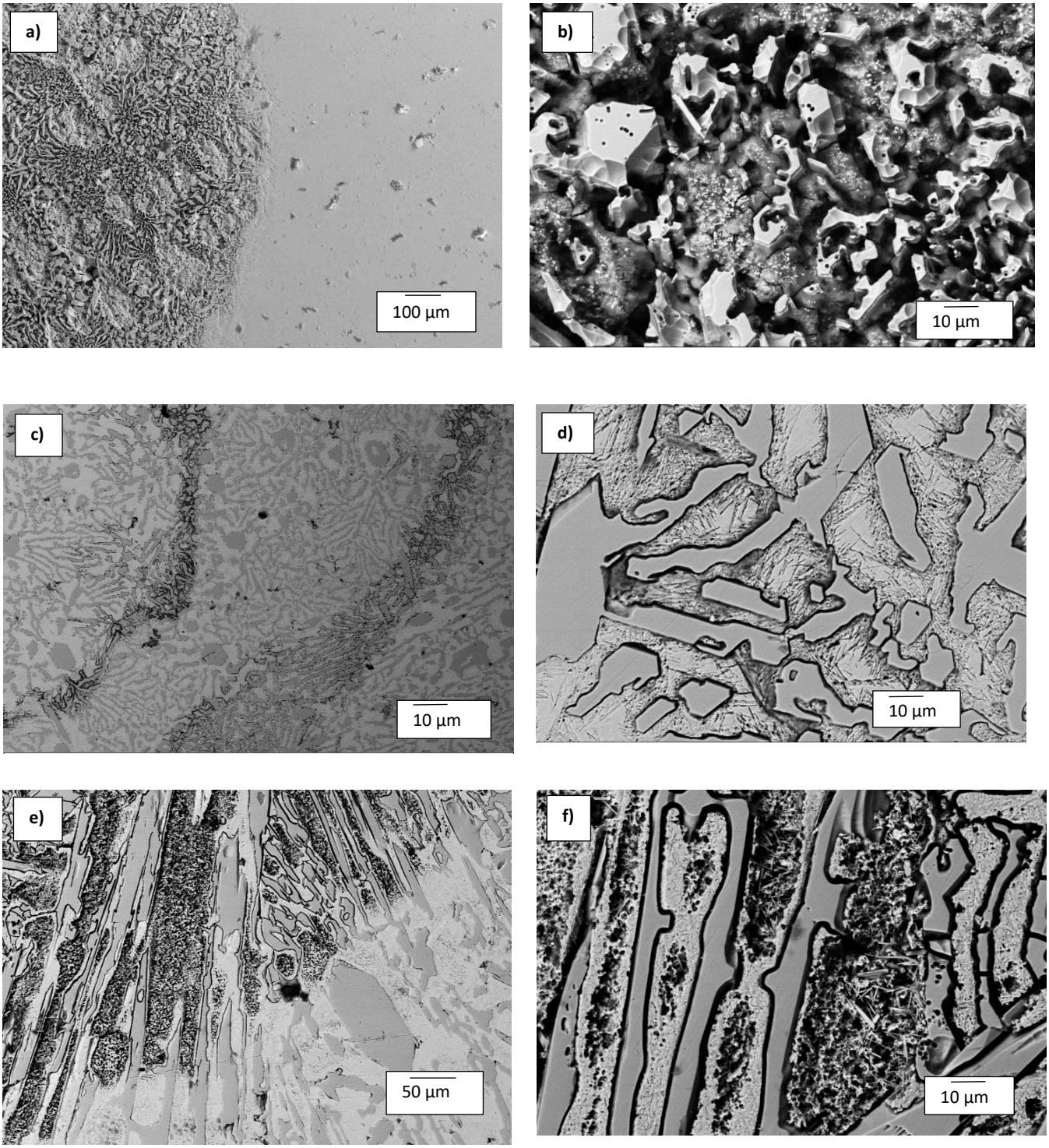

Figure 4.56: SEM-BSD micrographs of: (a-b) HCWCI-1, (c-d) HCWCI-2 and (e-f) HCWCI-3 after undergoing electrochemical tests in 1M H_2SO_4.

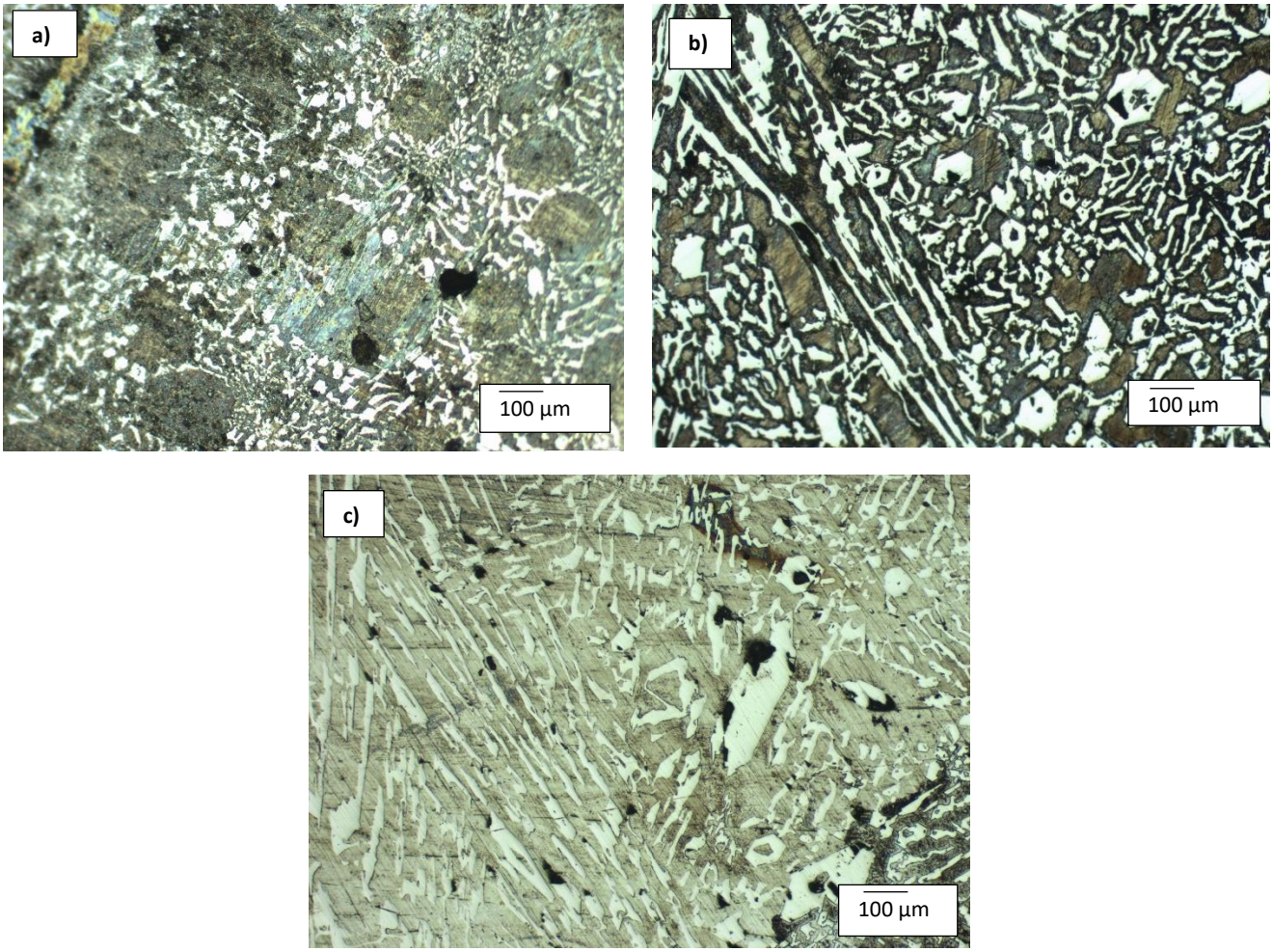

Figure 4.57: Optical micrographs of: (a) HCWCI-1, (b) HCWCI-2 and (c) HCWCI-3 after undergoing electrochemical tests in 1M H_2SO_4.

The Hadfield steel

The SEM and optical micrographs for the Hadfield steel are presented in Figure 4.58 and 4.59, respectively. The micrographs focus on the corrosive mechanisms that occurred on the austenite grains, the carbide-rich grain boundaries and the carbide inclusions within the austenite grains.

The corrosive product (passive layer) can be seen in Figure 4.58 (a) and (b) characterised as a cracked dark-grey layer covering some parts of the corroded surface. The product layer is seen segregating within and around pits, grain boundaries and regions that are rich in carbide inclusions. The vertical black lines seen in Figure 4.58(c) shows that the twin boundaries also suffered chemical attack during the polarisation test. The same mechanisms were reported

by Garcia et al. (2010) and Abreu et al. (2007). It is also noteworthy that there are large amounts of corrosion products that appeared as pits and craters after they were unintentionally delaminated during or after the electrochemical test. These large craters and micropores can be seen more prominently in Figure 4.58 (c) and in Figure 4.59.

Figure 4.58 (b) shows the occurrence of what is called a hills-and-valleys morphology observed on the corroded regions. The same morphology was reported by Ozgowicz et al. (2012) and they reported that the observed surface after polarisation tests were as a result of mechanism known as the hydrogen depolarisation mechanism which was common on surfaces that have undergone corrosion in an acidic medium.

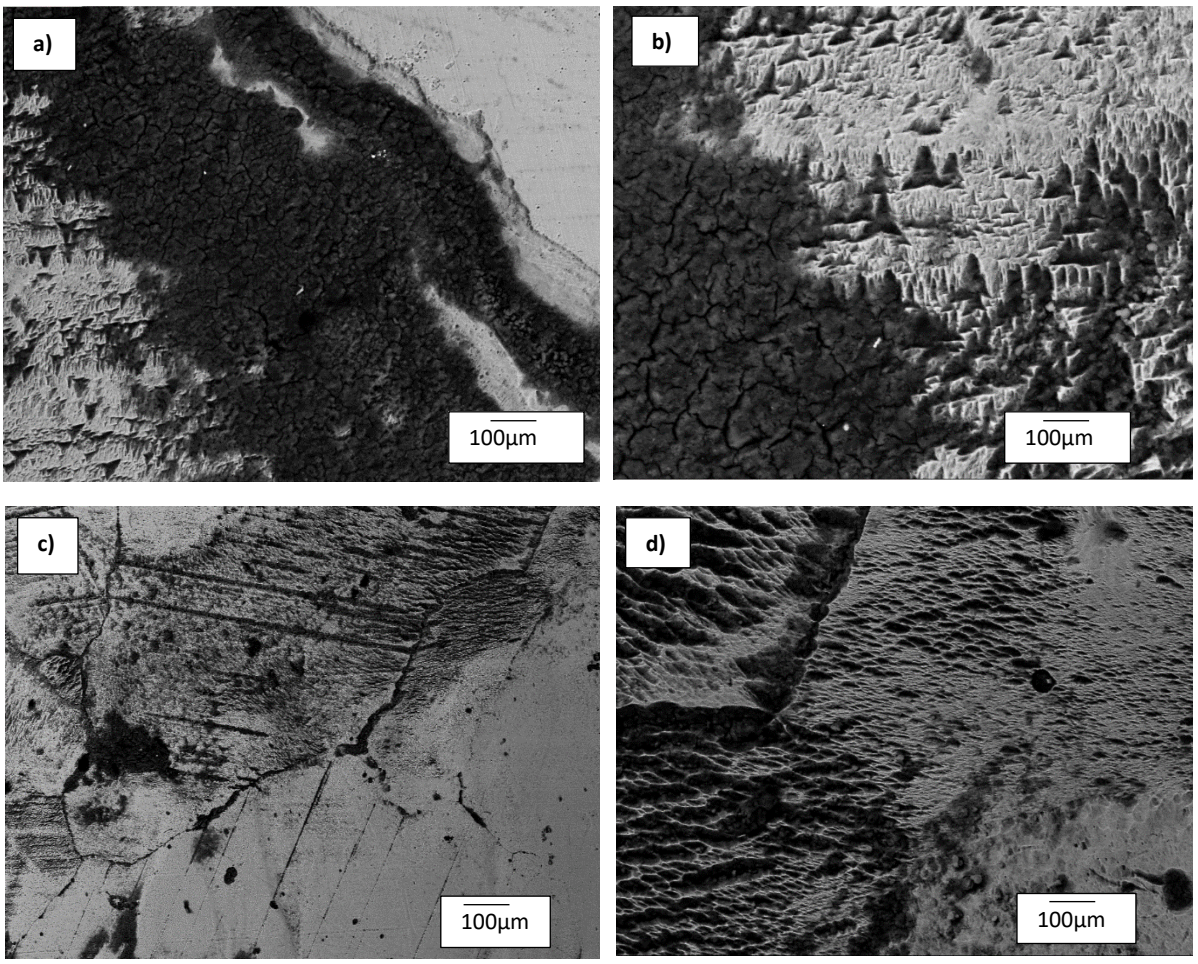

Figure 4.58: SEM-BSD micrographs of Hadfield steel after undergoing electrochemical tests in 1M H_2SO_4.

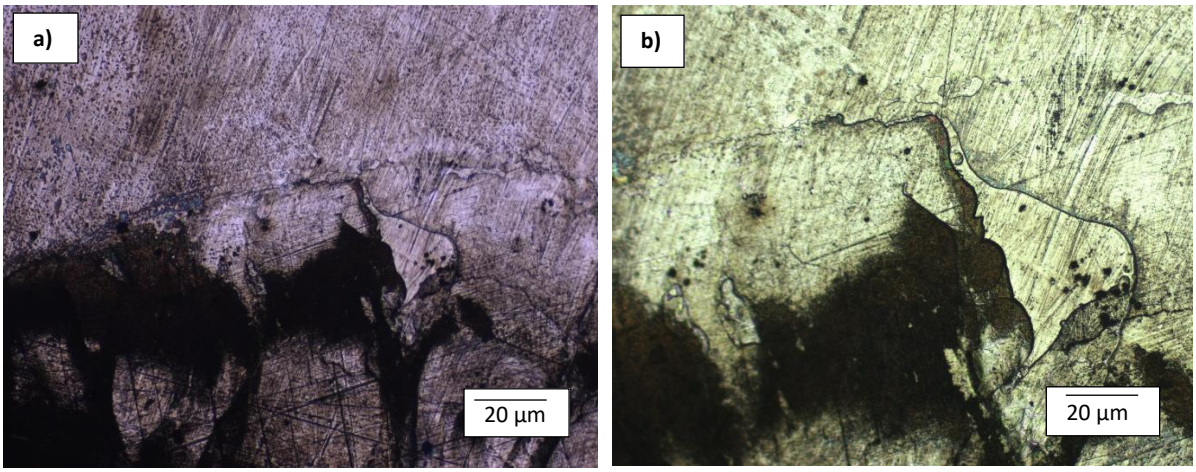

Figure 4.59: Optical micrographs of Hadfield steel after undergoing electrochemical tests in 1M H_2SO_4.

Chapter 5

5. DISCUSSION

The wear properties of the WC-Co alloys were investigated and compared to the properties of HCWCI alloys and Hadfield steel for the selection of a suitable material to be used a protective liner on chutes and skips. The mechanical and microstructural properties and their effects on the wear mechanisms experienced by materials during testing also forms part of the discussion.

The cobalt content and the WC grain size of the WC-Co alloys were varied in this work. The cobalt content was varied between 6 to 12 wt% and the grain size was between 0.4-2.3 µm. The composition of the chromium content of the HCWCI alloys was varied and only one grade of Hadfield steel was investigated.

This section begins with the discussion of the mechanical and microstructural properties of the investigated materials, followed by a discussion on the wear mechanisms observed during rubber wheel abrasive wear, solid particle erosion testing, and sliding wear of the materials. A brief discussion about the materials' electrochemical response to corrosion in a 1M sulfuric acid medium is included. Finally, a selection of the material most suitable for the lining of chutes and skips will be made. This selection will be based mainly on the performance of the material and its resistance against both mechanical and wear tests.

5.1 Mechanical and Microstructural Properties

5.1.1 WC-Co cemented carbides

The hardness and the Palmqvist fracture toughness of the WC-Co cemented carbides were determined using the Vickers macroindentation method. An indentation force of 30 kgf was used.

The hardness and toughness of tungsten carbide based hardmetals are known to be anisotropic due to the crystallographic structure of the WC grains within the alloy (Ndlovu, 2009). Therefore, direction of the induced dislocations plays a major role in the hardness and toughness of the hardmetals. The anisotropic property was observed when the WC grain size and the Co binder content of the investigated was varied.

The largest Vickers hardness value was exhibited by the finest grained WC-Co alloy and the lowest Vickers hardness was exhibited by the alloy that was most coarse. The hardness of the WC cemented alloys have been extensively researched and was found to increase with a decrease in both the grain size of WC particles and cobalt content (Ndlovu, 2009).

The increase in the hardness value experienced by the finely grained alloy (WC-12Co) was as a result of the densely populated and constrained WC particles. The decreased grain sized structure further decreased the binder free mean path as explained by Gurland and Bardzil (1955). The decrease in the binder free mean path increases the yield strength of the material hence, causing difficulty in which dislocations move around the matrix during indentation. The effect of the fine and densely populated WC particles and its resistance against the plastically deforming indentation is depicted in a schematic presented in Figure 5.1

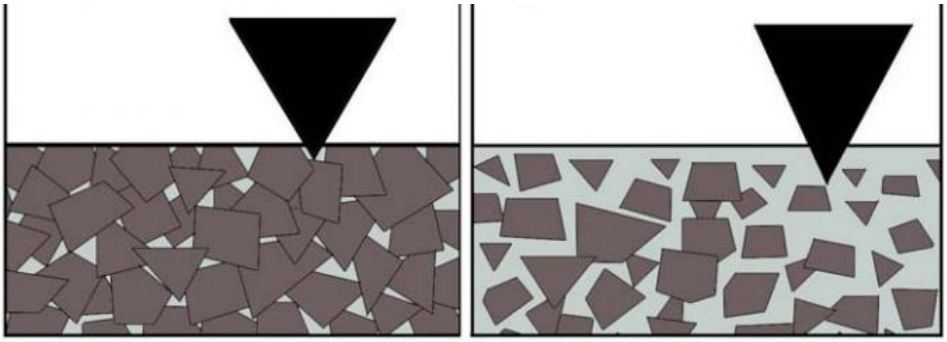

Figure 5.1: Schematic depicting a WC-Co structure with: (a) densely populated WC particles and (b) loosely packed WC particles and their effect against penetration by a Berkovich indenter. Adapted from *(Ndlovu, 2009).*

The addition of chromium in WC-12Co and the influence it had on the hardness of the alloy could not be directly measured in the matrix. However, its effects were observed by the way the grains were more refined compared to the other unalloyed samples, as well as the increased hardness for the WC-12Co. However, the downfall of the combination of the mechanical and microstructural properties exhibited by the WC-12Co is its low fracture toughness value. This makes the alloy prone to fracture upon impact because of its brittle nature. This is a problem since the material to be used as a protective liner against varying types of wear in chutes and skips should be both hard and exhibit good toughness.

The difference in the WC grain sizes between the WC-6Co and WC-8Co alloys was very small as was their behaviour against slurry abrasion. They both exhibited wear rates that were a magnitude larger than that exhibited by the WC-12Co alloy. In this regard, a smaller grain size and a higher Vickers hardness value resulted in a much lower wear rate and therefore, better resistance to wear by slurry abrasion. The influence of the hardness on the rate of wear was more prominent than the influence of their binder content against slurry abrasion. However, the opposite behaviour was observed with solid particle erosion wear tests.

The WC-Co alloy that consisted of the lowest binder content, WC-6Co, exhibited the lowest steady state erosion rate and the alloy that had the highest binder content, WC-12Co, exhibited the highest erosion rate. This trend was also observed by Pugsley and Allen (1999) and Adler et al. (2001). The content of the Co binder seems to be the determining factor against the samples' behaviour against erosive wear. It was recorded by Finnie (1960) and Levy (1986) that in ductile materials (Co binder), the eroding particles created craters and subsequently embedded themselves in the binder material.

These embedded particles would then act as a protective shield against the other jetted eroding particles. This would in turn cause a decrease in the mass loss of the target material since the damaging effects of the oncoming eroding particles made less contact with the target material. This observation can be used to explain why the WC-12Co alloy experienced the highest overall mass loss. The WC particles were more refined which made the structure of WC-12Co more densely populated by the hard particles. This in turn caused less exposure of the ductile Co hence less shielding by the embedded eroding particles. This phenomenon is schematically depicted for the surface of a sample in Figure 5.2.

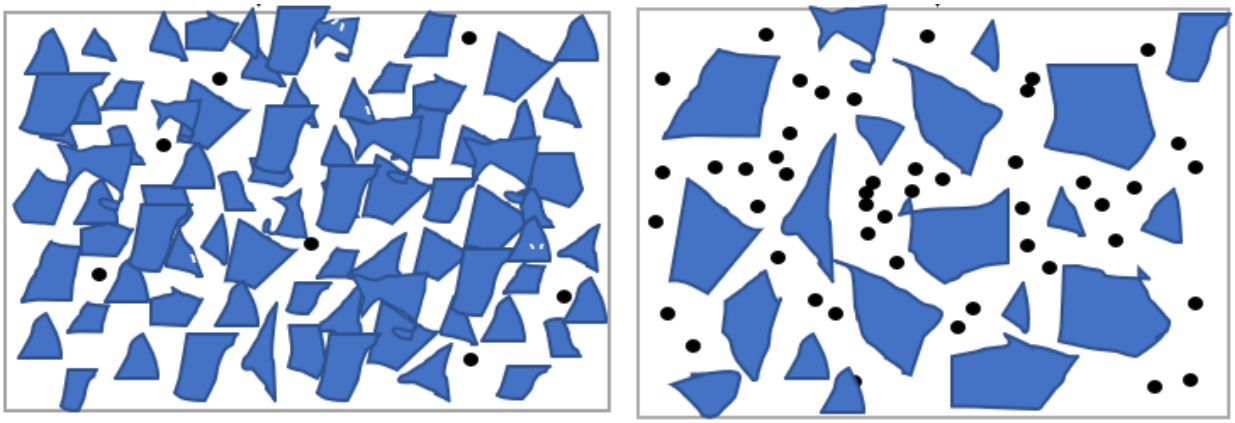

Figure 5.2: Schematic showing the surfaces of the embedded particles during erosion: (a) dense packing of refined WC particles with limited surface for embedding of erodant and (b) sparsely packed coarse WC particles with a large surface area for embedding of erodant.

The size and shape of the WC particles (hence the surface hardness) seemed to have had a bigger influence on the wear rate of the pins sliding against the surface of the WC-Co alloys during the PoD sliding wear tests. The alloy with the most refined structure, WC-12Co resulted in the largest pin volume loss. The pin sliding against the WC-12Co alloy exhibited a wear rate that was a magnitude larger than the other two alloys. The WC-12Co sample was observed to also have exhibited the highest resistance during sliding wear, resulting in a higher coefficient of friction and therefore, more adhesion of the pin on the surface of the alloy.

During the pin-on-disc sliding wear, the increase in CoF in the initial sliding meters may be as a result of the increased force required for sliding to occur due to the detachment of the soft asperities on both the surfaces of the pin and disc (Chowdhury & Helali, 2008). The higher the CoF value, the more detached the initial asperities are, and the more force is required for sliding to occur against the surfaces just as outlined by Masilela (2018). This tends to cause more contact between the pin and disc, which in turn causes an increased detachment of wear debris on the wear track. This detachment in wear debris as well as the possible increase in temperature gives rise to the appearance of abrasive and adhesive wear mechanisms on the pins and the surfaces of the discs (Hernandez, 2014).

5.1.2 HCWCI alloys

Most mechanical properties of white cast irons alloys and their responses to damage by wear are highly dependent on the morphology of the reinforcing constituents. Moreover, their exceptional resistance to abrasive and impact wear is primarily attributed to the high hardness provided by the presence, chemical makeup, and nature of the reinforcing carbide particles (El-Aziz et al., 2015). The alloying elements, including Cr and C, also have a great influence in the way these alloys respond to wear. The investigated HCWCI alloys viz. HCWCI-1, HCWCI-2, and HCWCI-3 all contained different amounts of Cr (20, 22 and 25 wt%, respectively) in their structure. This resulted in three different alloys that contained Cr-rich carbides that were different in shape, size, and frequency of occurrence.

The mechanical and microstructural effects of the HCWCI alloys against wear will be discussed by focusing on the hardness, chromium/carbon content, and the morphology of the reinforcing carbides.

HCWCI-2 and HCWCI-3 both contained larger rod-like (longitudinal) primary carbides in their structures. The large rod-like structures were surrounded by smaller rod-like carbides, smaller hexagonally-shaped (transverse) carbides as well as eutectic primary carbides. The eutectic carbides can be seen occurring more in HCWCI-3 than the HCWCI-2 alloy.

According to Powell (1980) the increase in Cr results in the separate shafting of the rod-like primary carbides during solidification. This not only increases the strength of the high-chromium cast irons, but also improves the toughness of the structure. Refined rod-shaped (longitudinal) carbides have superior mechanical properties than bulky hexagonally-shaped (transverse) carbides (Wu et al., 2006).

The structure of HCWCI-1 consisted mostly of fine eutectic carbides surrounded by even smaller primary carbides that were both rod-like and hexagonally shaped. The rod-shaped primary carbides were very thin, refined and stretched longer in the HCWCI-1 alloy. The high hardness value exhibited by HCWCI-1 was as a result of its fine grain structure which can be attributed to the presence of vanadium its structure.

The high carbon content also accounts for the occurance of the primary eutectic carbides, and therefore, an increased bulk hardness (Wu et al., 2006). The relationship between the

occurance of the eutectic carbides and the hardness value can also be seen with HCWCI-3 and HCWCI-2. As mentioned before, the occurance of eutectic primary carbides was more frequent in HCWCI-3 than in HCWCI-2, hence HCWCI-3 exhibited a higher hardness value when compared to HCWCI-2. In addition to that, it was clear that the alloys that contained higher compositions of chromium in their structures (HCWCI-2 and HCWCI-3) exhibited wear rates that were way less than that exhibited by HCWCI-1. However, further increasing the chromium content resulted in an adverse effect against slurry abrasion wear since HCWCI-3 contained the highest chromium content and exhibited a higher wear rate than HCWCI-2. The same trend of results were found by El-Aziz et al. (2015); Zumelzu et al. (2002) and Cetinkaya (2006). They all concluded that increasing chromium in high-chromium cast irons decreased the alloys' resistance to abrasion wear. The pattern observed was the alloy that exhibited the lowest abrasive wear loss consisted of the lowest Cr/C ratio.

During the slurry abrasion wear testing, the two alloys that contained the highest volume of primary eutectic carbides (HCWCI-1 and HCWCI-3) exhibited the highest wear rates. HCWCI-1 had the least occuring Cr-rich primary carbides in its structure and it displayed the least resistance to slurry abrasion. A possible reason, as outlined by Wu et al. (2006,) is that a highly hyperuetectic high chromium cast iron is very brittle and highly prone to damage by large fracturing forces. Therefore, the high wear volume loss seen with HCWCI-1 could be as a result of the alloy undergoing chipping and spalling caused by its brittle structure. The HCWCI-3 alloy exhibited large and bulky longtitudinal primary carbides which had an adverse effect on the mechanical structure of HCWCI alloys during slurry abrasion tests. The alloys either becomes too hard and brittle to use for lining applications where impact is high, or the austenitic matrix gets too exposed from lack of smaller reinforcing carbides in between. This further causes the hardness of the structure to be non-uniform at regions without the hard carbides.

HCWCI-2 had about an equal amount of eutectic, rod-like, and hexagonally shaped carbides in its structure and it displayed the best resistance to slurry abrasion. It also displayed a high volume of smaller in size primary carbides which performed better against slurry abrasive wear than large bulky carbides (such as the ones obseerved with HCWCI-3). This goes to show that a structure that has a combination of smaller sized eutectic, rod-like, and hexagonally shaped carbides has a better influence against slurry abrasion wear than a hard surfaced

HCWCI alloy with a high volume of primary eutectic carbides or one with a high volume of large and bulky longtitudinal primary carbides.

During erosion wear testing, HCWCI-1 displayed the lowest wear rate, closely followed by HCWCI-3. HCWCI-2 exhibited the highest wear rate and therefore it performed the worst against erosion wear. The erosion wear rate values of HCWCI-1 and HCWCI-3 showed little difference in their wear rate values because they displayed similar microstructures of eutectic carbides in their systems. However, it should be noted that the least hardest alloy, HCWCI-2, exhibited the lowest mass loss during erosive wear despite its high volume of hard Cr-rich carbides. The most plausible reason, as previously oulined, could be as a result of the overly exposed austenitic matrix. This happens when the structure consists more of large and bulky primary carbides and less of the smaller reinforcing primary carbides. Additionally, a HCWCI alloy containing large primary carbides is said to cause the enhancement of the plastic strain of the matrix, resulting in rapid material removal of the carbides (Aptekar &Kosel, 1985). This same level of reasoning is why the HCWCI-1 alloy outperformed the other two alloys during the erosive wear tests, where the refined and densely packed eutectic carbides offered exceptional resistance against the eroding particles.

The work by Yousif and Ataiwi (2018) contradicts the mass loss and work hardening relationship experienced by the HCWCI alloys investigated in this study. They recorded that two of their investigated HCWCI alloys exhibited the highest mass loss during the erosion process and did not experience any increase in hardness. This deviation might be due to the different alloying elements and compositions contents that the alloys investigated contain. However, the directly proportional relationship between the overall mass loss and the initial hardness seen with the HCWCI alloys during erosion correlates with the findings observed in literature where the two hardest HCWCI alloys (HCWCI-1 and HCWCI-3) experienced the lowest overall mass loss (Yousif & Ataiwi, 2018)

The pins that were slid against the HCWCI alloys during the pin-on-disc tests portryed varying wear volume losses and CoF values. There is, however, a clear trend between the wear volume losses exhibited by the pins and the CoF values: the alloy whose pin exhibited the highest wear volume loss also displayed the highest CoF value. Although it is widely recognised that an increase in CoF increases the wear rate of a material, there has not been a mathematical expression to link the two quantities (Rus et al., 2013). The two hardest

HCWCI alloys were also observed to have displayed lower CoF values. The same trend was seen with the research work conducted by Moore & Tegart (1952) where they documented that even though hardness had little effect on the CoF, there was evidence in their work that the CoF value was lower in harder metals than in was in softer ones.

The largely exposed and bulky primary carbides seen occurring in the HCWCI-2 seemed to have had a greater impact on the alloys' resistance against sliding wear using 316 SS pins. The pin that was used on the surface of the HCWCI-2 alloy exhibited the highest wear volume loss against the disc of the alloy. This provided evidence that the morphology of the surface of the alloys with large Cr-rich carbides was preferrential against wear by sliding when compared to the other two alloys. The high wear resistance of the HCWCI-2 alloy was aided by the large primary carbides.

5.1.3 The Hadfield steel

The surface hardness of Hadfield steels plays the biggest role in determining the wear resistance of the metal (Lu et al., 2001). The surface hardness of high manganese Hadfield steels can be attributed to the hard precipitated carbides along the austenitic grains as well as the austenitic matrix itself (Moghaddam, 2011). The precipitated carbides were produced from varying alloying elements that dissolved during solidification. However, the main distinguishing property of the Hadfield steel from any other conventional steel used as liners is its work-hardening abilities. Dastur and Leslie (1981) added in their investigated work that the surface hardness of the Hadfield steel was more of a function of their general dislocation structure than the actual microstructure. Sabzi and Farzam (2019) added that the work-hardening seen occurring in Hadfield steels happens when there is localized plastic deformation leading to strain induced transformation to ε, γ or α martensite, hinderances between dislocations, and mechanical twinning.

The work-hardening capabilities of the investigated Hadfield steel were seen to be more prominently highlighted during the rubber wheel abrasion wear tests. The slurry abrasion test had an external normal load of 25N against the Hadfield steel sample and the dry sand abrasive test exerted an external normal force of 130N. In both the rubber wheel tests, the wear resistance of the Hadfield steel against abrasion was low during the early abrading stages but began to increase as the rate of work-hardening increased. This was due to the

slow wear conditions when the work-hardening of the steel was at its minimum (Sabzi & Farzam, 2019).

The generation of dislocations and their movements within the crystal structure were induced more during the dry sand abrasion test than they were during the slurry abrasion test. The proof of the strain-hardening that occurred on the material was shown in the extent of the increased hardness as well as the lower wear volume losses experienced by the Hadfield steel during and after dry sand abrasive test. During dry sand abrasion test, the Hadfield steel exhibited a peak hardness of 289 HV_{30} and an overall increase up to 286 from 250 Vickers after a duration of 40 minutes. These hardness values were lower during the slurry abrasion tests and the reason for that was because of the low abrasive wear force exerted by the 25N normal load which was not large enough to cause high dislocation slip bands and twinning (Xu & Li, 2006; Efstathiou & Sehitoglu, 2009; Ge et al., 2017; Xu et al., 2017).

The precipitated carbides found within and along the austenite grains boundaries were not hard and frequent enough to resist the damage caused by the eroding particles exerted by the alumina oxides. Although the steel exhibited remarkable work-hardening, it displayed the weakest resistance to erosion when compared to the performance of the other materials against erosion. The Hadfield steel's inability to adequately resist volume loss during erosion was primarily as a result of the morphology of the matrix. The matrix of the Hadfield steel is not reinforced with hard particles like the other two materials, hence its weak resistance to erosion wear.

The 316 SS pin and the Hadfield steel disc had similar microstructures (Figure 5.3) and similar chemical make-up, and they therefore exhibit similar adhesive properties when rubbed against one another during processes that involves high sliding friction. Thus, the relationship

between the wear behaviour of the pin against the surface of the disc is more dependent on the surface hardness of the pin and/or the disc.

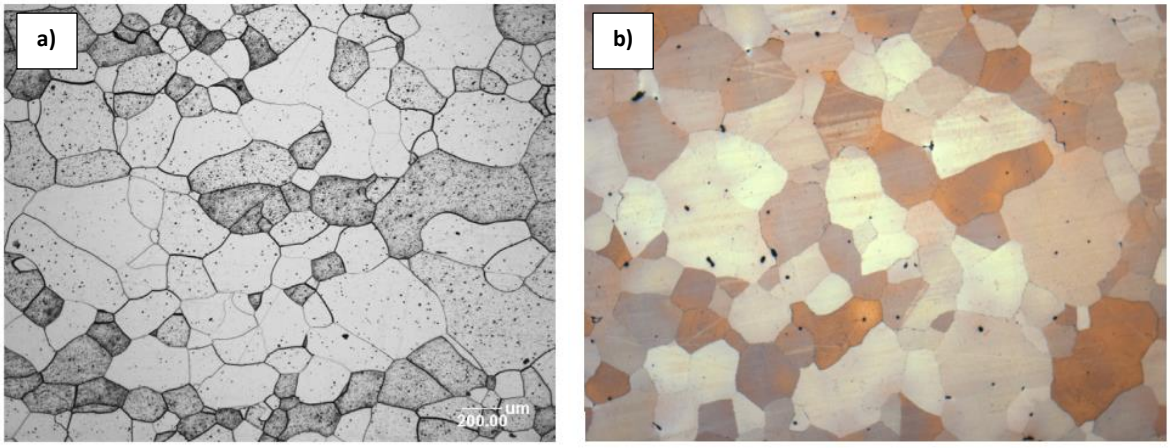

Figure 5.3: Optical micrographs showing the microstructures of: (a) aged 316L stainless steel and (b) solutionised high manganese Hadfield steel *(Han et al., 2014; Havel, 2017).*

The 316 SS pin that slid against the Hadfield steel disc experienced the lowest wear volume loss during the pin-on-disc test. The pin exhibited a wear rate that was a magnitude smaller than all the other investigated materials. The pin did not display severe damage and adhesion of material onto the Hadfield steel because 316 SS has a higher hardness value when compared to Hadfield steel. The hardness of the 316 SS was 749 Vickers unit, which is substantially higher than Hadfield steel even after it has experienced its optimum work-hardening value of 550 Brinell (± 647 Vickers unit). Therefore, the surface of the Hadfield steel showed weak resistance against the 316 SS during the pin-on-disc.

5.2 Wear mechanisms and Effects

All the materials investigated in this project experienced varying volumetric wear losses when subjected to the different tribometers that were used to measure their behaviour against wear. Their responses against wear varied because the materials consisted of varying chemical make-ups and microstructures. These different behaviours can be attributed to the wear mechanisms experienced by the materials during the wear tests. In this section, the

dominant wear mechanisms experienced by the investigated materials and their effects on the resistance against volumetric wear losses are discussed.

5.2.1 Rubber wheel abrasion wear

The wear mechanisms observed on the surfaces of the samples after undergoing the rubber abrasive wear test were similar. However, the wear processes seen with the WC-Co alloys showed a slight deviance from the HCWCI alloys and the Hadfield steel.

The main deformation mechanisms observed in the HCWCI alloys and the Hadfield steel during abrasive wear were microploughing and microcutting. This was expected since these two wear mechanisms were observed to be the frequently occurring mechanisms during abrasion wear. However, no ploughing nor cutting was experienced by any of the WC-Co alloys. This resistance against the microploughing and the microcutting of the WC-Co alloys can be attributed to their ultra-hard surfaces. The dependence of what type of wear deformation occurs during abrasion is governed by the ratio of the hardness of the silica sand abrasives to the surface hardness of the metals (H_a/H_m) (Pirso et al., 2011). The lower the ratio, the more difficult it becomes for the abrasives to penetrate through to the surface of the metals (Ndlovu, 2009). Metals that have ratios less than 1.0 are in the lowest wear zones where the deformation and the material mass loss of metals are very minimal. WC-Co alloys exhibited H_a/H_m ratios that were lower than 1.0 because the hardness value of the SiO_2 abrasives was not hard enough to cause severe damage. The HCWCI alloys and the Hadfield steel had H_a/H_m ratios that were higher than 1.2, hence why these metals experienced excessive wear volume loss in a form of microploughing and microcutting.

The two main damaging wear mechanisms that were seen occurring with the WC-Co during slurry abrasion was the extrusion of the cobalt binder and particle pull-out. The finer WC-Co alloy (WC-12Co) showed the least wear rate because it exhibited the least binder extrusion and WC grain pull-out. The extrusion and smearing of the cobalt binder were seen occurring less with the WC-12Co alloy than they did with the other two alloys. The finer grained WC-Co alloy (WC-12Co) experienced less wear damages than the courser grained WC-Co alloys. This was seen to also have been the case with the work conducted by Ndlovu (2009) on varying

grain sizes and cobalt content. The refined structured WC-Co alloys exhibited minimal wear deformations when compared to their course counterparts (Ndlovu, 2009; Ma et al., 2017).

The HCWCI alloys experienced a combination of wear mechanisms during slurry abrasion wear tests. Microploughing and microcutting were the dominant deformation mechanisms observed whereas microcracking was the least occurring mechanism. The HCWCI alloys showed severe damage by gouging during the slurry abrasion process, and this was because the abrading particles were harder than the bulk surface hardness of the alloys. The H_a/H_m ratios of the alloys were over 1.2, which places the alloys at a high wear regime. In this wear regime the particles can easily penetrate and damage the surface of the metals and remove "chunks" of material with the help of the normal load exerted against them.

The HCWCI-2 alloy exhibited the least wear rate, and this was in line with the minimal damage seen to have occurred upon close examination of the optical micrographs. The most severe damage was observed on the surface of the HCWCI-1 alloy. It consisted of deep cut-off grooves and large depressions where the material (carbides and/or the matrix) was removed. This kind of damage was consistent with the high wear rate experienced by HCWCI-1.

With the Hadfield steel, the two dominant wear mechanisms were also microploughing and microcutting. The cleanly cut grooves were an indication that the dominating mechanism changed from microploughing to microcutting as outlined by Tressia et al. (2017) and Prieto et al. (2015). It also indicated how soft the material was compared to the abrasive particles. The Hadfield steel exhibited a H_a/H_m ratio of 4.4 which was four times larger than the other investigated materials.

The steel experienced no material buildup along the grooves, therefore, no hindrance caused by hard particles prevented the SiO_2 abrasives from severe damage. This further indicated how different the wear mechanisms for materials without reinforcing hard particles are to those that are reinforced against abrasion wear. Frequent and deeper grooves were visible with Hadfield steel during the slurry abrasion wear when compared to the other investigated metals, thus the high wear rates. The same wear mechanisms observed during the slurry abrasion wear were seen occurring on the Hadfield steel during dry sand abrasion wear, only

that the dent where the rubber wheel made contact with the surface of the steel was deeper and more worn off.

3.2.2 Solid particle erosion wear

Both the ductile phase (Co binder) and the brittle phase (WC particles) of the investigated cemented carbide alloys experienced some sort of material loss mechanism during the erosion process. At some point the two phases and the eroding particle combined together due to plastic deformation caused by the force of the eroding particles, leading to some regions being partially covered with a mechanically mixed layer (Antonov et al., 2017). Both WC-6Co and WC-8Co alloys displayed more of these dispersed patches of layers because they had a larger surface of exposed cobalt in between the WC particles. As a result, the two exhibited the highest resistance against erosion. The mechanically mixed layers (MML) were analysed by EDS and were found to contain high amounts of the Co binder and Al_2O_3 particles to the presence of cobalt, aluminium and oxygen. The EDS also detected traces of tungsten and carbon in the layer which, according to the work reported by Antonov et al. (2017), were analysed to be fragments of WC particles that were refined and spalled into the layer during high force impact. These regions of MML acted as protective layers against further deleterious effects of the impact caused by the eroding particles. The layers were strongly attached and not easily removed (Antonov et al., 2017).

The SEM micrographs show regions where the binder phase experienced cracks and pits left by Co extrusion. These cracks and pits left by the extruded cobalt binder become filled with the embedded Al_2O_3 particles which then acted as a protective shield against further deterioration of the surface. Figure 5.4 is a schematic presentation of the process where (a) the eroding particle impacts the binder phase creating a crater with material extruded on either sides and (b) the crater is filled with the chipped or embedded particle which acts as a protective layer. Unlike the MML, the embedded particles were removed after some time of being eroded. The particles became lose from lack of support from the craters and this resulted to material loss of the binder. Thereafter, further removal of the cobalt was experienced by the WC-Co alloys as outlined by Tilly's (1972) two-stage extrusion and

fragmentation mechanism theory. However, in as much as WC-6Co and WC-8Co experienced damage to their surface, the MML and Al_2O_3 -filled craters counteracted the damage.

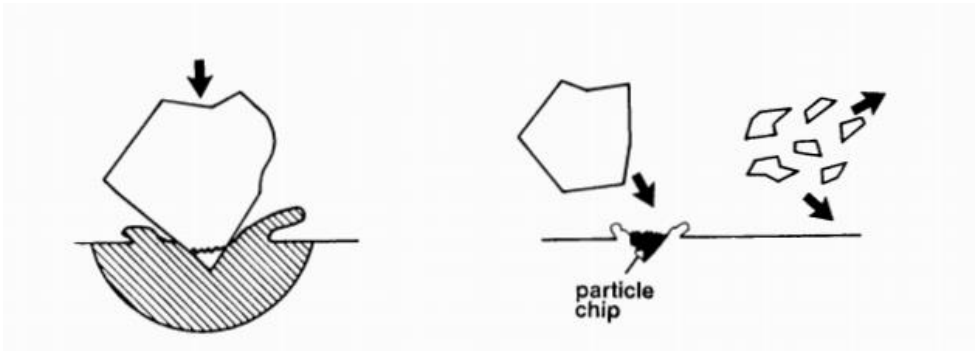

Figure 5.4: Schematic presentation of the process where (a) the eroding particle impacts the binder phase creating a crater and (b) crater filled with eroding particles *(Tilly, 1972).*

The brittle mechanisms were prominent with the WC particles. The WC particles were mostly removed from the surface of the coarse alloys as individual particles whereas in WC-12Co, the particles were removed as an agglomeration. The large fragments consisted of refined WC particles that underwent microfragmentation during impact and whole WC particles all bounded together by cobalt. The removal of the large fragments seen occurring with WC-12Co are responsible for the excessive rate of wear of the alloy.

Just as observed with the WC-Co alloys, the HCWCI alloys also experienced a combination of ductile and brittle wear mechanisms during solid particle erosion wear. These mechanisms were more visible with the HCWCI alloys since the alloys had a fair amount of visible ductile and carbide phases in their structure. In reinforced metals, the removal of the matrix or/and the primary carbides (or the resistance thereof) works in conjunction with each other. This means if the carbides are too plastically deformed then the matrix will not be protected from the eroding particles and conversely, when the matrix is deformed it creates cracks around the carbides which makes it easier for the carbides to fall out from the binder during the erosion process.

The three HCWCI alloys experienced similar material removing mechanisms but at varying intensities and the level of these intensities are primarily dictated by the volume fraction of the Cr-rich primary carbides and therefore, their overall bulk hardness (Aptekar & Kosel, 1985). The predominant erosion mechanism seen occurring in the primary carbides was edge fracturing and the predominant erosion mechanism seen occurring in the matrix was edge rounding (ductile cutting). Kosel and Ahmed (1992) and Sapate and RamaRao (2005) observed similar mechanisms of edging in their work. Edge fracturing was seen by the sharp chippings of the brittle carbides whereas edge rounding was seen by the less angular grooves where the eroding particles made contact with the matrix.

The process of carbide removal involved different mechanisms: (1) residual stresses associated with the plastic deformation of the matrix formed around the carbides. This results in the lateral vent cracks that lead to the falling out of the carbides, (2) fatigue resulting from the constant microfracturing of the carbides by the eroding particles (Hansen, 1979; Al-Bukhaiti et al., 2006). HCWCI-2 experienced the severest carbide removal followed by HCWCI-3. HCWCI-1 also experienced carbide removal but it was not as severe.

Extruded lips were observed on some of the worn surface indicating that microploughing took place. However, it was the ductile chipping and cutting of the extruded material by further impacting that resulted to the excessive loss of material. HCWCI-2 experienced a severe case of ductile chipping and cutting of the extruded material than the other two HCWCI alloys. This was, as previously stated, because of how the alloy consisted of larger and bulkier primary carbides and few smaller reinforcing carbides, causing the matrix to be more exposed to the harsh effects of the eroding particles thus, rendering it more vulnerable to ductile chipping and cutting. Although visible all over the eroded surfaces, HCWCI-1 and HCWCI-3 exhibited less severe damages to their matrix phase. This can be primarily attributed to the occurring of the refined eutectic carbides in their structures.

Hadfield steel experienced ductile erosion wear mechanisms during the eroding process. The erodent particles produced severe grooves and pits on the surfaces which resulted in excessive mass loss of the steel. The Hadfield steel does not contain any hard reinforcing particles in its structure hence it exhibited the highest volumetric wear loss. The softness of the material was characterised by the extent in which the eroding particles were embedded onto the target material. The force of impact against the target material can observed by the

manner in which cracks emanated from the craters where the erodent particles were embedded. Striations were also observed occurring frequently where large particles indented the surface. This indicated that the surface experienced fatigue stress during the eroding process. This phenomenon was also seen occurring with the work conducted by Laguna-Camacho et al. (2012) on different steel types.

5.2.3 Sliding wear

The sliding wear tests were conducted under a relatively low load and linear speed in the absence of lubrication. The 316 stainless steel ball bearings were used as pins and they had a hardness of 749 Vickers unit. The surfaces of the WC-Co alloys were harder than the pins, therefore, the alloys did not exhibit any severe bulk deformation. Because the pins were the less hard counterparts, the damage caused by the externally exerted normal force was mostly incurred by the pins. No microploughing and microcutting were observed on the WC-Co alloys because the worn off debris were not hard enough to abrade and penetrate the surfaces. This observation was made by examining the wear tracks on the WC-Co alloys using high magnification SEM micrographs. Upon close inspection, the SEM micrographs revealed a thin translucent layer of the thinly smeared layer of the 316 SS pins over the WC particles (Figure 5.5). This either meant that the 316 SS pins and the WC particles had dissimilar atomic bonding characteristics hence why cold welding between the two metals did not occur, or the external load and speed were not sufficient to result in total adherence of the metals to one another. In addition, the extrusion of cobalt was more frequent than the WC grain pull-out because cobalt has a higher compatibility to most of the elements that make up the 316 SS viz. Ni, Mn, Zn, and Fe.

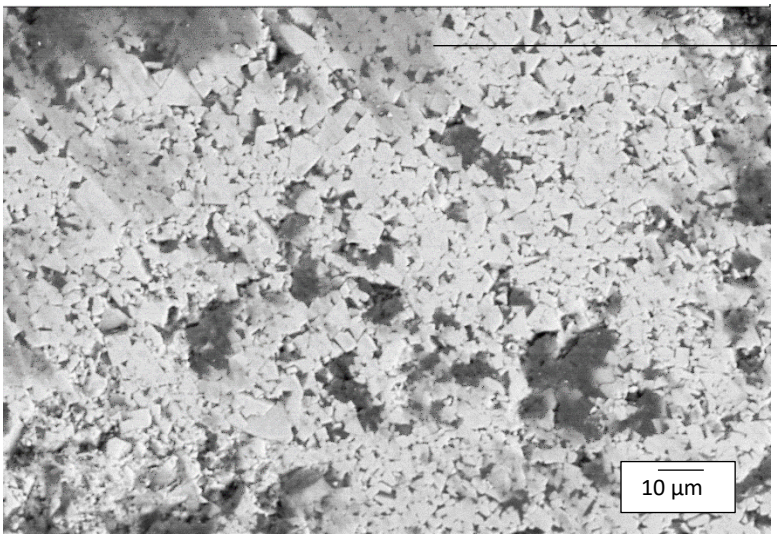

Figure 5.5: SEM-BSD micrograph of WC-8Co showing translucent layer of the 316 SS pin over the WC particles.

Because of its high surface hardness and high CoF value, one would expect that the pin sliding against the WC-12Co alloy would wear out more and leave more of its worn-out debris around the alloy's wear track, however, it was the pin sliding against WC-8Co disc (followed by WC-6Co) that exhibited a high volume of the worn-out pin on its wear track. A conceivable reason for the high volume of worn-out metal deposited across the wear track of the WC-8Co alloy could be due to the bigger holes and depressions left behind by the coarse WC particles after being pull-out from the binder. The sharp edges of the depressions then acted as gouging sites and the holes were where the debris from the pin filled and piled into, Figure 5.6. The surface of the WC-12Co disc was densely packed with small WC particles, and even though the alloy experienced grain pull-out, the holes and depressions left behind were smaller and less deep. This provided a smoother track for the pin to slide on without coming across severely damaging ridges.

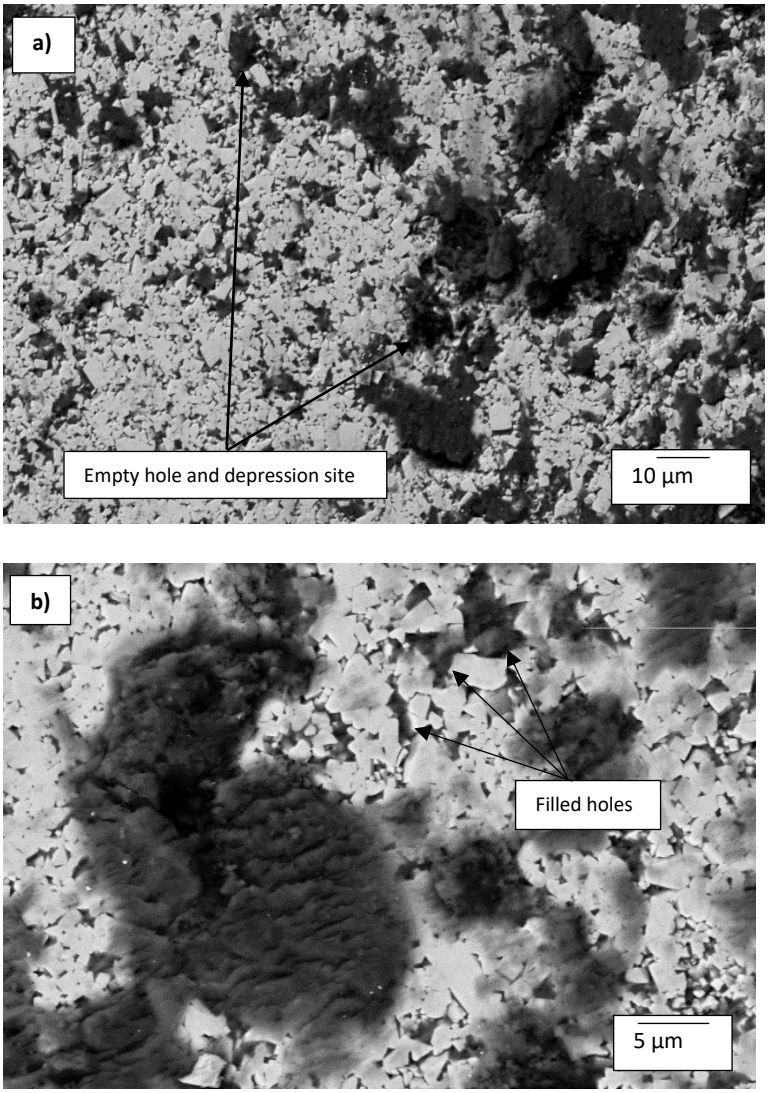

Figure 5.6: SEM-BSD micrograph of WC-8Co after pin-on-disc: (a) empty holes and depression where the WC particles were removed and (b) holes filled by the gouged off pins.

The surfaces of HCWCI-1 and HCWCI-3 alloys exhibited a more pronounced appearance of the "reptile skin" (ripples) than HCWCI-2 after undergoing the pin-on-disc wear test. The ripples and ridges seen occurring on the three alloys show that the matrix was extruded and displaced under an externally applied normal load. The primary carbides experienced the least damage and deformation when compared to the damage seen with the matrix. This was because the matrix smeared across the carbides, creating a layer that covered most of the hard carbides during the sliding process. The intensity of the extrusion and smearing of the matrix seen in HCWCI-2 could have been as a result of the pressure transferred by the sliding loaded pin. This subsequently resulted to the wearing down of asperities of the pins by the

hard carbides which then further caused the displacement of the matrix and the removal of thin layers of the large primary carbides.

Compositional analysis of the as received HCWCI alloys revealed that only HCWCI-1 and HCWCI-2 had Ni in its system. EDS analysis was conducted after the alloys have underwent sliding wear and the analysis revealed traces of Ni in all the alloys. This shows that there was transference of material from the 316 SS pin onto the worn surfaces of the HCWCI alloys through either atomic bonding, cold welding, or heated-friction adherence. HCWCI-2 exhibited a larger volume of the adhered pin on its surface than the other two alloys, showing that its surface was more damaging to the 316 SS pin which can be further attributed to its frequently occurring combination of large, small and eutectic primary carbides.

Microploughing and microcutting were recognised by the parallel continuous grooves observed on the surfaces of the alloys, more especially on the HCWCI-1 alloy. HCWCI-2 and HCWCI-3 alloys showed only feint grooves around their wear tracks. This is because the two alloys consisted of a larger surface area of extruded Cr-rich primary carbides which made it difficult for the pins to cause deep and prominent grooves.

EDS further showed the presence of oxygen on the surface of all three alloys. The presence of oxygen could mean that the alloys also experienced oxidative wear during the sliding wear process. Oxidative wear occurs when oxide films such as Fe_3O_4 are generated when two metallic counterparts slide against each other. The oxide films prevent metallic bonding between the two components by creating a mask over one or both metals, resulting in lower wear rates and fine oxygen-containing wear debris (Wei et al., 2011). The surface of HCWCI-2 contained the highest amount of oxygen as shown by the EDS analysis. There could be a relationship between the extent of the high wear volume loss seen with the pin sliding against the surface of HCWCI-2, the high oxygen found on the surface of the HCWCI-2 disc, the Cr content present in the HCWCI-2, and the morphology of the occurring carbides.

With Hadfield steel, the wear deformation caused by the pins sliding against the surface were more severe because the bulk hardness of the 316 SS pin was about 500 Vickers unit more than the hardness of the Hadfield steel. The worn surfaces characterised by the parallel continuous grooves caused by microploughing and microcutting were much more frequent and prominent. The worn off debris from the pins were more damaging to the Hadfield steel

because of the low hardness exhibited by the surface of the steel. The steel also showed more damages to its surface than the other investigated metals because it was the only metal that did not contain any hard reinforcing particles.

The Hadfield steel also experienced delamination and galling (adhesive wear) of the austenitic matrix. Delamination wear and galling are generally caused by the frictional force generated by the pin continuously sliding over the surface thus heating and softening it in the process. Because the pins were harder than the surface of the disc, the softened regions got welded onto the pins hence causing the spalling of the Hadfield steel (Tikotkar, 2012). The generation of frictional heating during sliding wear also resulted in regions on the surface of the disc where the precipitated carbides contained high compositions of oxygen. Tikotkar (2012) reported that the generation of oxide films during the sliding wear was common with Hadfield steels. These films formed over the precipitated carbides and minimised the interaction between the pins and the discs, thus lowering the frictional force and ultimately, the rate of wear. However, the effect of the oxidative film on the wear rate was not quantified since the surfaces of the disc was not examined periodically during the 500m sliding distance.

The final wear mechanism seen occurring on the Hadfield steel during sliding wear was the extrusion of the matrix (Figure 5.7). The extruded matrix can be seen piling around the hard precipitated carbides. The austenite matrix was then removed from around the carbides, resulting in excessive wear volume loss and a high wear rate.

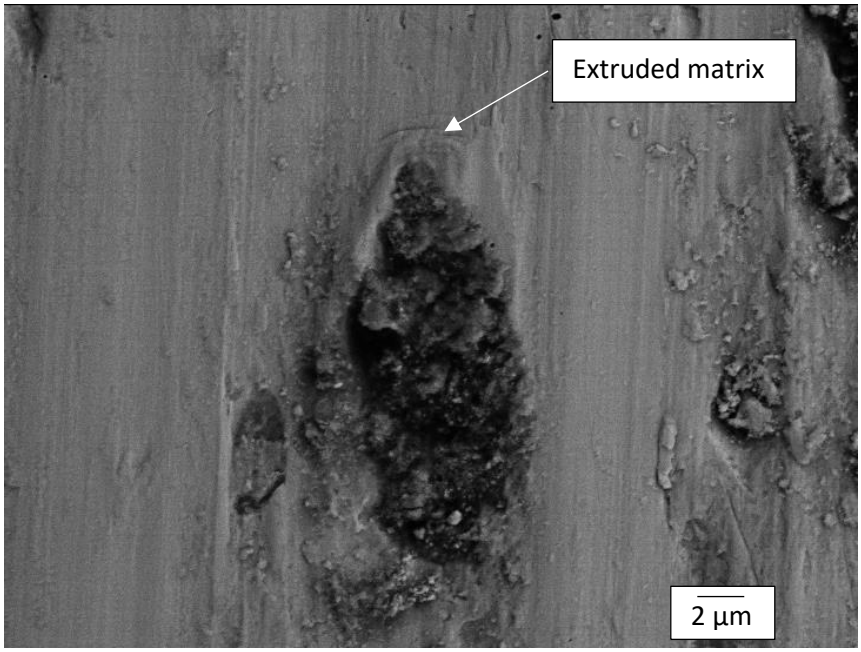

Figure 5.7: SEM-BSD micrograph of the investigated Hadfield steel showing extruded matrix pilled around a precipitated carbide inclusion.

5.2 Electrochemical Behaviour of the Investigated Materials

The corrosion behaviour of the WC-Co cemented carbides, HCWCI alloys and the Hadfield steel was investigated by conducting electrochemical polarisation tests in 1M sulfuric acid. It was observed that all the investigated materials (except HCWCI-2) showed an active-psuedopassive transition behaviour during electrochemical tests. Figure 4.53 shows the potentiodynamic polarisation curves of the samples indicating the psuedopassivity region where maximum current densities were reached which were then followed by a slight decrease. This feature was observed and outlined by Human and Exner (1996); Esmailzadeh et al. (2018); Marimuthu and Kannoorpatti (2016). Moreover, from the obtained results, it is clear that the WC-Co alloys as a group behave similarly, and have similar E_{corr} and i_{corr} values, and therefore corrosion rates. In the same fashion the HCWCI behaved similarly and displayed closely related open circuit corrosion potentials and corrosion currents. There was hardly a difference between the corrosion current densities of all these alloys and they all show closely related corrosion rates.

The comparative behaviour of the WC-Co alloys in 1M H_2SO_4 was shown in Table 4.15 and Figures 4.54 and 4.55. WC-12Co showed better resistance to corrosion compared to the other two alloys. This conclusion was characterised by the low current density and corrosion rate that WC-12Co exhibited after undergoing electrochemical tests. EDS analysis also showed the preferential corrosion of the cobalt binder. This was characterised by the decrease in the cobalt content and an increase amount of WC, sulphur, and oxygen on the corrosion products formed during the electrochemical process. This behaviour was also observed by the work conducted by Thanjekwayo (2009) on the electrochemical work performed on WC-Co alloys with varying ruthenium contents.

The SEM micrographs of the alloys that were taken after the alloys were exposed to the corrosive environment revealed that WC-6Co and WC-8Co experienced severe corrosion attack on their surfaces. The preferential manner in which the acidic medium selectively dissolved into the grain boundaries around the WC particles lead to the same conclusion reported by (Human and Exner, 1997; Sutthiruangwong and Mori, 2003; Pugsley and Sockel, 2004) that the Co binder phase was attacked more vigorously compared to the WC grains. WC-12Co's good resistance to corrosion can thus be attributed to the manner in which the WC particles were more exposed to the corrosive medium than the Co binder, hence behaving as a shield against the dissolution of the Co binder. So instead of the acidic medium attacking the alloy, it created a translucent corrosion product layer that covered the surface of the alloy (Figure 5.8), which could or could have not assisted as a protective shield against further corrosive attack.

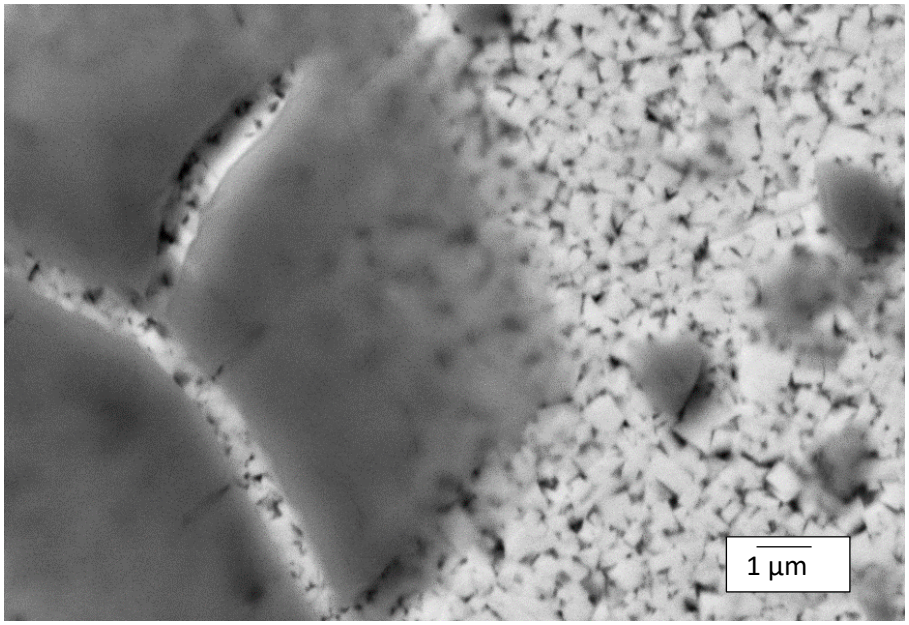

Figure 5.8: SEM-BSD micrograph of WC-12Co alloy showing cracked translucent layer of corrosion product.

The levels of chromium and other alloying elements can significantly influence the corrosion behaviour of HCWCI alloys (Marimuthu & Kannoorpatti, 2016; Mampuru et al., 2016; Ngqase & Pan, 2020). However, only the effect of chromium, carbon and the morphology of the microstructure (matrix and the second phase) of the alloys and the effect they had on the resistance of corrosion of HCWCI alloys will be discussed.

The comparative results obtained from the polarisation tests carried out on the HCWCI alloys are summarised in Table 4.15. HCWCI-2 had the lowest value for corrosion current density and therefore, the lowest corrosion rate. This behaviour can be attributed to the alloy's chromium and carbon content, and the morphology of its occurring primary carbides. HCWCI-2 exhibited a better response to corrosion than HCWCI-1 because it contained a higher content of chromium (Tian & Taylor, 2011). Moreover, since carbon is the main carbide forming alloying element in cast irons, less of it means there was excess chromium retained in the matrix, thus improving the overall resistance of the alloy. The same observation was recorded in the work conducted by (Zumelzu et al., 2004; Tanga et al., 2009; El-Alziz et al., 2015).

HCWCI-3 contained the highest chromium content of the three alloys, and it was thus expected that it would exhibit the best resistance to corrosion, but the opposite was observed. The corrosion rate of the alloy decreased with an increase in chromium. However, an increase in carbon was also observed, thus affecting the Cr/C ratio and reversing the effects of chromium. This ultimately had an adverse influence on the resistance of the alloy.

Figures 4.56(a-b) and Figure 4.56 (e-f) shows that the alloys that contained high volume fractions of primary eutectic carbides, HCWCI-1 and HCWCI-3, suffered severely from localised corrosion. Poolthong et al. (2004) and El-Aziz (2015) observed the same trends. They recorded that the matrix phase close to the eutectic carbides was deprived from chromium causing the extensive corrosive attack seen with the two alloys. The black lines seen encapsulating the primary Cr-rich carbides in HCWCI-2 and HCWCI-3 are zones where the most depletion of Cr was observed, showing that corrosion attack in 1M H_2SO_4 was initiated around the carbides.

The hard primary carbides occurring in HCWCI-2 and HCWCI-3 were observed to be inert to corrosion attack and the eutectic primary carbides seen in HCWCI-1 exhibited negligible damage during the electrochemical polarisation tests. Indicating that the corrosion behaviour of white cast irons was strongly depended on the composition and morphology of their matrix.

Table 4.15, which is the summary of the electrochemical parameters of the investigated materials, shows that the Hadfield steel exhibited the poorest resistance to corrosion in 1M H_2SO_4. The steel displayed the highest i_{corr} and therefore, the highest corrosion rate. However, Hadfield steel showed a similar E_{Corr} value when compared with the E_{Corr} values exhibited by the HCWCI alloys. This shows that the alloys (HCWCI and the Hadfield steel) experienced the same tendency to corrode. This was expected since both materials consisted mainly of austenite in their structures.

The regions where the surface exhibited the hills-and-valley morphology was in fact tiny craters and pores where the surface suffered severe chemical attack. Other researchers that observed the same surface structure reported that this was as a result of hydrogen penetrating deeper through the cracks of the passive layer (corrosion product), bringing about rapid deterioration of the surface (Ozgowicz et al, 2012;). The hills-and-valley

morphology is seen occurring predominately on the austenitic phase. This process is known as the hydrogen polarisation mechanism and it occurs when the hydrogen ions in electrolytic form are reduced in cathodic areas from the metal by electrons to gaseous hydrogen, resulting in a continuous flow of electrons from the surface of the metal (Curioni & Scenini, 2015). This corrosion process caused by hydrogen impact thereby causes the formation of tiny craters that are close together, separated by a network of strips of uncorroded metal that look like laths (Figure 4.58 (d)).

It was reported by other researchers that the severely attacked surfaces were as a result of the protective passive layer being removed during the polarisation process, causing more damage to the exposed and unprotective surface (Garcia et al, 2010; Grajcar et al., 2010; Ozgowicz et al., 2012).

The dark lines seen around the grain boundaries, metal-carbide inclusions and the non-metallic inclusion such as sulphide inclusions are regions that Garcia et al. (2010) reported were caused by hydrogen penetrating deeper into the surface of the steel. Abreu et al. (2007) adds that areas such as grain boundaries, twin boundaries and non-metallic inclusions are regions where the accumulation of hydrogen is mostly seen during corrosion.

5.3 Overview of the Performance of the Investigated Metals

The dominant and most damaging wear mechanism occurring in chutes and skips, as detailed in Chapter 1, is abrasive wear. Therefore, the materials to be used as protective lining plates or similar surface engineering methods should adequately counteract the damaging effects of abrasive wear. The effects of abrasion wear were simulated using the rubber wheel abrasion wear tribometer at a laboratory scale. Chutes and skips do not only experience abrasive wear during operation thus to further understand the wear mechanisms occurring on the investigated metals, other forms of mechanical wear and their mechanisms were also investigated, including electrochemical corrosion tests. An overview of the overall performance of the investigated metals is outlined in this section. The costs, although of high importance when selecting materials to be used as protective liners for bulk material handling equipment in the mining industry, will not be discussed in detail.

3.2.1 Rubber wheel abrasion wear

The WC-Co alloys displayed the best resistance against low stress abrasive wear. The alloys showed no microploughing and microcutting on their surfaces during the abrasion process. The alloys exhibited no major wear deformation during abrasion wear apart from regions where WC particles were pulled-out and at regions where the cobalt binder was extruded. WC-12Co exhibited the best overall resistance against slurry abrasive wear (Figure 5.9). It also exhibited the best overall resistance to surface deformation. In the case of resistance against low stress abrasion, a WC-Co alloy with refined WC particles bound by an adequate amount of Co was favourable. The least favourable was the Hadfield steel. HCWCI-2 displayed a moderate resistance against abrasion wear but performed the best in comparison to the other two HCWCI alloys.

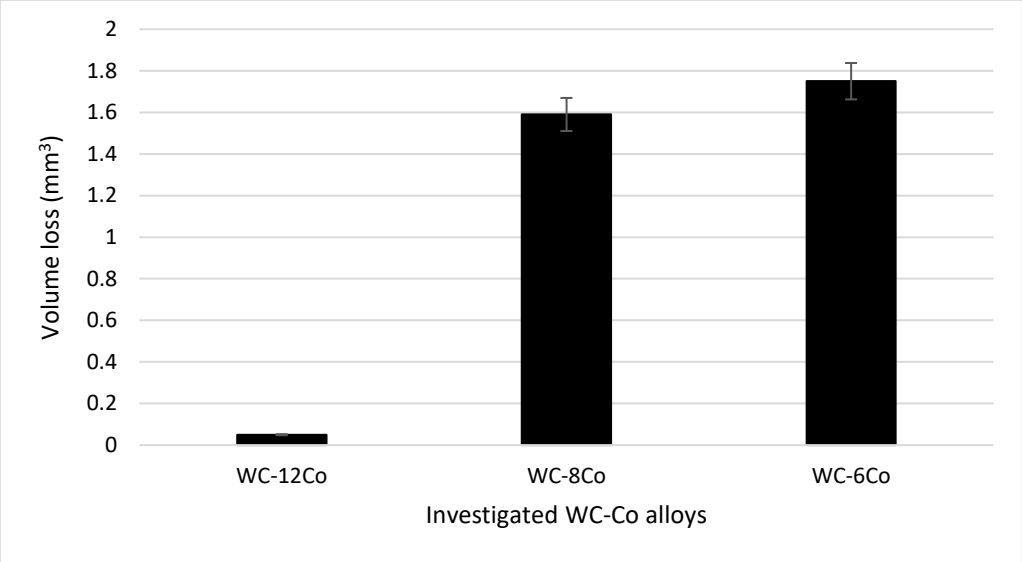

Figure 5.9: Volumetric wear loss of the investigated WC-Co alloys after slurry abrasion wear.

5.3.2 Sliding wear

The 316 SS pins were not hard enough to penetrate the surfaces of the WC-Co alloys. The wear tracks on the discs of the alloys were just made out of smudges and chunks of the worn-

out pins. Henceforth, the quantifying criterion for the performance of the investigated metals will be by observing the damages exhibited by the discs as well as the manner in which the pins became completely worn.

From visual inspections using high magnification SEM micrographs, the WC-12Co alloy showed the best resistance to both two-body and three-body abrasion wear generated by the pin and wear debris sliding against it. The SEM micrographs also reveal that the WC-12Co alloy exhibited very minimal WC particles removal during the sliding process. Because the particles were very small and densely packed, there was also minimal Co extrusion and pull-out. The pin sliding against the WC-12Co disc showed the lowest wear rate in comparison to the other WC-Co alloy, proving that the surface was smooth and not severely damaged enough to cause extreme material gouging of the pin.

The HCWCI-2 disc exhibited the least damage to its surface in comparison to the other two HCWCI alloys. The pin sliding against the surface of the disc exhibited the highest wear rate, proving that the reinforcing Cr-rich carbides were very hard and effective at resisting damage by the abrading pin. Hadfield steel exhibited the worst resistance against sliding wear. It also exhibited the most severe wear deformation in the form of microploughing and microcutting. The pin sliding against the Hadfield steel disc showed the lowest wear rate, proving that the surface of the Hadfield steel was very soft compared to that of the pin, resulting in a large volume of the steel being removed.

5.3.3 Solid particle erosion wear

Solid particle erosion was carried out on WC-Co alloys, HCWCI alloys and Hadfield steel. The alloys displayed different responses against the impacting forces of the erodent as they were jetted onto the target materials. The different wear mechanisms and volumetric wear losses were due to the varying microstructures and morphologies that the metals exhibited. The WC-Co alloys displayed the poorest overall resistance against wear as a collective. The behaviour and performances of the alloys, therefore the selection thereof, were quantified based on their volumetric wear loss and the damages the metals incurred during the erosive wear process.

The chemical make-up and microstructure of the HCWCI alloys contributed to their excellent displayed resistance against solid particle erosion. HCWCI-1 and HCWCI-3 displayed steady state erosion rates that were a magnitude smaller than all the other investigated materials. The morphological damages observed with the HCWCI alloys- especially HCWCI-1, were minimal when compared to the damages exhibited by the WC-Co alloys and the Hadfield steel. HCWCI-2 displayed the poorest resistance of the HCWCI alloys which was, as previously mentioned, due to its large and bulky carbide grains.

WC-12Co and Hadfield steel exhibited the highest volumetric wear losses. WC-12Co mainly displayed brittle wear mechanisms whereas the steel portrayed ductile erosive wear mechanisms. Therefore, with regards to the performance of the investigated metals against solid particle erosion, HCWCI-1 is rendered a pragmatic solution against impact force given that the alloy did not exhibit severe brittle wear response in a form of the removal of large fragments during the erosion process nor did it experience excessive material loss by means of ductile cutting just as observed with the Hadfield steel.

5.3.4 Electrochemical corrosion

Electrochemical polarization tests were used to evaluate the corrosion behaviour of the investigated materials in 1M H_2SO_4. Their response to corrosion was used to evaluate their performance under an acidic environment. Just like mechanical wear, the corrosive property of a material is a behavioural parameter that is often tested at a laboratory scale to simulate the operational conditions that the materials will be exposed to.

The investigated metals were exposed to an acidic electrolyte because most chutes and skips are exposed to acid-ironstone/acidic underground water in the mining and mineral processing industry. Corrosion wear is just as severe of a damage on ore transportation structures as mechanical wear is which is why it is always wise to also rank the corrosive response of a material when selecting a protective liner for chutes and skips.

Of the WC-Co alloys, it was WC-12Co sample that showed the best resistance to corrosion. The surface of the WC-12Co succumbed little to no chemical damage after electrochemical polarization tests. WC-6Co and WC-8Co experienced similar corrosion rates and therefore

they exhibited the same degree of damage on their surfaces. The grain size and morphology of the WC particles of the WC-12Co alloy contributed the most to its resistance against corrosion in an acidic environment.

HCWCI-2 exhibited the best overall performance against corrosion. The alloy displayed negligible damage when exposed to an acidic environment. The chromium content and the morphology of the Cr-rich carbides attributed to its performance against corrosion. HCWCI-1 experienced the second poorest after Hadfield steel and HCWCI-3 displayed adequate resistance against the corrosive environment.

Hadfield steel responded the worst during electrochemical tests and therefore displayed the harshest damage to its corroded surface.

The WC-Co alloys showed varied tribological and corrosive responses when compared to the HCWCI alloys and the Hadfield steel. A visual summary of the performances of the investigated materials for all the conducted tests are tabulated in Table 5.1. The materials are ranked from 1 to 7. A value of 7 indicates that hat particular material performed the least of the 7 materials investigated.

Table 5.1: Summary of the ranking of the investigated materials for all tests.

	WC-6Co	WC-8Co	WC-12Co	HCWCI-1	HCWCI-2	HCWCI-3	Hadfield steel
Slurry Abrasion	3	2	1	6	4	5	7
Steady state erosion	4	3	6	1	5	2	7
Pin-on-disc	5	4	6	2	1	3	7
Electrochemical corrosion	3	4	2	6	1	5	7

Green = excellent

Yellow = acceptable

Red = unacceptable

5.4 Material Selection and Hypotheses Validation

Part of the formulated hypothesis states that the WC-Co cemented carbide alloys would exhibit the highest bulk hardness compared to the other investigated materials and would therefore exhibit the best resistance to wear since the response to wear is inversely proportional to the hardness of materials. The other part of the hypothesis states that the WC-Co alloys would be prone to sudden mechanical fracture due to rapid crack propagation as a result of its brittle nature. WC-12Co exhibited the highest bulk hardness value and performed excellent against the conducted wear and electrochemical corrosion tests with the exception being its poor performance against solid particle erosion wear.

The brittle behaviour exhibited by WC-12Co during the erosion process was expected since the very nature of WC-Co cemented carbides is known to be hard and brittle and relatively weak against the sudden fracturing forces like those exhibited by the impacting particles. However, its refined structure and binder content were advantageous against abrasive and sliding wear which are the two predominantly occurring wear mechanisms on chutes and skips in the mining and mineral processing industry. Additionally, WC-12Co performed substantially well against corrosion in an acidic environment, making it a viable solution for the lining of chutes and skips against wear and corrosion damage.

Although the WC-Co alloys performed exceptionally well against most of the wear and electrochemical corrosion tests performed, their brittle nature as well as their weight may be problem in applications where impact forces are involved. Hadfield steel would also perform poorly as the degree of impact experienced by chutes and skips may not be sufficient enough to activate its exceptional work-hardening abilities. Therefore, HCWCI alloys would perform best for this application.

Chapter 6

6. Conclusions

In this study, a systematic investigation of the wear properties of three grades of WC-Co cemented carbides, three grades of HCWCI alloys and one grade of Hadfield steel was conducted in order to select the most suitable protective wear lining material for chutes and skips. The main objective was to carry out different wear tests and determine the wear mechanisms of the investigated materials at microscopic and macroscopic scale. Electrochemical polarisation tests were also conducted on the materials to rank their corrosive performance. The materials' response to mechanical and corrosion wear were used as the main criterion for the selection of the best material to be used as a protective liner.

Dry sand and slurry rubber wheel abrasion wear tests were conducted to simulate and investigate the abrasive wear mechanisms and the main findings are:

- The WC-Co cemented carbides showed the best resistance to the rubber wheel abrasion tests.
- The WC-Co alloy with the finest grain structure 0.4-2.3 μm and the highest binder content (12 wt%) exhibited the lowest abrasion wear rate.
- HCWCI-1, which had the lowest chromium content and the highest volume fraction of eutectic primary carbides, showed the least resistance to the rubber wheel abrasion test. HCWCI-2 exhibited the best resistance to the rubber wheel abrasion test.
- The Hadfield steel displayed the poorest resistance to abrasion wear.
- The main wear mechanisms encountered by the HCWCI alloys and Hadfield steel were microploughing and microcutting. Microploughing and microcutting were not

observed on the WC-Co alloys that were investigated in this study probably due to their high hardness.

The main findings of the pin-on-disc sliding wear are:

- The WC-12Co alloy experienced the least damages to its surface. It exhibited little extrusion of the Co binder during the sliding wear process.
- Of the HCWCI alloys, it was the frequent occurrence of the large and bulky Cr-rich primary carbides that attributed to HCWCI-2's high resistance to abrasion wear.
- Hadfield steel succumbed to the worst damage to its surface and therefore, exhibited the highest abrasion wear rate.
- The main mechanism observed occurring on the surfaces of the metals was the adhesion of the pin material onto the discs and conversely, the transference of the adhered material from the surface of the discs to the pins.

The main findings of the solid particle erosion wear tests are:

- The high chromium white cast iron alloys that contained the highest volume fraction of eutectic primary carbides (HCWCI-1 followed by HCWCI-3) exhibited the highest resistance to solid particle erosion.
- The WC-12Co structure was too brittle to withstand the impact force by the jetted Al_2O_3 particles. Therefore, it responded poorly when compared to the other investigated materials.
- Hadfield steel exhibited the largest volumetric wear loss during the wearing process and therefore, showed the worst resistance to erosion wear.
- The main erosion wear mechanism seen with the brittle phases (WC particles and Cr-rich primary carbides) was microfragmentation and grain fallout. The main erosion wear mechanisms seen with the softer phases (Co binder and the austenitic matrix) were plastic deformation ridges, extrusion and ductile cutting.

The main findings obtained from the potentiodynamic polarisation tests are:

- The high Cr/C ratio of HCWCI-2 contributed to the alloy's excellent resistance to corrosive attack.
- WC-12Co performed fairly good against corrosion. It performed second best after HCWCI-2. This characteristic can be attributed to its densely packed WC particles which shielded against the aggressive dissolution of the Co binder.
- Hadfield steel exhibited the worst resistance to the corrosive attack in H_2SO_4.

The best wear and corrosion resisting material for the application would be WC-Co, however, its high density means it is very heavy for the area it is required to cover. This would require expensive surface engineering applications and manufacturing expenses. The Hadfield steel would suffer severe corrosion and mechanical deterioration; therefore, this means the best material of those investigated in this work for the application of liners would be the HCWCI.

7. Recommendations for Further work

It was observed that the stainless steel ball pins used in this study to abrade against the alloys during the pin-on disc tests were not hard enough produce clean-cut results. This is because the pins wore out more instead of the discs. It is therefore recommended that ceramic ball pins be used rather.

An alkaline solution such as NaOH can be added to the study to rank the alkalinity of the materials during the electrochemical corrosion tests.

Tribocorrosion tests would have also been a great ranking technique to analyse the investigated materials of their responses against corrosive wear.

An extensive analysis on the effect of alloying elements and what contributions they have on the alloys' responses against the tests carried out.

REFERENCES

Thanjekwayo, N. P. (2009). *The influence of Ru additions on the corrosion.* Degree of Masters, University of the Witwatersrand, Engineering and the Built Environment, Johannesburg. Retrieved November 2019, from http://wiredspace.wits.ac.za/handle/10539/8625

Abdelbary, A. (2014). 2 - Sliding mechanics of polymers. *Wear of Polymers and composites, 2014*, 37-66.

Abreu , H., Carvalho, S., Neto, P., Santos, R., Freire, V., Silva, P., & Tavares, S. (2007). Deformation induced martensite in an AISI 301LN stainless steel: Characterization and influence on pitting corrosion resistance. *Materials Research, 10*(2007), 359-366.

Adamiak, M. (2012). *Abrasion resistance of materials* (Vol. 1). Croatia: InTech. Retrieved June 2021, from http://www.issp.ac.ru/ebooks/books/open/Abrasion_Resistance_of_Materials.pdf

Adler, T. A., James, C. R., Tylczak, J. H., & Hawk, J. A. (2001). *EROSIVE WEAR OF SELECTED MATERIALS FOR FOSSIL ENERGY APPLICATIONS.* Albany Research Center, Department of energy, Albany . Retrieved from https://core.ac.uk/download/pdf/71314204.pdf

Ahmed, S., Thakare, S., Shrivastava, R., Sharma, S., & Sapate, S. G. (2017). A review on slurry abrasion of hard surface steels. *Materials today: Proceedings, 5*(2), 3524-3532. Retrieved June 2019, from https://www.sciencedirect.com/science/article/pii/S2214785317328730

Al-Bukhaiti, M., Ahmed, S., Badran, F., & Emara, K. (2006). Effect of impingement angle on slurry erosion behaviour and mechanisms of 1017 steel and high-chromium white cast iron. *Wear, 262*(2007), 1187-1198. Retrieved July 2020, from https://www.researchgate.net/publication/222086653_Effect_of_impingement_angle_on_slurry_erosion_behaviour_and_mechanisms_of_1017_steel_and_high-chromium_white_cast_iron

Allen, C. (1981). The selection of abrasion-corrosion-resistant materials for gold-mining equipment. *Journal of the South African Institution of Mining and Metallurgy*. Retrieved December 2019, from https://www.saimm.co.za/Journal/v081n10p289.pdf

Alqallaf, J., Ali, N., Teixeira, J., & Addali, A. (2020). Solid Particle Erosion Behaviour and Protective Coatings for Gas Turbine Compressor Blades-A Review. *MDPI: Processes, 8*(984), 1-42.

Antonov, M., Yung, D. L., Goljandin, D., Mikli, V., & Hussainova, I. (2017). Effect of erodent particle impact energy on wear of cemented carbides. *Wear, 2017*, 507-515. Retrieved March 2021, from https://www.researchgate.net/profile/Der-Liang-Yung/publication/317336690_Effect_of_erodent_particle_impact_energy_on_wear_of_cemented_carbides/links/59d133cbaca2721f43674547/Effect-of-erodent-particle-impact-energy-on-wear-of-cemented-carbides.pdf

Aptekar, S., & Kosel, T. H. (1985). Erosion of white cast irons and stellite. *Materials Science*. Retrieved from https://www.semanticscholar.org/paper/Erosion-of-white-cast-irons-and-stellite-Aptekar-Kosel/51eba3d48aca175918e7bb24bf418df986bc969a

ASTM G105-20. (2020). *tandard Test Method for Conducting Wet Sand/Rubber Wheel Abrasion Tests.* West Conshohocken, PA.

ASTM G59-97. (2014). *tandard Test Method for Conducting Potentiodynamic Polarization Resistance Measurements.* West Conshohocken, PA.

ASTM International. (2015). *Standard Test Method for Wear Testing with a Pin-on-Disk Apparatus (ASTM G99).* West Conshohocken, PA, USA. Retrieved August 2019, from https://standards.globalspec.com/std/10072001/ASTM%20G99

ASTM International. (2016). *Standard Test Method for Measuring Abrasion Using the Dry Sand/Rubber Wheel Apparatus (G65-16e1).* West Conshohocken, PA, USA. Retrieved August 2019, from https://www.astm.org/Standards/G65.htm

ASTM International. (2018). *Standard Test Method for Conducting Erosion Tests by Solid Particle Impingement Using Gas Jets(ASTM G76 - 18).* West Conshohocken, PA, USA. Retrieved August 2019, from https://www.astm.org/Standards/G76

Atamert, S., & Bhadeshia, H. (1990). Microstructure and stability of Fe-Cr-C hardfacing alloys. *Materials Science and Engineering A, 130*, 101-111.

Atapek, H., & Polat, S. (2013). A study of wear of high-chromium cast iron under dry friction. *Metal Science and Heat Treatment, 55*(3), 14-16. Retrieved August 2020, from https://www.researchgate.net/publication/257626858_A_study_of_wear_of_high-chromium_cast_iron_under_dry_friction

Balasubramanian, V., Varahamoorthy, R., Ramachandran, C. S., & Babu, S. (2008). Abrasive slurry wear behavior of stainless steel surface produced by plasma transferred arc hardfacing process. *Surface and coating technology, 202*(16), 3903-3912. Retrieved June 2019, from https://www.academia.edu/31437901/Abrasive_slurry_wear_behavior_of_stainless_steel_surface_produced_by_plasma_transferred_arc_hardfacing_process

Ball, A., & Bohm, H. (n.d.). The design and performance of steels in an abrasive-corrosive mining environment. *IMechE, C189/87*, 595-602.

Ball, A., & Ward, J. J. (n.d.). An approach to material selection for corrosive abrasive wear by systematic in-situ and laboratory testing procedures. *Tribology International, 18*(6), 347-351.

Barao, V., Sukotjo, C., & Mathew, M. (2019). Fundamentals of Linking Tribology and Corrosion (Tribocorrosion) for Medical Applications: Bio-tribocorrosion. Retrieved May 2019, from https://www.researchgate.net/publication/286006751_Fundamentals_of_Linking_Tribology_and_Corrosion_Tribocorrosion_for_Medical_Applications_Bio-tribocorrosion

Beimeng, Q., Beijia, W., Chenguang, W., & Yixing, Y. (2013). Electrochemical behavior of cast iron in the presence of bacteria in water distribution systems. *International Journal of Electrochemical Science, 8*, 1813-1821. Retrieved February 2021, from https://citeseerx.ist.psu.edu/viewdoc/download?doi=10.1.1.655.1296&rep=rep1&type=pdf

Bhattacharyya, S. (1966). A friction and wear study of hadfield manganese steel. *Wear, 9*(6), 451-461. Retrieved January 2021, from https://www.sciencedirect.com/science/article/abs/pii/0043164866901360

Bhushan, B. (1999). *Principles and Applications of Tribology* (Vols. Mechanical Engineering - Design). Wiley.

Bingley, M., & Schnee, S. (2005). A study of the mechanisms of abrasive wear for ductile metals under wet and dry three-body condition. *Wear, 258*, 50-61. Retrieved June 2019, from https://www.researchgate.net/publication/240396285_A_study_of_the_mechanisms_of_abrasive_wear_for_ductile_metals_under_wet_and_dry_three-body_condition

Bitter, J. G. (1963). A study of erosion phenomena part I. *Wear, 6*(1), 5-21. Retrieved January 2021, from https://www.sciencedirect.com/science/article/pii/0043164863900036

Blau, P. (2005). On the nature of running-in. *Tribology International, 38*(11-12). Retrieved June 2020, from https://www.sciencedirect.com/science/article/abs/pii/S0301679X05001994

Bowditch, S. (2017). *Addressing wear and abrasion of metals in the mining industry.* Retrieved May 2019, from Chesterton: https://chestertondocs.chesterton.com/Arc/EN24641_MiningCampaign_Ebook-FINAL.pdf

Bricín, D., Špirit , Z., & Kříž, A. (2018). Metallographic analysis of the suitability of a WC-Co powder blend for selective laser melting technology. *Materials Science Forum, 919*, pp. 3-9. Retrieved December 2020, from https://www.scientific.net/MSF.919.3

Broitman, E. (2017). Indentation Hardness Measurements at Macro-, Micro-, and Nanoscale: A Critical Overview. *Tribology Letters, 23*(2017). Retrieved January 2021, from https://link.springer.com/article/10.1007/s11249-016-0805-5

Brookes, K. (1975). Hardmetal and other Hard Materials. *International Carbide Data,* Hertfordshire, Uk.

Brooks, C. R. (1996). *Principles of the Heat Treatment of Plain Carbon and Low Alloy Steels.* ASM International.

Byrd, S. (2016). Hardness-Testing Machine Shopping Tips. *Tinius Olsen*. Retrieved December 2019, from https://www.linkedin.com/pulse/hardness-testing-machine-shopping-tips-shawn-byrd

Celis, P. (2009). Basics of tribocorrosion. *KULeuven*. Retrieved December 2019, from https://www.chemeng.ntua.gr/seminars/download/Erasmus%20Athens%20Basics%20Tribocorrosion%20Sept.%202009.pdf

Çetinkaya, C. (2006). An investigation of the wear behaviours of white cast irons under different compositions. *Materials & Design, 27*(6), 437-445. Retrieved January 2021, from https://www.sciencedirect.com/science/article/abs/pii/S0261306904003267

Chen, W., Biswas, S., & Roberts, A. (2017). Abrasion wear resistance of wall lining materials in bins and chutes during iron ore mining. *International Journal of Mineral Processing, 167*. Retrieved August 2019

Chintha, A. R. (2019). Metallurgical aspects of steels designed to resist abrasion, and impact-abrasion wear. *Materials Science and Technology, 35*(10), pp. 1133-1148. doi:https://doi.org/10.1080/02670836.2019.1615669

Chotěborský, R., Hrabě, P., Müller, M., Savková, J., Jirka, M., & Navrátilová, M. (2009). Effect of abrasive particle size on abrasive wear. Retrieved September 2019, from https://www.agriculturejournals.cz/publicFiles/10581.pdf

Chowdhury, M. A., & Helali, M. (2008). The effect of amplitude of vibration on the coefficient of friction for different materials. *Tribology International, 41*(4), 307-314. Retrieved March

2021, from https://www.sciencedirect.com/science/article/abs/pii/S0301679X07001375#:~:text=From%20these%20figures%2C%20it%20is,different%20rates%20for%20different%20materials.

Chowdhury, M., & Nuruzzaman, D. (2013). Experimental investigation of friction and wear properties of different steel materials. *Tribology in Industry, 35*(1), 45-50. Retrieved January 2021, from https://www.researchgate.net/publication/288371043_Experimental_Investigation_on_Friction_and_Wear_Properties_of_Different_Steel_Materials

CorrosionPedia. (2016). *White Cast Iron.* Retrieved December 2019, from Corrosionpedia Feed of the Terms and Educational Resources for Corrosion Professionals: https://www.corrosionpedia.com/definition/5425/white-cast-iron

Cortie, M. B., McEwan, J. J., & Enright, D. P. (1996). Materials selection in the mining industry: Old and new issues. *Journal of the South African Institute of Mining and Metallurgy, 96*(4), 145-156. Retrieved June 2019, from https://www.saimm.co.za/Journal/v096n04p145.pdf

Cuffari, B. (2020). *Impact of Nanotechnology on Construction Materials.* Retrieved December 2020, from AzoNano: https://www.azonano.com/article.aspx?ArticleID=5548

Curioni, M., & Scenini, F. (2015). The Mechanism of Hydrogen Evolution During Anodic Polarization of Aluminium. *Electrochimica Acta, 180*, 712-721. Retrieved January 2021, from https://www.sciencedirect.com/science/article/pii/S0013468615303261

Czichos, H., Saito, T., & Smith, L. (2011). *Springer Handbook of Metrology and Testing.*

Da Silva, A., Schubert, W., & Lux, B. (2001). The Role of the Binder Phase in the WC-Co Sintering. *Materials Research, 4*(2). Retrieved December 2020, from https://www.scielo.br/scielo.php?script=sci_arttext&pid=S1516-14392001000200003

Dalai, R., Das, S., & Das, K. (2018). Effect of thermo-mechanical processing on the low impact abrasion and low stress sliding wear resistance of austenitic high manganese steels. *Wear*. Retrieved December 2020, from https://www.researchgate.net/publication/328279209_Effect_of_thermo-mechanical_processing_on_the_low_impact_abrasion_and_low_stress_sliding_wear_resistance_of_austenitic_high_manganese_steels

Dastur, Y. N., & Leslie, W. C. (1981). Mechanism of work hardening in Hadfield manganese steel. *Metallurgical Transactions A, 12*(5), 749-759. doi: 10.1007/BF02648339

De la Peña O'Shea , A., Ramirez de la Piscina, H., Aromi, G., Jose, L., & Fierro, G. (2009). Development of Hexagonal Closed-Packed Cobalt Nanoparticles Stable at High Temperature. *Chemistry of Chemicals, 21*(23), 5637-5643.

Doğan, O., Hawk, J., & Laird, G. (1997). Doğan, Ö. N., Hawk, J. A., & Laird, G. (1997). Solidification structure and abrasion resistance of high chromium white irons. *Metallurgical and materials transactions A, 28*(6), 1315-1328.

Domeij, B. (2017). *On the solidification of compacted and spheroidal graphite irons.* Dissertation Series No. 24, 2017 , Jönköping University, Department of Materials and Manufacturing, Jönköping. Retrieved April 2021, from https://www.diva-portal.org/smash/get/diva2:1095932/FULLTEXT01.pdf

Dugas, R., Forero-Saboya, J., & Ponrouch, A. (2019). Methods and Protocols for Reliable Electrochemical Testing in Post-Li Batteries (Na, K, Mg, and Ca). *hem. Mater., 31*(21), 8613-8628. Retrieved February 2020, from https://pubs.acs.org/doi/10.1021/acs.chemmater.9b02776

Efstathiou, C., & Sehitoglu, H. (2009). Strain Hardening and Heterogeneous Deformation During Twinning in Hadfield Steel. *Acta Materialia, 58*, 1479-1488. doi:10.1016/j.actamat.2009.10.054

El-Aziz, K., Zohdy, K., & Sallam, H. E. (2015). Wear and Corrosion Behavior of High-Cr White Cast Iron Alloys in Different Corrosive Media. *Journal of Bio- and Tribo-Corrosion , 1*(25). Retrieved August 2020, from https://link.springer.com/article/10.1007/s40735-015-0026-8#citeas

Eliaz, N. (2019). Corrosion of Metallic Biomaterials: A Review. *MDPI: Materials, 12*(3). Retrieved January 2021, from https://www.ncbi.nlm.nih.gov/pmc/articles/PMC6384782/

Elyyan, M. (2017). *Ansys*. Retrieved December 2020, from Better Particle Erosion Fluid Dynamics Modeling in Ansys Fluent 18: https://www.ansys.com/fr-fr/blog/erosion-fluid-dynamics-modeling

Engqvist, H., Botton, G., Ederyd, S., Phanuel, M., Fondelius, J., & Axên, N. (2000). Wear phenomena on WC-based face seal rings. *International Journal of Refractory Metals and Hardmaterials, 18*, 39-46.

Esmailzadeh, S., Aliofkhazraei, M., & Sarlak. (2018). Interpretation of Cyclic Potentiodynamic Polarization Test Results for Study of Corrosion Behavior of Metals: A Review. *Protection of Metals and Physical Chemistry of Surfaces , 54*(5), 976-989. Retrieved January 2021, from https://www.researchgate.net/publication/328197771_Interpretation_of_Cyclic_Potentiodynamic_Polarization_Test_Results_for_Study_of_Corrosion_Behavior_of_Metals_A_Review

Espallargas, N., Johnsen, R., Torres, C., & Muñoz, I. (2013). new experimental technique for quantifying the galvanic coupling effects on stainless steel during tribocorrosion under equilibrium conditions. *Wear, 307*(1-2), 190-197.

Exner, H. E. (1979). Physical and chemical nature of cemented carbides. *Int. Metals Rev*, 149-173.

Fabijabić , T., Ćorić, D., Musa, M., & Sakoman, M. (2017). Vickers Indentation Fracture Toughness of Near-Nano and Nanostructured WC-Co Cemented Carbides. *MDPI: Metals, 7*(4). Retrieved January 2020, from https://www.mdpi.com/2075-4701/7/4/143

Fan, Y., Huang, W., Yang, X., Shi, D., & Li, S. (2019). Mechanical properties deterioration and its relationship with microstructural variation using small coupons from serviced turbine blades. *Material Science & Engineering A, 757*(2019), 134-145. Retrieved January 2020, from https://www.researchgate.net/profile/Fan-Yongsheng-3/publication/332760951_Mechanical_properties_deterioration_and_its_relationship_with_microstructural_variation_using_small_coupons_sampled_from_serviced_turbine_blades/links/5d301d4892851cf4408d0034/Mech

Feng, C., Chen, D., Xu , M., Shen, C., Yang, L., & Jiang, J. (2020). Study of solid particle erosion Wear resistance of WC–Co Cemented carbide. *Journal of Failure Analysis and Prevention, 20*(2). Retrieved March 2021, from https://www.researchgate.net/publication/340258981_Study_of_Solid_Particle_Erosion_Wear_Resistance_of_WC-Co_Cemented_Carbide/stats

Filipovic, M., Romhanji, E., & Kamberovic, Z. (2012). Chemical Composition and Morphology of M7C3 Eutectic Carbide in High Chromium White Cast Iron Alloyed with Vanadium. *ISIJ International, 52*(12), 2200-2204.

Finnie, I. (1959). Erosion of surfaces by solid particles. *Wear, 3*(2), 87-103. Retrieved March 2021, from https://www.sciencedirect.com/science/article/pii/0043164860900557

Finnie, I. (1960). Erosion of Surfaces by Solid Particles. *Wear*. Retrieved April 2021, from http://dx.doi.org/10.1016/0043-1648(60)90055-7

Finnie, I. (1972). Some observations on the erosion of ductile metals. *Wear, 19*(1), 81-90. Retrieved March 2021, from https://www.sciencedirect.com/science/article/abs/pii/0043164872904449?via%3Dihub

Fischer, A., & Mischler, S. (2006). Tribocorrosion: fundamentals, materials and applications. *Journal of Physics: Applied Physics, 39*(15). Retrieved June https://iopscience.iop.org/article/10.1088/0022-3727/39/15/E01/meta, 2020

Frankel, G. S., & Sridhar, N. (2008). Understanding localized corrosion. *Materials Today, 11*(10), 38-44.

Frankenthal, R. P., & Sinclair, J. D. (2001). Electronic Materials and Devices, Corrosion of. In E. o. Edition). New Jersey: Elsevier. Retrieved December 2019, from https://www.sciencedirect.com/science/article/pii/B0080431526004733#!

Frayne, C. (2010). Environmental Modification for Cooling, Heating and Potable Water Systems. In *Material Science and Materials Engineering* (Vol. 4, pp. 2930-2970). Georgia: Elsevier. Retrieved December 2019, from https://www.sciencedirect.com/science/article/pii/B978044452787500161X

French, D., & Thomas, D. (1965). Hardness anisotropy and slip in WC crystals. *Transactions of the American Institute of Mining, Metallurgical and Petroleum Engineers*, 950-952.

Friedrich, K. (2015). Multifunctionality of Polymer Composites. In *Routes for achieving multifunctionality in reinforced polymers and composite structures* (Vol. 1, pp. 3-41).

Garcia, E. G., Herrera-Hernandez, H., Juarez-Garcia, J. M., Pardave, M. E., & Romo, M. A. (2010). Electrochemical and microscopy study of localised corrosion on a sensitized stainless steel AISI 304. *ESC Transactions, 29*(1), 93-102.

Gates, J. (2003). Wear Plates and Material Selection for Sliding Abrasion. *Australian Journal of Mining*.

Ge, S., Wang, Q., & Wang, J. (2017). The impact wear-resistance enhancement mechanism of medium manganese steel and its applications in mining machines. *Wear, 376-377*(Part B), 1097-1104.

Gee, M. G., Gant, A., & Hutchings, I. (2002). *Rotating Wheel Abrasive Testing: Measurement Good Practice Guide No. 55.* Institute for Manufacturing University of Cambridge, National Physical Laboratory. Retrieved January 2021, from https://eprintspublications.npl.co.uk/2543/1/mgpg55.pdf

Glaeser, W. (1992). *Materials for tribology* (Vol. 20). Amstrdam, The Netherlands: Elsevier Science. Retrieved July 2019, from https://www.sciencedirect.com/bookseries/tribology-series/vol/20/suppl/C

Glaeser, W. (1992). *Materials for Tribology* (Vol. 20). Amsterdam, The Netherlands: Elsevier Science.

Grajcar, A., Krukiewicz, W., & Kołodziej, S. (2010). Corrosion behavior of plastically deformed high-Mn austenitic steels. *Journal of achievements in materials and manufacturing engineering, 43*(1). Retrieved January https://www.researchgate.net/publication/49600799_Corrosion_behavior_of_plastically_deformed_high-Mn_austenitic_steels, 2021

Gurland, J., & Bardzil, P. (1955). Relation of strength, composition and grain size of sintered WC-Co alloys. *Transactions of the AIME 203*, 311-315.

Han, J., Li, H., & Xu, H. (2014). Microalloying effects on microstructure and mechanical properties of 18Cr–2Mo ferritic stainless steel heavy plates. *Materials & Design, 58*, 518-526. Retrieved June 2020, from https://www.sciencedirect.com/science/article/abs/pii/S0261306914001174

Hardness and Modulus of The Lamellar Microstructure in PST-TiAl Studied by Nanoindentations and AFT. (n.d.). *Acta mater, 49*(5), 901-903.

Havel, D. (2017). *Austenitic Manganese Steel: A Complete Overview.* Columbia Steel Casting Co., Inc. Retrieved February 2020, from https://www.sfsa.org/doc/2017-4.1%20Columbia%20-%20Havel.pdf

Haynes. (n.d.). *Haynes International*. (H. International, Producer, & Corrosion guide) Retrieved April 2021, from Metal-to-metalsliding wear: https://www.haynesintl.com/alloys/corrosion-guide/metal-to-metal-sliding-wear

He, X., Pearson, I., & Young, K. (2008). Self-pierce riveting for sheet materials: State of the art. *Journal of Materials Processing Technology, 199*(1-3), 27-36. Retrieved November 2019, from https://www.sciencedirect.com/science/article/abs/pii/S0924013607009946

Hernandez, S. (2014). *High Temperature Wear Processes.* Luleå University of Technology, Department of Engineering Sciences and Mathematics. Retrieved January 2020, from https://www.diva-portal.org/smash/get/diva2:989814/FULLTEXT01.pdf

Holmes, R. E. (1991). *Selection of Materials for the Lining of Chutes.* Retrieved May 2019, from CKIT: https://www.ckit.co.za/secure/conveyor/papers/bionic-research-1/j-bri1-paper09.htm

Human, A. M. (1994). *The corrosion of tungsten carbide based cemented carbides.* PhD thesis, Technical University of Darmstadt.

Human, A. M., & Exner, H. E. (1996). Electrochemical behaviour of tungsten-carbide hardmetals. *Material Science and Engineering, A209*, 180-191.

Human, A. M., & Exner, H. E. (1997). Relationship between electrochemical behaviour and in-service. *Int. J. Refract. Metals & Hard Mater, 15*, 65-71.

Hutchings, I. (1981). A model for the erosion of metals by spherical particles at normal incidence. *Wear, 70*(3), 269-281. Retrieved March 2021, from https://www.sciencedirect.com/science/article/abs/pii/0043164881903471?via%3Dihub

Hutchings, I. (2017). *Tribology 2nd Edition: Friction and Wear of Engineering Materials.* Phillip Shipway.

Hutchings, I. M. (1992). *Tribology : friction and wear of engineering materials.* London: Edward Arnold.

Hutchings, M. (1983). Introduction to the microscopy of erosion. *Journal of Microscopy, 130*(3), 331-338. Retrieved February 2020, from https://onlinelibrary.wiley.com/doi/abs/10.1111/j.1365-2818.1983.tb04553.x

Imurai, S., Thanachayanont, C., Pearce, J., & Chairuangsri, T. (2015). Microstructure And Erosion-Corrosion Behaviour Of As-Cast High Chromium White Irons Containing Molybdenum In Aqueous Sulfuric-Acid Slurry. *Archives of Metallurgy and Materials, 60*(2). Retrieved December 2019, from https://www.researchgate.net/publication/283176101_Microstructure_And_Erosion-Corrosion_Behaviour_Of_As-Cast_High_Chromium_White_Irons_Containing_Molybdenum_In_Aqueous_Sulfuric-Acid_Slurry#fullTextFileContent

Israelachvili, J., & Ruths, M. (1995). *Surface Forces and Nanorheology of Molecularly Thin Films.* Berlin: Springer Handbooks.

Jacuinde, A. B., & Rainforth, W. M. (2001). The wear behaviour of high-chromium white cast irons as a function of silicon and Mischmetal content. *Wear, 250*(1-12), 449-461. Retrieved May 2020, from https://www.sciencedirect.com/science/article/pii/S0043164801006330?via%3Dihub

Jafarzadeh, S., Chen, Z., & Bobaru, F. (2019). *Computational modeling of pitting corrosion.* Retrieved October 2020, from De Gruyter: https://www.degruyter.com/document/doi/10.1515/corrrev-2019-0049/html

Jaimes, V. (2013). *Abrasive Wear Assessment of X-70 Steel and Polyurethane.* University of Alberta, Department of Mechanical Engineering. Alberta. Retrieved January 2021, from https://citeseerx.ist.psu.edu/viewdoc/download?doi=10.1.1.851.3537&rep=rep1&type=pdf

Jia, K., Fischer, T., & Gallois, B. (1998). Microstructure, hardness and toughness of nanostructured and conventional WC-Co composites. *Nanostructured Materials, 10*(5). Retrieved February 2020, from https://www.sciencedirect.com/science/article/abs/pii/S0965977398001238

Jiang, J., Li, S., Yu, W., & Zhou, Y. (2019). Microstructural characterization and abrasive wear resistance of a high chromium white iron composite reinforced with in situ formed TiCx. *Materials Chemistry and Physics, 224*, 169-174. Retrieved November 2020, from https://www.sciencedirect.com/science/article/abs/pii/S0254058418310575

Jones, D. A. (1992). *Principles and Prevention of Corrosion* (Vol. 2nd Edition). New Jersey: Prentice Hall.

Jones, D. A. (1996). *Principles and Prevention of Corrosion* (Vol. 2). Prentice Hall.

Kamran, S., Chen, K., Patnaik, P., Yun, Y., & Han, Y. (2011). Current status of modeling erosion and erosion-corrosion for alloys and protective coatings. *2*, pp. 70-82. New York: NRC Protected A.

Kandeva-Ivanova, M., Vencl, A., & Karastoyanov, D. (2016). *Advanced tribological coatings for heavy-duty applications: Case studies.* Balgaria: Publishing House of Balgarian Academy of Sciences. Retrieved August 2019, from https://www.researchgate.net/publication/308694629_Advanced_Tribological_Coatings_For_Heavy-Duty_Applications_Case_Studies

Kang, Y., Oh, J., Lee, H., & Lee, S. (2001). Effects of carbon and chromium additions on the wear resistance and surface roughness of cast high-speed steel rolls. *Metallurgical and Materials Transactions A, 32*(10), 2515-2525. Retrieved February 2021, from https://www.researchgate.net/publication/225127187_Effects_of_carbon_and_chromium_additions_on_the_wear_resistance_and_surface_roughness_of_cast_high-speed_steel_rolls

Karantzalis, A., Lekatou, A., & Diavati, E. (2009). Effect of Destabilization Heat Treatments on the Microstructure of High-Chromium Cast Iron: A Microscopy Examination Approach. *Journal of Materials Engineering and Performance volume, 18*, 1078-1085. Retrieved Febraury 2021, from https://link.springer.com/article/10.1007/s11665-009-9353-6?shared-article-renderer

Koji, K., & Koshi, A. (2000). *Wear Mechanism: Modern Tribology Handbook* (Vol. 1). (B. Bharat, Ed.) Columbus, Ohio, USA: CRC Press.

Konadu, D. (2009). *Corrosion Behaviour of WC-VC-Co Hardmetal in Various Acidic and Chloride Containing Media.* Degree of Master of Science, University of the Witwatersrand, Engineering, Johannesburg. Retrieved December 2020, from https://core.ac.uk/download/pdf/39667595.pdf

Kosel, T. H., & Ahmed, T. (1992). Erosion of ceramic materials. *Trans Teck, 1992*, 149-94.

Laguna-Camacho, J. R., Vite-Torres, M., Gallardo-Hernández, E. A., & Vera-Cárdenas, E. E. (2012). Solid Particle Erosion on Different Metallic Materials. *Tribology in engineering*. Retrieved January 2021, from https://www.intechopen.com/books/tribology-in-engineering/solid-particle-erosion-on-different-metallic-materials

Laguna-Camacho, J., Marquina-Chávez, A., Méndez-Méndez, J., Manuel, V., & Gallardo-Hernández, E. (2013). Solid particle erosion of AISI 304, 316 and 420 stainless steels. *Wear*, 398-405. Retrieved March 2020, from https://www.researchgate.net/publication/256913770_Solid_particle_erosion_of_AISI_304_316_and_420_stainless_steels

Lai, J. P., Pan, H. J., Cui, H. R., & Xiao, C. A. (2016). Effects of Si on the microstructures and mechanical properties of high-chromium cast iron. *Journal of Materials Engineering and Performance, 25*(2016), 4617-463. Retrieved May 2020, from https://link.springer.com/article/10.1007%2Fs11665-016-2331-x#citeas

Laird, G., Gundlach, R., & Rohrig, K. (2000). Abrasion-resistant cast iron handbook. *American Foundry Society*.

Landolt, D., Mischler, S., Stemp, M., & Barril, S. (2004). Third body effects and material fluxes in tribocorrosion systems involving a sliding contact. *Wear, 256*(5), 517-524.

Lavakumar, A. (2017). Physical metallurgy of ferrous alloys. In *Concepts in Physical Metallurgy* (Vol. Chapter 8, pp. 8-45). Morgan & Claypool Publishers. Retrieved April 2021, from https://iopscience.iop.org/book/978-1-6817-4473-5/chapter/bk978-1-6817-4473-5ch8

Levy, A. V. (1986). The platelet mechanism of erosion of ductile metals. *Wear, 108*(1), 1-21. Retrieved January 2021, from https://www.sciencedirect.com/science/article/abs/pii/0043164886900852

Liu, K., Wang, F., Li, C., & Su, L. (2005). Influence of vanadium on microstructure and properties of medium-chromium white cast iron. *Iron and Steel, 40*(V1105-6), 207-211.

Lopez-Ortega, A., Arana, J. L., & Bayon, R. (2018). Tribocorrosion of Passive Materials: A Review on Test Procedures and Standards. *International Journal of Corrosion, 2018*, 24. Retrieved June 2019, from https://www.hindawi.com/journals/ijc/2018/7345346/

Lotta, S., & Hannula, J. (2015). Microstructural Comparison of Spray-Formed and Conventionally Cast 2.5C–19Cr High-Chromium White Iron. *Metallogr. Microstruct. Anal., 4*(1), 261-262.

Lu, Z., Zhou, Y., Rao, Q., & Jin, Z. (2001). An investigation of the abrasive wear behavior of ductile cast iron. *Journal of Materials Processing Technology, 116*(2-3), 176-181. Retrieved June 2020, from https://www.sciencedirect.com/science/article/abs/pii/S0924013601010135

Luyckx, S. B. (1997). The preparation and properties of hardmetals. *1997*. Johannesburg, South Africa.

Lv, H., Zhou, R., Li, L., Ni, H., Zhu, J., & Feng, T. (2018). Effect of Electric Current Pulse on Microstructure and Corrosion Resistance of Hypereutectic High Chromium Cast Iron. *Materials, 11*(11), 2220. Retrieved January 2021, from https://www.researchgate.net/publication/328836830_Effect_of_Electric_Current_Pulse_on_Microstructure_and_Corrosion_Resistance_of_Hypereutectic_High_Chromium_Cast_Iron#fullTextFileContent

Ma, R., Ju, S., Chen, H., & Shu, C. (2017). Effect of cobalt content on microstructures and wear resistance of tungsten carbide-cobalt-cemented carbides fabricated by spark plasma sintering. *IOP Conference Series: Materials Science and Engineering*, *207.* Shanghai. Retrieved January 2021, from https://iopscience.iop.org/article/10.1088/1757-899X/207/1/012019/pdf

Machio, C. N., Konadu, D. S., Potgieter, J. H., Potgieter-Vermaak, S., & Van der Merwe, J. (2012). Corrosion of WC-VC-Co hardmetal in neutral chloride containing media. *IRSN Corrosion, 2013*.

Mahlami, C. S., & Pan, X. (2014). An Overview on high manganese steel casting. *World Foundry Congress. 71.* Johannesburg: Bilbao. Retrieved June 2020, from https://ujcontent.uj.ac.za/vital/access/services/Download/uj:4731/CONTENT1?view=true

Mampuru, L. A., Maruma, M. G., & Moema, J. S. (2016). Grain refinement of 25 wt% high-chromium white cast iron by addition of vanadium. *Journal of the Southern African Institute of Mining and Metallurgy, 116*(10), 969-972. Retrieved June 2020, from http://dx.doi.org/10.17159/2411-9717/2016/v116n10a12

Marimuthu, V., & Kannoorpatti, K. (2016). corrosion behaviour of high-chromium white iron hardfacing alloys in an alkaline solution. *Journal of Bio- and Tribo-Corrosion, 26*(2016). Retrieved June 2019, from https://link.springer.com/article/10.1007/s40735-016-0056-x#citeas

Marinescu, D., Rowe, B., Ohmori, H., & Dimitrov, B. (2013). *Tribology of Abrasive Machining Processes* (2 ed.). Elsevier. Retrieved Febraury 2020, from https://www.sciencedirect.com/science/article/pii/B9781437734676010016

Masilela, S. (2018). *Assessment of the friction behaviour of selected base oils under oscillatory sliding conditions.* Master of Engineering, University of Pretoria, Chemical Engineering, Pretoria. Retrieved January 2021, from https://repository.up.ac.za/bitstream/handle/2263/67797/Masilela_Assessment_2018.pdf?sequence=1&isAllowed=y

Mathew, M., Pai, S., Pourzal, R., & Wimmer, M. (2009). Significance of Tribocorrosion in Biomedical Applications:Overview and Current Status. *Advances in Tribology, 2009*. Retrieved August 2020, from https://www.researchgate.net/publication/284674060_Tribocorrosion_Review_current_status_and_future_perspective

Meredith, B., & Milner, D. R. (1976). *Densification Mechanisms in the Tungsten Carbide-Cobalt System.* doi:https://doi.org/10.1179/pom.1976.19.1.38

Mishra, B., & Pak, J. (2006). *Corrosion in the Mining and Mineral Industry.* Retrieved November 2020, from ASM Handbooks Online: https://doi.org/10.31399/asm.hb.v13c.a0004219

Moghaddam, E. G., Varahram, N., & Davami, P. (2012). On the comparison of microstructural characteristics and mechanical propertiesof high-vanadium austenitic manganese steels with the Hadfield steel. *Materials Science and Engineering A, 532*, 260-266. Retrieved November 2020, from https://www.researchgate.net/publication/251608124_On_the_comparison_of_microstructural_characteristics_and_mechanical_properties_of_high-vanadium_austenitic_manganese_steels_with_the_Hadfield_steel#fullTextFileContent

Mohanta, N., & Acharya, S. (2015). Mechanical and Tribological Performance of Luffa cylindrica Fibre-Reinforced Epoxy Composite. *Bioresources, 10*(4). Retrieved September 2019, from https://www.researchgate.net/publication/283776740_Mechanical_and_Tribological_Performance_of_Luffa_cylindrica_Fibre-Reinforced_Epoxy_Composite

Moore, A., & Tegart, W. (1952). Relation between friction and hardness. *Proceedings of the royal society A: Mathematical, physical and engineering sciences*. Retrieved December 2020, from https://royalsocietypublishing.org/doi/abs/10.1098/rspa.1952.0234

Mori, G., Zitter, H., Lackner, A., & Schretter, M. (2001). Influencing the Corrosion Resistance of Cemented Carbides by addition of Cr2C3, TiC and TaC. *International Plansee Semina, 2*. Retrieved February 2021, from http://www.wococarbide.com/Uploads/2017-10-11/59ddade7cf665.pdf

Mulser, M., Baumann, A., Ebert, S., & Petzoldt, F. (2014). Materials of High Hardness and Wear Resistance joined to Stainless Steel by 2C-MIM. *Conference: International World Congress on Powder Metallurgy & Particulate Materials*. Retrieved November 2020, from https://www.researchgate.net/publication/303934786_Materials_of_High_Hardness_and_Wear_Resistance_joined_to_Stainless_Steel_by_2C-MIM

Munir, S., Pelletier, M., & Walsh, W. (2016). Potentiodynamic Corrosion Testing. *Journal of Visual Experiments, 2016*(115). Retrieved November 2020, from https://www.ncbi.nlm.nih.gov/pmc/articles/PMC5091994/

Nahvi, M., Shipway, P., & Mccartney, D. (2009). Particle motion and modes of wear in the dry sand–rubber wheel abrasion test. *Wear*, 2083-2091. Retrieved December 2020, from https://www.researchgate.net/publication/222896292_Particle_motion_and_modes_of_wear_in_the_dry_sand-rubber_wheel_abrasion_test

Nair, R., Griffin, D., & Randall, N. (2009). The use of the pin-on-disk tribology test method to study three unique industrial applications. *Wear, 267*(5), 823-827. Retrieved January 2020, from https://www.researchgate.net/publication/248325324_The_use_of_the_pin-on-disk_tribology_test_method_to_study_three_unique_industrial_applications

Ndlovu, S. (2009). *The Wear Properties of Tungsten Carbide-Cobalt Hardmetals from the Nanoscale up to the Macroscopic Scale.* Docter in Engineering Thesis, Friedrich-Alexandra University , Materials Science, Erlang. Retrieved from https://www.researchgate.net/publication/296062262_The_Wear_Properties_of_Tungsten_Carbide-Cobalt_Hardmetals_from_the_Nanoscale_up_to_the_Macroscopic_Scale

Neale, M. J. (1996). *Tribology handbook* (Vol. 2). Oxford, United Kingdom: Butterworth-Heinemann. Retrieved May 2019, from https://epdf.pub/tribology-handbook-second-edition.html

Neale, M. J. (1996). *Tribology handbook.* Oxford, United Kingdom: https://doi.org/10.1016/j.matpr.2017.11.600. doi:https://doi.org/10.1016/B978-0-7506-1198-5.X5000-0

Ngqase, M., & Pan, X. (2020). An overview on types of white cast irons and high chromium white cast irons. *International Conference on Multifunctional Materials (ICMM-2019). 1495.* Johannesburg: IOP Publishing. Retrieved January 2021

Obianyo, I. (2019). *LABORATORY MANUAL FOR HARDNESS TEST.* frican University of Science and Technology, Department of Materials Science and Engineering, Abuja. Retrieved January 2021, from https://www.researchgate.net/publication/331481791_LABORATORY_MANUAL_FOR_HARDNESS_TEST

Ogwu, A., & Davies, T. (1992). Proposed selection rules for suitable binders in cemented hard metals with possible applications for improving ductility in intermetallics. *Journal of Materials Science, 27*(19). Retrieved August 2020, from https://www.researchgate.net/publication/226590205_Proposed_selection_rules_for_suitable_binders_in_cemented_hard_metals_with_possible_applications_for_improving_ductility_in_intermetallics

Okechukwu, C., Dahunsi, O., Oke, P., Oladele, O., & Dauda, M. (2017). Prominence of Hadfield Steel in Mining and Minerals Industries: A Review. *INTERNATIONAL JOURNAL of ENGINEERING TECHNOLOGIES-IJET, 3*(2), 83-90.

Olawale, O., Ibitoye, S., & Shittu, M. (2013). Workhardening Behaviour and Microstructural Analysis of Failed Austenitic Manganese Steel Crusher Jaws. *Materials Research , 16*(6), 1274-1284. Retrieved December 2020, from

https://www.researchgate.net/publication/260763734_Workhardening_Behaviour_and_Microstructural_Analysis_of_Failed_Austenitic_Manganese_Steel_Crusher_Jaws

Ozgowicz, W., Kurc-Lisiecka, A., & Grajcar, A. (2012). Corrosion Behaviour of Cold-Deformed Austenitic Alloys. *Environmental and Industrial Corrosion - Practical and Theoretical Aspects*. Retrieved February 2021, from https://www.intechopen.com/books/environmental-and-industrial-corrosion-practical-and-theoretical-aspects/corrosion-behaviour-of-cold-deformed-austenitic-alloys?fst=0&jwsource=cl&l=ri&r=1

Özkavak, H., Şahin, Ş., Saraç, F., & Alkan, Z. (2019). Comparison of wear properties of HVOF sprayed WC-Co and WC-CoCr coatings on Al alloys. *Materials Research Express*. Retrieved from https://iopscience.iop.org/article/10.1088/2053-1591/ab2ee1/pdf

Page, J. (1991). Example of good and bad chute design. *CKIT.* Retrieved 2019, from https://www.ckit.co.za/secure/conveyor/papers/bionic-research-1/f-bri1-paper05.htm

Panchal, K. (2016). Life Improvement of Hadfield manganese steel castings. *International Journal of Scientific Development and Research (IJSDR), 1*(5). Retrieved September 2020, from https://www.researchgate.net/publication/325168862_Life_Improvement_of_Hadfield_manganese_steel_castings#fullTextFileContent

Panchal, K. (2016). Life Improvement of Hadfield Manganese Steel Castings. *International Journal of Scientific Development and Research (IJSDR), 1*(5), 817-825. doi:ISSN: 2455-2631

Paz-Triviño, F., Buitrago-Sierra, R., & Santa, J. (2020). Wear resistance and hardness of nanostructured hardfacing coatings. *Dyna (Medellin, Colombia), 87*(214), 146-154. Retrieved January 2021, from https://www.researchgate.net/publication/343228372_Wear_resistance_and_hardness_of_nanostructured_hardfacing_coatings

Pejaković, V., Jisa, R., & Franek, F. (2015). Abrasion resistance of selected commercially available polymer materials. *TRIBOLOGIA - Finnish Journal of Tribology, 1*(33).

Pirolini, A. (2015). *Galvanic Corrosion of Steel and Other Metals.* Retrieved December 2019, from AZoM: https://www.azom.com/article.aspx?ArticleID=11833

Pirso, J., & Viljus, M. (2011). Three-body abrasive wear of cermets. *Wear*, 11-12. Retrieved January 2021, from https://www.researchgate.net/publication/232380301_Three-body_abrasive_wear_of_cermets

Pitt, C., Chang, Y., Wadsworth, M., & Kotlyar, D. (n.d.). Pitt, C. H., Y. M. Chang, M. E. Wadsworth, and D. Kotlyar. "Laboratory abrasion and electrochemical test methods as a means of determining mechanism and rates of corrosion and wear in ball mills. *International Journal of Mineral Processing, 22*(1-4), 361-380.

Poolthong, N., Nomura, H., & Takita, M. (2004). Effect of Heat Treatment on Microstructure and Properties of Semi-solid Chromium Cast Iron. *Materials Transactions, 45*(3), 880-887.

Powell, G. L. (1980). Morphology of eutectic M3C and M7C3 in white iron castings. *Materials Forum, 3*, 33-40. Retrieved April 2020, from http://www.scielo.org.za/scielo.php?script=sci_nlinks&ref=2125328&pid=S2225-62532016001000014000015&lng=en

Powell, G., & Randle, V. (1997). The effect of Si on the relationship between orientation and carbide morphology in high chromium white irons. *Journal of Materials Science, 32*(1997), 561-565.

Prieto, G., Rabbia, G., Tuckart, W., & Monslave, A. (2015). Abrasion resistance of high Mn steel alloys. *Third international workshop of tribology*, *13-14.* Buenos Aires. Retrieved May 2020, from https://www.researchgate.net/publication/275582587_Abrasion_resistance_of_high_Mn_steel_alloys#fullTextFileContent

Pugsley, V. A., & Allen, C. (1999). Microstructure/property relationships in the cavitation erosion of tungsten carbide–cobalt. *Wear, 233-235*, 93-103. Retrieved March 2021, from Microstructure/property relationships in the cavitation erosion of tungsten carbide–cobalt

Pugsley, V. A., & Sockel, H. G. (n.d.). Corrosion fatigue of cemented carbide cutting. *Materials Science and Engineering, A366*, 87-95.

Qiao, D., Xie, K., & Kamali, A. (2020). Green production of hydrogen-doped faceted cobalt microcrystals using water-assisted molten salt electro-reduction method. *Materials Advances, 7*(2020).

Rathod, A., Sapate, S. G., & Khatirkar, R. (2013). *Applied mechanics and materials* (Vols. 446-447). Switzerland: Trans Tech Publications. Retrieved May 2019, from https://www.scientific.net/AMM.446-447.126

Rendón, J., & Olsson, M. (2009). Abrasive wear resistance of some commercial abrasion resistant steels evaluated by laboratory test methods. *Wear, 267*(11), 2055-2061.

Revie, W., & Uhlig, H. (2008). *Corrosion and Corrosion Control: An Introduction to Corrosion Science and Engineering.* New York: John Wiley & Sons, Inc. A. Retrieved September 2019, from http://repository.um-palembang.ac.id/id/eprint/9112/1/Corrosion%20and%20corrosion%20control%20an%20introduction%20to%20corrosion%20science%20and%20engineering%20%28%20PDFDrive.com%20%29.pdf

Roberts, A. W. (2003). Chute Performance and Design for Rapid Flow Conditions. *Chemical Engineering and Technology, 26*(2). doi:https://doi.org/10.1002/ceat.200390024

Roberts, A. W., Oom, M., & Wiche, S. J. (1996). Concept of boundary friction adhesion and wear in bulk solid handling. *International Conference on Bulk Materials Storage, Handling and Transformation.* Newcastle N.S.W: National conference publication (Institution of Engineers, Australia). Retrieved May 2019, from https://www.ckit.co.za/secure/conveyor/papers/bionic-research-1/e-bri1-paper04.htm

Roebuck, B. (2006). Extrapolating hardness-structure property maps in WC/Co hardmetal. *International Journal of Refractory Metals and Hard Materials, 24*(1-2), 101-108. Retrieved July 2020, from https://www.sciencedirect.com/science/article/abs/pii/S0263436805000545

Roebuck, B., Bennett, E., Lay , L., & Morrell , R. (2008). *Measurement Good Practice Guide No. 9: Palmqvist Toughness for Hard and Brittle Materials.* Centre for Materials Measurement and Technology: National Physical Laboratory, Department for Innovation, Universities & Skills.

Rozentals. (1992). *Chute Problems- Causes and Solutions.* (R. P. Stahura, Ed.) Retrieved May 2019, from CKIT: https://www.ckit.co.za/secure/conveyor/papers/bionic-research-2/a-bri2-paper01.htm

Rubin, P., Larker, R., Navara, E., & Antti, M. (2018). Graphite Formation and Dissolution in Ductile Irons and Steels Having High Silicon Contents: Solid-State Transformations. *Metallography, Microstructure, and Analysis, 7*, 587-595. Retrieved March 2021, from https://link.springer.com/article/10.1007/s13632-018-0478-6

Rus, D., Capitanu, L., & Badita, L. (2014). A qualitative correlation between friction coefficient and steel. *Friction, 2*(47-57). Retrieved September 2020, from https://link.springer.com/content/pdf/10.1007%2Fs40544-014-0038-2.pdf

Sabzi, M., & Farzam, M. (2019). Hadfield manganese austenitic steel: a review of manufacturing processes and properties. *Materials Research Express, 6*(10). Retrieved February 2020, from https://iopscience.iop.org/article/10.1088/2053-1591/ab3ee3

Sacks, N. (2002). *The wear and corrosive-wear response of tungsten carbide-cobalt hardmetals under woodcutting and three body abrasion conditions.* PhD Thesis, University of Erlangen-Nürnberg: Doktor-Ingenieur, Germany, Faculty of Engineering . Retrieved November 2019, from https://opus4.kobv.de/opus4-fau/frontdoor/index/index/year/2004/docId/43

Saito, H., Lwabuchi, A., & Shimizu, T. (2006). Effects of Co content and WC grain size on wear of WC cemented carbide. *Wear, 261*(2), 126-132. Retrieved January 2020, from https://www.researchgate.net/publication/229307172_Effects_of_Co_content_and_WC_grain_size_on_wear_of_WC_cemented_carbide/stats

Salguero, J., Martinez, J., Del Sol, I., & Ponce, M. (2018). Application of Pin-On-Disc Techniques for the Study of Tribological Interferences in the Dry Machining of A92024-T3 (Al–Cu) Alloys. *MDPI: Materials, 11*(7), 1236.

Sant, S. B., & Smith, R. W. (1985). Strength of Metals and Alloys. In H. J. McQueen, & J. P. Bailon (Ed.), *INTERNATIONAL SERIES ON THE STRENGTH AND FRACTURE OF MATERIALS AND STRUCTURES*, (pp. 12-16). Montreal. doi:doi.org/10.1016/B978-0-08-031642-0.50001-5

Sapate, S. G., & RamaRao, A. V. (2006). Erosive wear behaviour of weld hardfacing high chromium cast irons: effect of erodent particles. (206-212, Ed.) *Tribological International, 39*(3). Retrieved May 2020, from https://www.sciencedirect.com/science/article/pii/S0301679X05000423

Schubert, W. D., Neumeister, H., Kinger, G., & Lux, B. (1998). Hardness to toughness relationship of fine-grained WC-Co hardmetals. *International journal of refractory metals and hard metals, 16*(2), 133-142. Retrieved September 2020, from https://reader.elsevier.com/reader/sd/pii/S0263436898000286?token=3E911AEFB270D6C7BFE36BDC794E447DCA709F5373438E4966B730B0C828518566019437ED9FFDCEFDD986B217AD1F40&originRegion=eu-west-1&originCreation=20210420115219

Schumacher, W. (1985). Corrosion wear synergy of alloy and stainless steels. *Proceedings of International Conference on Wear of Materials* .

Sebeya, T. T. (2013). *An investigation into the causes of the difference in the corrosion behaviour of WC-Co and WC-VC-Co.* Degree of Masters, University of the Witwatersrand, Faculty of

Engineering and the Built Environment, Johannesburg. Retrieved October 2019, from https://core.ac.uk/download/pdf/39671834.pdf

Sipos, K., Lopez, M., & Trucco, M. (2008). Surface martensite white layer produced by adhesive sliding wear-friction in AISI 1065 Steel. *Latin American Journal of Metallurgy and Materials, 28*(1), 46-50. Retrieved June 2019, from http://www.rlmm.org/archivos/28(1)/RLMM%20Art-08V28N1-p46.pdf

Solomon, I. (2013). Wear-resistance technology reduces cost for mines. *Mining Weekly*. Africa. Retrieved May 2019, from https://www.miningweekly.com/article/wear-resistant-technology-reduces-costs-for-mines-2013-09-27/rep_id:3650

Srivastava, A. K., & Das, K. (2008). Microstructural characterization of Hadfield austenitic manganese steel. *Journal of Materials Science* . doi:10.1007/s10853-008-2759-y

Stachowiak, G. W., Batchelor, A., & Stachowiak, G. B. (2004). *Experimental methods in tribology: Preface* (Vol. 44). USA: Elsevier Science.

Subramanyam, D., Swansiger, A., & Avery, H. (1990). *Austenitic Manganese Steels-Properties and Selection: irons, steels, and high-performance alloys* (Vol. 1). ASM Handbook.

Sutthiruangwong, S., & Mori, G. (2003). Corrosion properties of Co-based cemented carbides in acidic solutions. *International Journal of Refractory Metals and Hard Materials, 21*(3-4), 135-145. Retrieved January 2021

Tang, X. H., Chung, R., Pang, C., Li, D., Hinckley, B., & Dolman, K. (2011). Tang, X. H., et al. "Microstructure of high (45 wt.%) chromium cast irons and their resistances to wear and corrosion. *Wear, 271*(9-10), 1426-1431.

Tchuindjang, T. J., Torres, I. N., Flores, P., Habraken, A. M., & Lecomte-Beckers, J. (2015). Phase transformations and crack initiation in a high chromium cast steel under hot compression tests. *Journal of Materials Engineering and Performance, 2009*(2014). Retrieved from https://www.researchgate.net/publication/273455982_Phase_Transformations_and_Crack_Initiation_in_a_High-Chromium_Cast_Steel_Under_Hot_Compression_Tests#fullTextFileContent

Tian, H., & Taylor, P. (2011). "Corrosion Study on high Alloyed white cast irons in acidic and chloride containing solutions, Preceedings of the *Corrosion*.

Tikotkar, R. G. (2012). Effect of Frictional Force and Wear Rate on Hadfield Steel. *International Journal of Engineering Research & Technology, 1*(6). Retrieved April 2021, from https://www.ijert.org/research/effect-of-frictional-force-and-wear-rate-on-hadfield-steel-IJERTV1IS6378.pdf

Tilly, G. P. (1972). A two stage mechanism of ductile erosion. *Wear, 23*(1), 87-96. Retrieved March 2021, from https://www.sciencedirect.com/science/article/pii/0043164873900446

Tran, S. (2018). Microstructure Investigations of WC-Co Cemented Carbide Containing eta-phase and Cr. Retrieved April 2020, from https://uu.diva-portal.org/smash/get/diva2:1237216/FULLTEXT01.pdf

Tressia, G., Penagos, J. J., & Sinatora, A. (2017). Effect of abrasive particle size on slurry abrasion resistance of austenitic and martensitic steels. *Wear, 376-377*(A), 63-69. Retrieved March 2021, from https://www.sciencedirect.com/science/article/pii/S0043164817301941

Vallance, S., Kitchen, H., Ritter, C., Gregory, D., Kingman, S., & Dimitrakis, G. (2012). Probing the microwave interaction mechanisms and reaction pathways in the energy-efficient, ultra-rapid synthesis of tungsten carbide. *Green Chemistry, 14*(8), 2184-2192. Retrieved September 2019, from https://www.researchgate.net/publication/255759949_Probing_the_microwave_interaction_mechanisms_and_reaction_pathways_in_the_energy-efficient_ultra-rapid_synthesis_of_tungsten_carbide

Van Aarde, M. N. (2009). *The Optimisation of Transfer Chutes in the Bulk Material Industry.* Dissertation for degree, North-West University, Mechanical Engineering, Potchestroom. Retrieved September 2019, from https://pdfs.semanticscholar.org/e2c7/29b21b1d72cfc345a76217cf8346ef5a99e0.pdf

Vaughan, R. A. (1991). *The effects of hardness, toughness, microstructure and thermomechanical heating on the erosion of ceramic and ultrahard materials.* University of Cape Town, Materials Engineering, Cape Town. Retrieved January 2021, from https://open.uct.ac.za/bitstream/handle/11427/18218/thesis_ebe_1991_vaughan_r_a.pdf?sequence=1

Vdovin, K., Pesin, A., Feoktistov, N., & Gorlenko, D. (2018). Surface Wear in Hadfield Steel Castings DOPED with Nitrided Vanadium. *Optimization of Industrial Casting Processes, Metals 8*(10), 845. Retrieved January 2020, from https://www.mdpi.com/2075-4701/8/10/845

Venturelli, B., Albertin, E., & Roberto de Farias Azeved, C. (2018). The effect of the austenite grain refinement on the tensile and impact properties of cast Hadfield steel. *Materials Research, 25*(5). Retrieved October 2020, from https://www.researchgate.net/publication/326785143_The_effect_of_the_austenite_grain_refinement_on_the_tensile_and_impact_properties_of_cast_Hadfield_steel#fullTextFileContent

Vreeburg, W. P. (2018). *Redesign of a Tata Steel Chute with Dust Liberation Problems.* Master's degree thesis, Delft University of Technology, Mechanical Engineering, Transport Engineering and Logistics, Delft. Retrieved March 2020, from https://pdfs.semanticscholar.org/4098/175dcdd1738fd3d0b7ac0e82685b7ecb0868.pdf

WebCorr. (n.d.). *Different Types of Corrosion: Recognition, Mechanisms & Prevention*. (Webcorr) Retrieved from Pitting corrosion.

Wei, M. X., Chen, K. M., Wang, S., & Cui, X. (2011). Analysis for Wear Behaviors of Oxidative Wear. *Tribological Letters, 42*, 1-7. Retrieved November 2020, from https://www.researchgate.net/publication/241005471_Analysis_for_Wear_Behaviors_of_Oxidative_Wear

Wu, X., Xing, J., Fu, H., & Zhi, X. (2007). Effect of titanium on the morphology of primary M7C3 carbides in hypereutectic high chromium white iron. *Materials Science and Engineering: A, 457*(1-2), 180-185. Retrieved March 2021, from https://www.sciencedirect.com/science/article/abs/pii/S0921509306026372

Xia, R., Li, B., Wang, X., Yang, Z., & Liu, L. (2019). Screening the Main Factors Affecting the Wear of the Scraper Conveyor Chute Using the Plackett–Burman Method. *Mathematical problems in engineering, 2019*, 11. Retrieved May 2020, from https://www.hindawi.com/journals/mpe/2019/1204091/xcx

Xiaodong, D., Guodong, S., Yifei, W., & Jianfeng, W. (2009). Abrasion Behavior of High Manganese Steel under Low Impact Energy and Corrosive Conditions. *Advances in Tribology, 2009*. Retrieved January 2021, from https://www.hindawi.com/journals/at/2009/685648/

Xiaoyun, L., Wei, W., Fangqiu, Z., Lanjun, L., & Xianfeng, Z. (2011). Influence of impact energy on work hardening ability of austenitic manganese steel and its mechanism. *China Foundry, 9*(3). Retrieved June 2020, from https://core.ac.uk/download/pdf/27059414.pdf

Xu, L., Vose, C., & StJohn, D. (1993). Abrasive wear study of selected white cast irons as liner materials for the mining industry. *Wear, 162-164*(B), 820-832. Retrieved March 2021, from https://www.sciencedirect.com/science/article/pii/004316489390083X

Xu, L., Wei, S., Zhou, H., Zhang, G., & Li, J. (2017). Effects of carbides on abrasive wear properties and failure behaviours of high speed steels with different alloy element content. *Wear, 376-377*(Part B), 968-974.

Xu, Z., & Li, L. (2006). Wear behavior of austenite steel matrix composite reinforced by in situ granular eutectics in impact abrasion. *Materials Science and Engineering:A, 428*(1-2), 256-261.

Yaer, X., Shimizu, K., Matsumoto, H., Kitsudo, T., & Momono, T. (2008). Erosive wear characteristics of spheroidal carbides cast iron. *Wear, 264*(11-12), 947-957. Retrieved September 2019, from https://www.mendeley.com/catalogue/ce34124f-454a-381e-88d8-b7af01f16e30/

Yildizli, K., Eroglu, M., & Karamiş, M. B. (n.d.). Erosive wear behaviour of hardfacing austenitic manganese deposit. *Tribology in Industry, 27*(3), 15-21. Retrieved March 2021 , from https://www.researchgate.net/publication/279588977_Erosive_wear_behaviour_of_hardfacing_austenitic_manganese_deposit

Yousfi, A. (2016). *Microstructure Development of WC-Co Based Cemented Carbides During Creep Testing.* Chalmers University of Technology, Department of Physics. Goteborg: Chalmers Reproservice. doi:ISSN 0346-718X

Yousif, I. F., & Ataiwi, A. H. (2017). Destabilization heat treatment effect on erosive war characteristics of high chromium white cast iron. *Kufa Journal of Engineering*. Retrieved September 2020, from https://www.researchgate.net/publication/325161722_DESTABILIZATION_HEAT_TREATMENT_EFFECT_ON_EROSIVE_WEAR_CHARACTERISTICS_OF_HIGH_CHROMIUM_WHITE_CAST_IRON

Zelders, H. G. (1949). La corrosion superficielle dans le circuit de lavage des charbonnages des mines de l'état Néerlandais,. *Met. Corros, 65*(283), 25-76.

Zhang, P., Li, S. X., & Zhang, Z. (2011). General relationship between strength and hardness. *Materials Science and Engineering A*, 62-73. Retrieved December 2020, from https://www.researchgate.net/publication/251608066_General_relationship_between_strength_and_hardness

Zum Gahr, K. H. (1987). *Microstructure and Wear of Materials* (Vol. 10). North Holland, Amsterdam, The Netherlands: Elsevier Publications.

Zumelzu, E., Cabezas, C., Goyos, I., Parada, O., & Opitz, O. (2002). Wear and corrosion behaviour of high-chromium (14–30% Cr) cast iron alloys. *Journal of Materials Processing Technology,*

128(1-3), 250-255. Retrieved March 2021, from https://www.sciencedirect.com/science/article/abs/pii/S0924013602004582

Article

Electrochemical Corrosion Behaviour of Different Grades of WC-Co, High-Cr White Cast Irons and Hadfield Steel in 1 M Sulphuric Acid

Johannes H. Potgieter [1,2] , David Whitefield [1,*] and[2]Vivian Motsumi [1]

[1] School of Chemical and Metallurgical Engineering, University of the Witwatersrand, Private Bag X3, P.O. Wits, Johannesburg 2050, South Africa;
[2] Department of Natural Sciences, Manchester Metropolitan University, Chester Street, Manchester M1 5GD, UK
* Correspondence: David.Whitefield@wits.ac.za

Citation: Potgieter, J.H Whitefield, D.; Motsumi, V.; . Electrochemical Corrosion Behaviour of Different Grades of WC-Co, High-Cr White Cast Irons and Hadfield Steel in 1 M Sulphuric Acid. ***Materials*** **2021,** ***14,*** **x. https://doi.org/10.3390/xxxxx**

Academic Editor(s): Amir Mostafaei

Received: 28 July 2021
Accepted: 08 October 2021
Published:

Publisher's Note: MDPI stays neutral with regard to jurisdictional claims in published maps and institutional affiliations.

Copyright: © 2021 by the authors. Licensee MDPI, Basel, Switzerland. This article is an open access article distributed under the terms and conditions of the Creative Commons Attribution (CC BY) license (http://creativecommons.org/licenses/by/4.0/).

Abstract: Electrochemical polarisation tests were carried out on three grades of WC-Co cemented carbides to investigate the corrosive behaviour of the hardmetals and rank them as viable protective liners for chutes and skips in the mining industry. The cobalt binder content and WC particle size varied. The binder content ranged from 6–12 wt%, and the grain size of the WC particles ranged from 0.4–2.3 μm. The performance of the WC-Co hardmetal was compared to three different grades of high chromium white cast irons and Hadfield steel. The cast irons varied in both their chromium content and the morphology of the Cr-rich primary carbides. Potentiodynamic polarisation and linear polarization resistance scans were used to determine the corrosion current density and other electrochemical parameters. The microstructural characteristics of the samples were analysed using Scanning Electron Microscope(SEM) with Energy Dispersive Spectroscopy (EDS), and optical microscopy. The potentiodynamic scans revealed that, although the WC-Co alloys were found to have generally improved corrosion resistance, it was the high-Cr white cast iron (22 wt% Cr) that recorded the lowest corrosion current density and therefore displayed the best resistance against corrosive attack in 1 M H_2SO_4. The Hadfield steel exhibited the poorest resistance to corrosion and therefore, suffered the most degradation to its exposed surface.

Keywords: WC-Co alloys; hadfield steel; High-Cr white cast irons (HCWCI), mining industry; tribocorrosion

1. Introduction

The movement and storage of ore in the mining and minerals processing industry requires chutes and skips. Large structural items in the mining industry like chutes and skips consume large quantities of engineering materials [1]. In order to prevent production stoppages and a possible substantial loss of capital due to the premature mechanical failure of these structural components, there is a need to design wear- and corrosion-resistant liners at specific locations of high deterioration to limit the damage experienced during operation [2–14]. Corrosion wear is just as severe on ore transportation structures as mechanical wear, which is why it is wise to also rank the corrosive response of a material when selecting a protective liner for chutes and skips.

There are many wear and corrosion mechanisms involved during the handling of ore in mines [1,11,12]. Understanding the synergistic effects of these surface-degrading mechanisms enables the engineer to design and develop lining plates or similar surface-protective methods that would offer optimal effectiveness in protecting the components against both wear and corrosion [2,15]. Since chutes and skips are not only subjected to mechanical wear in mining applications but are also in contact with chemically aggressive environments, the selection of the lining materials should also be designed for ultimate corrosion resistance. This present study is aimed at evaluating the electrochemical responses of different grades of tungsten carbide cobalt (WC-Co), high chromium white cast irons (HCWCI) and Hadfield steel, and determining which material offers the best resistance against corrosive attack in 1 M H_2SO_4.

WC-Co cermets are hard monocarbide grains cemented in a soft binder matrix of tough cobalt metal by liquid phase sintering [16]. Although WC-Co hardmetals are known for their excellent resistance to wear [17–20], they have also demonstrated fair resistance to chemical attack in corrosive environments [21–24]. Generally, the two-phased WC-Co cermets do not passivate in acidic media [25,26]. The process of corrosion in aggressive media favours the selective dissolution of cobalt, while the WC particles remain inert, leaving a skeleton of WC particles on the surface [21]. The WC particles of the hardmetals can also corrode, but this only occurs at significantly higher potentials [27]. The process of corrosion of WC-Co hardmetals is shown in Equations (1) and (2) [28].

$$Co \rightarrow Co^{2+} + 2e^- \quad (1)$$

$$WC + 5H_2O \rightarrow WO_3 + CO_2 + 10H^+ + 10e^- \quad (2)$$

In their studies, Human and Exnar [18] investigated other properties of WC-Co hardmetals that could possibly influence their resistance to corrosion, and it was found that grain size had no effect on the electrochemical attack of the hardmetals in 1M H_2SO_4. However, recent research shows that the microstructural characteristics such as growth inhibitors and the grain size of WC particles influenced the electrochemical corrosion resistance of the WC-Co cemented carbides [29–33]. Liu et al. [30] found that there is a linear relationship between the grain sizes and the corrosion current density. The chemical nature of the matrix, such as the addition of grain growth inhibitors to ultrafine-sized powders, has also been found to significantly influence the corrosion behaviour of WC-Co cemented carbides [34]. Another general trend observed was that the corrosion rate of WC-Co alloys increased with an increase in Co content. Human and Exner [18] found that the composition of the binder phase was of great importance to the corrosion resistance of cemented carbides They added that the alloys experienced a mass loss during corrosion when all other parameters, such as the grain size of the WC particles, were kept constant. Similar to the WC-Co cemented carbides, HCWCI are not only exceptional at resisting severe abrasive and erosive environments, but they have also proven to perform well in different corrosive environments. Their resistance to chemically corrosive environments, such as reducing acids, has been found to be strongly influenced by the presence of high levels of alloying elements [35]. Tian et al. [36] and El-Aziz et al. [37] reported that alloys that contained high ratios of Cr/C in their microstructures were the most suitable to resisting

damage by corrosion. This implies that the carbon content has to be relatively low so that excess concentrations of chromium can be found in the matrix to further improve the corrosion resistance of the matrix [35,38]. Furthermore, El-Aziz et al. [37] discovered in their work that a high-volume fraction of large bulky primary carbides in the form M_7C_3 were advantageous in harsh corrosive environments by forming secondary carbides and primary eutectic carbides.

High-manganese austenitic steels, also known as Hadfield steels (HS), are traditionally used as wear-resistant alloys in harsh applications wherein high impact abrasion, high fracture toughness and moderate resistance to corrosion are required [39,40]. The corrosion of conventional steels in acidic media is one of the most common failure mechanism in the minerals processing industry [41]. There are a few studies available on the corrosion behaviour of Hadfield steels in acidic media [41–44]. In their studies, Grajcar et al. [41] reported that the substantial mass loss of high-manganese steel in 1 M H_2SO_4 solution was due to the hydrogen depolarisation mechanism, which was subsequently accompanied by the local cracking of the previously formed product layer, resulting in the protective passive layer being removed during the polarisation process, causing further significant damage to the exposed and unprotected surface [43,45,46]. Moreover, MnS inclusions were reported to act as initiating sites of pitting corrosion in steels [42].

To study the comparative corrosion resistance of the investigated materials, potentiodynamic polarisation scans were carried out. The surfaces of the corroded samples were examined and characterised using Scanning Electron Microscope- Energy Dispersive Spectroscopy (SEM, EDS), and light optical microscopy. The investigated metals were exposed to an acidic electrolyte (H_2SO_4) because most chutes and skips are exposed to acid-ironstone/acidic underground water in the mining and mineral processing industry. Furthermore, this medium provided a fast and easy way to compare the corrosion resistance of the different alloys against each other.

This investigation had two main foci, namely, firstly to compare the corrosion resistance of the typically employed WC-Co alloys with the cheaper Hadfield steel widely applied in the mining industry and secondly to establish whether both the WC-Co alloy group and the Hadfield steel could be replaced by much cheaper, and at this stage, experimental high-chromium white cast iron compositions. The successful achievement of the latter goal would offer the mining industry real economic advantages if acceptable and comparable corrosion resistance compared to the Hadfield steel and the WC-Co alloys could be achieved. At the same time, the production of experimental high-chromium white cast irons as production materials could create new uses for chromium in the mining industry and lead to increased job creation opportunities in an economy with unacceptably high unemployment rates.

2. Experimental Procedure

2.1. Metallographic Preparation

The as-received samples were sectioned into 10 mm × 10 mm × 5 mm blocks using a precision cutting machine. The samples were cleaned with

ethanol after cutting to remove any debris formed during cutting. The test surfaces of the samples were wet-ground using silicon carbide papers with sizes ranging from 220- to 1200-grit to achieve a flat top surface that was free from coarse scratches. Thereafter, a mirror-like surface was achieved with a 3 μm pan cloth followed by a 1 μm diamond spray. The specimens were washed with distilled water and the polished surfaces of the WC-Co and Hadfield steel samples were etched using Murakami's reagent and 5% Nital, respectively. The HCWCI samples required no etching since the microstructures of the alloys were easily revealed during polishing using colloidal silica. The tested area for all samples was kept at 0.25 cm^2. The chemical composition of the samples used in this study, viz. WC-Co, HCWCI, and Hadfield steel, are summarised in Tables 1 and 2.

Table 1. Nominal composition of the investigated WC-Co alloys.

Samples	Composition (wt%)			
	W	**C**	**Co**	**Cr**
WC-6Co	86.0	7.9	6.1	---
WC-8Co	83.1	9.1	7.8	---
WC-12Co	79.6	7.5	12.0	0.9

Table 2. Nominal compositions of the investigated HCWCI alloys and the Hadfield steel.

Sample	Composition (wt%)												
	Cr	**Si**	**Fe**	**Mn**	**S**	**Ni**	**V**	**P**	**Mo**	**Cu**	**Al**	**N**	**C**
HCWCI-1	20.2	0.2	60.0	0.7	---	---	0.5	---	---	---	---	---	Bal.
HCWCI-2	22.2	0.4	65.2	---	---	---	---	---	---	---	---	---	Bal.
HCWCI-3	24.5	0.9	58.2	0.9	0.3	1.3	---	---	---	---	---	---	Bal.
Hadfield steel	0.34	0.58	85.0	12.4	<0.001	0.04	---	0.035	0.46	0.03	0.03	0.02	Bal.

2.2. Microstructure Analysis

An optical microscope and scanning electron microscope (SEM) were used to examine the microstructures, surface morphology and chemical analysis of the investigated samples in their as-received condition and after the electrochemical tests. The optical microscope used was an Olympus SC50. The SEM used was the Zeiss high-vacuum scanning electron microscope (Zeiss, Germany) equipped with an energy-dispersive X-ray spectrometry (EDS). The SEM-EDS operated at 20 keV and the micrographs were taken in both backscattered electron (BSE) and secondary electron (SE) mode. ImageJ software (Zeiss, Germany) was used to determine the grain sizes of the investigated specimens.

2.3. Potentiodynamic Corrosion Testing Procedure

A 1 M H_2SO_4 solution was used for the corrosion testing. A fresh solution was prepared for each test. A cylindrical three-electrode 900 mL Pyrex glass cell was used for this experiment. The cell consisted of a graphite counter electrode, a silver/silver chloride reference electrode immersed in a 3 M KCl solution and the working electrode. The potentiodynamic polarization scans were carried out at room temperature (25 ± 1 °C) in a water bath where the temperature could be closely regulated. The electrodes were connected to an Autolab potentiostat (Metrohm, Switzerland) and the characteristic electrochemical parameters such as the corrosion potential (E_{Corr}), current density (i_{Corr}) and the corrosion

rates (CR) were defined by using Nova software. The test procedure was set as follows:

1. Open circuit potential (OCP) for 1 h.

2. Linear potentiodynamic scans.

The scans were carried out from −0.2 V versus the OCP to 1.5 V versus the reference electrode. The scan rate and step potential were set at 5 mV/s and 1.6 mV, respectively. Each experiment was conducted in triplicate to ensure the repeatability of the results.

3. Results

3.1. Metallurgical Microstructure of the Investigated Samples

The grain sizes of the investigated specimens are summarized in Table 3. Because the morphology of the primary carbides found in the HCWCI alloys are mostly continuous, their sizes were determined based on 80% of their area range per analysed alloy.

Table 3. Summary of the primary carbide area range of the HCWCI alloys, WC grain sizes and the austenite grain sizes of the Hadfield steel.

HCWCI Alloys (μm^2)			**WC-Co Alloys (μm)**			**Hadfield Steel (μm)**
HCWCI-1	**HCWCI-2**	**HCWCI-3**	**WC-6Co**	**WC-8Co**	**WC-12Co**	**HS**
25–1450	280–5330	65–2745	2.2	2.3	0.4	300

3.1.1. WC-Co Cemented Carbides

Figure 1a–c are the SEM micrographs of WC-8Co, WC-12Co and WC-6Co, respectively. The binder content (Co) of the cemented carbide samples ranged between 6–12 wt.%, and the samples had grain sizes between 0.4–2.3 μm. WC-12Co contained the finest WC grains in its structure, whereas WC-6Co exhibited a much coarser structure. The refined structure of WC-12Co can be attributed to the chromium present in the form Cr_2C_3.

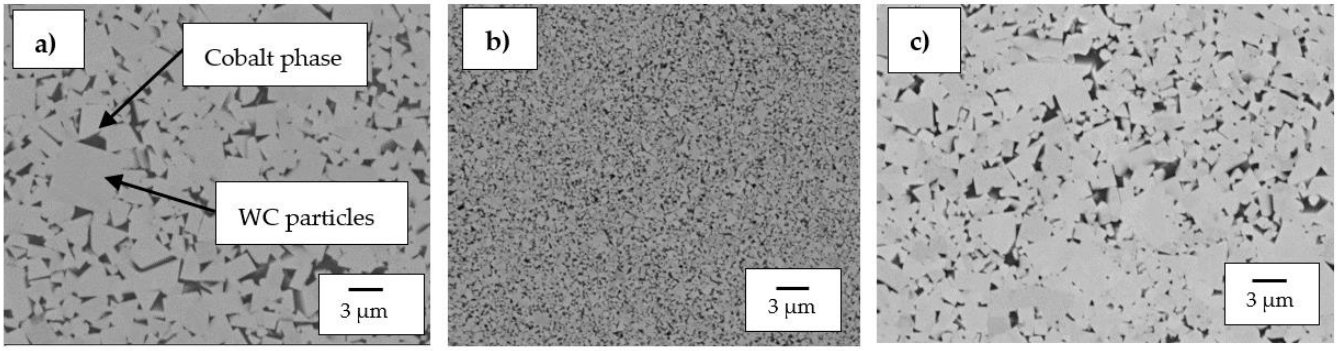

Figure 1. SEM micrographs of the investigated WC-Co alloys: (**a**) WC-8Co, (**b**) WC-12Co, and (**c**) WC-6Co.

3.1.2. High-Cr White Cast Irons

The optical micrographs of HCWCI-1, HCWCI-2 and HCWCI-3 are shown in Figures 2–4, respectively. HCWCI-2 and HCWCI-3 exhibited larger primary carbides in their microstructures than HCWCI-1. This is because of their increased Cr contents, which promote the formation of Cr-rich carbides. HCWCI-3 exhibited larger longitudinal primary carbides and larger hexagonally shaped transverse primary carbides. This is because Cr stabilizes carbides during the solidification of white cast irons, hence promoting the formation and dispersion of hard Cr-rich and (Fe, Cr_x)C_Y carbides. All three alloys contained a high density of rod-shaped and isolated M_7C_3 carbides, which are expected when the Cr content exceeds 15% [4748]. The ImageJ software revealed that about 80% of the primary carbides of the HCWCI-1 had an area in the range 25–1450 μm², whereas the primary carbides of the HCWCI-2 and HCWCI-3 alloys had an area in the range 280–5330 and 65–2745 μm², respectively.

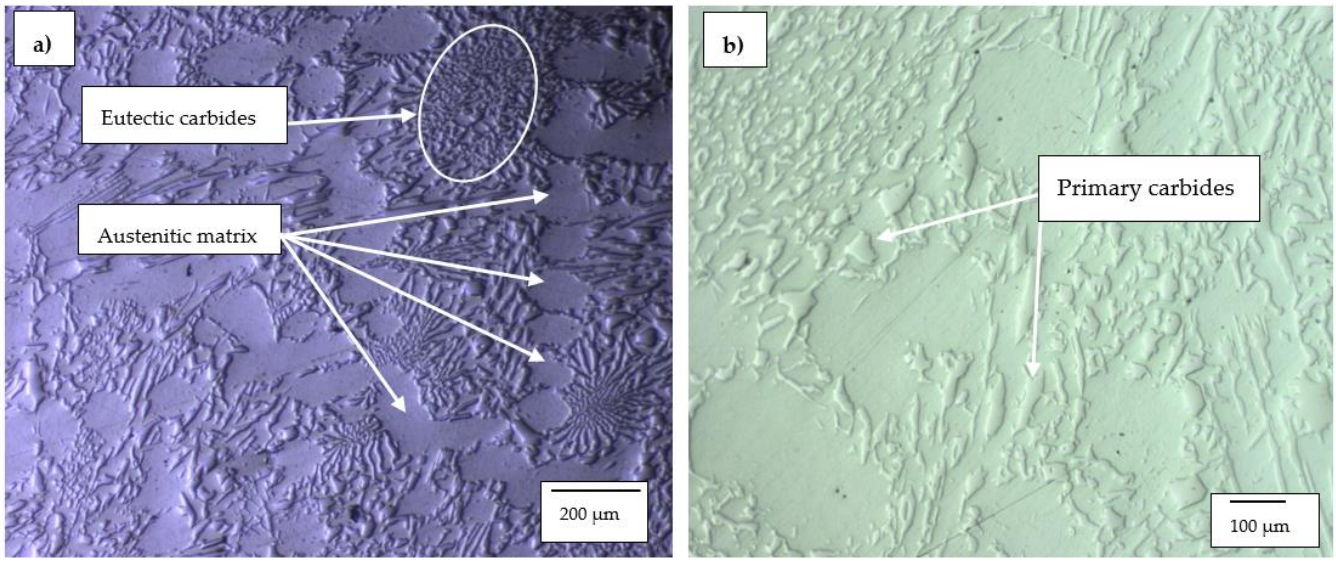

Figure 2. *Optical microscope micrographs of the investigated high-chromium white cast iron alloy: (**a**) HCWCI-1 at 50× and (**b**) HCWCI-1 at 200×.*

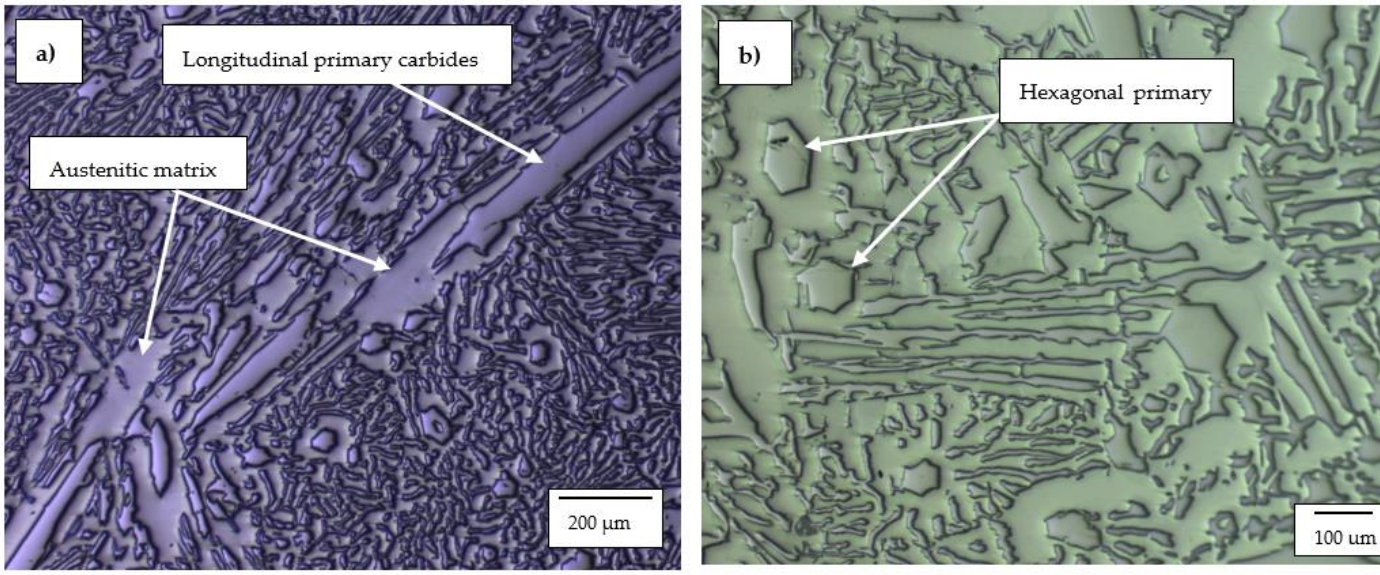

Figure 3. Optical microscope micrographs of the investigated high-chromium white cast iron alloy: (**a**) HCWCI-2 at 5× and (**b**) HCWCI-2 at 20×.

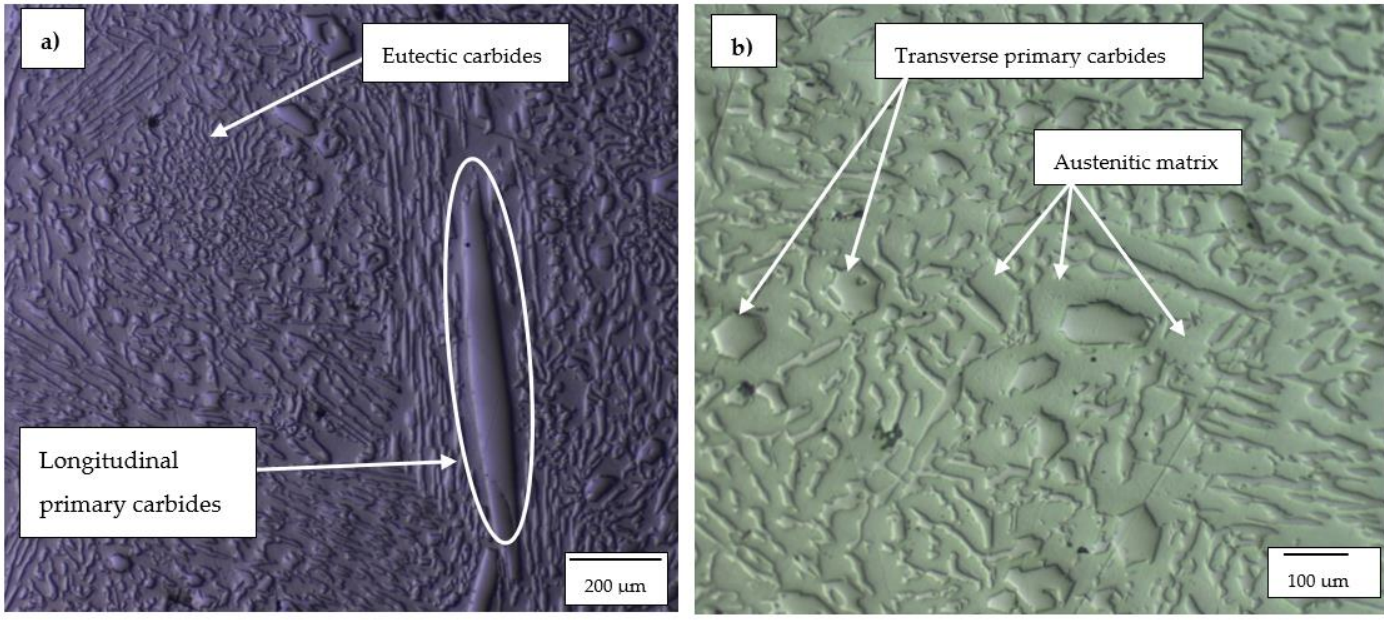

Figure 4. Optical microscope micrographs of the investigated high-chromium white cast iron alloy: (**a**) HCWCI-3 at 5× and (**b**) HCWCI-3 at 20×.

3.1.3. Hadfield Steel

The optical micrographs of the Hadfield steel alloy are shown in Figure 5a,b. The Mn and C composition of the investigated Hadfield steel are 12.4% and 1.1%, respectively. This implies the steel's Mn/C composition ratio lies within the original standards of the austenitic manganese steel. The Hadfield steel consists of a Cr content of 0.3 wt%, which is essential for the yield strength and corrosion resistance of the Hadfield steel [49,50]. The Hadfield steel had a grain size of 300 µm.

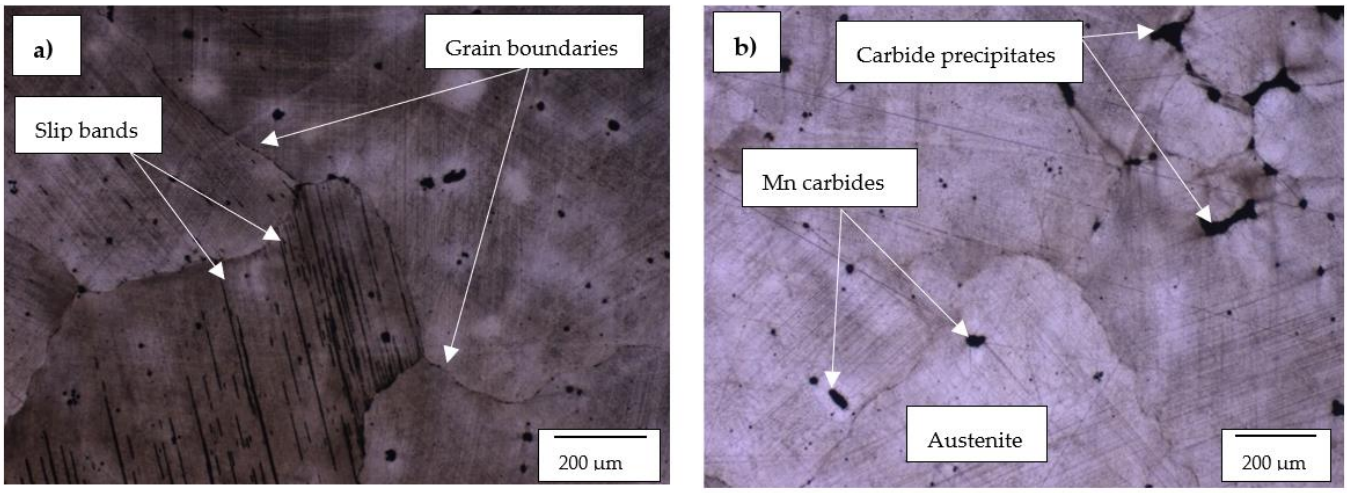

Figure 5. Optical microscope micrographs of the investigated Hadfield steel showing (a)the grain boundaries, slip bands and (b) carbide precipitates.

3.2. Electrochemical Corrosion Behaviour of the Investigated Alloys

3.2.1. Open Circuit Potential (OCP)

The OCP (E_{OC}) values and the variations therein were measured for an hour in 1 M H_2SO_4 as presented in Figure 6. The recorded OCP values started off unstable, displaying random fluctuations in the first few minutes of measuring. The Hadfield steel was observed to be the alloy showing less stability, followed by HCWCI-3 and then HCWCI-1. WC-12Co displayed the highest starting potential (most noble) and finally stabilised at a higher potential than the other investigated carbide metals. The HCWCI-3 alloy was observed to have displayed the lowest starting potential (least noble) and continued to stabilise at the lowest potential when compared to the other metals. The WC-Co alloys behaved similar as a group and displayed similar trends during the measuring of the OCP. This trend was similar for all the iron-based alloys (HCWCI alloys and the Hadfield steel).

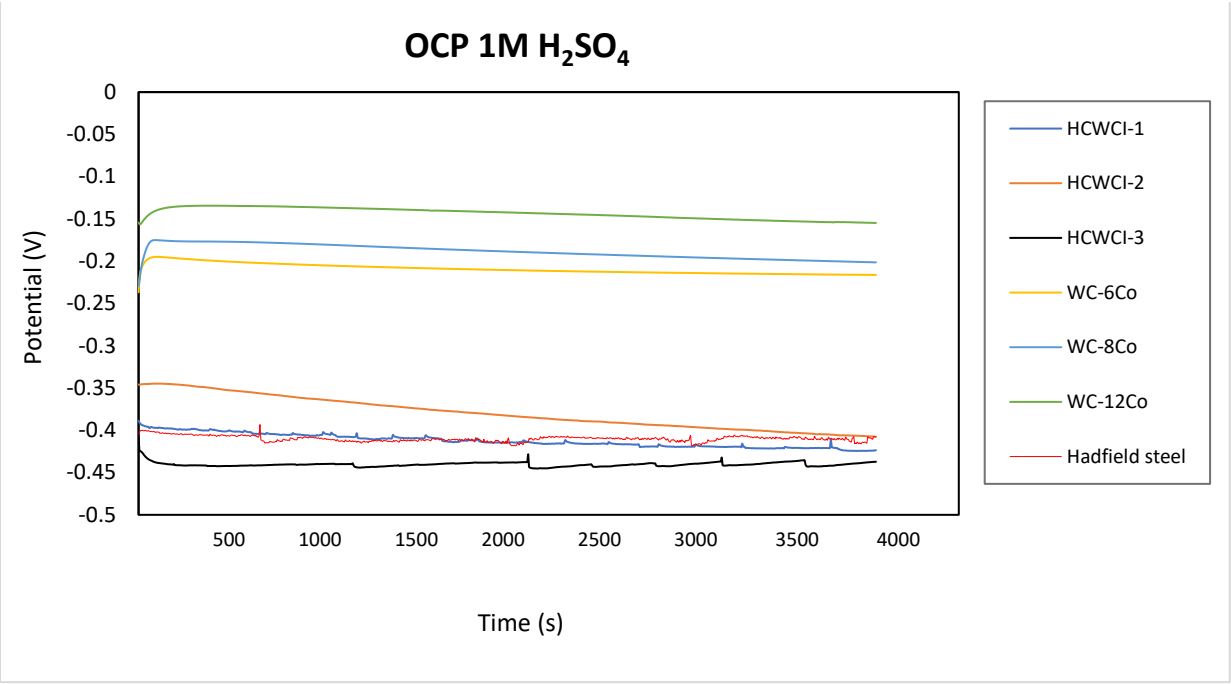

Figure 6. Open Circuit Potential behaviour of the investigated metals in 1 M H_2SO_4.

3.2.2. Potentiodynamic Polarisation Measurements

The polarisation scan curves are presented in Figure 7. The curve profiling of the samples showed a typical active-pseudopassive transition behaviour (although showing small passive regions) with the exception of HCWCI-2, which did not show any passive behaviour. Again, the WC-Co curves showed similar behaviour and the iron-based metals gave similar curves. Comparing the potentials of WC-6Co and WC-8Co, WC-6Co displayed a lower tendency to corrode. This was expected because WC-6Co contained a smaller amount of cobalt in its system, which directly influences the corrosion of WC-Co cemented carbides [18].

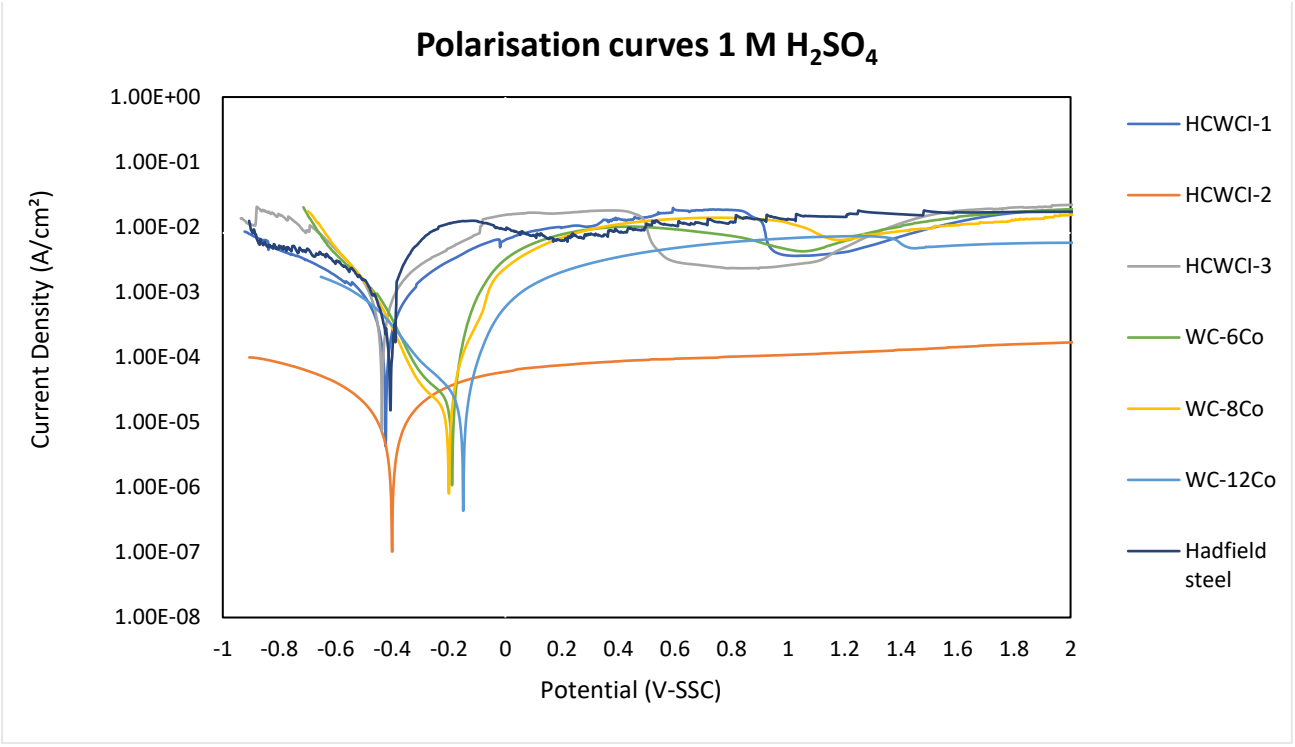

Figure 7. Potentiodynamic polarisation curves of the WC-Co alloys, HCWCI alloys and Hadfield in 1 M H_2SO_4.

Table 4 gives a summary of the electrochemical parameters of the WC-Co, HCWCI and Hadfield steel alloys obtained from the electrochemical polarisation scans using 1 M H_2SO_4 as a corroding medium.

The corrosion potential values (E_{Corr}) {XE "Corrosion potential values:(E_{Corr})"} of the WC-Co alloys became less noble with an increase of cobalt, with the exception of WC-12Co, which contained the highest Co content but exhibited the most noble value of −0.149 V. In the same manner, WC-12Co also exhibited the lowest value for current density (185 μm/cm²) and suffered minimal corrosive attack compared to WC-8Co and WC-6Co, which recorded current density values of 359 μm/cm² and 399 μm/cm², respectively. The i_{corr} value of WC-6Co was very similar to the i_{corr} exhibited by WC-8Co, which was expected considering that the two alloys had similar WC particle sizes, lower Co content and no other alloying elements. Generally, WC-Co cemented carbides with low Co contents have lower i_{corr} values when compared with WC-Co alloys with higher Co [18,51]. However, WC-12Co exhibited the lowest i_{corr} value and thus, exhibited the lowest corrosion rate (CR) value of the three investigated WC-Co alloys.

Although there was little difference between the E_{Corr} values of the HCWCI alloys, HCWCI-2 showed the most noble E_{Corr} value (−0.401 V), while HCWCI-1 and HCWCI-3 gave E_{Corr} values of −0.423 and −0.437 V, respectively. An increase in Cr was advantageous to HCWCI-2 and detrimental to HCWCI-3. This trend was observed with the alloys' i_{corr} and CR values. An increase of Cr from 20 wt% (HCWCI-1) to 22 wt% (HCWCI-2) had a tremendous effect on the i_{corr} and CR value as both values decreased by an order of magnitude of three and two, respectively. A further increase of Cr to 25 wt% (HCWCI-3) had an adverse effect on

the alloy's resistance to corrosion. HCWCI-3 experienced slightly higher corrosion resistance than HCWCI-1. This influence of Cr on the resistance of the high-chromium cast iron to corrosion was also observed by other researchers [52].

Hadfield steel exhibited the poorest resistance to corrosion compared to the other investigated metals but exhibited an E_{Corr} value (−0.406 V) that was similar to that displayed by the cast iron alloys. The i_{corr} and CR values of the Hadfield steel were very similar to those of HCWCI-1.

Table 4. Electrochemical parameters of the investigated materials.

Sample	E_{corr} (V)	i_{corr} (μA/cm²)	CR (mmpy)
WC-6Co	−0.189 ± 0.015	399.2 ± 1.2	0.09 ± 0.01
WC-8Co	−0.199 ± 0.01	359.2 ± 1.1	0.10 ± 0.02
WC-12Co	−0.149 ± 0.02	185.5 ± 2.4	0.04 ± 0.06
HCWCI-1	−0.423 ± 0.033	1033.4 ± 14.2	0.35 ± 0.01
HCWCI-2	−0.401 ± 0.014	9.96 ± 1.7	1.93×10^{-3} ± 0.58
HCWCI-3	−0.437 ± 0.021	801.2 ± 2.3	0.19 ± 0.2
HS	−0.406 ± 0.001	1084.7 ± 10.8	0.45 ± 0.17

Of the WC-Co alloys, it was the WC-12Co sample that showed the best resistance to corrosion based on its recorded i_{corr} and therefore, CR values during the potentiodynamic and linear polarization resistance scanning. Since WC-12Co contains the highest content of the binder phase, one would expect WC-12Co to exhibit the highest tendency to corrode when compared to the other two WC-Co alloys. However, the alloy has a very fine microstructure that consists of WC particles that are very closely packed together. This kind of structure prevents the binder phase from being exposed to the corroding medium, hence preventing excessive corrosion. Additionally, the alloy also has traces of Cr, which has been proven to be beneficial to the WC-Co's ability to resist corrosion under acidic conditions [53].

The surface of the WC-12Co suffered little to no chemical damage after electrochemical polarization tests. WC-6Co and WC-8Co experienced similar corrosion rates, and therefore, they exhibited the same degree of damage on their surfaces. The corrosion behaviour of the investigated WC-Co alloys was noticed to be strongly influenced by the grain size and morphology of the WC particles. This is in contrast to the studies recorded by Human and Exner [18]. They found that the grain size and morphology of WC-Co hardmetals had no significant effect on the carbides' resistance to corrosion in an acidic environment.

Of all the investigated specimens, HCWCI-2 exhibited the best overall performance resisting corrosion. The alloy displayed negligible damage when exposed to an acidic environment. The chromium content and the morphology of the Cr-rich carbides was shown to be crucial for corrosion resistance in white cast irons and therefore contributed to its exceptional corrosion resistance.

Hadfield steels responded the worst during electrochemical tests and displayed the most damage to its exposed surface.

The tendency of these investigated alloys to corrode can also be attributed to their reinforcing particles, viz. WC in the WC-Co hardmetals and the Cr-rich primary carbides in the white cast irons. In a study investigating the corrosion behaviour of WC and Cr_3C_2-based coatings by Luiz et al. [54], the Cr_3C_2-based coatings outperformed the WC-based coatings in resisting corrosive attack. This was seen to also be the case between the two best-performing alloys (WC-12Co and HCWCI-2) investigated in this study. The Cr_3C-based alloys, such as the Cr-rich primary found in HCWCI-2, proved to be more inert to chemical degradation in 1M H_2SO_4 than WC particles.

3.3. Analysis of the Microstructure after Electrochemical Test

3.3.1. WC-Co Cemented Carbides

The SEM and optical micrographs for the WC-Co alloys are presented in Figures 8 and 9, respectively. The SEM micrographs of WC-6Co and WC-8Co were all observed under the same magnification of 2000× except for WC-12Co, which was taken at 5000×. This was because the corrosion products left on the WC-12Co were very small compared to the other two WC-Co alloys.

The SEM micrographs of the three investigated WC-Co alloys displayed different topographical morphologies after electrochemical tests were conducted on them. However, WC-6Co and WC-8Co exhibited similar characteristics to each other that were very different from what was observed on the surface of the WC-12Co alloy. WC-6Co and WC-8Co both showed cracks on their surfaces where the corrosive medium penetrated. Sebeya [27] reported the same continuous cracked film on the surface of the WC-10Co sample he investigated in a similar corrosive environment. With WC-6Co (Figure 8a), the cracks formed by the corrosion product can be seen forming around individual WC particles and cracking on the Co phase, whereas with WC-8Co, the cracks were formed around an agglomeration of WC particles. It is not clear as to why this was the case as both alloys exhibited a negligible difference in their CR values. WC-12Co contained translucent patches of the corrosion product and not the cracked layer seen with WC-6Co and WC-8Co. The corrosion product layers observed on the surface of the WC-12Co alloy were discontinuous and had different patch sizes and did not seem to have severely penetrated and attacked the binder as observed with the other two WC-Co alloys. The WC-12Co alloy's resistance to severe corrosive attack can be attributed to its refined and densely packed WC structure, which prevents the Co phase to be excessively exposed to the corroding media [30,33]. The optical micrographs of the WC-Co alloys show WC-8Co (Figure 9b) as having the most severe corrosion attack on its surface. Localised corrosion in the form of large pits can be seen occurring mostly with the WC-8Co alloy, which was also observed to be the case in the work conducted by Bricín et al. [26].

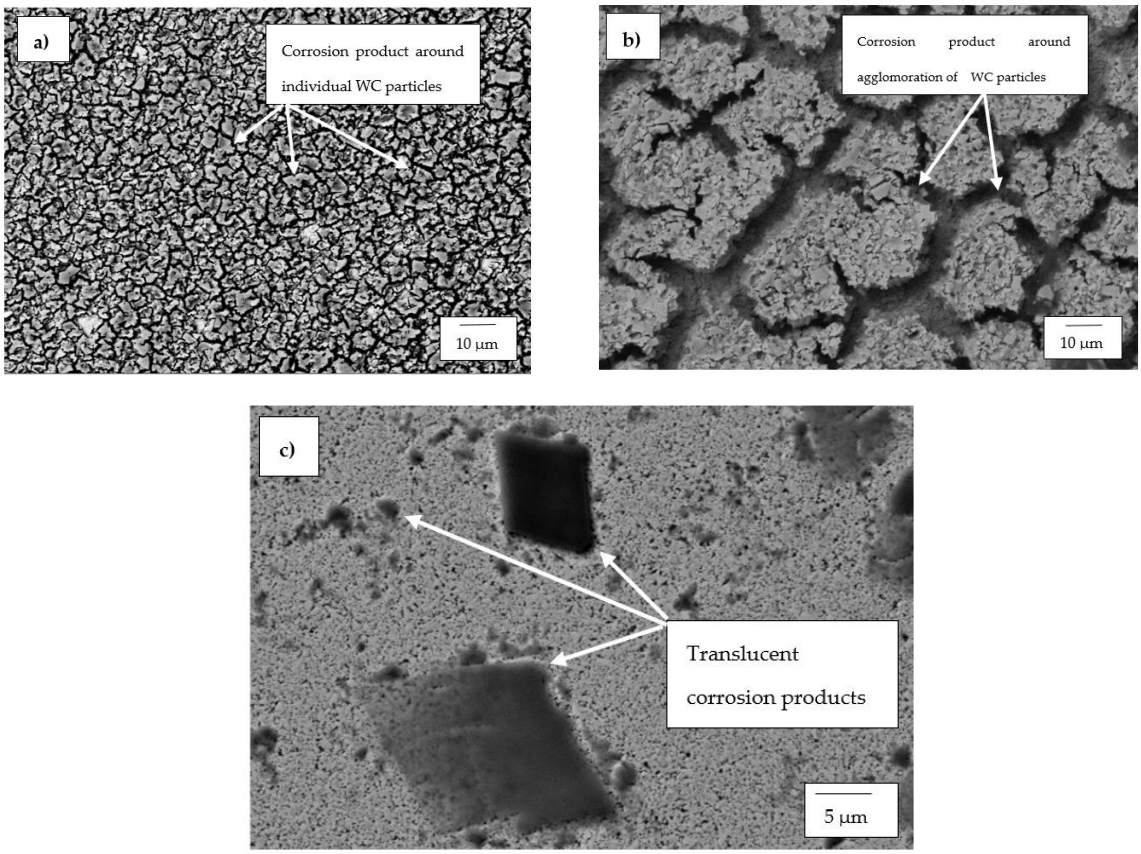

Figure 8. SEM micrographs of: (**a**) WC-6Co, (**b**) WC-8Co and (**c**) WC-12Co after undergoing electrochemical tests in 1 M H_2SO_4.

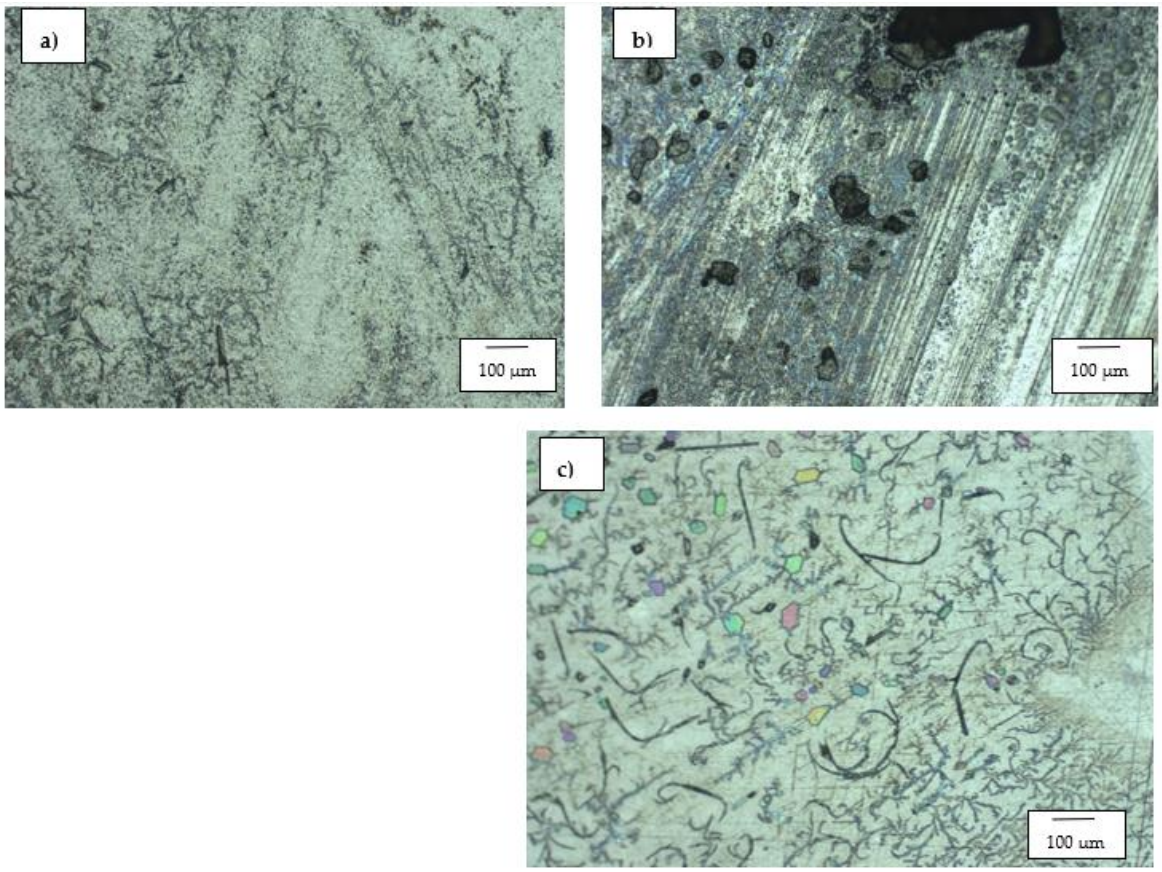

Figure 9. Optical micrographs of: (**a**) WC-6Co, (**b**) WC-8Co and (**c**) WC-12Co after undergoing electrochemical tests in 1 M H_2SO_4.

3.3.2. HCWCI Alloys

The SEM for the HCWCI alloys are presented in Figure 10. Figure 10a–f present the SEM micrographs of HCWCI-1, HCWCI-2 and HCWCI-3, respectively.

It was observed that HCWCI-1 experienced the most severe corrosion attack after polarisation tests in 1 M H_2SO_4. The appearance of the corroded surface of the HCWCI-1 alloy correlated with its high current density and corrosion rate. HCWCI-1 underwent uniform corrosion damage on its surface, and this is characterised by the manner in which corrosive medium dissolved the matrix, leaving a slightly corroded skeleton structure of the primary eutectic carbides.

The corroded surface of the HCWCI-2 alloy (Figure 10 c,d) portrays a strange corrosion morphology. Some regions of the surface (Figure 10a) that were completely exposed to the corrosive medium appear like they did not undergo any corrosive attack. However, upon close inspection, chemical attack was slightly visible on the matrix, proving that there was evidence of corrosion that took place. Additionally, the corroded grain boundaries around the Cr-rich primary carbides provide further proof that the surface did in fact undergo corrosion. Lack of obvious corrosion mechanisms like pitting or cracks in the matrix of HCWCI-2 is an indication that the alloy exhibited good corrosion resistance behaviour during the electrochemical tests. This was also confirmed by the same

observation recorded by Beimeng et al. [55] and the alloy's low current density and corrosion rate.

Similar to HCWCI-1, HCWCI-3 was expected to exhibit a severe corrosion attack on its matrix. This was expected because HCWCI-3 displayed a similar structure to that of HCWCI-1, which consists of a relatively higher volume fraction of eutectic primary carbides than HCWCI-2. HCWCI-1 and HCWCI-3 suffered more from localised corrosion than HCWCI-2 as shown in Figure 10. This phenomenon was also observed by El-Aziz et al. [37] where the structure that contained a volume fraction of eutectic primary carbides exhibited the most severe localised corrosion in the form of pits and microcrevices.

The only characteristic that the HCWCI alloys had in common was the inert behaviour the primary carbides exhibited during anodic polarisation tests. The corrosive damages in all the alloys were observed occurring in their matrices.

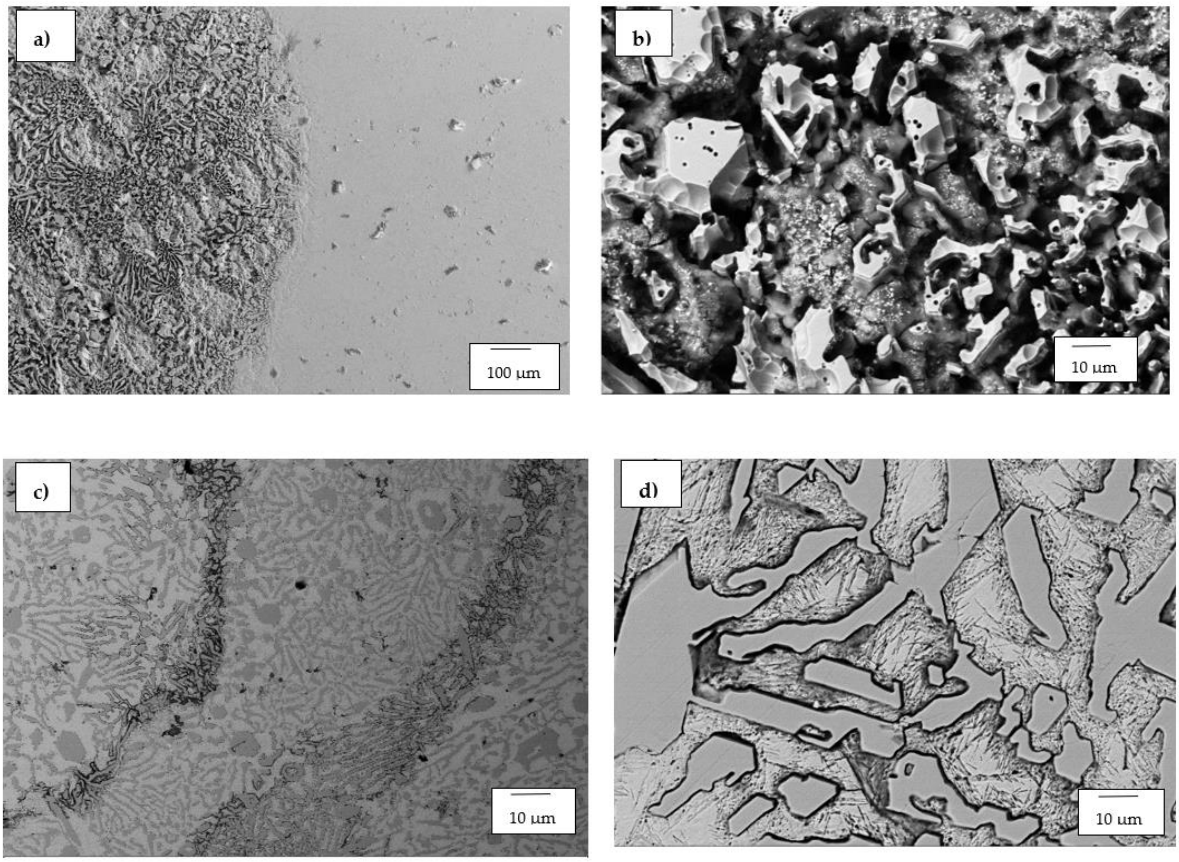

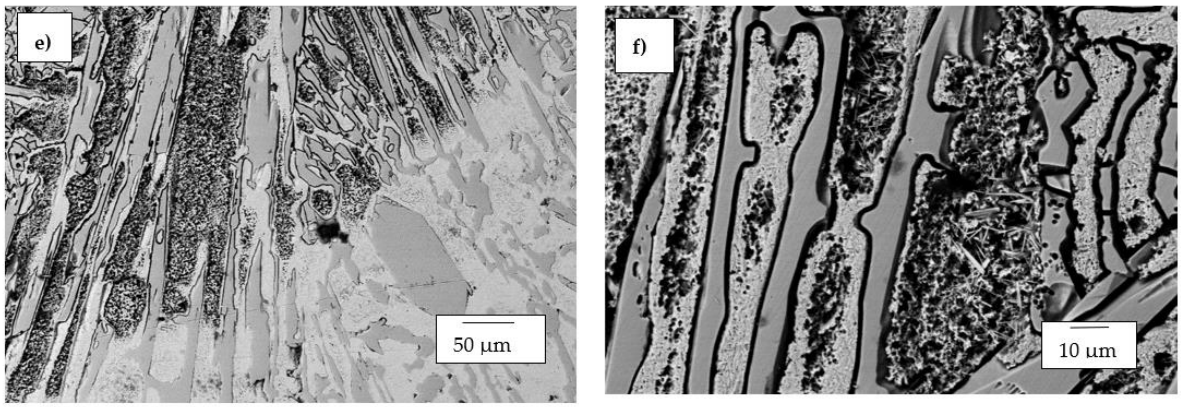

Figure 10. SEM micrographs of: (**a**,**b**) HCWCI-1, (**c**,**d**) HCWCI-2 and (**e**,**f**) HCWCI-3 after undergoing electrochemical tests in 1 M H_2SO_4.

3.3.3. The Hadfield Steel

The SEM micrographs for the Hadfield steel are presented in Figure 11. The micrographs focus on the corrosive mechanisms that occurred on the austenite grains, the carbide-rich grain boundaries and the carbide inclusions within the austenite grains.

The corrosive product (passive layer) is shown in Figure 11a,b characterised as a cracked dark-grey layer covering some parts of the corroded surface. The product layer is observed segregating within and around pits, grain boundaries and regions that are rich in carbide inclusions. The vertical black lines seen in Figure 11c shows that the twin boundaries also suffered chemical attack during the polarisation test. The same mechanisms were reported by Garfias-Garcia et al. [45] and Zhang and Zhu [46]. It is also noteworthy that there are large amounts of corrosion products that appeared as pits and craters after they were unintentionally delaminated during or after the electrochemical test. These large craters and micropores are shown more prominently in Figure 11c.

Figure 11b shows the occurrence of what is referred to as hills-and-valleys morphology observed on the corroded regions. The same type of morphology was reported by Ozgowicz et al. [43], and they reported that the observed surface after polarisation tests was a result of a mechanism known as the hydrogen depolarisation, which is common on surfaces that have undergone corrosion in an acidic medium.

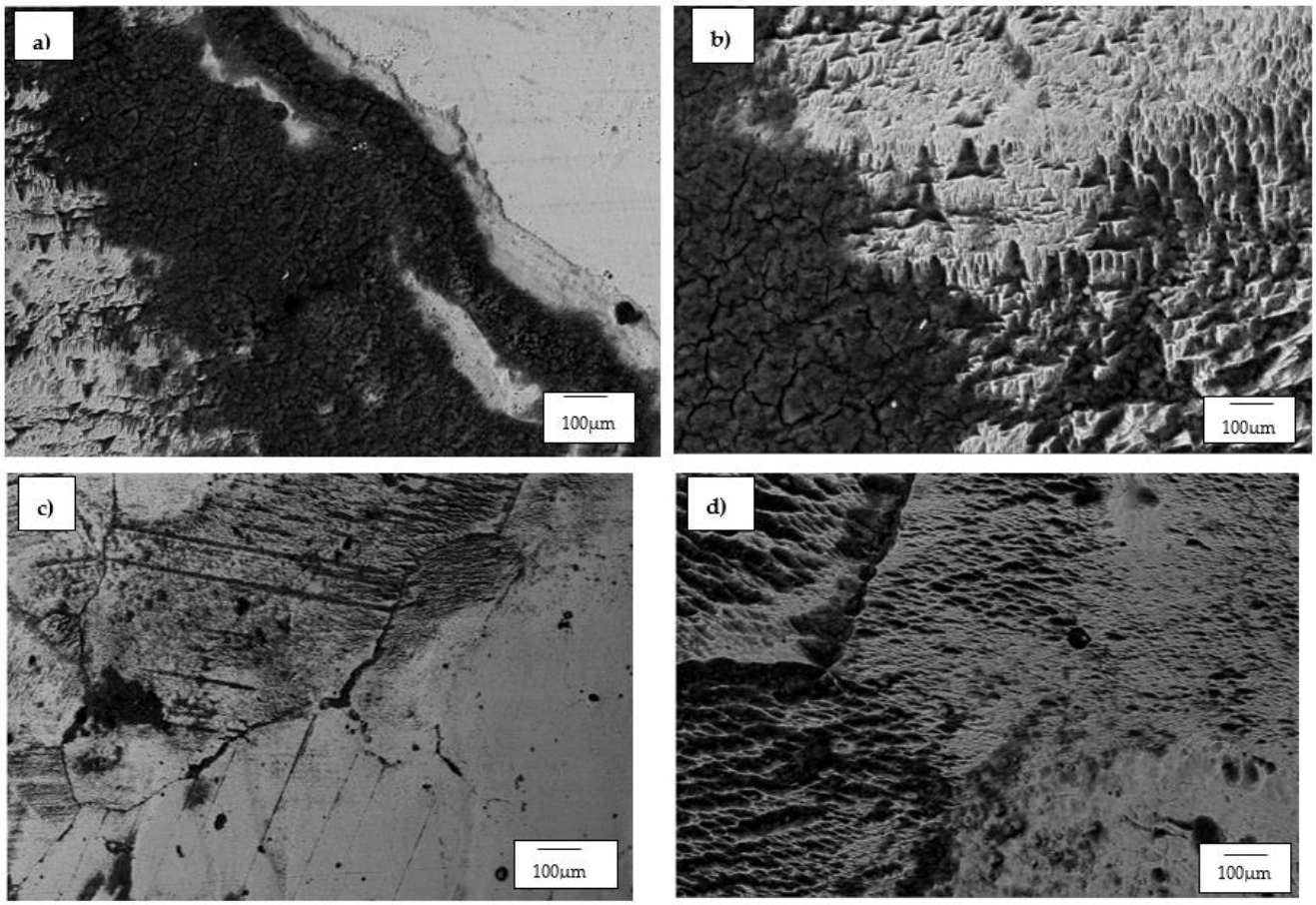

Figure 11. SEM micrographs of Hadfield steel after undergoing electrochemical tests in 1 M H_2SO_4 showing: (a) corrosion product on grain boundaries, (b) morphology after corrosion referred to as 'Hills-and-valleys', (c) corrosion product on slip-bands, and (d) corrosion product on austenite matrix.

4. Discussions

The electrochemical corrosion behaviour of the WC-Co cemented carbides, HCWCI alloys and the Hadfield steel was investigated by conducting electrochemical polarisation tests in 1 M sulfuric acid. It was observed that all of the investigated materials (except HCWCI-2) showed an active-psuedopassive transition behaviour during electrochemical tests. Figure 7 shows the potentiodynamic polarisation curves of the samples indicating the psuedopassivity region wherein maximum current densities were reached, which were then followed by a slight decrease. This feature was observed and outlined by Human and Exner [18], Marimuthu and Kannoorpatti [52] and Esmailzadeh et al. [56]. Moreover, from the obtained results, it is clear that the WC-Co alloys as a group behave similarly and have similar E_{corr} and i_{corr} values and therefore, similar corrosion rates. In the same fashion, the HCWCI behaved similarly and displayed closely related open circuit corrosion potentials and corrosion currents. There was hardly a difference between the corrosion current densities of all of these alloys, and they all show closely related corrosion rates.

The comparative behaviour of the WC-Co alloys in 1 M H_2SO_4 is shown in Table 4 and Figures 6 and 7. WC-12Co showed better resistance to corrosion compared to the other two WC-CO alloys. This conclusion was characterised by the low current density and corrosion rate that WC-12Co exhibited after undergoing electrochemical tests.

The SEM micrographs of the alloys that were taken after the alloys were exposed to the corrosive environment revealed that WC-6Co and WC-8Co experienced severe corrosion attack on their surfaces. The preferential manner in which the acidic medium selectively dissolved the grain boundaries around the WC particles lead to the same conclusion reported by Human and Exner [18], Sutthiruangwong and Mori [34], Thanjekwayo [57] Pugsley and Sockel [58], that the Co binder phase was attacked more vigorously compared to the WC grains. Figure 12 shows the SEM micrograph of WC-12Co alloy where the cracked translucent layer of the corrosion product can be seen. WC-12Co's good resistance to corrosion can thus be attributed to the manner in which the WC particles were more exposed to the corrosive medium than the Co binder, hence behaving as a shield against the dissolution of the Co binder. So instead of the acidic medium attacking the alloy, it created a translucent corrosion product layer that covered the surface of the alloy, which could or could have not assisted as a protective shield against further corrosive attack.

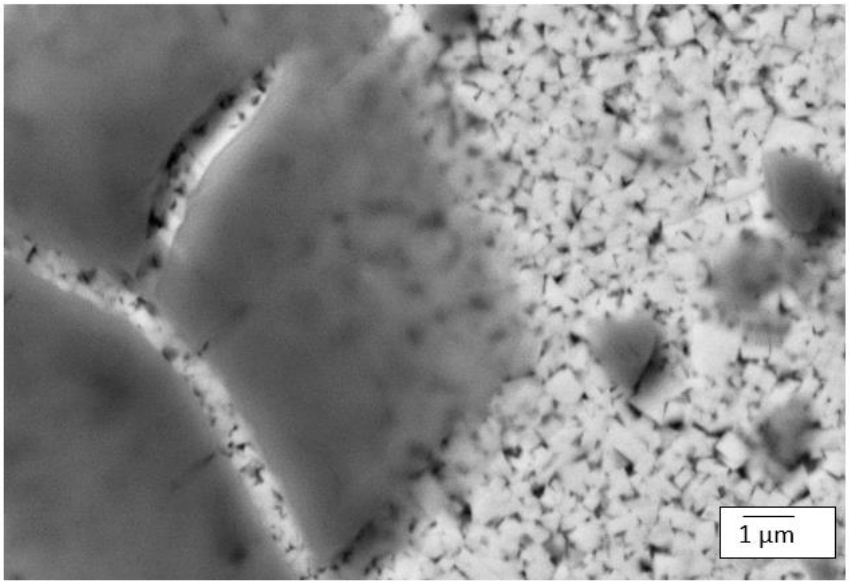

Figure 12. SEM micrograph of WC-12Co alloy showing the cracked translucent layer of corrosion product.

The EDS results given in Figures 13, 14 and 15 are typical of the results obtained from the WC-Co, HCWCI, and Hadfield steel alloys respectively. EDS analysis of WC-8Co (Figure 13) showed the preferential

dissolution of the cobalt binder. This was characterised by the decreased cobalt content and the traces of tungsten, carbon, sulphur and oxygen found in the cobalt phase. The EDS results also show very low traces of sulphur on the WC phases. This behaviour was also observed by the work conducted by Thanjekwayo [57] on the electrochemical work performed on WC-Co alloys with varying ruthenium contents.

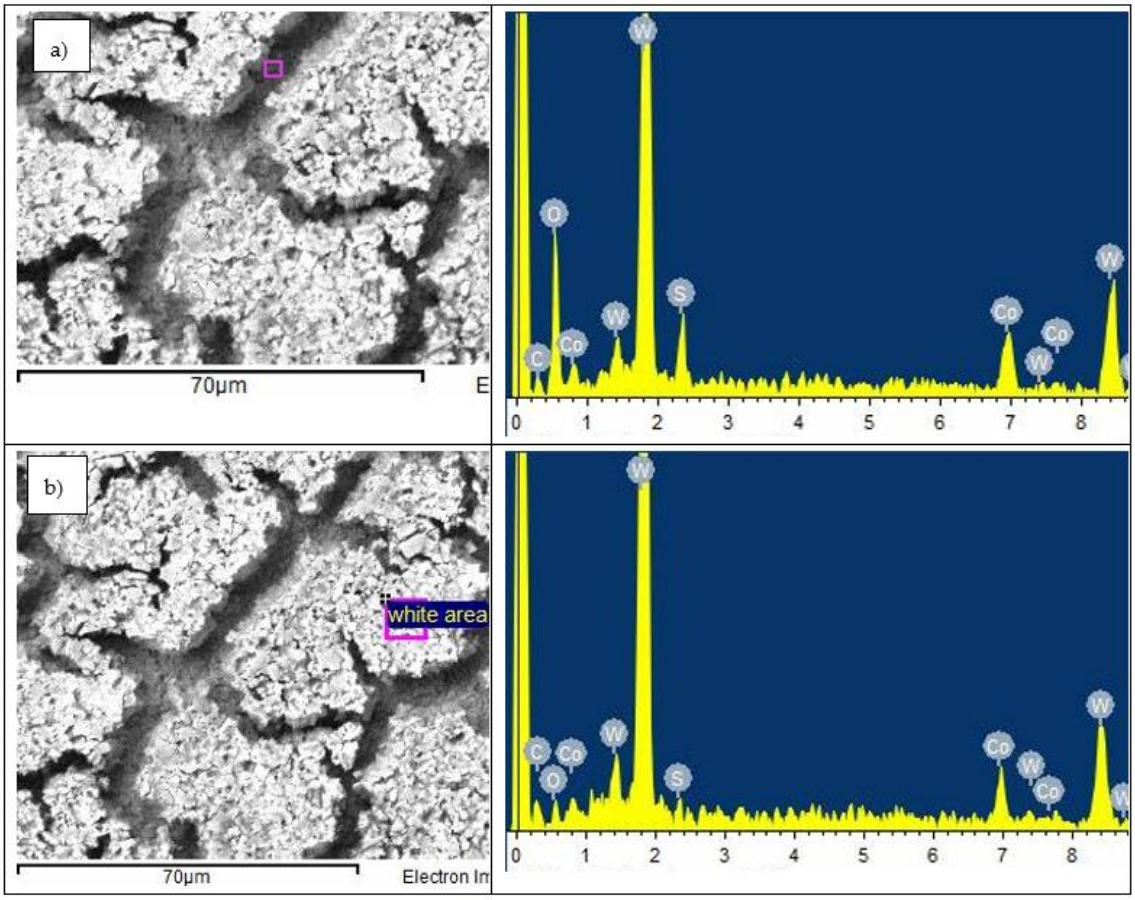

Figure 13. SEM-EDS micrograph of WC-8Co showing EDS analysis on the corrosion product layer after undergoing an electrochemical corrosion process in 1 M H_2SO_4.

Different contents of chromium and other alloying elements can significantly influence the corrosion behaviour of HCWCI alloys. However, only the effect of chromium, carbon and the morphology of the microstructure (matrix and the second phase) and the effect they had on the resistance of corrosion of HCWCI alloys will be discussed.

HCWCI-2 had the lowest value for corrosion current density and therefore, the lowest corrosion rate. This behaviour can be attributed to the alloy's chromium and carbon content and the morphology of its occurring primary carbides. HCWCI-2 exhibited a better response to corrosion than HCWCI-1 because it contained a higher content of chromium [36]. Moreover, since carbon is the main carbide-forming alloying element in cast irons, less of it means there was excess chromium retained in the matrix, thus improving the overall resistance of the alloy. The same observation was recorded in work conducted by other researchers [35,37,59].

HCWCI-3 contained the highest chromium content of the three alloys, and it was thus expected that it would exhibit the best resistance to corrosion, but the opposite was observed. However, an increase in carbon was also observed, thus affecting the Cr/C ratio and reversing the effects of chromium. This ultimately had an adverse influence on the resistance of the alloy.

Figure 10a,b,e,f show that the alloys that contained high-volume fractions of primary eutectic carbides, HCWCI-1 and HCWCI-3, suffered severely from localised corrosion. El-Aziz [37] and Poolthong et al. [60] observed the same trends. They recorded that the matrix phase close to the eutectic carbides was deprived of chromium, causing the extensive corrosive attack seen with the two alloys. The black lines seen encapsulating the primary Cr-rich carbides in HCWCI-2 and HCWCI-3 are zones wherein the most depletion of Cr was observed, showing that corrosion attack in 1 M H_2SO_4 was initiated around the carbides.

The hard primary carbides occurring in HCWCI-2 and HCWCI-3 were observed to be inert to corrosion attack, and the eutectic primary carbides seen in HCWCI-1 exhibited negligible damage during the electrochemical tests. The EDS result from the HCWCI-3 alloy (Figure 14) shows that there were no traces of sulphur on the bulky primary carbides, whereas the needle-like structure on the matrix contained a high composition of sulphur. This indicates that the corrosion behaviour of white cast irons strongly depended on the composition and morphology of their matrix.

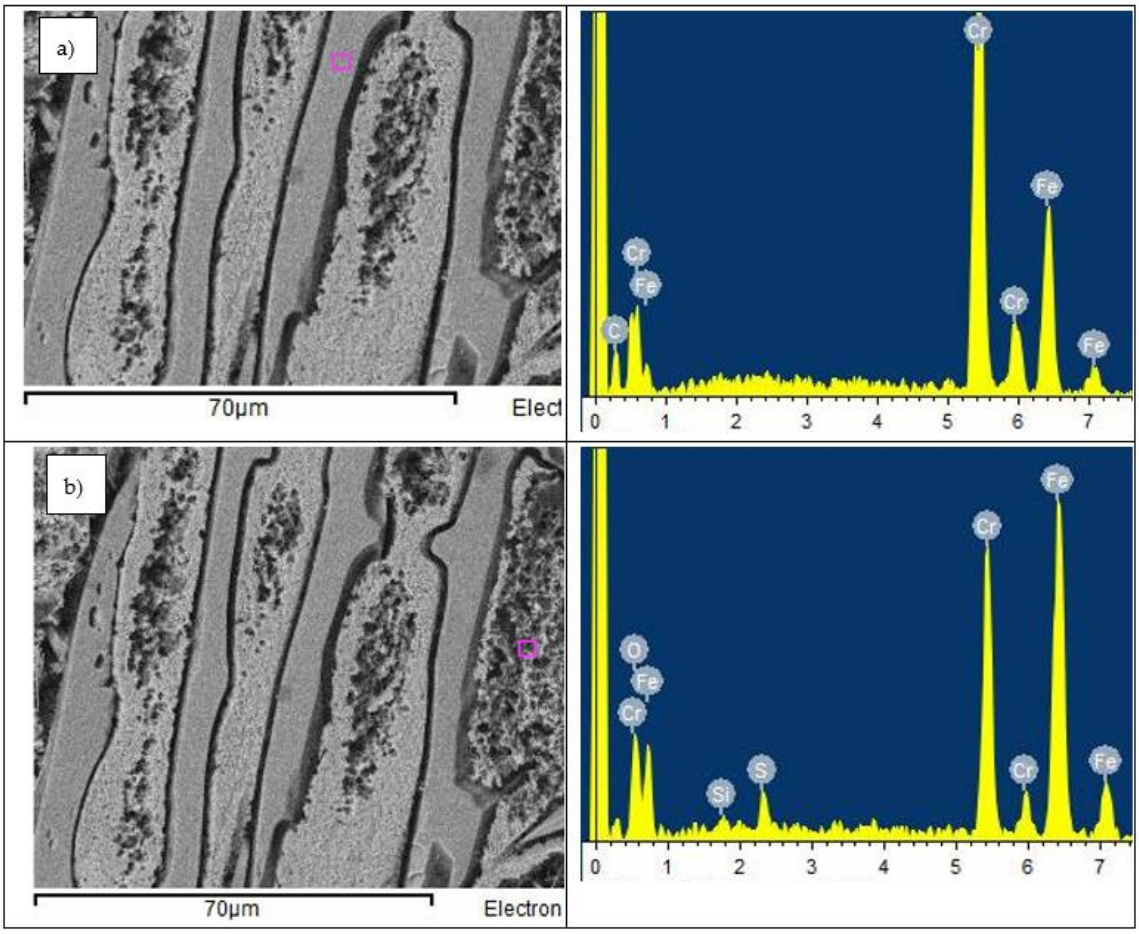

Figure 14. SEM-EDS micrograph of HCWCI-3 showing EDS analysis on: (**a**) primary carbide, and (**b**) needle-like austenitic matrix after undergoing electrochemical corrosion process in 1 M H_2SO_4.

Table 4, which is the summary of the electrochemical parameters of the investigated materials, shows that the Hadfield steel exhibited the poorest resistance to corrosion in 1 M H_2SO_4. The steel displayed the highest i_{corr} and therefore, the highest corrosion rate. However, Hadfield steel showed a similar E_{Corr} value when compared with the E_{Corr} values exhibited by the HCWCI alloys. This shows that the alloys (HCWCI and the Hadfield steel) experienced the same tendency to corrode. This was expected since both material types consisted mainly of austenite in their structures.

The regions where the surface exhibited the hills-and-valley morphology was in fact tiny craters and pores where the surface suffered severe chemical attack. Other researchers that observed the same surface structure reported that this was a result of hydrogen penetrating deeper through the cracks of the passive layer (corrosion product), bringing about the rapid deterioration of the surface [43]. The hills-and-valley morphology is seen occurring predominately on the austenitic phase. This process is known as the hydrogen polarisation mechanism, and it occurs when the hydrogen ions in electrolytic form are reduced in cathodic areas of the metal by electrons to gaseous hydrogen [61]. This corrosion process caused causes tiny craters that are close together, separated by a network of strips of uncorroded metal that look like laths (Figure 11d). Figure 15, which is the EDS results of the Hadfield steel surface, show that these uncorroded laths did not contain sulphur,

It was reported by other researchers that the severely attacked surfaces were as a result of the protective passive layer being removed during the polarisation process, causing more damage to the exposed and unprotective surface [41,43,45].

The dark lines seen around the grain boundaries, metal-carbide inclusions and the non-metallic inclusion, such as sulphide inclusions, are regions that Garfias-Garcia et al. [45] reported were caused by hydrogen penetrating deeper into the surface of the steel. Abreu et al. [62] adds that areas such as grain boundaries, twin boundaries and non-metallic inclusions are regions where the accumulation of hydrogen is mostly seen during corrosion.

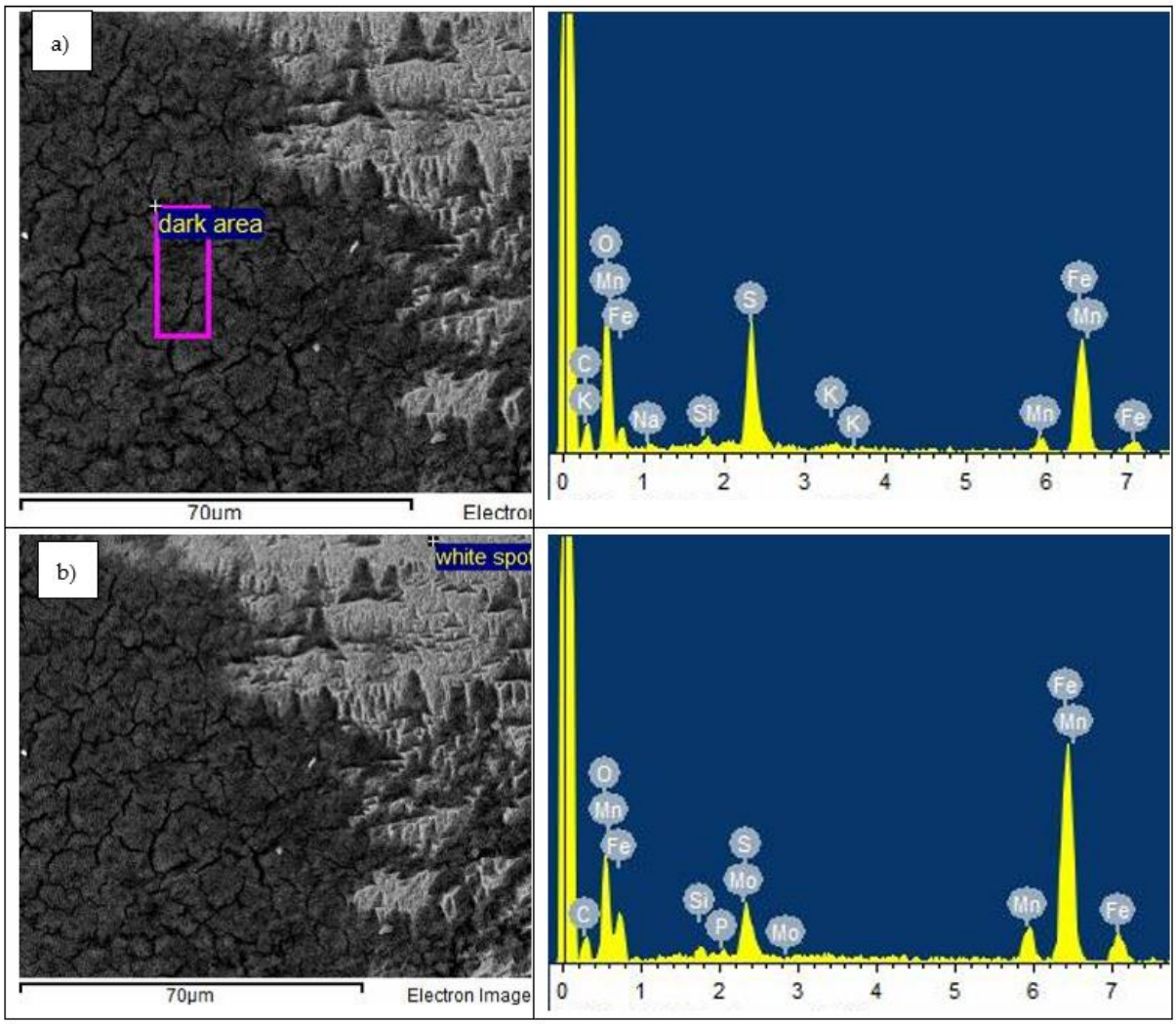

Figure 15. SEM-EDS micrograph of the Hadfield steel showing EDS analysis on: (a) darkened area of the corrosion product, and (b) lighter area of the corrosion product after undergoing electrochemical corrosion process in 1 M H_2SO_4.

The three HCWCI materials considered in this study have all proven to perform exceptionally well in resisting wear, and from this work, the corrosion resisting properties of the HCWCI-2 alloy have been shown to be the best. However, from a practical viewpoint, the material to be used as protective lining plates for chutes and skips in the mining industry must be light and relatively inexpensive. The cemented carbide materials would probably resist wear and corrosion very well, but their weight would place extra stress on any structure, as they are generally double the density of mild steel. The Hadfield steels are the least inexpensive; however, these would need very high force of impacts to develop their work-hardening ability, which is not always guaranteed. The HCWCI alloys are a good option as these are approximately the same weight as structural steels used to construct chutes and skips. With the increasing operating costs in the mining industry in recent years, the costs of the HCWCI alloys (relative to the cemented carbide grades), as well as their

ability to resist both wear and corrosion, would make them a good option for practical use.

5. Conclusions

The corrosion behaviour of different grades of WC-Co, high-Cr white cast irons and Hadfield steel in an acidic medium were investigated using electrochemical techniques. The main conclusions obtained from this study are as follows:

1. The WC-Co alloys behaved similarly as a group and displayed similar electrochemical trends. In the same fashion, the iron-based alloys (HCWCI and the Hadfield steel) showed similar behaviours. However, as a group the WC-Co alloys performed better and are more corrosion-resistant than the HCWCIs and the Hadfield steel.

2. The WC-12Co alloy, which contained the highest Co binder content and the finest WC particles in its structure, displayed the best resistance to corrosion compared to the other two WC-Co alloys. This characteristic can be attributed to its densely packed WC particles which shielded it against the aggressive dissolution of the binder. WC-12Co also contained traces of Cr in the form Cr_3C_2, which further contributed to the alloy's resistance to corrosion. Microstructure is hence an important characteristic to consider in terms of the corrosion resistance of the alloys from a specific group, not only chemical composition.

3. The corrosion resistance of the HCWCI group was shown to be strongly influenced by the volume fraction of Cr-rich primary carbides. HCWCI-2 (22 wt% Cr), which consisted of larger rod-like primary carbides in its structure, displayed exceptional resistance against corrosive attack. Although not as good as the WC-Co alloys, this level of corrosion performance indicates that the experimental HCWCI alloys can be developed into cost-effective alternatives for the mining industry.

4. HCWCI-2 recorded a corrosion resistance that was superior to all the investigated specimens. While one clearly would have to consider potential wear conditions as well, its surface succumbed to the least corrosive degradation in comparison to the other investigated alloys in this study. The Hadfield steel exhibited the poorest resistance to the corrosive attack and suffered the harshest degradation to its surface. Therefore, although it is widely perceived to be a suitable material for mining applications where both wear and corrosion must be taken into consideration, it should in the opinion of the authors not be recommended for use.

5. Based on the work conducted in this study and the results thereof, the most eligible corrosion resisting material for the proposed application of serving as a protective liner for chutes and skips in acidic environments is HCWCI with a Cr content of 22 wt%.

6. One should be cautious to not only be guided by corrosion resistance of the evaluated materials for application in chutes and liners for the mining industry, as wear resistance is also of great importance in such environments. A follow-up study is therefore in progress on the wear behaviour of the evaluated alloys to arrive at a final decision of whether the more expensive WC-Co alloys can be replaced by a new group of HCWCI alloys.

Author Contributions: D.W. and J.H.P. supervised the research conducted by V.M. V.M. wrote the first draft of the paper, with D.W. and J.H.P. revising and correcting it before submission. All authors have read and agreed to the published version of the manuscript.

Funding: The authors would like to acknowledge the University of the Witwatersrand and Riocarb Pty. Ltd. for funding this work.

Acknowledgments: The authors would like to acknowledge the School of Chemical and Metallurgical Engineering (Wits University), especially P. Dinham for preparing the SEM images, R. Gurney and the workshop technicians for preparing the samples and the administrative staff. The authors would also like to acknowledge UltraMat for providing the WC-Co samples, M. Smit from Mintek for providing the Hadfield steel and Mitak for providing the High-Cr white cast iron samples.

Conflicts of Interest: The authors declare no conflict of interests.

References

1. Cortie, M.B.; McEwan, J. J.; Enright, D. P. Materials selection in the mining industry: Old issues and new challenges. *J. South Afr. Inst. Min. Metall.* **1996**, *4*, 145-156.
2. Roberts, A. W.; Oom, M.; Wiche, S. I. Concept of boundary friction adhesion and wear in bulk solid handling. In *International Conference on Bulk Materials Storage,* Proceedings of the Chute Design Conference, Newcastle, UK, 1996.
3. Neale, M.J. *Tribology Handbook*; Butterworth-Heinemann: Oxford, UK, 1996; Volume 2.
4. Rathod, A.; Sapate, S.G.; Khatirkar, R. Scaling laws of wear by slurry abrasion of mild steel. *Appl. Mech. Mater.* **2013**, 446–447, doi:10.1016/j.wear.2018.05.010.
5. Vreeburg, W.P. Redesign of a Tata steel chute with dust liberation problems. Master's Thesis, Delft University of Technology, Delft, Netherlands, 2018.
6. Van Aarde, M.N. The optimisation of transfer chutes in the bulk materials industry. Master's Thesis, North-West University, Potchestroom, South Africa, 2009.
7. Page, J. Examples of Good and Bad Chute Design. In *Anglo American Corporation of South Africa Limited*, Proceedings of the Chute Design Conference, South Africa, 1991.
8. Chen, W.; Biswas, S.; Roberts, A. Abrasion wear resistance of wall lining materials in bins and chutes during iron ore mining. *Inter. J. Min. Process.* **2017**, *167*, 42–48.
9. Rozentals, J. Chute problems: Causes and solutions. Proceedings of the Chute Design Conference, USA, 1992.
10. Xia, R.; Li, B.; Wang, X.; Yang, Z.; Liu, L. Screening the main factors affecting the wear of the scraper conveyor chute using the Plackett-Burman method. Math. *Probl. Eng*. **2019**, *11*, doi:10.1155/2019/1204091.
11. Holmes, R. E. Selection of materials for the lining of chutes. In *Bionic Research Institute*, Proceedings of the Chute Design Conference, 1991.
12. Chintha, A. R. Metallurgical aspects of steels designed to resist abrasion and impact-abrasion wear. *Mater. Sci. Tech.* **2019**, *35*, pp. 1133-1148.
13. Davis, J.R. *Surface Engineering for Corrosion and Wear Resistance*; ASM International: London, UK, 2001.
14. Neale, M.J.; Gee, M. *Guide to Wear Problems and Testing for Industry*; William Andrew Pub: Norwich, UK, 2001.
15. Glaeser, W. *Materials for Tribology*; Elsevier: Amsterdam, Netherlands, 1992; Volume 20.

16. Pittari III, J. J.; Murdoch, H. A.; Kileczewski, ; Hornbuckle, B. C.; Swab, J. J.; Darling, K. A.; Wright, J. C. Sintering of tungsten carbide cermets with an iron-based ternary alloy binder: Processing and thermodynamic considerations. *Inter. J. Refract. Metals Hard Mater.* **2018**, *76*, 1-11.
17. Kaytbay, S.; El-Hadek, M. Wear resistance and fracture mechanics of WC–Co composites. *International Journal of Materials Res.* **2014**, *105*, 557-565.
18. Human, A. M.; Exner, H. E. The relationship between electrochemical behaviour and in-service corrosion of WC based cemented carbides. *Inter. J. Refract. Metals Hard Mater.* **1997**, *15*, 65-71.
19. Luyckx, S.; Love, A. The relationship between the abrasion resistance and hardness of WC-Co alloys. *J. South Afr. Inst. Min. Metall.* **2004**, *104*, 579-582.
20. Ndlovu, S. The wear properties of tungsten carbide-cobalt hardmetals from nanoscale up to macroscale. Ph.D Thesis, Friedrich-Alexander-Universität Erlangen-Nürnberg (FAU): Erlagen, Germany, 2009.
21. Potgieter, J.H.; Olubambi P.; Potgieter-Vermaak S. S. The corrosion behaviour of WC-Co-Ru alloys in aggressive chloride media. *Inter. J. Electrochem.* **2014,** *2014*, 1-11.
22. Bozzini, B.; De Gaudenzi, G. P.; Serra, M.; Fanigliulo A.; Bogani, F. Corrosion behaviour of WC-Co based hardmetal in neutral chloride and acid sulphate media. *Mater. Corr.* **2017**, *5*, 328-334.
23. Alar, Z.; Alar, V.; Fabijanic, T. A. Electrochemical corrosion behaviour of near-nano and nanostructured WC-Co cemented carbides. *Metal.* **2017**,*7, 69*.
24. Brookes, K. J. Corrosion damage in WC-Co. *Metal Pwdr. Rpt.* **2015**, *70*, 1-6.
25. Richter, J.; Michalik, R. Corrosion resistance of WC-Co and WC-Ni type sintered carbides in acetic acidic water solution. *Mater. Corr.* **2018**, *70*, 128-134.
26. Bricin, D.; Spirit, Z.; Kriz, A. Metallographic analysis of the suitability of a WC-Co powder blend for selective laser melting technology. *Mater. Sci. Forum.* **2018**, *919,* 3-9.
27. Sebeya, T.T. An investigation into the causes of the differences in the corrosion behaviour of WC-Co and WC-VC-Co. Master's Thesis, University of the Witwatersrand, Johannesburg, South Africa, 2013.
28. Human, A. M. The corrosion of tungsten carbide based cemented carbides. PhD Dissertation, Technical University of Darmstadt, Darmstadt, Germany, 1994.
29. Alar, Ž.; Alar, V.; Fabijanic, T. A. Electrochemical corrosion behavior of near-nano and nanostructured WC-Co cemented carbides. *Metals* **2016**, 7, 69.
30. Liu, C.; Liu, Y.; Ma, Y.; Liu, W.; He, Y. Influence of μ-size WC on the corrosion behaviour of ultrafine WC/WC-Co cemented carbides. *J. of Superhard. Mater.* **2019**, 41, 334-344.
31. Aqilah, N.; Kamdi, Z.; Todi, A. L. Wear and corrosion behaviour of tungsten carbide based coating on carbon steel. *Int. J. Integr. Eng.* **2018**, 10, 119-125.
32. Kellner, F.; Hildebrand, H.; Virtanen, S. Effect of WC grain size on the corrosion behaviour of WC-Co based hardmetals in alkaline solutions. *Int. J. Refract. Hard. Met.* **2009**, 27, 806-812.
33. Imasato, S.; Sakaguchi, S.; Okada, T.; Hayashi, Y. Effect of WC grain size on the corrosion resistance of WC-Co cemented carbides. *J. Stage.* **2001**, 48, 609-615.
34. Sutthiruangwong, S.; Mori, G. Corrosion properties of Co-based cemented carbides in acidic solutions. *Int. J. Refract. Hard. Met.* **2003**, 21, 135-145.
35. Tang, X.H.; Chung, R.; Pang, C.J.; Li, D.Y.; Hinckley, B.; Dolman, K. Microstructure of high (45 wt.%) chromium cast irons and their resistances to wear and corrosion. *Wear* **2011**, *271*, 1426–1431.
36. Tian, H.H.; Taylor, P.A. Corrosion Study on high Alloyed white cast irons in acidic and chloride containing solutions. In *International Corrosion Conference Series*, *Proceedings of the Corrosion*, National Association of Corrosion Engineers: Houston, TX, USA, 2011.
37. El-Aziz, K.; Zohdy, K.; Sallam, H. E. Wear and corrosion behavior of high-Cr white cast iron alloys in different corrosive media. *J. Bio- and Tribo-Corr.* **2015**, *1,* 1-12.
38. Kiahosseini, S.; Baygi, S.; Khalaj, G.; Khoshakhlagh, A.; Samadipour, R. A Study on Structural, Corrosion, and Sensitization Behavior of Ultrafine and Coarse Grain 316 Stainless Steel Processed by Multiaxial Forging and Heat Treatment. *J. Mater. Eng. Perform.* **2018**, 27, 271-281.

39. Tikotkar, R. G. Effect of Frictional Force and Wear Rate on Hadfield Steel. *Inter. J. Eng. Res. Tech.* **2012**, , *1*, 1-7.
40. Xiaodong, D.; Guodong, S.; Yifei, W.; Jianfeng, W. Abrasion behavior of high manganese steel under low impact energy and corrosive conditions. *Adv. Tribol.* **2009**, *2009*, doi:10.1155/2009/685648.
41. Grajcar, A.; Krukiewicz, W.; Kotodziej, S. Corrosion behavior of plastically deformed high-Mn austenitic steels. *J. Achiev. Mater. Manuf. Eng.* **2010**, *43*, 228-235.
42. Gavriljuk, V.G.; Tyshchenko, A.I.; Razumov, O.N.; Petrov, B.Y.N.; Shanina, D.; Berns, H. Corrosion-resistant analogue of Hadfield steel. *Mater. Sci. Eng*. **2006**, *420*, 47–54.
43. Ozgowicz, W.; Kurc-Lisiecka A.; Grajcar, A. Corrosion behaviour of cold-deformed austenitic alloys. In *Environmental and Industrial Corrosion-Practical and Theoretical Aspects*, Proceeding in the Intech Open: London, UK, 2012.
44. Sabzi, M.; Farzam, M. Hadfield manganese austenitic steel: A review of manufacturing processes and properties. *Mater. Res. Expr*. **2019**, *6*, 1065c2.
45. Garfias-Garcia, E.; Colin-Paniagua, F.A.; Herrera-Hernandez, H.; Juarez-Garcia, J.M.; Palomar-Pardave, M.E.; Romero-Romo, M.R. Electrochemical and Microscopy study of localised corrosion on a sensitized stainless steel AISI 304. *ECS Trans*. **2010**, *29*, 93–102.
46. Zhang, Y. S.; Zhu, X. M. Electrochemical polarisation and passive film analysis of austenitic Fe-Mn-Al steels in aqueous solutions. *Corr. Sci.* **1999**, *41*, 1817-1833.
47. Ngqase, M.; Pan, X. An overview on types of white cast irons and high chromium white cast irons. In *J. Phys: Conf. Ser*.**1495** 0.12023, , 2020.
48. Powell, G.L. Morphology of eutectic M3C and M7C3 in white iron castings. *Mater. Forum* **1980**, *3*, 33–40.
49. Chen, C.; Zhang, F. C.; Wang, F.; Liu, H.; Yu, B. D. Effect of N+Cr alloying on the microstructures and tensile properties of Hadfield steel. *Mater. Sci. Eng.* **2017**, *679*, 95-103.
50. Abdel-Karim, R.; Naguib, A.; El-Mahallawi, I. Evaluation of effect of chromium on wear performance of high manganese steel. *Mater. Sci. Tech.* **2013**, *17*, 1385-1390.
51. Machio, C.N.; Konadu, D.S.; Potgieter, J.H.; Potgieter-Vermaak, S.; Van der Merwe, J. Corrosion of WC-VC-Co hardmetal in neutral chloride containing media. *Inter. Sch. Res. Not.* **2013**, *2013*, doi:10.1155/2013/506759.
52 Marimuthu, V.; Kannoorpatti, K. Corrosion behaviour of high-chromium white iron hardfacing alloys in an alkaline solution. *J. Bio- Tribo-Corr.* **2016**, *26*, doi:10.25913/5eb39d64badee.
53. Mori, G.; Zitter, H.; Lackner, A.; Schretter, M. Influencing the corrosion resistance of cemented carbides by addition of Cr2C3, TiC and TaC. *Int. Plansee Semin.* **2001**, *2*, 222-236.
54. Luiz, L. A.; De Andrade, J.; Pesqueira, C. M.; De Araujo Fernandes Siqueira, I. B.; Sucharski, G. B.; De Sousa, M. J. Corrosion behaviour and galvanic corrosion resistance of WC and CR3C2 cermet coatings in Madeira River water. *J. Therm. Spray Technol.* **2021**, *30*, 205-221.
55. Beimeng, Q.; Beijia, W.; Chenguang, W.; Yixing, Y. Electrochemical behavior of cast iron in the presence of bacteria in water distribution systems. *Inter. J. Electrochem. Sci*. **2013**, *8*, 1813–1821.
56 Esmailzadeh, S.; Aliofkhazraei, M.; Sarlak, H. Interpretation of cyclic potentiodynamic polarization test results for study of corrosion behavior of metals: A Review. *Prot. Met. Phys. Chem*. **2018**, *54*, 976–989.
57. Thanjekwayo, N.P. The influence of Ru additions on the corrosion. Master's Thesis, University of the Witwatersrand, Johannesburg, South Africa, 2009.
58. Pugsley, V.A.; Sockel, H.G. Corrosion fatigue of cemented carbide cutting. *Mater. Sci. Eng*. *A* **2004**, *366*, 87–95.
59. Zumelzu, E.; Cabezas, C.; Goyos, I.; Parada, O.; Opitz, O. Wear and corrosion behaviour of high-chromium (14–30% Cr) cast iron alloys. *J. Mater. Process. Technol.* **2021,** 128, 1-3,250-255.
60. Poolthong, N.; Nomura, H.; Takita, M. Effect of Heat Treatment on Microstructure and Properties of Semi-solid Chromium Cast Iron. *Mater. Trans*. **2004**, *45*, 880–887.
61. Curioni, M.; Scenini, F. The Mechanism of Hydrogen Evolution During Anodic Polarization of Aluminium. *Electrochim. Acta* **2015**, *180*, 712–721.
62. Abreu , H.; Carvalho, S.; Neto, P.; Santos, R.; Freire, V.; Silva, P.; Tavares, S. Deformation induced martensite in an AISI 301LN stainless steel: Characterization and influence on pitting corrosion resistance. *Mater. Res*. **2007**, *10*, 359–366.